technische universität
dortmund

Dissertation zur Erlangung des akademischen Grades
eines Doktors der Naturwissenschaften

Search for flavour-changing neutral currents in processes with a single top quark in association with a photon using a deep neural network at the ATLAS experiment at $\sqrt{s} = 13\,\text{TeV}$

Gregor Geßner
geboren in Beckum

2019

Lehrstuhl für Experimentelle Physik IV
Fakultät Physik
Technische Universität Dortmund

Der Fakultät für Physik der Technischen Universität Dortmund in Dortmund zur Erlangung des akademischen Grades eines Doktors der Naturwissenschaften vorgelegten Dissertation.

Erstgutachter: Prof. Dr. Kevin Kröninger
Zweitgutachter: Prof. Dr. Wolfgang Wagner
Vorsitzender der Prüfungskomission: Prof. Dr. Jan Kierfeld
Vertreter der wiss. Mitarbeiter: Dr. Anton Savitsky

Datum des Einreichens der Arbeit: 23. Oktober 2019
Datum der mündlichen Prüfung: 18. Dezember 2019

Abstract

In this thesis, a search for flavour-changing neutral currents in processes involving a singly produced top quark and a photon is presented. In this search, proton-proton collision data are used which were collected by the ATLAS experiment at the LHC and correspond to an integrated luminosity of $81\,\mathrm{fb}^{-1}$. The top quark is assumed to decay into a b quark and a W boson, which is supposed to decay leptonically. Events are selected whose final state contains exactly one photon, one charged lepton, one b-tagged jet and a certain magnitude of missing transverse momentum. The background contributions, that arise from events with either an electron or a jet misidentified as photon, are estimated using data-driven techniques. The signal is modelled in an effective field theory. The signal coupling is assumed to be either left- or right-handed and to involve either an up quark or a charm quark. Assuming only one of these signal couplings being present at a time, a discriminant is constructed using a deep neural network which classifies events into signal and background candidates. A profile likelihood fit is performed to improve the background prediction and to estimate the signal strength. Since no signal contribution is observed in data and the data are found to be consistent with the background expectation, upper exclusion limits are set on the branching ratios $\mathcal{B}(t \to u\gamma)$ and $\mathcal{B}(t \to c\gamma)$. The observed limits at a confidence level of 95 % on the branching ratio are $\mathcal{B}(t \to u\gamma, \text{left-handed}) < 2.8 \times 10^{-5}$, $\mathcal{B}(t \to u\gamma, \text{right-handed}) < 6.1 \times 10^{-5}$, $\mathcal{B}(t \to c\gamma, \text{left-handed}) < 22 \times 10^{-5}$ and $\mathcal{B}(t \to c\gamma, \text{right-handed}) < 18 \times 10^{-5}$. These limits are interpreted as limits on the cross section for the production of a top quark and a photon via a flavour-changing neutral current, and as limits on the absolute value of the sum of the Wilson coefficients $C_{\mathrm{uB}}^{(ij)*}$ and $C_{\mathrm{uW}}^{(ij)*}$ for the left-handed and $C_{\mathrm{uB}}^{(ij)}$ and $C_{\mathrm{uW}}^{(ij)}$ for the right-handed couplings.

Zusammenfassung

In dieser Disseration wird die Suche nach quarkflavourverändernden neutralen Strömen vorgestellt, die in Prozessen mit einem einzeln produzierten Top-Quark und einem Photon auftreten. Die untersuchten Daten wurden am ATLAS-Detektor am LHC in Proton-Proton Kollisionen aufgezeichnet und entsprechen einer integrierten Luminosität von $81\,\text{fb}^{-1}$. Es wird angenommen, dass das Top-Quark in ein b-Quark und ein W-Boson zerfällt, das wiederum leptonisch zerfällt. Es werden Ereignisse selektiert, deren Endzustand aus genau einem Photon, einem geladenen Lepton, einem b-tagged Jet und einem Mindestbetrag an fehlendem transversalen Impuls besteht. Die Untergrundbeiträge von Ereignissen, in deren Endzustand entweder ein Elektron oder ein Jet fälschlicherweise als Photon identifiziert wurde, werden mit Daten-basierten Techniken abgeschätzt. Das Signal wird im Kontext einer effektiven Feldtheorie modelliert. Die angenommene Signalkopplung ist entweder links- oder rechtshändig und involviert entweder ein Up-Quark oder ein Charm-Quark. Unter der Annahme, dass nur eine dieser Signalkopplungen zeitgleich präsent ist, wird jeweils ein tiefes neuronales Netz trainiert, um Ereignisse als Signal- oder Untergrundkandidaten zu klassifizieren. In einem Profile-Likelihood-Fit wird die Untergrundvorhersage verbessert und die Signalstärke abgeschätzt. Weil kein Signalbeitrag in Daten gefunden wurde und die Untergrundvorhersage mit den Daten übereinstimmen, werden obere Ausschlussgrenzen auf die Verzweigungsverhältnisse $\mathcal{B}(t \to u\gamma)$ und $\mathcal{B}(t \to c\gamma)$ gesetzt. Die beobachteten Ausschlussgrenzen auf das Verzweigungsverhältnis mit einem Konfidenzniveau von 95 % sind $\mathcal{B}(t \to u\gamma, \text{linkshändig}) < 2{,}8 \times 10^{-5}$, $\mathcal{B}(t \to u\gamma, \text{rechtshändig}) < 6{,}1 \times 10^{-5}$, $\mathcal{B}(t \to c\gamma, \text{linkshändig}) < 22 \times 10^{-5}$ und $\mathcal{B}(t \to c\gamma, \text{rechtshändig}) < 18 \times 10^{-5}$. Diese Ausschlussgrenzen werden als Ausschlussgrenzen auf den Produktionswirkungsquerschnitt eines Top-Quarks und eines Photons durch einen quarkflavourverändernden neutralen Strom und als Ausschlussgrenzen auf den Absolutwert der Summe der Wilson-Koeffizienten $C_{\text{uB}}^{(ij)*}$ und $C_{\text{uW}}^{(ij)*}$ für die linkshändigen und $C_{\text{uB}}^{(ij)}$ und $C_{\text{uW}}^{(ij)}$ für die rechtshändigen Kopplungen interpretiert.

Contents

1 Introduction

1.1 Motivation of analysis

The Standard Model (SM) of particle physics describes the current knowledge in this field in a minimal model. It includes all known elementary particles and three of the four fundamental interactions. For decades, a huge variety of experiments has been performed with increasing precision at different facilities whose results confirm the SM. Thus, the SM is one of the most precisely tested models in physics.

Nevertheless, the SM lacks to explain some observations in nature which leads to several open questions widely discussed in physics. For instance, based on cosmological observations, only less than 5 % of the mass in our universe is assumed to be described by the SM. The residual mass is assumed to arise from Dark Matter and Dark Energy. Another issue is the observed baryonic asymmetry in our universe which exceeds the imbalance between matter and anti-matter predicted by the SM. However, as many predictions of the SM agree with several experimental outcomes with a high precision, the SM is seen as a lower-energy limit of a greater theory.

Many so-called Beyond the Standard Model (BSM) theories exist which extend the SM and give answers to some of its open questions. Such extensions may predict physical quantities whose values deviate from those of the SM. In several BSM models, deviations may arise for cross sections of processes including a flavour-changing neutral current (FCNC). In such processes, the flavour of a quark is changed in a neutral current (NC) interaction without altering its electric charge. In the SM, any FCNC is forbidden at tree level, i.e. by a direct coupling, and highly suppressed by the Glashow-Iliopolus-Maiani (GIM) mechanism in processes including a loop of a particle. As a consequence, the SM predicts tiny cross sections for such processes. In contrast, multiple BSM theories include effects that increase those cross sections. Consequently, searches for FCNCs enable to probe the SM and to look for hints for BSM physics. As the data of current experiments become sensitive to them, numerous searches for processes involving such an FCNC are performed. But so far, neither a hint for a deviation from the SM in processes including an FCNC nor a hint for any BSM model has been found.

The top-quark sector is well suited to search for FCNCs with a high precision. On the one hand, the top quark[1] plays an extraordinary role in many BSM theories. On the other hand, it has unique properties like a large mass which result in specific kinematic properties of events including a top quark. As no FCNC in the top-quark sector has been observed yet, exclusion limits are set on the branching ratios $\mathcal{B}(t \to qX)$ with $q = u, c$ and $X = g, Z, \gamma, H$. In Figure 1, the currently best experimental limits are shown and compared to the SM expectation and to the maximal predictions of selected BSM theories. While the SM predicts branching ratios below 10^{-11}, the predictions of the BSM models exceed them by several orders of magnitude. As the observed limits have already reached the predictions of BSM models, searches for FCNCs in the top-quark sector work superbly to either confirm or constrain BSM models.

In this thesis, the search for FCNCs in processes with a singly produced top quark in association with a photon is presented [11]. It is the first search for such processes in which data taken at a centre-of-mass energy of $\sqrt{s} = 13\,\text{TeV}$ are studied and in which proton-proton collision data recorded at the ATLAS experiment at the Large Hadron Collider (LHC) are used. In this search, the clean signature of photons left in the detector as well as the unique kinematic properties of the signal processes are exploited. Four signal couplings are tested which are modelled in an effective field theory (EFT). They are either left-handed (LH) or right-handed (RH) and involve either an up quark or a charm quark. Both the production- and decay-mode processes are taken into account for which Feynman diagrams are shown in Figure 2. In the production mode, a top quark is singly produced in association with a photon. In the decay mode, a $t\bar{t}$ system is created with one top quark decaying SM-like and the other via an FCNC. Although both processes interfere when an additional quark is emitted in the production mode, interference effects are found to be negligible at the reached centre-of-mass energy [12]. For each signal coupling, a deep neural network (NN) is trained to construct a discriminating variable which separates signal-like events from background candidates. As no signal contribution is found in data and the data are consistent with the background prediction, exclusion limits on the branching ratios $\mathcal{B}(t \to u\gamma)$ and $\mathcal{B}(t \to c\gamma)$ are calculated. The observed $95\,\%$ confidence level (CL)

---

[1] Throughout this thesis, charge-conjugated particles and processes are implied.

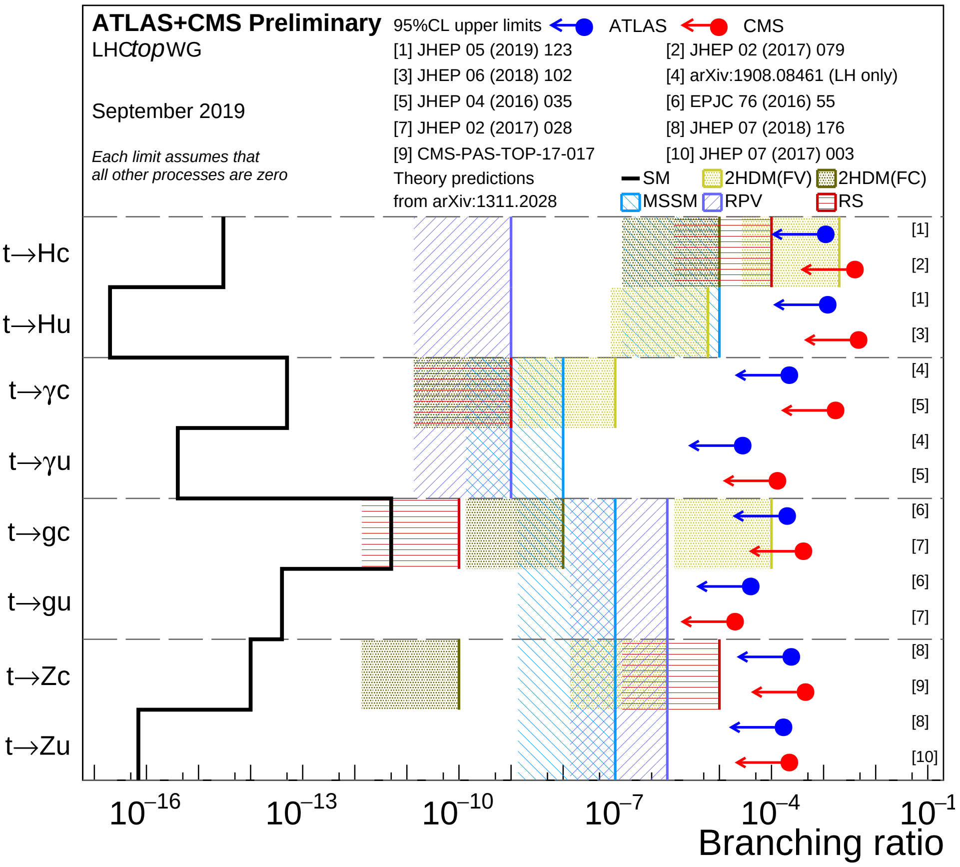

Figure 1: Summary [1] of the currently best observed 95 % CL limits on the branching ratios of the top quark decaying via an FCNC involving a neutral boson $t \to Xq$ ($X = g, Z, \gamma, H; q = u, c$) by the ATLAS and CMS collaborations. For the exclusion limits for the decay $t \to \gamma q$ set by the ATLAS collaboration, only the left-handed coupling is assumed. These observed limits are compared to the SM predictions [2] and the maximal predictions of several BSM theories. These BSM models are the 2HDM with flavour violating Yukawa coupling (*2HDM(FV)*) [3, 4], the 2HDM with flavour conservation (*2HDM(FC)*) [5], the MSSM with 1 TeV squarks and gluinos (*MSSM*) [6], the MSSM with R-parity violation (RPV) [7, 8], and the model with a warped extra dimension in the Randall-Sundrum framework (RS) [9, 10].

exclusion limits amount to $\mathcal{B}(t \to u\gamma, \mathrm{LH}) = 2.8 \times 10^{-5}$, $\mathcal{B}(t \to u\gamma, \mathrm{RH}) < 6.1 \times 10^{-5}$, $\mathcal{B}(t \to c\gamma, \mathrm{LH}) < 22 \times 10^{-5}$ and $\mathcal{B}(t \to c\gamma, \mathrm{RH}) < 18 \times 10^{-5}$. These limits are interpreted as limits on the production cross section $\sigma(pp \to t\gamma)$ including either a $tu\gamma$ or $tc\gamma$ coupling, and as limits on the absolute value of the sum of Wilson coefficients $C_{\mathrm{uB}}^{(ij)*}$ and $C_{\mathrm{uW}}^{(ij)*}$ for the LH and $C_{\mathrm{uB}}^{(ij)}$ and $C_{\mathrm{uW}}^{(ij)}$ for the RH couplings. This search improves the previously best experimental limits on those branching ratios [13] by an order of magnitude and yields the best limits to date.

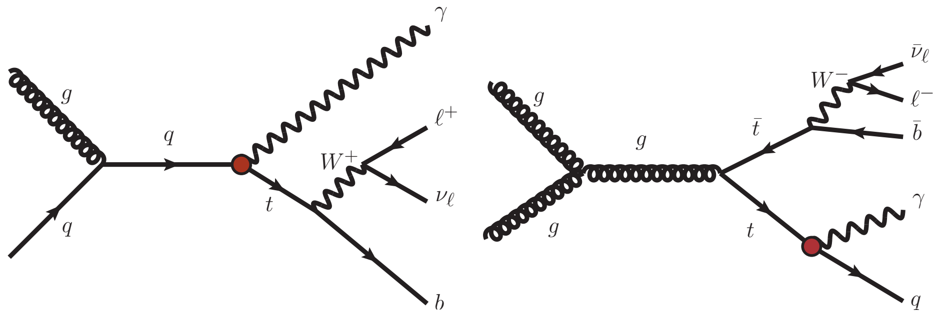

(a) Production mode: $qg \to t\gamma \to \ell^+\nu_\ell b\gamma$ **(b)** Decay mode: $gg \to t\bar{t} \to \ell^-\bar{\nu}_\ell\bar{b}\,q\gamma$

Figure 2: Exemplary Feynman diagrams for processes containing an FCNC with a $tq\gamma$ coupling with $q = u, c$ at tree level in the production (a) and decay mode (b). The coupling of interest is marked as red dot.

This thesis is structured following the general analysis strategy. In Section 2, the theoretical principles of the SM, BSM models of interest and the EFT to describe processes including an FCNC are introduced. The ATLAS detector located at the LHC is presented in Section 3. The data and simulated samples are described in Section 4. In Section 5, the reconstruction and identification (ID) of physics objects are explained. In Section 6, the measurement of the photon ID efficiency focusing on the matrix method is detailed. The event selection is summarised in Section 7 and the estimation of background contributions is given in Section 8. In Section 9, the separation of signal from background events using a deep NN is explained. The estimations of the sources of systematic uncertainties are described in Section 10. The statistical analysis and the final exclusion limits are presented in Section 11. In Section 12, concluding remarks are given.

1.2 Definition of common variables and conventions

The ATLAS detector and kinematic properties of physics objects are described using common variables which are motivated by the cylindrical geometry of the detector. A right-handed coordinate system is defined with its origin being the nominal collision point of the beams. The x-axis points to the centre of the LHC, while the y-axis points upwards perpendicularly to its plane. Both axes build up the transverse plane. The z-axis goes along the beam pipe. For the reconstruction of physics objects, the four-momentum, p^μ, is defined as

$$p^\mu = \begin{pmatrix} E \\ \vec{p} \end{pmatrix} = \begin{pmatrix} \sqrt{m_0^2 + p_x^2 + p_y^2 + p_z^2} \\ \vec{p} \end{pmatrix} , \tag{1}$$

whereby E denotes the total energy, m_0 is the rest mass, and $\vec{p} = (p_x, p_y, p_z)^\mathrm{T}$ is the momentum. Other kinematic variables are:

$$\text{transverse momentum: } p_\mathrm{T} = |\vec{p}_\mathrm{T}| = \sqrt{p_x^2 + p_y^2} , \tag{2}$$

$$\text{azimuthal angle: } \phi = \arctan\left(\frac{p_x}{p_y}\right) \in (-\pi, \pi] , \tag{3}$$

$$\text{polar angle: } \theta = \arctan\left(\frac{p_\mathrm{T}}{p_z}\right) \in [0, \pi] , \tag{4}$$

$$\text{rapidity: } y = \frac{1}{2} \ln\left(\frac{E + p_z}{E - p_z}\right) \in (-\infty, \infty) , \tag{5}$$

$$\text{pseudorapidity: } \eta = -\ln\left[\tan\left(\frac{\theta}{2}\right)\right] \in (-\infty, \infty) , \tag{6}$$

$$\text{angular distance in the } \eta\text{-}\phi \text{ plane: } \Delta R = \sqrt{(\Delta\eta)^2 + (\Delta\phi)^2} . \tag{7}$$

The impact parameter of a reconstructed particle is defined as the distance of closest approach of its (extrapolated) trajectory to another object.

In this thesis, natural units are used, i.e. the physical constants c and $\hbar$ equal unity. Consequently, energies, momenta and masses are given in units of energy. Moreover, the electric charge of a particle, q_p, is given in units of the absolute value of the electric charge of an electron, $|q_e| = 1.6 \times 10^{-19}\,\mathrm{C}$. When drawing Feynman diagrams, the horizontal axis represents the time, while the vertical axis illustrates any space coordinate. Charged leptons and anti-leptons are commonly referred to as $\ell^{(\mp)}$, other anti-particles are indicated by a bar over the letter. The W^+ and W^-

bosons are commonly referred to as W bosons, and the superscript of the Z^0 boson is typically omitted.

1.3 Publications and collaborations

In this thesis, different analyses are presented which were performed in collaboration with other scientists at various institutes. In the following, my specific contributions to these analyses are listed:

- **ATLAS Collaboration, *Search for flavour-changing neutral currents in processes with one top quark and a photon using 81 fb^{-1} of pp collisions at $\sqrt{s}$ = 13 TeV with the ATLAS experiment*, Phys. Lett. B 800 (2020) 135082**
  This search is the main topic of my thesis. I worked on each of its components which are: the development of an analysis strategy, the simulation of the production-mode process of the production mode, the definitions of physics objects and regions, the background estimations, the separation of signal from background by a deep neural network, the estimation of uncertainties, the statistical analysis and the setting of exclusion limits.

- **M. Barros et al., *Study of interference effects in the search for flavour-changing neutral current interactions involving the top quark and a photon or a Z boson at the LHC*, 2019, arXiv: 1909.08443**
  For this study, I was one of the supervisors of Salvatore La Cagnina who worked on the quantification of the interference effects for the $tu\gamma$ and $tc\gamma$ coupling. As supervisor, for instance, I helped with technical issues, discussed intermediate results and next steps of the analysis.

- **ATLAS Collaboration, *Measurement of the photon identification efficiencies with the ATLAS detector using LHC Run 2 data collected in 2015 and 2016*, Eur. Phys. J. C 79 (2019)** and **G. Geßner on behalf of the ATLAS Collaboration, *Photon identification with the ATLAS detector*, PoS EPS-HEP2017 (2017) 760**
  For the measurement presented in these publications, I worked on the matrix method (a.k.a inclusive method) which measures the photon identification efficiency.

2 Theoretical principles

The current understanding of particle physics is summarised in the SM [14–16]. It was developed by various physicists over decades in the 20th century, while the interplay between theoretical predictions and experimental observations inspired a continuous development to its current formulation. In today's experiments, the SM is challenged in high-precision measurements.

As the SM cannot explain all of the observations in nature, multiple BSM theories exist which extend the SM. A special phenomenon is the FCNC. In a process including an FCNC, a quark is converted into another quark which has the same electric charge, while emitting an electrically neutral boson. In the SM, such processes are highly suppressed, whereas their probabilities are increased in several BSM theories. Such deviations are extensively searched for as they may hint to BSM physics. In many searches, a model-independent approach is used to describe hypothetical processes. Such an approach is relied on a EFT which ignores the inner structure of a coupling. But to this day, no hint for any BSM model has been found.

In Section 2.1, a brief overview of the SM is given. FCNCs in the SM and in BSM theories of interest are explained in Section 2.2, focusing on the top-quark sector. The EFT used to describe the FCNC interactions is presented in Section 2.3. Interferences between processes with an FCNC interaction including a top quark and a photon are described in Section 2.4.

2.1 Overview of the Standard Model of particle physics

The SM is a quantum field theory (QFT). It describes all elementary particles such as quarks and leptons and three of the four fundamental interactions. Every particle arises from an excited state of a quantum field and is defined by a unique set of quantum numbers. The three interactions are the strong, weak and electromagnetic force which are represented by internal gauge symmetries and mediated by characteristic force carriers. Only the gravitational force is not yet included. Its effects, however, are negligible at the energy scales currently reached in experiments in particle physics. Another component of the SM is the Higgs mechanism [17–19] which is responsible for the mass of all elementary particles. It introduces an additional quantum field whose excited state is the Higgs boson (H).

In Figure 3, the elementary particles of the SM with selected quantum numbers and their participation in the different interactions are illustrated. Their properties are detailed in the following sections.

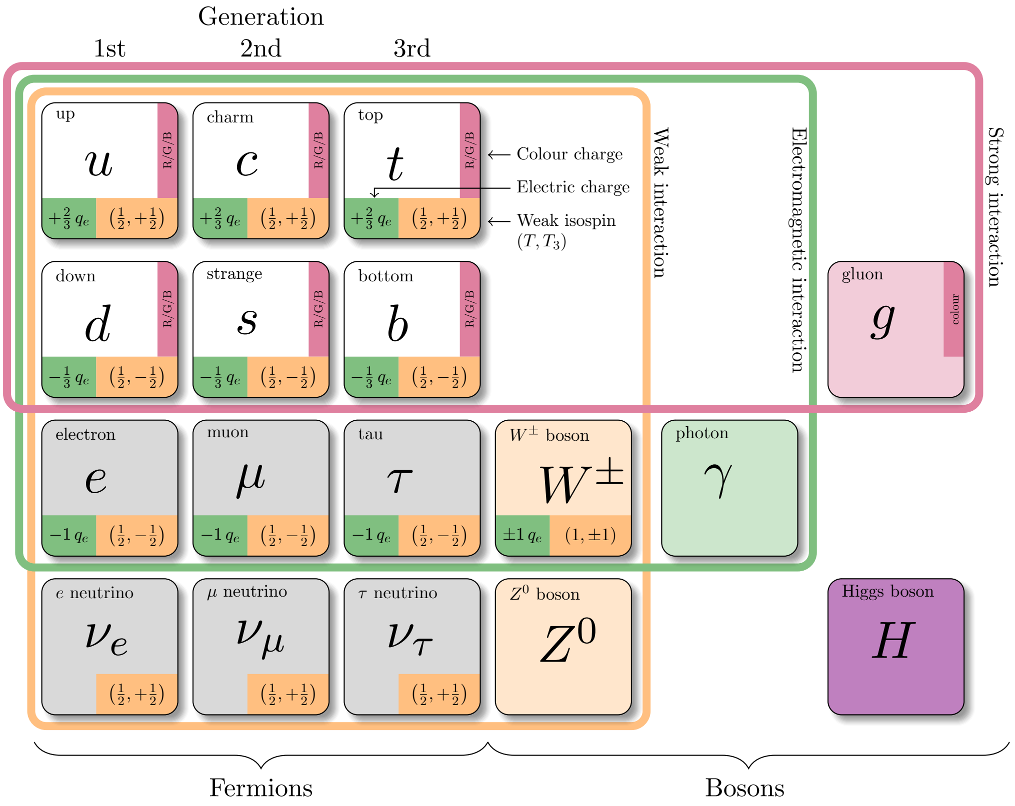

Figure 3: Illustration of the fundamental particles in the SM and how they interact. As quantum numbers, the colour and electric charge, and the weak isospin are shown. The quarks and leptons are shown as white and grey boxes, respectively. The mediators of the forces are shown as colour-shaded boxes corresponding to the colour code of the interaction. The Higgs boson is shown in purple.

The dynamics and kinematics of the quantum fields are controlled by a Lagrangian density function. It contains 19 free parameters which describe masses, mixing angles of quark flavours, coupling strengths of the interactions and symmetry-violating phases. They have been measured directly or indirectly in multiple experiments. Multi-dimensional fits taking into account the individual measurements are performed to obtain the most precise values for those parameters.

2.1.1 Matter particles: quarks and leptons

The elementary particles forming our matter are fermions, which have a half-integer spin, and classified as quarks or leptons. They are grouped into three generations sorted by their mass. The quarks and the electrically charged leptons of the first generation are the lightest and only stable particles of their kind. They form the matter of which we are made. The particles of the other generations are more massive and decay into lighter particles. The uncharged leptons are the neutrinos which are assumed to be massless in the SM. The counterpart of each particle is its anti-particle which has opposite charges.

A particular property of an elementary particle is its chirality which is a Lorentz-invariant quantity. Its LH projection is computed using the operator $P_L = (1 - \gamma^5)/2$ with the Dirac matrix γ^5, while the RH projection is computed using $P_R = (1 + \gamma^5)/2$. The chirality of a massless particle is equal to its helicity, or handedness. When both its spin and momentum point into opposite directions, it is LH, and RH in the case of the same direction. The helicity is not Lorentz-invariant, e.g. for massive particles, it depends on the reference frame.

Quarks

There are six quarks with different flavours. The up quark (u) and down quark (d) form the first generation, and the charm quark (c) and strange quark (s) build the second generation. The top quark (t), which is discussed in more detail in Section 2.1.3, and bottom quark (b) are the quarks of the third generation. The mass of the quarks ranges from $\mathcal{O}(1\,\mathrm{MeV})$ for the lightest quarks to $\mathcal{O}(100\,\mathrm{GeV})$ for the heaviest quarks. Each quark carries a colour charge, red (R), blue (B) or green (G), and a defined electric charge of either $+2/3\,q_e$ or $-1/3\,q_e$. With respect to the weak interaction[1], LH quarks form weak isospin doublets. Each doublet consists of an up-type quark with the weak isospin and its third component of $(T, T_3) = (1/2, +1/2)$, and a down-type quark with $(1/2, -1/2)$. The RH fermions build weak isospin singlets, i.e. $T = 0$. The same holds for anti-quarks with altered handedness.

All quarks participate in the strong and electromagnetic interaction. Only the quarks of a weak isospin doublet may interact via the weak force, whereas those of a singlet do not.

Leptons

The other fermions in the SM are the six leptons. Each of the three generations consists of a lepton with an electric charge of $1\,q_e$ and an electrically neutral neutrino. The first generation is formed by the electron (e) and its electron neutrino (ν_e). The second generation consists of the muon (μ) and its partner (ν_μ). The tau (τ) and the tau neutrino (ν_τ) build the last generation. The mass of the charged leptons ranges from $\mathcal{O}(100\,\mathrm{keV})$ to $\mathcal{O}(1\,\mathrm{GeV})$, while the neutrinos are assumed to be massless. The LH leptons and RH anti-leptons form weak isospin doublets with $(T, T_3) = (1/2, \pm 1/2)$, analogously to the quark sector. The RH leptons and LH anti-leptons build singlets.

All charged leptons may interact via the electromagnetic force, while the neutrinos do not participate in this interaction. The leptons that are part of a weak isospin doublet may interact via the weak interaction, while those of a singlet do not participate in it. None of the leptons interact via the strong interaction, since leptons do not carry a colour charge.

2.1.2 Interactions

In the SM, three of the four fundamental interactions are described. They are mediated by bosons, which have an integer spin. Above a certain energy scale, the electromagnetic and the weak force are unified into the electroweak interaction.

---

[1] Note that for elementary fermions, the flavour eigenstates w.r.t to the weak interaction and the mass eigenstates are different.

Strong interaction

The strong force holds together the atomic nucleus and binds the constituents of the nucleons within this core. The theoretical description of the strong interaction is called quantum chromodynamics (QCD), represented by the non-abelian unitary group $SU_C(3)$. The subscript C refers to the colour charge to which the mediators of this force couple. The gauge bosons and force carriers are the massless gluons (g) of which eight different configurations exist. These configurations differ in the superposition of colour charges. As a consequence, self-interactions among gluons are possible. Since quarks are the only fermions carrying a colour charge, they are the only fermions participating in the strong interaction. The range of this force is infinite, i.e. the gluon has an infinite lifetime.

The coupling constant of the strong force, $\alpha_s(Q)$, is a function of the energy, Q, which is transferred by a gluon in an interaction. The dependence of this running coupling on the energy results in two peculiar effects. At high energies, the coupling becomes tiny. As a consequence, quarks can be treated as quasi-free particles. This phenomenon is called asymptotic freedom. At low energies, the coupling reaches high values which forces the quarks to form composites, called hadrons. This so-called hadronisation happens at a time scale of $\mathcal{O}\left(10^{-24}\,\mathrm{s}\right)$. This effect is known as colour confinement. Hadrons are colour neutral, achieved by the presence of all three colour charges, or of a colour and its anti-colour charge. Hadrons are categorised by the number of valence quarks which determine all quantum numbers of a hadron. Mesons consist of a quark and an anti-quark. Baryons contain three quarks. The most prominent baryons are the neutron (n) and the proton (p) which consist of three quarks of the first generation. Tetraquarks are comprised of four quarks and were discovered at the Belle experiment in 2003 [20]. Pentaquarks consist of five quarks and were firstly observed by the LHCb experiment in 2015 [21]. Hadrons with even more valence quarks may exist, too.

Within a hadron, gluons may be created, and annihilated or split into quark-anti-quark pairs. All the elementary particles present in a hadron are commonly denoted as partons. Each parton carries an unknown fraction, x, of the momentum of the hadron. The probability to find a parton, i, with a certain fraction of the momentum is given by its parton distribution function (PDF), $f_i(x, Q)$, which depends on the energy, Q. These functions are different for each hadron and have been measured at different facilities, as the SM does not predict them.

Electromagnetic interaction

The electromagnetic force is present in our daily life, e.g. as electricity or mobile communication. This interaction is represented by the symmetry group $U_{\mathrm{QED}}(1)$ and described by the quantum electrodynamics (QED). Its mediator is the photon (γ) which is a massless gauge boson. It only couples to particles that have an electric charge. As the photon is electrically neutral, self-interactions are forbidden. The coupling constant is given by the fine-structure constant, $\alpha_{\mathrm{QED}}(Q)$, which is a function of the energy, Q, and rises with increasing energy. The range of this interaction is infinite, i.e. the photon has an infinite lifetime.

Weak interaction

The weak force is responsible for $\beta^{\pm}$ decays, for instance, and is described by the symmetry group $SU_L(2)$. Its force carriers are the massive W^+, W^- and Z^0 boson. They couple to the third component of the weak isospin, T_3, i.e. the interaction is purely LH. The W bosons are electrically charged with $q_{\mathrm{W}} = 1\,q_e$ and have a mass of $m_{\mathrm{W}} = (80.379 \pm 0.012)\,\mathrm{GeV}$ [22]. The Z boson is electrically neutral and its mass equals $m_{\mathrm{Z}} = (91.1876 \pm 0.0021)\,\mathrm{GeV}$ [22]. Due to the relatively large mass of the mediators, the force acts only on small distances of subatomic ranges. Both mediators decay after a mean lifetime of $\mathcal{O}\left(10^{-25}\mathrm{s}\right)$ into a pair of leptons or quarks. The coupling constant, $\alpha_{\mathrm{W}}(Q)$, is a function of the energy, Q, and becomes stronger at higher energies. The coupling is identical for both W bosons, but slightly different for the Z boson.

Electroweak unification

The electroweak interaction unifies the electromagnetic and the weak force. While at low energies, both forces act differently, they both appear as part of a unified interaction above an energy of $\mathcal{O}(100\,\mathrm{GeV})$. Its group product is given by $SU_L(2) \times U_Y(1)$. The subscript Y denotes the weak hypercharge which is defined using the electric charge and third component of the weak isospin of a particle as $2\,(q_p - T_3)$. The four massless gauge bosons are the W^1, W^2, W^3 and B boson. Due to the spontaneous electroweak symmetry breaking to U_{QED}, induced by the Higgs mechanism, four superpositions of the gauge bosons are obtained. Three of them become massive by gauging the quantum fields, which matches observations. The combination of the W^1 and W^2 bosons results in the $W^{\pm}$ bosons as

$$\begin{pmatrix} W^+ \\ W^- \end{pmatrix} = \frac{1}{\sqrt{2}} \begin{pmatrix} 1 & i \\ 1 & -i \end{pmatrix} \begin{pmatrix} W_1 \\ W_2 \end{pmatrix} . \tag{8}$$

The electrically neutral bosons γ and Z are obtained by

$$\begin{pmatrix} \gamma \\ Z \end{pmatrix} = \begin{pmatrix} \cos\theta_{\mathrm{W}} & \sin\theta_{\mathrm{W}} \\ -\sin\theta_{\mathrm{W}} & \cos\theta_{\mathrm{W}} \end{pmatrix} \begin{pmatrix} B \\ W_3 \end{pmatrix} \tag{9}$$

with the Weinberg angle being defined as

$$\cos\theta_{\mathrm{W}} = \frac{m_{\mathrm{W}}}{m_{\mathrm{Z}}} . \tag{10}$$

Each electroweak interaction containing two fermions is described by a current, J^{μ}. It is distinguished between a charged current (CC) associated to a W boson and an up-type and down-type particle, and a NC involving either a photon or a Z boson and either two up-type or down-type particles. The current J^{μ} has a vectorial and an axial-vector component, indicated by the letters V and A, respectively, and is expressed by

$$J^{\mu} \propto \overline{\psi}_f G \gamma^{\mu} \left(c_{\mathrm{V}} - c_{\mathrm{A}} \gamma^5 \right) \psi_i \tag{11}$$

with the initial ψ_i and final fermion state $\overline{\psi}_f$, the coupling constant G, the Dirac matrices γ, and the charge parameters c_{V} and c_{A}. The coupling constant and the charged parameters depend on the type of current and the participating boson. In Table 1, an overview of the parameters for the different currents is given. The NC associated to the photon is vector-like only. Its coupling strength equals the electron charge. The parameter c_{V} is proportional to the electric charge of the participating fermion, q_p. Both currents that include a massive boson have a vectorial–axial-vectorial ($V - A$) structure, while their coupling constants and parameters slightly differ from each other.

The peculiarity of the CC is that it allows for transitions of quark flavours between two generations. Thereby, an up-type quark changes over to a down-type quark

Table 1: Overview of the parameters which characterise the types of current of the electroweak interaction. The participating boson, the coupling strength G, and the charge parameters c_{V} and c_{A} are given.

Boson	Current	G	c_{V}	c_{A}
γ	NC	q_e	$z = q_p/q_e$	0
W boson	CC	$g = q_e/\sin\theta_{\mathrm{W}}$	T_3	T_3
Z boson	NC	$g' = g/\cos\theta_{\mathrm{W}}$	$T_3 - z\sin^2\theta_{\mathrm{W}}$	T_3

and vice versa. The transition probabilities are given by the Cabibbo-Kobayashi-Maskawa (CKM) matrix, V_{CKM}, [23, 24], which describes the mixing of the quark flavour eigenstates of the weak interaction with their mass eigenstates. It is a 3×3 unitary matrix usually parametrised by three mixing angles and a symmetry-violating phase. By convention, it connects the quark flavour eigenstates, $q' = d', s', b'$, of the down-type quarks to their mass eigenstates, $q = d, s, b$, and is written as

$$\begin{pmatrix} d' \\ s' \\ b' \end{pmatrix} = \begin{pmatrix} V_{\mathrm{ud}} & V_{\mathrm{us}} & V_{\mathrm{ub}} \\ V_{\mathrm{cd}} & V_{\mathrm{cs}} & V_{\mathrm{cb}} \\ V_{\mathrm{td}} & V_{\mathrm{ts}} & V_{\mathrm{tb}} \end{pmatrix} \begin{pmatrix} d \\ s \\ b \end{pmatrix} , \tag{12}$$

whereby the indices refer to the different quark flavours. The diagonal elements describe transitions within a generation and are close to unity. The off-diagonal elements, however, decrease with increasing distance from the diagonal and describe transitions between two generations. The transition probability from quark i to quark j is proportional to the square of the matrix element $|V_{ij}|^2$.

2.1.3 The top quark

The top quark was discovered at the Tevatron at the DØ and CDF experiments in 1995 [25, 26]. It is the most massive particle in the SM with a mass of $m_{\mathrm{top}} = (172.9 \pm 0.4)\,\mathrm{GeV}$ [22]. This results in a mean lifetime of $\mathcal{O}\left(10^{-25}\,\mathrm{s}\right)$ which is smaller than the hadronisation time. For this reason, the top quark typically decays before it may form a hadron. This is an outstanding property and makes it an important ingredient in a variety of probes of the SM and in searches for hints for BSM physics.

In pp collisions at the LHC at a centre-of-mass energy of $\sqrt{s} = 13\,\text{TeV}$, top quarks are predominantly produced in pairs via the strong interaction. The dominant production process is the gluon fusion process, $gg \to t\bar{t}$, as shown in the Feynman diagrams for the s- and t-channel at leading order (LO) in QCD[2] in Figures 4a and 4b, respectively. In the s-channel, the total centre-of-mass energy is transferred, while in the t-channel only a fraction of it is transferred. The annihilation of a quark and an anti-quark is another production process of a $t\bar{t}$ system, $q\bar{q} \to t\bar{t}$, as shown in the Feynman diagram at LO in Figure 4c.

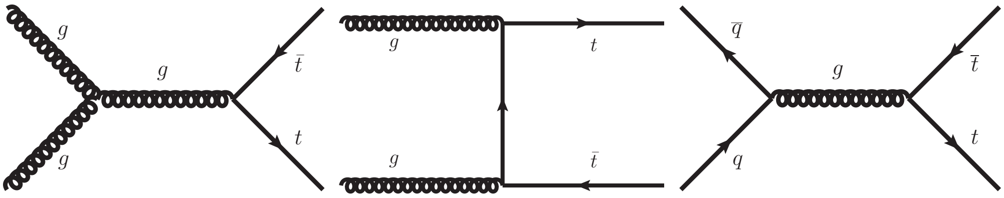

(a) Gluon fusion, s-channel **(b)** Gluon fusion, t-channel **(c)** $q\bar{q}$ annihilation

Figure 4: Feynman diagrams for the $t\bar{t}$ production via the strong interaction at LO by gluon fusion in the s- (a) and t-channel (b) and by the $q\bar{q}$ annihilation (c).

Besides the pair production, top quarks can be produced singly via the electroweak interaction. It is distinguished between the dominant t-channel, tW-channel and s-channel, as seen in the Feynman diagrams at LO in Figure 5. In the t-channel, an up-type quark and a b quark exchange a W boson and a single top quark is produced in association with another down-type quark, $q_1 b \to t q_2$. The b quark in the initial state originates from a gluon splitting within one of the protons. In the tW-channel, a gluon and a b quark interact, and a W boson and a top quark are produced, $gb \to Wt$. In the s-channel, a quark and an anti-quark are annihilated resulting in a W boson, which decays into a b quark and a top quark, $q_1 \bar{q}_2 \to t\bar{b}$.

The top quark only decays via the electroweak interaction. Since the CKM matrix element $|V_{\text{tb}}|$ is approximately unity, it almost exclusively decays into a b quark and a W boson. Other decay channels into another down-type quark in association with a W boson are suppressed because the respective CKM matrix elements are

---

[2] The process at LO is the process with the least number of interactions as possible. If not stated otherwise, the orders given refer to the number of QCD interactions.

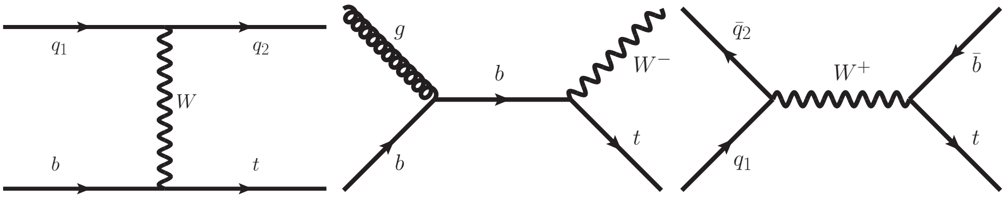

(a) t-channel **(b)** tW-channel **(c)** s-channel

Figure 5: Feynman diagrams for the single-top quark production via the electroweak interaction at LO in the t- (a), tW- (b), and s-channel (c).

tiny. The total width, Γ, of the top quark is measured to be $1.42^{+0.19}_{-0.15}$ GeV [22]. It is strongly dominated by the partial width $\Gamma(t \to Wb)$ which is used to approximate the total width. The branching ratio of a particular decay is defined as the partial width of a certain decay over the total width. The decay of the top quark is classified depending on the subsequent W-boson decay either as leptonic or hadronic.

2.1.4 Higgs mechanism

The Higgs mechanism gives mass to all elementary particles. It introduces an isospin doublet ϕ and a potential $V(\phi)$ of the form

$$V(\phi) = \mu^2 \phi^\dagger \phi + \lambda^2 \left(\phi^\dagger \phi\right)^2 \tag{13}$$

with the parameters $\mu^2 < 0$ and $\lambda^2 > 0$. The basis of the doublet is rotated in a way that the first component becomes zero. The vacuum expectation value, v, of the second component is equal to $v = |\mu/\lambda| = 246\,\text{GeV}$, i.e. the ground state being the state of the lowest energy is different from zero. Such a ground state breaks the electroweak symmetry. In general, every breaking of a continuous and global symmetry enforces a so-called Goldstone boson to exist [27]. In the case of the Higgs mechanism, four such bosons are required. Three of them are eliminated by gauging the electroweak quantum fields, which results in the massive W and Z bosons. The last Goldstone boson is identified with the Higgs boson, named in honour of Peter Higgs who did outstanding work to develop this mechanism next to François Englert, Robert Brout and others. The Higgs boson was discovered as the last particle of the SM at the ATLAS and CMS experiments in 2012 [28, 29].

The Higgs mechanism allows for gauge invariant mass terms for fermions in the Lagrangian density of the SM. Those terms describe the coupling of the fermion fields to the Higgs field. The coupling strength between both fields, which is called Yukawa coupling, y_f, is proportional to the mass of the respective fermion.

2.1.5 Open questions

The SM is well tested and many experiments confirmed its predictions. However, it leaves several open questions which are reasoned by observations or related to the mathematical framework of the SM. A selection of these questions is listed below.

Number and values of parameters The numbers and values of the parameters in the SM are not predictable. It is unclear why there are 19 free parameters, and what the origin of their values is.

Unification of forces It is desired to combine the strong and the electroweak interaction into a Grand Unified Theory. Eventually, a Theory of Everything is sought which combines the gravitational and the other three fundamental forces.

Concept of naturalness For aesthetic reasons, the parameters of a model are thought to be of similar orders of magnitude. In the SM, however, the values are spread over many orders of magnitude, e.g. the masses of the particles ranging from $\mathcal{O}(1\,\mathrm{keV})$ to $\mathcal{O}(1\,\mathrm{GeV})$. The hierarchy problem is closely connected to it, which refers to an unnatural fine-tuning of parameters. The Higgs mass would diverge at the `Planck` scale, $\Lambda_\mathrm{P} = 10^{19}\,\mathrm{GeV}$, at which gravitational effects become relevant. This divergence would arise from quantum loop corrections of quarks to the propagator of the Higgs boson. They are artificially cancelled out by an appropriate renormalisation.

Neutrino masses In contrast to the prediction of the SM, neutrinos are found to be massive in observations of neutrino oscillations [30–32]. Moreover, it is still an open question if neutrinos are Majorana particles, which means they are their own anti-particles, or if anti-neutrinos exist, i.e. neutrinos are Dirac particles.

Dark Matter and Dark Energy Based on observations, e.g. of the rotational velocity of stars around the centre of their galaxy, cosmological models assume that around 25 % of the mass in our universe is made up by Dark Matter, which is an unknown form of matter. Dark Energy is assumed to represent roughly 70 % of the mass, which is an unknown form of energy and would explain the measured expansion of our universe. Only the residual fraction of 5 % of the content in our universe is assumed to be described by the SM.

Matter-anti-matter asymmetry In our universe, a large predominance of matter over anti-matter is observed. However, the SM only predicts a much smaller imbalance between them which is induced by symmetry violations.

Various BSM theories have been developed to answer those open questions. Such theories modify an interaction, change the flavour or mass eigenstates of the fermions, or introduce new particles or dimensions. However, as the predictions of the SM precisely agree with the outcomes of many experiments, it is seen as the lower-energy limit of an even greater theory.

2.2 Flavour-changing neutral currents

The flavour of an elementary fermion may be changed in a CC or in an NC. A CC involves an electrically charged boson, while an NC is associated with an electrically neutral boson. Focusing on the top-quark sector, the top quark may decay either into a down-type quark and a W boson in a CC, or via an FCNC into another up-type quark and either a Z boson, photon, gluon or Higgs boson. The SM predicts branching ratios $\mathcal{B}(t \to qX)$ with $q = u, c$ and $X = \gamma, Z, g, H$ of the order of 10^{-16} to 10^{-12} [2], while the branching ratios in BSM models are up to $\mathcal{O}\left(10^{-3}\right)$. All these branching ratios predicted by the SM and their maximal predictions in BSM models are shown in combination with the currently best experimental limits set by the ATLAS and CMS collaborations in Figure 1. The experimental limits have already reached the sensitivity of some BSM models which motivates to continue to search for FCNCs.

Various searches for processes including an FCNC in the top-quark sector have been conducted at different accelerators and detectors in the last decades. Impressive results were achieved at the experiments at the Hadron-Elektron-Ringanlage (HERA) [33], where electrons or their anti-particles, called positrons, were collided with protons, at the Tevatron [34] colliding protons with anti-protons, and at the Large Electron-Positron Collider (LEP) [35], where positron-electron collision data were studied. All these facilities are already shut down. In these days, searches using data taken at the ATLAS and the CMS detector at the LHC reach the highest sensitivity for processes including an FCNC and involving a top quark. To this day, no hint for any FCNC in the top-quark sector has been observed and exclusion limits on the branching ratios $\mathcal{B}(t \to qX)$ with $q = u, c$ and $X = \gamma, g, Z, H$ have been set. The best exclusion limits obtained by the different experiments are illustrated in Figure 6. Over time, the limits improved from $\mathcal{O}(0.01)$ by more than three orders of magnitude. The currently best limits are achieved for the decays $t \to ug$ and $t \to u\gamma$ which are of $\mathcal{O}\left(10^{-4}\right)$, while the latter one is derived in this analysis. As the Higgs boson was firstly discovered at the LHC in 2012, exclusion limits on the branching ratios $\mathcal{B}(t \to uH)$ and $\mathcal{B}(t \to cH)$ were only set by the ATLAS and CMS experiments. At HERA and LEP, where leptons participated in the collisions, the branching ratios for the top-quark decay involving either a photon or a Z boson are correlated, which gives a smooth transition between the respective limits. As at LEP, leptons were exclusively collided, no limits on the branching ratios $\mathcal{B}(t \to ug)$ and $\mathcal{B}(t \to cg)$ were set. The improvements of the limits achieved while operating the LHC are outstanding and yield the currently best limits for the branching ratios of each of the decays.

2.2.1 Occurrences in the Standard Model

In the SM, CCs are responsible for changing the flavour of a quark. FCNCs involving an electrically neutral boson are forbidden at tree level since NCs are diagonal in flavour space, and only couple up-type to up-type quarks and down-type to down-type quarks. Off-diagonal elements allowing for flavour changes, however, are zero. At higher orders of the electroweak interaction, FCNCs are highly suppressed by the GIM mechanism [57]. This mechanism is based on interferences which occur when both the initial and final state of a process are indistinguishable. For example, the two processes for the leptonic decay of the neutral anti-kaon, $\bar{K}^0$, into a $\mu^-\mu^+$ pair have an identical initial and final state, as shown in so-called box diagrams in Figure 7. This anti-kaon decays electroweakly in association with two W bosons and with either an up or a charm quark. The probability of each individual process is

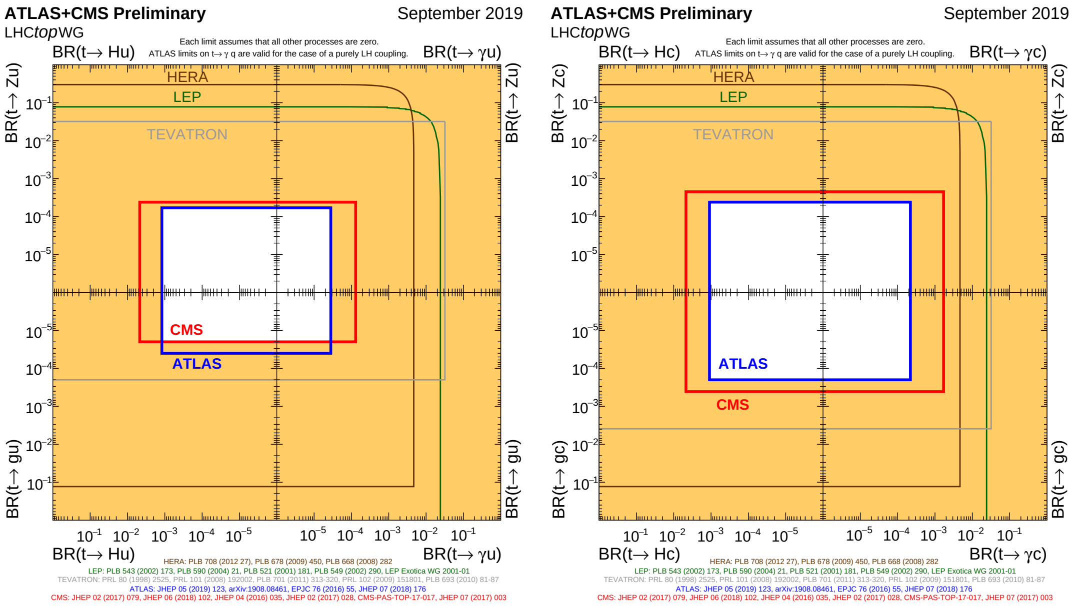

(a) $t \to Xu$ **(b)** $t \to Xc$

Figure 6: Illustration [1] of the 95 % CL limits on the branching ratios of $t \to Xu$ (a) and $t \to Xc$ (b) with $X = \gamma, g, Z, H$ set by the experiments at the accelerators HERA [36–38], Tevatron [39–43] and LEP [44–48] as well as by the CMS [13, 49–53] and ATLAS [11, 54–56] collaborations at the LHC.

almost the same. This probability is expressed as cross section, which consists of the so-called matrix element describing the interaction of the particles in the initial and final states, and of the integration over the phase space. But as the matrix elements of the individual processes have an opposite sign, the processes interfere destructively. Consequently, a tiny total cross section is obtained which is proportional to the term $\left|m_{\mathrm{u}}^{2} - m_{\mathrm{c}}^{2}\right| / m_{\mathrm{W}}^{2}$ with the mass of the up quark, m_{u}, and that of the charm quark, m_{c}. As the difference between the squares of both masses is negligible in relation to the square of the W-boson mass, this process is suppressed. The same argument holds for other processes including an FCNC.

In the top-quark sector, FCNCs only occur in so-called loop diagrams at higher orders of the electroweak interaction. In Figure 8, the decay of a top quark in an NC interaction associated to a photon is shown. The top quark couples to a down-type

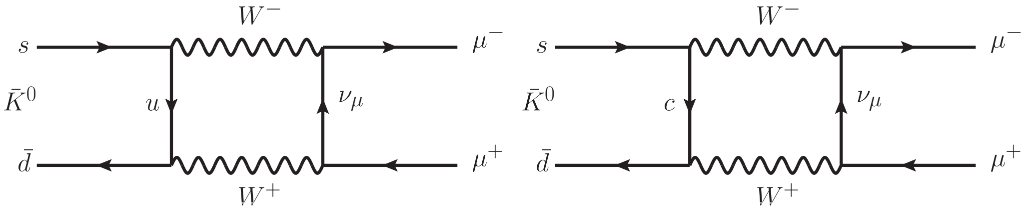

(a) $\bar{K}^0 \to \mu^-\mu^+$ involving an up quark **(b)** $\bar{K}^0 \to \mu^-\mu^+$ involving a charm quark

Figure 7: Feynman diagrams for the leptonic decay of the neutral anti-kaon, $\bar{K}^0$, into a muon and an anti-muon involving either an up (a) or a charm quark (b).

quark, q_1, and the W boson which form a loop. The down-type quark, q_1, is either a d, s or b quark and the W boson radiates a photon. The outgoing up-type quark, q_2, is either an up quark or a charm quark. Due to the GIM mechanism, the total cross section is small which translates into tiny branching ratios $\mathcal{B}(t \to u\gamma)$ and $\mathcal{B}(t \to c\gamma)$ of $\mathcal{O}\left(10^{-16}\right)$ and of $\mathcal{O}\left(10^{-14}\right)$, respectively.

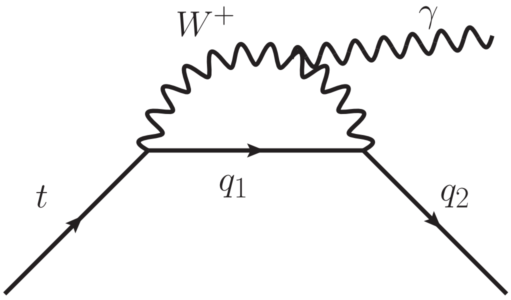

Figure 8: Feynman diagram of the decay of the top quark via an NC interaction including a photon in the SM. The label q_1 refers to a down-type quark being either a d, s, or b quark, and the label q_2 refers to an up-type quark being either an u or a c quark.

2.2.2 Occurrences in models beyond the Standard Model

In several BSM models, the cross sections of processes including an FCNC are increased compared to the SM expectation. A few of these models allow the top quark to directly decay into a photon and either an up or a charm quark, as depicted in Figure 9. The direct coupling is marked as red dot which is forbidden in the SM. In the following, selected BSM models are briefly explained which increase the probability of processes including an FCNC.

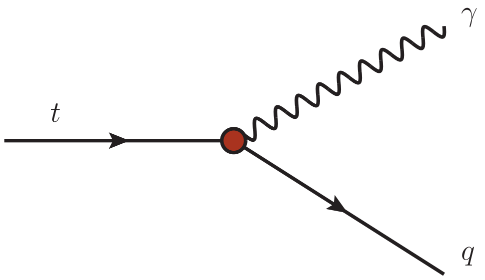

Figure 9: Feynman diagram for the decay of the top quark into a photon and an up-type quark with $q = u, c$ via an FCNC at tree level, as allowed in some BSM theories. The direct coupling, which is not allowed in the SM, is marked as a red dot.

2-Higgs-Doublet models with flavour violation

A simple extension of the SM is the introduction of a second Higgs doublet. Such models are called 2-Higgs-Doublet models (2HDMs) [58–61]. The two doublets give rise to five bosons: two Higgs bosons, h and H, with different masses, $m_h < m_H$, a pseudoscalar state, A, and two electrically charged bosons, $H^{\pm}$. The already discovered Higgs boson may be either identified with one of the bosons h or H, or a superposition of both. Those additional bosons are candidates for Dark Matter and in addition, the model provides an answer to the naturalness problem.

In 2HDMs, the up- and down-type quarks are both allowed to couple to the additional Higgs doublet. When diagonalising the mass matrix of the quarks, their flavour matrix contains non-vanishing off-diagonal elements which allow for FCNCs at tree level. In some 2HDMs, an additional symmetry is introduced to forbid these FCNCs. In contrast, models that keep this current are classified as models of type III [3, 62]. The couplings allowing for an FCNC are called flavour-violating Yukawa couplings. Their coupling strengths are defined to be proportional to the quark mass. In this way, a natural hierarchy is introduced to enhance the branching ratios of top-quark decays via an FCNC, while the ratios of decays of the first and second generation quarks via an FCNC are kept at a minimum[3]. This ensures that such models are in agreement with the precise results of searches for FCNCs including lighter quarks. The predicted branching ratio $\mathcal{B}(t \to cH)$ goes up to 2×10^{-3} [3, 4]. For the decay $t \to c\gamma$, the maximal branching ratio is of $\mathcal{O}(10^{-7})$.

Minimal-supersymmetric Standard Model

The minimal-supersymmetric Standard Model (MSSM) [63] joins the 2HDM and supersymmetry by demanding the minimal number of superpartners. These superpartners are bosonic counterparts of the fermions and vice versa. They have a mass of $\mathcal{O}(1\,\mathrm{TeV})$, whereof some are Dark Matter candidates. In addition, this model gives explanations for the naturalness problem and unifies the gauge couplings of the three fundamental interactions.

In the MSSM, the preservation of the lepton and baryon number is violated since many renormalisable couplings are introduced. In experiments, however, their preservation was precisely tested and no hint for any violation has been found. To solve this contradiction, the R-parity is introduced which is an additional symmetry. It connects the baryon and lepton numbers, and the spin. As a consequence, the preservation of the baryon and the lepton number is ensured.

In the MSSM, FCNCs happen in loop diagrams, such as shown in Figure 8. Additional loops are formed by the fermionic superpartners of the force carriers in combination with the bosonic superpartners of the quarks. Such loops are caused by the flavour mixing of the bosonic superpartners, analogously to that of quarks. The branching ratios of the top quark decaying via an FCNC reach values up to $\mathcal{O}\left(10^{-5}\right)$ for masses of the superpartners of $1\,\mathrm{TeV}$ [6]. The branching ratio $\mathcal{B}(t \to q\gamma)$ with $q = u, c$ is maximally of $\mathcal{O}\left(10^{-8}\right)$.

Some versions of the MSSM allow for R-parity violating terms in their Lagrangian density by characteristic couplings of the quarks to their superpartners. However, either the lepton or the baryon number is still preserved to be consistent with previous observations. In versions violating the lepton-number preservation, the branching ratios of decays via an FCNC are of $\mathcal{O}\left(10^{-7}\right)$ [7, 8] because the lepton-number violating couplings are tightly constrained by experiments. Versions that conserve

---

[3] This fact explains why the branching ratio $\mathcal{B}(t \to q\gamma)$ is only computed for $q = c$ in Figure 1.

the lepton number allow for branching ratios up to $\mathcal{O}\left(10^{-6}\right)$ [7, 8]. For the branching ratio $\mathcal{B}(t \to q\gamma)$ with $q = u, c$, effects below $\mathcal{O}\left(10^{-9}\right)$ are predicted.

Models with a warped extra dimension

Another approach in BSM physics is the introduction of a new fifth dimension, which was proposed by Randall and Sundrum in 1999 [64, 65]. Such models include all four fundamental interactions and give an answer to the hierarchy problem.

In Randall-Sundrum models, the SM only describes the projections of the quantum fields visible in one temporal and three spatial coordinates. The projections of the fermion fields in the additional dimension are more complex and controlled by their coupling to the Higgs field. These projections allow for FCNC interactions between the fermions and so-called Kaluza-Klein particles [66, 67], which correspond to the gauge bosons. As the projection of the top quark in the fifth dimension couples the strongest to those Kaluza-Klein particles, the branching ratios for processes with an FCNC in the top-quark sector are increased to $\mathcal{O}\left(10^{-4}\right)$ [9, 10]. For the $tc\gamma$ coupling, the maximal branching ratios are of $\mathcal{O}\left(10^{-9}\right)$.

2.3 Effective field theory

As it is inconvenient for analyses to test all available extensions of the SM, EFTs are deployed [68] which allow for model-independent searches. Such an EFT approximates an underlying physical theory by considering only the relevant degrees of freedom. As a consequence, the microscopic structures of interactions are not described. In contrast, it is accepted that such an approach is only valid up to a certain energy scale of new physics, Λ.

The EFT used in this search extends the SM by introducing new effective couplings [69]. This theory is required to contain the gauge groups of the SM, the degrees of freedom of the SM and to be reducible to the SM at low energies. The Lagrangian density of this EFT, $\mathcal{L}_{\mathrm{EFT}}$, is composed of the SM Lagrangian density, $\mathcal{L}_{\mathrm{SM}}^{(4)}$, which is of the fourth order of the mass, and additional densities of order five, $\mathcal{L}^{(5)}$, and six, $\mathcal{L}^{(6)}$, as

$$\mathcal{L}_{\mathrm{EFT}} = \mathcal{L}_{\mathrm{SM}}^{(4)} + \mathcal{L}^{(5)} + \mathcal{L}^{(6)} + \mathcal{O}\left(\frac{1}{\Lambda^3}\right) . \tag{14}$$

Since the Lagrangian density $\mathcal{L}^{(5)}$ introduces lepton-flavour violating couplings, it is ignored in this search. Moreover, Lagrangian densities are neglected which are of higher order than six since they are suppressed by multiples of the scale of new physics. Consequently, only the density $\mathcal{L}^{(6)}$ remains which is expressed by operators, $\mathcal{O}_x$. They describe new couplings among the quantum fields or modify the SM couplings. The strength of each operator is given by a characteristic Wilson coefficient, C_x, and suppressed by the square of the scale of new physics Λ as

$$\mathcal{L}^{(6)} = \frac{1}{\Lambda^{(6-4)}} \sum_x C_x \mathcal{O}_x \,. \tag{15}$$

When obeying the baryon-number conservation, this density consists of $15+19+25 = 59$ independent operators which contain either none, two or four fermion fields, respectively. Seven of them give rise to FCNCs at tree level in the top-quark sector. These seven operators include two fermion fields and the Higgs field. The tqH with $q = u, c$ coupling is described by three operators, whereas two operators correspond to the tqg coupling. The remaining two operators are responsible for FCNC interactions in the electroweak sector. Following the notation in Ref. [69], these two operators are written as

$$\mathcal{O}_{\mathrm{uB}}^{(ij)} = (\bar{q}_i \sigma^{\mu\nu} r_j)\widetilde{\varphi} B_{\mu\nu} \,, \tag{16}$$

$$\mathcal{O}_{\mathrm{uW}}^{(ij)} = (\bar{q}_i \sigma^{\mu\nu} \tau^I r_j)\widetilde{\varphi} W_{\mu\nu}^I \,. \tag{17}$$

Hereby, $\bar{q}_i$ is the LH quark doublet and r_j the RH quark singlet, $\sigma^{\mu\nu}$ is defined as $\frac{1}{2}\left[\gamma^\mu, \gamma^\nu\right]$ with the gamma matrices, γ^α, τ^I is the Pauli matrix, $\widetilde{\varphi}$ is the complex conjugate of the Higgs field doublet with $(\widetilde{\varphi})^j = \varepsilon_{jk}(\varphi^k)^*$ and $\varepsilon_{12} = 1$ being totally anti-symmetric, and $B_{\mu\nu}$ and $W_{\mu\nu}^I$ are the $U(1)_Y$ and $SU(2)_L$ field tensors, respectively. The indices i and j correspond to the quark generations. As the top quark is always involved, one of the indices equals three, while the other is either one or two corresponding to an up or charm quark, respectively. Both operators allow for FCNCs with a tqZ or $tq\gamma$ coupling with $q = u, c$ and are used to describe the signal processes in this search.

2.4 Interferences of processes including a flavour-changing neutral current involving a top quark and a photon

Both the tqZ and $tq\gamma$ couplings with $q = u, c$ may occur in production- and decay-mode processes. Exemplary Feynman diagrams with an FCNC at tree level are depicted for the $tq\gamma$ coupling in Figure 2. When considering initial states consisting of protons, as in pp collisions, and including diagrams for the production-mode process with an additional quark in the final state, interferences between both processes may occur. Such interference effects are studied and quantified [12] in the context of the EFT presented in Section 2.3. Therefore, the individual processes are simulated separately as well as simultaneously for pp collisions at $\sqrt{s} = 13\,\mathrm{TeV}$. Then, their predictions are compared to each other.

Focusing on the $tq\gamma$ coupling, the prescription of the decay-mode process is $pp \to t\bar{t}$ with $t\bar{t} \to W\bar{b}\gamma q$ with $q = u, c$. The production-mode process is described by $pp \to t\gamma$ and $pp \to t\gamma j$ with $t \to Wb$. The parton j is either a gluon, quark or anti-quark. Diagrams in the production mode that include an intermediate anti-top quark are excluded to avoid the production of a $t\bar{t}$ pair. Whereas diagrams of the production-mode process without an additional parton in the final state do not introduce interferences with the decay-mode process, those with an additional parton interfere if $j = u, c$. When simulating both processes simultaneously, also referred to as the total process, the prescription is $pp \to t\gamma$ and $pp \to t\gamma j$ with $t \to Wb$ and j being a gluon, quark or anti-quark. Thereby, interference effects are calculated within the EFT used. In the simulation of the processes, it is distinguished between the $tu\gamma$ and the $tc\gamma$ coupling and between the left- and the right-handedness. Only one coupling is assumed to be present at a time. The W bosons are supposed to decay into leptons of the first two generations. As an uncertainty, the renormalisation and factorisation scales are varied, which are used in the computation of the matrix elements.

The interference effects are studied at parton and detector level. Parton level means that only the hard scattering of the protons and the hadronisation of the final-state partons are simulated, while for the detector level the approximate response of the CMS detector is simulated exemplarily, too. For both levels, the cross-section weighted sum of the production- and decay-mode processes is confronted with the total process. Distributions of different kinematic properties are compared to each other, while any deviation between the distributions of the sum and those of the total process would hint at non-negligible interference effects.

In Figure 10, the normalised photon p_{T} spectra at the parton and detector levels are shown separately for the production- and decay-mode processes, their sum and the total process for the LH $tu\gamma$ coupling. In the bottom panel, the ratio of the total process to the sum is shown. At both levels, the same behaviour is observed. Photons of the production-mode process tend to have a high energy as they recoil against the massive top quark. Since in the decay mode, both top quarks typically rest in the laboratory frame, the total energy of this process is restricted to approximately twice the top-quark mass. Consequently, interference effects may only occur up to this energy. As the mass of the photon and that of the up-type quark are negligible compared to the top-quark mass, both decay products get a similar amount of the top quark's energy. Thus, in the decay mode, the photon energy is typically around half of the top-quark mass and reaches values up to 300 GeV. The photon p_{T} distribution of the sum of both processes is found to be compatible with the distribution of the total process. Any deviation is covered by the uncertainty of the scales and no hint for any interference effect is found. As the same behaviour is seen in other distributions as well as for the other $tq\gamma$ couplings and for the tqZ couplings, it is concluded that interference effects between processes of the production and decay mode are negligible in searches for FCNCs performed at the LHC.

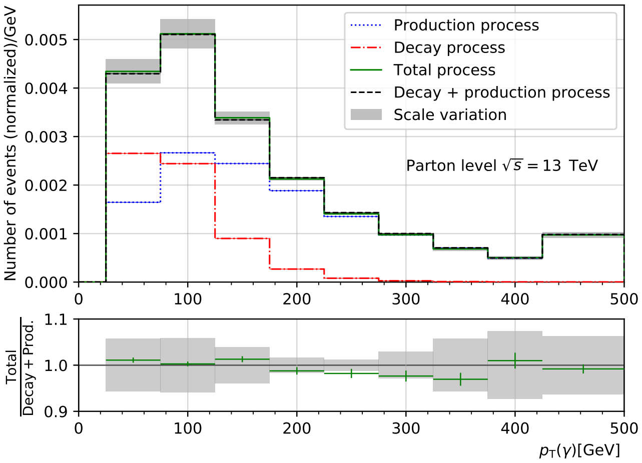

(a) Signal

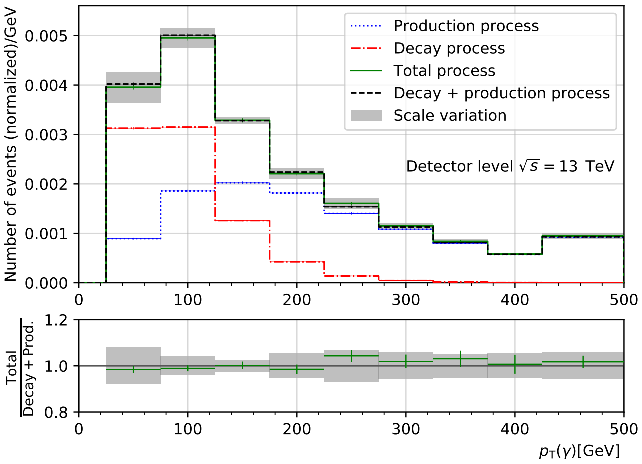

(b) Signal

Figure 10: Photon p_T spectrum at parton (a) and detector level (b) for the processes of the production and decay mode, their sum and the total process [12]. In the bottom panel, the ratio of the sum to the total process is shown. The statistical uncertainties and the uncertainty due to the scales are included.

3 The ATLAS experiment at the LHC

The elementary particles and fundamental interactions have been studied at a diversity of experiments for more than a century. While the first experiments were constructed in small laboratories, current experiments are huge facilities to face the challenges of today's particle physics. A pioneer in particle physics is CERN, the *European Organisation for Nuclear Research*. CERN is an international organisation for research founded in 1954 and located near Geneva. It successfully contributed to numerous discoveries of particles and high precision measurements of SM properties. At the CERN site, different accelerators and diverse detectors were built and expanded. In those accelerators, different sorts of particles are sped up which are either shot on fixed targets or brought to collision. In such collisions, both elastic and inelastic scattering processes happen. The signatures of the outgoing particles are recorded by specific detectors.

The current accelerator complex is shown in Figure 11. Smaller and typically older accelerators are used to pre-accelerate particles which are injected into larger machines. The LHC is the latest expansion stage which is the largest particle accelerator in the world to date. Huge detectors are situated at different segments of the LHC. One of these detectors is the ATLAS experiment which is a multi-purpose detector. With its data, precision measurements are performed and it is searched for hints of new physics phenomena. In the following, the LHC and the ATLAS experiment are described in detail.

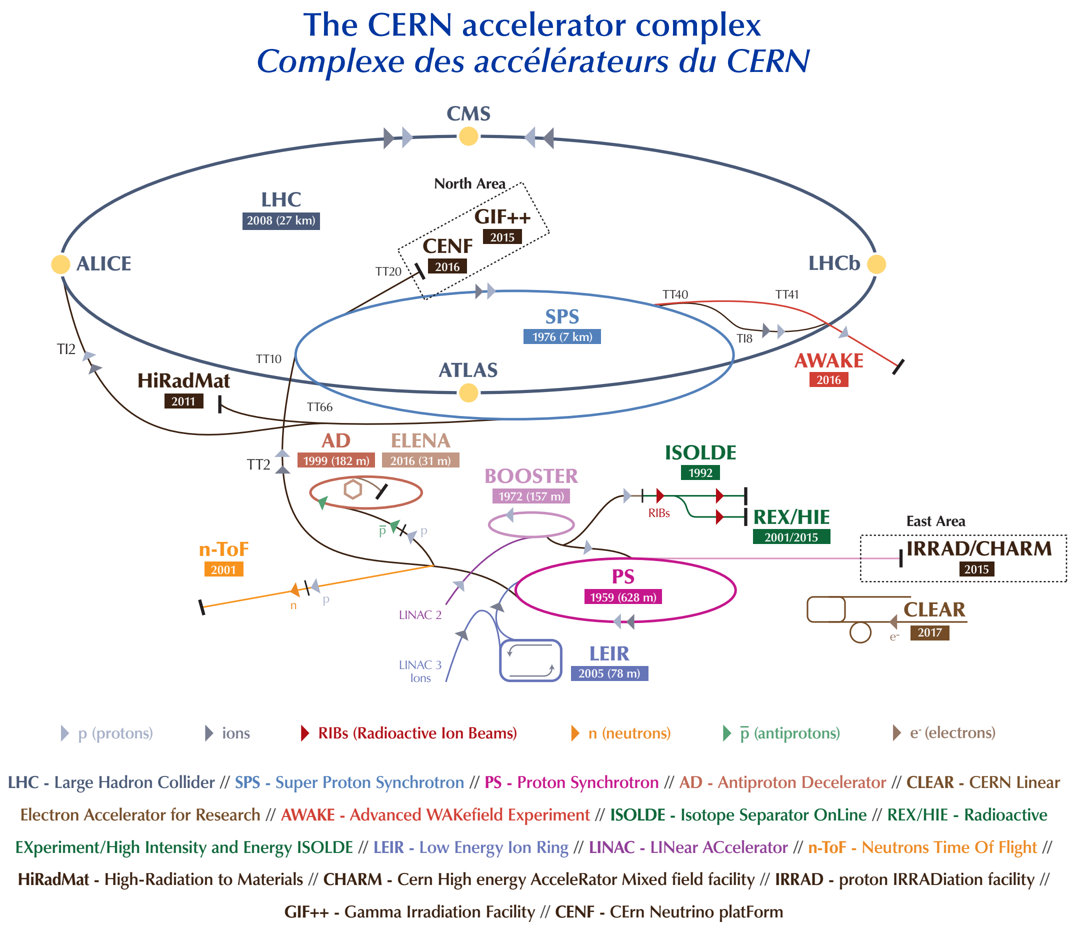

Figure 11: Overview of the current accelerator complex at CERN with its various experiments [70]. Different types of particles are accelerated and led into different machines. For the different facilities, the year of commissioning is given. For storage rings, the circumference is indicated.

3.1 The Large Hadron Collider

The currently largest machine at CERN is the LHC [71]. It is a circular accelerator built under the surface and has a circumference of 26.7 km. Two bunched particle beams circulate around the LHC in opposite direction in evacuated beam pipes. The beams are controlled by dipole, quadrupole and other multipole magnets. Each dipole magnet measures 15 m in length and its magnetic field strength reaches up to 8.4 T. Its purpose is to bend and guide the beams through the ring. The elements including quadrupole magnets have a size of 4 m and create a magnetic field of 6.9 T. In them, the magnets are arranged with alternating polarity to focus the beams. The other multipole magnets vary in size and are also used to focus the beams. All magnets are cooled down to a temperature of 1.9 K using liquid helium to become superconducting. Each beam traverses eight superconducting radiofrequency cavities. They contain an electromagnetic field which switches its polarisation with a frequency of 400 MHz at a maximal voltage of 2 MV. The purpose of those cavities is to accelerate the particles of the beams by providing a gradient of 5 MV/m, and to maintain the bunch structure.

Before the particles are injected into the LHC, they are passed through different facilities to pre-accelerate them. In the case of proton beams, the particles start in the Radio Frequency Quadrupole (RFQ) where they are bunched and sped up to 750 keV. Their acceleration continues in the Linear Accelerator 2 (LINAC2) which the protons leave with an energy of 50 MeV. Next, they are led into the Proton Synchrotron Booster (PSB) where they are accelerated to 1.4 GeV. Subsequently, they are guided to the Proton Synchrotron (PS) where they are sped up to 25 GeV. As the stage prior to the LHC, the protons are filled into the Super Proton Synchrotron (SPS) where they reach an energy of 450 GeV. As last step, the proton bunches enter the LHC where they are accelerated to their final energy of 6.5 TeV. To induce heavy ion collisions, lead ions are accelerated to a maximal energy of 2.5 TeV in the LHC. During pre-acceleration, they pass the Linear Accelerator 3 (LINAC3) instead of the LINAC2, while the other facilities are the same. However, the maximal energies of the ions after the different accelerators are lower.

After the acceleration, the particles of the beams travel almost at the speed of light and circulate with a frequency of 11 kHz. Every proton beam consists of 2 808 bunches, each containing up to 10^{11} protons. The temporal distance between two bunches amounts to 25 ns at the final energy. The beams are brought to collision at dedicated interaction points where huge detectors are located. The bunch crossing rate amounts to 40 MHz which results in more than one billion collisions per second. The four main detectors are the following:

ALICE The ALICE experiment [72], whose acronym stands for *A Large Ion Collider Experiment*, is a multi-purpose detector built for heavy ion physics. In collisions of heavy ions, a quark-gluon plasma is created which has an extremely high density and a high temperature. This plasma resembles the state of the universe microseconds after the Big Bang. The physics programme of the ALICE collaboration is devoted to precisely measure this plasma.

ATLAS The ATLAS experiment [73], the shortcut for *A Toroidal LHC ApparatuS*, is a general multi-purpose detector for pp collisions. It aims to precisely measure different properties of the SM and search for hints of new physics phenomena. In its physics programme, both the Higgs boson and the top quark play an important role as they may open the window to BSM physics.

CMS The CMS experiment [74], standing for *Compact Muon Solenoid*, is another general multi-purpose detector. Its physics programme is similar to that of the ATLAS experiment. It aims to measure properties of the Higgs boson and the top quark, and searches for exotic phenomena.

LHCb The LHCb detector [75], abbreviating *Large Hadron Collider beauty*, is a single-arm forward spectrometer. It is specialised for high precision measurements in b-quark physics. Its main goal is to study in detail the disagreement of the observed and by the SM predicted matter-anti-matter imbalance in our universe. In their analyses, symmetry-violating and rare B-meson decays are predominantly investigated, which are hadrons including a b quark as valence quark.

3.2 The ATLAS detector

The ATLAS detector [73] is the largest detector ever built at a particle accelerator. It measures 25 m in diameter and 44 m in length, and weighs more than 7 000 t. Its physics programme is multifarious and comprises precision measurements of SM parameters and properties, as well as searches for exotic phenomena which might hint at BSM physics. In particular, processes including a Higgs boson or a top quark are focused on, as both particles are assumed to be good candidates to be connected to BSM physics.

The ATLAS detector has a cylindrical geometry and consists of four main parts. These components are the Inner Detector (InDet), the calorimeter system consisting of the Electromagnetic Calorimeter (ECAL) and the Hadronic Calorimeter (HCAL), and the Muon Spectrometer (MS), as assembled from the inside to the outside and illustrated in Figure 12. A magnet system provides magnetic fields which bend the curve of charged particles traversing the detector. This system includes a solenoid and toroidal magnet. In addition, so-called forward detectors are installed at certain distances from the ATLAS detector, mainly to measure the luminosity. Next to all these components, the Trigger and Data Acquisition (TDAQ) system is implemented to handle the enormous data rate and its storage. In the following, all the different constituents are briefly explained.

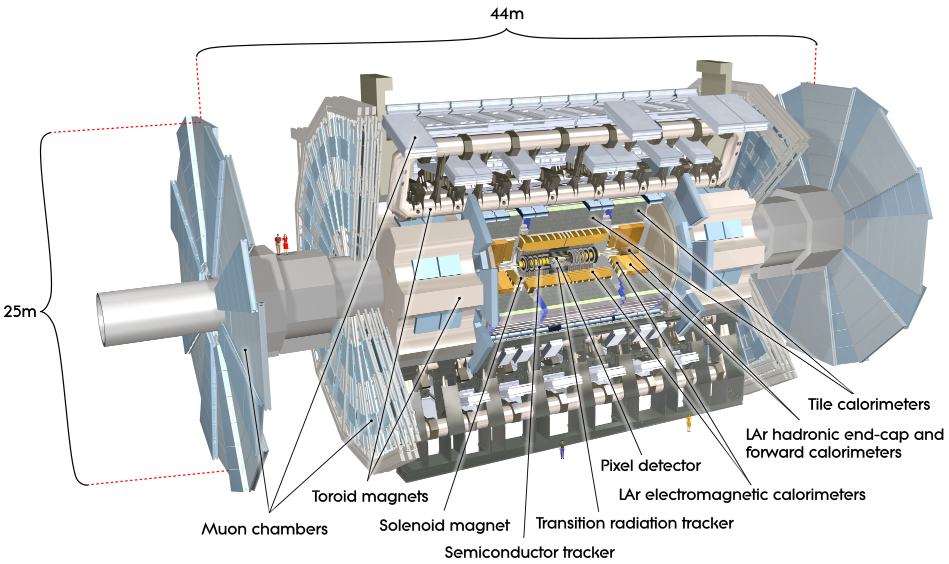

Figure 12: Overview of the ATLAS experiment with its different components [76].

3.2.1 Inner Detector

The InDet [77, 78] is the component closest to the beam pipe. It is built cylindrically around the nominal interaction point. The InDet measures 6.2 m in length and 2.1 m in diameter. It is surrounded by the superconducting solenoid [79–81] whose magnetic field penetrates the InDet. Its strength reaches up to 2 T. The purpose of the InDet is to measure the curved trajectories of charged particles like electrons or protons. These particles leave hits in the different layers of the InDet. Based on the hits, the momentum, direction and electric charge of those particles are reconstructed, while their trajectories are used to reconstruct the vertices of an event. Its spatial resolution for the impact parameter is 11 µm in transverse direction and 24 µm along the z-axis. A vertex is reconstructed with a resolution of 8 µm in the transverse plane and 24 µm along the beam direction. From the inside to the outside, the InDet itself consists of the Insertable B-layer (IBL) [82, 83], the Pixel detector [84, 85], the Semiconductor Tracker (SCT) and the Transition Radiation Tracker (TRT) [86].

The IBL has a radius of $31\,\mathrm{mm} < R < 40\,\mathrm{mm}$ and covers a pseudorapidity of $|\eta| < 3$. It consists of 14 carbon fibre staves where silicon sensors are installed on. It plays a vital part for the reconstruction of vertices displaced from the beam axis.

The Pixel detector is constructed of three barrel layers of silicon pixel sensors which have radii of 50.5 mm, 88.5 mm and 122.5 mm. On both sides of the nominal interaction point, three end-cap disks orthogonal to the beam pipe are installed covering a pseudorapidity of $|\eta| < 2.5$. With this component, it is able to separate tracks of the different particles despite the high density of particle tracks.

The SCT consists of four barrel layers between a radius of $299\,\mathrm{mm} < R < 514\,\mathrm{mm}$. Furthermore, nine end-disks on both sides of the nominal interaction point are installed which provide a coverage of $|\eta| < 2.5$. As sensor technique, silicon microstrip detectors are used. It provides important information to reconstruct particle tracks.

The TRT is the outermost part of the InDet and covers the area between $554\,\mathrm{mm} < R < 1082\,\mathrm{mm}$ and a pseudorapidity of $|\eta| < 2$. The barrel part consists of 5 544 drift tubes embedded in polymer fibres. The end cap is built from 122 880 tubes within polypropylene foil. The tubes are filled with a gas mixture of xenon, carbon dioxide and oxygen molecules. Due to a gas leakage, some tubes are filled with argon instead of xenon. The anodes inside of the tubes are of tungsten. The

TRT helps to identify particles that interact in the fibres and emit roentgen radiation. This radiation is absorbed in the tubes by ionisation processes.

3.2.2 Calorimeter system

The calorimeter system encloses the InDet and covers a pseudorapidity of $|\eta| < 4.9$. It consists of the ECAL [87] and the HCAL [88]. Both are constructed as sampling calorimeter with alternating layers of active material and passive absorbers. The passive absorbers have a high density to induce showers of incoming particles which are measured in the active material. The purpose of the calorimeter system is to measure the energy of photons, electrons and hadrons.

First, particles enter the ECAL which is meant to stop electrons and photons. These particles induce bremsstrahlung and the production of electron-positron pairs. Other particles only deposit a minor fraction of their energy in the ECAL. Next, the remaining particles reach the HCAL where hadrons are absorbed. Their showers are also created by bremsstrahlung, pair production and other processes. In total, the thickness of the calorimeter system amounts to eleven interaction lengths, λ, which is defined as the mean distance to reduce the number of relativistic charged particles by a factor of e^{-1} when passing through material.

Electromagnetic Calorimeter

In the ECAL, lead having a high density is used as absorbing material. Liquid argon (LAr) serves as detective material to reach a high energy resolution. The layers are arranged in an accordion-like shape as depicted in Figure 13. The barrel part covers a pseudorapidity of $|\eta| < 1.475$ and the end-cap region of $1.375 < |\eta| < 3.2$. In the transition region between the barrel and end caps, $1.37 \leq |\eta| \leq 1.52$, the first layer consists of a large amount of material, arising from support structures such as cables.

In the region up to $|\eta| < 2.5$, the ECAL consists of three layers with different granularity. The first layer, also called strip layer, is finely segmented into cells with a size of $\Delta\eta \times \Delta\phi = 0.0031 \times 0.0982$ in the regions of $|\eta| < 1.4$ and $1.5 < |\eta| < 2.4$, while the remaining regions have a granularity of $\Delta\eta \times \Delta\phi = 0.025 \times 0.0982$. At $\eta = 0$, the depth of this layer amounts to $4.4\,X_0$, where X_0 characterises the length for the energy loss of a particle induced by radiation in material. The second layer has a granularity of $\Delta\eta \times \Delta\phi = 0.025 \times 0.0245$ and measures $17\,X_0$ at $\eta = 0$. The

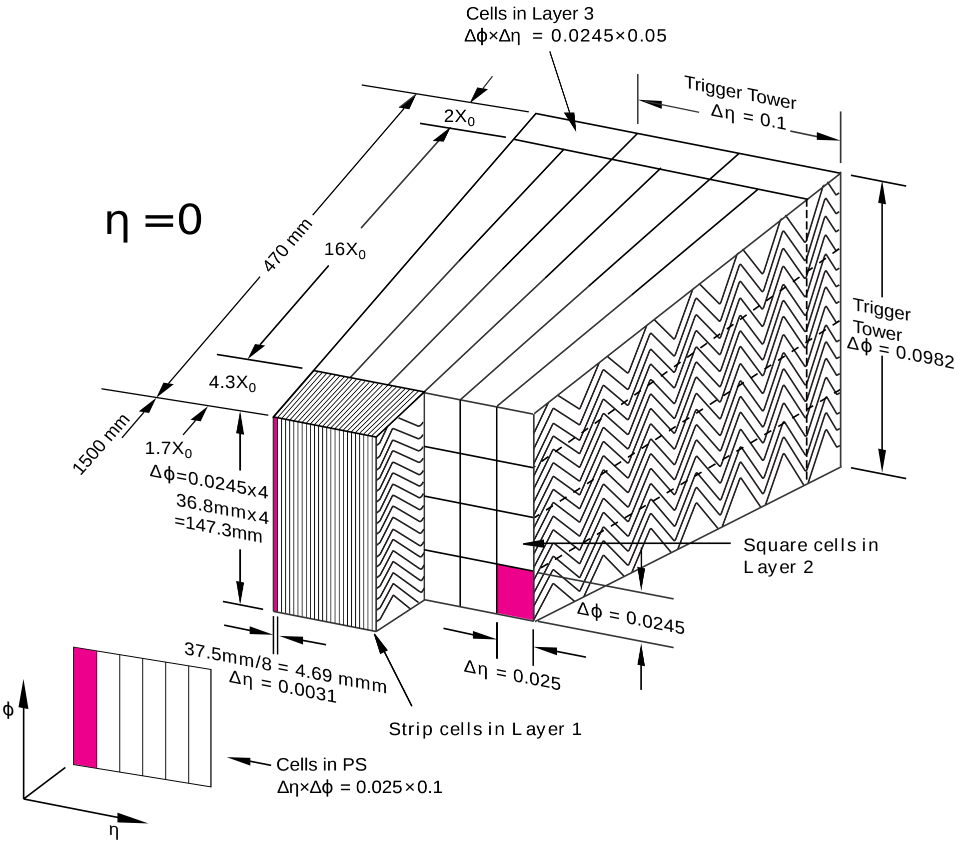

Figure 13: Partial view of the ECAL of the ATLAS detector with its lateral and longitudinal segmentation around $\eta = 0$ [87].

last layer has cells with a size of $\Delta\eta \times \Delta\phi = 0.05 \times 0.0245$ and a thickness of $2\,X_0$ at $\eta = 0$.

The fine granularity of the strip layer ensures that, for a transverse momentum up to $\mathcal{O}(100\,\text{GeV})$, a shower induced by a single photon can be well discriminated against that of an electron and those of two overlapping photons from a decay of a neutral hadron like a pion, $\pi^0 \rightarrow \gamma\gamma$. In the second layer, most of the energy of electrons and photons is deposited, while the third layer picks up the energy leakage of high-energetic showers.

In front of the strip layer with $|\eta| < 1.8$, a presampler layer is installed with a thickness of 1.1 cm in the barrel and 0.5 cm in the end-cap region. It consists of a

LAr layer and is used to correct for energy lost in the inner parts of the detector. In the central region of $|\eta| < 1.8$, the thickness of the material upstream of the presampler amounts to 2-3 X_0, while it increases to 5-6 X_0 in the transition region and around $|\eta| = 1.7$.

The energy resolution of the ECAL, σ_E, is estimated by

$$\frac{\sigma_E}{E} = \frac{a}{\sqrt{E}} \oplus \frac{b}{E} \oplus c\,, \tag{18}$$

with the energy, E, measured in GeV. The first term, called stochastic term, reflects the geometry of the calorimeter like its alternating layers. The parameter a lies in the range of 8 % to 11 % depending on the pseudorapidity. The second term represents the influence of noise with b being around 400 MeV and predominantly impacts low energies. The constant term, c, becomes important at high energies and is targeted to be below 0.7 %. It describes the impacts by e.g. the different cluster sizes, the mechanics of the modules, the calibration system and temperature inhomogeneities. In total, the ECAL features a high energy resolution in order to distinguish between single photons, photons from hadron decays and electrons.

Hadronic Calorimeter

The HCAL surrounds the ECAL and is one of the biggest detector components. It covers a pseudorapidity of $|\eta| < 4.9$ and its thickness measures about 10 λ. Its goal is to stop and measure the energy of hadrons.

The barrel and extended barrel regions cover $|\eta| < 0.8$ and $0.8 < |\eta| < 1.7$, respectively. Steel is used as absorbing material and plastic scintillating tiles serve as active detectors. In radial direction, it consists of three sampling layers with different granularity. The first two layers are segmented into $\Delta\eta \times \Delta\phi = 0.1 \times 0.1$ and have a thickness of 1.4 λ and 4.0 λ, respectively, at $\eta = 0$. The granularity of the last layer amounts to $\Delta\eta \times \Delta\phi = 0.2 \times 0.1$ with a thickness of 1.8 λ.

The end-cap and forward regions cover $1.5 < |\eta| < 3.2$ and $3.1 < |\eta| < 4.9$, respectively. The radiation resistant LAr technology is used since a very high radiation is expected. In the end-cap region, copper acts as absorbing material. This region is divided into four sampling layers with a granularity of $\Delta\eta \times \Delta\phi = 0.1 \times 0.1$ at $1.5 < |\eta| < 2.5$ and 0.2×0.2 at $2.5 < |\eta| < 3.2$. The forward calorimeter is segmented into three parts with a granularity of $\Delta\eta \times \Delta\phi \cong 0.2 \times 0.2$. In the first section, copper is used as absorber, while the absorber in the other two parts is made out of tungsten.

The energy resolution, σ_E and σ_{E_T}, of the HCAL is based on Equation (18) and depends on the pseudorapidity as different technologies are used. It is estimated as

$$\frac{\sigma_E}{E} = \frac{50\,\%}{\sqrt{E}} \oplus 3\,\% \quad \text{for } |\eta| < 3\,, \tag{19}$$

$$\frac{\sigma_{E_\mathrm{T}}}{E_\mathrm{T}} = \frac{100\,\%}{\sqrt{E}} \oplus 10\,\% \quad \text{for } 3 \leq |\eta| < 5\,. \tag{20}$$

In both estimations, the noise term is neglected as its impact is negligible compared to those of the other two terms. Since the purpose of the HCAL and that of the ECAL differ, the resolution of the HCAL is worse than that of the ECAL when considering particles with the same energy by design.

3.2.3 Muon Spectrometer

The MS [89] is the outermost part of the ATLAS detector and surrounds the calorimeter system. It covers a pseudorapidity of $|\eta| < 2.7$. Next to neutrinos, muons are the only particles passing through the calorimeter system without being stopped since they are minimally ionising at energies reached in the collisions. In the MS, tracks of muons are measured which enable to reconstruct their momentum, energy and electrical charge.

A magnetic field created by a toroidal magnet [90, 91] penetrates the MS. The magnet system is split into a barrel and two smaller end-cap toroids, which generate a magnetic field strength of 3.9 T and 4.1 T, respectively. Each toroid consists of eight superconducting air-core coils which are assembled concentrically around the beam axis. Muons with a pseudorapidity of $|\eta| < 1.0$ are bent by the field of the barrel toroid, while muons with a pseudorapidity within $1.4 < |\eta| < 2.7$ are impacted by fields of the end-cap toroids. In the transition region of $1.0 \leq |\eta| \leq 1.4$, a combination of the barrel and end-cap fields deflects the muons.

In the barrel region, the MS is built up by three cylindrical layers arranged around the beam axis. Three disks and a ring on both sides of the detector form the transition and end-cap regions. In each layer, Monitored Drift Tubes (MDTs) are used providing a spatial resolution of 80 µm. Each MDT consists of 2×3 monolayers of single-wire tubes. In a pseudorapidity of $2 < |\eta| < 2.7$ and in a part of the first disk, Cathode Strip Chambers (CSCs) are installed since they are able to deal with a six times higher flux than the MDTs. Each CSC is a multiwire proportional chamber providing a high time resolution of 7 ns and a spatial resolution of 60 µm.

For the trigger system, two other technologies are used. In the barrel region as part of the two outermost layers, Resistive Plate Chambers (RPCs) are used which have a gas gap with two parallel resistive plates. In the first and second disk, Thin-Gap Chambers (TGCs) are installed providing a good time resolution. They are designed similarly to the multiwire proportional chambers and arranged as doublets and triplets.

3.2.4 Forward detectors and luminosity measurement

For the luminosity measurement at the ATLAS experiment, a system integrated in the ATLAS machine and two forward detectors displaced from the detector are used. The Beam Conditions Monitor (BCM) [92] is integrated in the InDet. It monitors the beam conditions and protects the detector against huge radiation damages by inducing a beam dump, if necessary. Due to its high sensitivity for the particle flux, it provides information for the luminosity measurement. The Luminosity Measurement Using Cerenkov Integrating Detector-2 (LUCID-2) [93, 94] is located on both sides of the ATLAS detector in a distance of 17 m from the nominal interaction point. During data taking, it measures the integrated luminosity and provides information for the beam conditions and instantaneous luminosity by detecting inelastic proton-proton scattering in the forward direction through Cerenkov radiation. The other apparatus for the luminosity measurement is the Absolute Luminosity For ATLAS (ALFA) detector placed at a distance of 240 m away on both sides of the ATLAS experiment. It exploits the optical theorem by measuring the elastic-scattering amplitude in forward direction. This amplitude is related to the total cross section. By combining information from all three components, the integrated luminosity is determined with a precision of a few percent.

Another forward detector is the Zero-Degree Calorimeter (ZDC) situated 140 m away on both sides of the ATLAS experiment. Its purpose is to measure neutrons originating from heavy-ion collisions in order to determine the centrality of such collisions.

3.2.5 Trigger and Data Acquisition system

The large rate of bunch crossings of $\mathcal{O}(40\,\mathrm{MHz})$ happening at the ATLAS detector results in a large data stream. As this stream is too large to be read-out and written to tape, a trigger system is implemented to reduce this stream. This system looks for interesting signatures and has an event output rate of $\mathcal{O}(1\,\mathrm{kHz})$. The selected events are stored by the Data Acquisition (DAQ) system. In combination, it is called the TDAQ system [95, 96].

For the ATLAS experiment, a two-level trigger system is realised. It consists of the Level-1 (L1) hardware trigger [97] and of the software-based High Level Trigger (HLT)[95]. The L1 trigger processes a subset of information of the calorimeter system and the MS. It searches for simple signatures like high-p_T objects and makes a decision in about $2.5\,\mathrm{\mu s}$. It reduces the event rate to $\mathcal{O}(100\,\mathrm{kHz})$. For the HLT, the full event information is accessible and a reconstruction close to that performed offline is done. It decides within $200\,\mathrm{ms}$, resulting in the final event rate of $\mathcal{O}(1\,\mathrm{kHz})$. If the HLT accepts an event, it is stored locally by the DAQ system at the experiment site and then transferred to the CERN's computing centre for offline reconstruction.

As the analyses in the ATLAS collaboration are manifold, different trigger menus are implemented. Each menu looks for specific signatures in the detector. For instance, there are menus looking for a single physics object like a photon or a lepton, as well as menus searching for several different physics objects at a time.

4 Data and Monte-Carlo samples

The data recorded by the ATLAS detector are analysed in a diversity of measurements and searches. In such analyses, Monte-Carlo (MC) simulation techniques are deployed to model the processes potentially being present in data. As the strategy of each analysis is tailored to a particular goal, only a subset of data is selected which represents the most promising phase space to achieve the best possible result. In this search, events are of special interest which include a photon and a top quark. The top quark is assumed to decay leptonically. This selection is motivated by the signal process of the production mode as shown in Figure 2a.

4.1 Data

The pp collision data used for this analysis were collected by the ATLAS detector at the LHC at a centre-of-mass energy of $\sqrt{s} = 13\,\text{TeV}$ in the years 2015, 2016 and 2017. The dataset corresponds to an integrated luminosity of $81\,\text{fb}^{-1}$ with an uncertainty of $2.0\,\%$ [98] as determined by the LUCID-2 detector. Since the instantaneous luminosity was increased year by year, the average number of interactions per bunch crossing, called in-time pile-up, amounts to 13.4, 25.1 and 37.8 in 2015, 2016 and 2017, respectively.

4.2 Monte-Carlo samples

The MC samples used simulate all processes potentially being present in the subset of data. Next to the signal processes, background processes are modelled which arise from SM processes and exhibit the same or a similar final state. The background is composed of processes which contain one or two top quarks, or one or two W and Z bosons in the absence of a top quark.

For most processes, the simulation of events is divided into energy intervals or other properties to ensure a statistically sufficient number of simulated events in each region. In general, the generation of a MC sample proceeds in several steps: first, the matrix element of the process under study is computed. Then, events are generated. Subsequently, the hadronisation, parton shower and underlying events, which are interactions of the remnants of the protons, are simulated. Next, the detector response is simulated. Finally, simulated events from pile-up collisions are superimposed.

For the simulation of the response of the ATLAS detector, two procedures are deployed which differ in precision. The first method is fully based on the toolkit GEANT 4 [99]. It uses the full description of the ATLAS detector [100] which results in a precise modelling of the detector response, but is expensive in computing-time. The second technique utilises both GEANT 4 and the fast-simulation package AtlFastII (AFII) [101]. The InDet response is fully simulated by GEANT 4, while the calorimeter system is projected using a parameterisation included in the fast calorimeter simulation *FastCaloSim* [101] in order to reduce the computing time. Only for muons, the full detector including the calorimeter system is modelled using GEANT 4.

Events from pile-up collisions are simulated using PYTHIA 8.186 [102] with the A3 set of tuned parameters [103]. Those events are weighted according to the observed distribution of the number of pile-up events and overlaid on the other simulated events in a MC sample.

In the following, details on the samples for the signal and background processes are given. The top-quark mass m_{top} is set to 172.5 GeV for all samples.

4.2.1 Modelling of the signal processes with different couplings

The signal samples model the production- and decay-mode processes, as shown in Figure 2. Both signal modes include an FCNC which is described in the EFT presented in Section 2.3. The underlying Lagrangian density is implemented in the Universal FeynRules Output (UFO) model [104] TopFCNC [105, 106] at next-to-leading order (NLO). The scale of new physics is set to $\Lambda = 1\,\text{TeV}$. Events are generated by the MADGRAPH5_aMC@NLO 2.4.3 generator [107] using the NNPDF3.0NLO PDF set [108]. The spin correlation in the decay of the top quark into a W boson and a b quark is preserved by using MADSPIN [109, 110]. The hadronisation, parton shower and underlying events are simulated by PYTHIA 8.212

with the A14 tune [111] and NNPDF2.3LO PDF set [112]. The EvtGen 1.2.0 programme [113] is used to model the decay of mesons including a b or c quark. After event generation, the samples are processed with the AFII package.

For the production-mode process, four samples are generated, each containing around 500 000. For every sample, a different signal coupling is assumed which is either LH or RH and involves either an up quark or a charm quark. For the decay-mode process, four samples are generated, every containing 380 000 events. Two samples contain events simulated with the LH $tu\gamma$ coupling, while either the top quark or anti-top quark is assumed to decay via an FCNC. Analogously, two samples with the LH $tc\gamma$ coupling are produced. Since the masses of the particles stemming from the top-quark decay via an FCNC are negligible with respect to the top-quark mass, this analysis is not sensitive to any difference between the LH and RH coupling in the decay mode. Thus, only events with the LH coupling are simulated.

4.2.2 Background samples

A number of background processes are present in data arising from the SM. Some of them include one or more top quarks, while events of the other processes contain at least a W or Z boson. The response of the ATLAS detector for all background samples is modelled by the full simulation package, if not stated otherwise. In the following, the samples for the different background processes are detailed.

Processes including top quarks

Events of the $t\bar{t}$+γ process are modelled by the MadGraph5_aMC@NLO 2.3.3 generator using the NNPDF2.3LO PDF set at LO. The k-factor, which extrapolates the cross section from LO to NLO, equals 1.24 [114, 115]. The hadronisation, parton shower and underlying events are simulated using Pythia 8.212 with the A14 tune and NNPDF2.3LO PDF set. The decay of mesons including a b or c quark is performed by the EvtGen 1.6.0 programme.

Events of the $t\bar{t}$ and single-top quark processes, as shown in Figures 4 and 5, are simulated by Powheg-Box 2 [116–124] with the NNPDF3.0NLO PDF set at NLO. The overlap of single-top quark events in the tW-channel with $t\bar{t}$ events is removed using the diagram removal scheme [125, 126]. This scheme ignores diagrams in the tW-channel that include a $t\bar{t}$ pair. The Top++ 2.0 programme [127] is used to compute k-factors to extrapolate to next-to-next-to-leading-order+next-to-next-to-leading-logarithm accuracy [112, 128–133]. The spin correlation of the top quark's decay products is conserved by using MadSpin. Pythia 8.230 with the A14 tune and NNPDF2.3LO PDF set simulates the hadronisation, parton shower and underlying events. In the simulation of the $t\bar{t}$ process, the parameter h_{damp} is set to $1.5\,m_{\text{top}}$. It controls the transverse momentum of the firstly emitted gluon. The EvtGen 1.6.0 programme simulates the decay of mesons including a b or c quark.

To estimate the impact of the simulation setups for the $t\bar{t}$ and single top-quark processes, additional variation samples are produced. Once, the nominal generator of the matrix-element computation is replaced by MadGraph5_aMC@NLO 2.6.0 for the $t\bar{t}$ process and MadGraph5_aMC@NLO 2.6.2 for the single top-quark process, while the other settings are the same. At another time, Herwig 7.0.4 [134, 135] with the H7UE set of tuned parameters and MMHT2014lo68cl PDF set [136] replaces the nominal generator Pythia, while keeping the other configurations. The impact of the modelling of the initial state radiation (ISR) in the $t\bar{t}$ process is estimated by using a sample generated by doubling h_{damp} to $3\,m_{\text{top}}$, halving the factorisation and renormalisation scale and a varied A14 tune, while the other settings are kept. For all these variation samples, the fast-simulation package for the response of the ATLAS detector is used. In addition, variation samples are produced with the diagram subtraction (DS) scheme replacing the nominal diagram removal (DR) scheme for the single-top quark process of the tW-channel, while all other configurations are kept. In the DS scheme, the contributions of diagrams with a resonant $t\bar{t}$ pair are locally subtracted from the cross section.

The contribution of processes whose matrix elements contain a single top quark and a photon is estimated using the samples for the single top-quark process. Dedicated samples are not available. In events of the single top-quark process, photons may be radiated in the shower. Different estimations for the $t + \gamma$ process were performed and are found to have a negligible impact on the results.

Other processes including W and Z bosons

Events including a massive boson, but not a top quark, originate from the W+jets, W+γ+jets, Z+jets, Z+γ+jets or diboson processes. The diboson process is also called VV process. All these events are simulated using the Sherpa 2.2 generator [137] which combines the computation of the matrix element and the simulation of the hadronisation, parton shower and underlying events. The matrix elements of the W+jets and Z+jets processes are calculated at NLO for up to two partons in the final state, and at LO for up to four partons. The matrix elements for the W+γ+jets, Z+γ+jets and diboson processes are computed at NLO for up to one parton and at LO for up to three partons. All matrix elements are matched and merged in the parton-shower computation based on the Catani-Seymour dipole factorisation [138, 139] using the MEPS@NLO prescription [140–143]. The virtual QCD contributions in the matrix elements at NLO accuracy are corrected for by the OpenLoops library [144, 145]. The NNPDF3.0NNLO PDF set and the dedicated set of tuned parton-shower parameters developed by the Sherpa authors are used.

Removal of duplicate events in samples for the X+jets and X+γ+jets processes

The MC samples for the X+jets and X+γ+jets processes with $X = W, Z, t\bar{t}$ may contain duplicate events when a photon is radiated in an event of the X+jets process. To remove such duplications, an overlap removal is performed similar to that in Ref. [115]. It is based on information of the truth particle which is associated to the reconstructed photon. The truth particle is the particle originally simulated in the event generation. This particle is assigned a truth-particle identity, type and origin, while the latter two features describe the particle it originates from. The reconstructed photon is the physics objects which is reconstructed and identified by dedicated algorithms after simulating the detector response. Those algorithms are described in Section 5.2. To associate a truth to a reconstructed particle, the angular distance ΔR between them must be below a certain threshold.

For the overlap removal, the photon is categorised either as electron fake, when an electron is mis-reconstructed as photon, as hadronic fake, when a jet is mis-reconstructed as photon, or as prompt, when it originates from the hard scattering. The classification scheme used in simulation is given in the following.

$e \to \gamma$ fake A photon is considered as electron fake if either the truth-particle identity is equal to that of an electron, or the truth-particle identity equals that of a photon and a truth electron is within $\Delta R < 0.05$. The impact of different distance parameters was studied and is found to be negligible.

$j \rightarrow \gamma$ fake A photon is considered as hadronic fake when either the truth particle originates from a hadron or the truth type is that of a hadron.

Prompt photon If the photon does not match one of the fake categories, the photon is considered to originate from the hard scattering and denoted as prompt.

Events with a prompt photon are removed from all samples for the X+jets processes, whereas events including a fake photon are removed from the samples for the X+γ+jets processes. This procedure ensures that there is no overlap between those samples and that the prompt photon contributions are modelled by the samples of the X+γ+jets processes, while the fake photon contamination is described by the samples of the X+jets processes.

5 Reconstruction and identification of physics objects

For analyses using data recorded at the ATLAS detector, physics objects are reconstructed by dedicated algorithms using the information provided by the detector. In this section, the reconstruction of tracks, vertices and different physics objects used in this search is explained. After reconstructing a physics object, ID and isolation requirements are placed on its properties to discriminate it against other different objects. The physics objects considered are photons, electrons, muons, jets and missing transverse momentum.

5.1 Track and vertex reconstruction

For the reconstruction of a charged-particle track in the InDet, the New Tracking algorithm [146–148] is used. Stepwise, it combines hits measured in the different layers of the InDet by performing fits. After the fit, quality criteria are placed on the fitted track. It is required to have a minimal number of hits in the different components of the InDet and only a maximal number of missing hits in the single layers of those components. In addition, the transverse momentum associated to the fitted track must exceed 400 MeV and certain requirements on the transverse and longitudinal impact parameters must be fulfilled.

When two proton bunches collide within the ATLAS detector, several interactions between the protons may occur at a time. The positions of these interactions are reconstructed using tracks from the InDet. Their reconstruction happens in two steps [149, 150]. At first, tracks are matched to a possible vertex and then, the vertex position is computed using image reconstruction algorithms [151]. An interaction point is called *primary vertex* to which at least three tracks are associated. The main primary vertex is defined as the vertex maximising the sum of squared transverse momenta of associated tracks, $\sum p_{\mathrm{T}}^2$. At this vertex, a hard scattering is assumed to have happened.

Next to primary vertices, secondary vertices are searched for which are displaced from the beam axis. At such vertices, particles are assumed to have decayed which were either produced in the hard scattering or arose from hadronisation. Secondary vertices are required to have at least two associated tracks fulfilling loosened quality criteria, while the same reconstruction procedure as for primary vertices is applied.

5.2 Photons

The reconstruction and ID of photons [152, 153] are based on information from the InDet and calorimeter system. As the signatures of photons and electrons left in the detector look similar, their reconstruction proceeds in parallel. Thereby, tracks measured in the InDet play an important role to determine the type of particle, which is either an electron, an unconverted or a converted photon. Photon conversion means that the photon has interacted with the detector material upstream of the ECAL and produced an electron-positron pair. For the reconstruction of photons and electrons, two different algorithms exist, namely the sliding window (SW) [154, 155] and the supercluster algorithm [156, 157]. In analyses only using data recorded until the end of 2016, the SW algorithm is commonly used. In analyses including data taken in 2017 or later, the supercluster algorithm is recommended to be exclusively used which contains several improvements compared to the previous approach. Both algorithms are explained in the following.

5.2.1 Reconstruction using the sliding window algorithm

The SW algorithm builds clusters by summing up the energy of neighbouring cells within a rectangle. The cluster size depends on the particle type, while for each potential type the reconstruction goes on in parallel. The algorithm proceeds in several steps: the construction of towers, the seed-cluster finding, the track association to the seed cluster, the reconstruction of a conversion-vertex candidate, the matching of the conversion vertex to the seed cluster and the final formation of the cluster.

First, towers are built by combining cells of the ECAL in longitudinal direction. Therefore, the ECAL is divided into a grid of 200 × 256 towers in the η-ϕ plane.

Each tower measures $\Delta\eta \times \Delta\phi = 0.025 \times 0.0245$ corresponding to the granularity of the middle layer in the ECAL. In every tower, the energy of its cells is summed up.

Next, seed clusters are searched for by moving a fixed-sized window of 3×5 towers in the η-ϕ plane. A seed cluster is found if the sum of the energies of its towers is a local maximum and exceeds 2.5 GeV. Its position is estimated by the energy-weighted η and ϕ barycentres of all associated cells present in a slightly smaller window than the previous one. This ensures to be as little sensitive to noise as possible. After scanning the ECAL for seed clusters, duplicate seed clusters are removed. If two seed clusters overlap, the cluster with the lower energy is removed.

Then, reconstructed tracks associated to the main primary vertex are loosely matched to the seed clusters. Such tracks must be closer than certain angular distances in η and ϕ between the barycentre of the seed cluster and the extrapolated track's intersection point with the second layer of the ECAL. Thereby, bremsstrahlung effects are taken into account for low-energy tracks. Loosely matched tracks having hits in the IBL, Pixel detector or SCT are refitted using the Gaussian-sum-filter technique [158, 159] which improves the resolution of track parameters.

Subsequently, conversion-vertex candidates are reconstructed in the InDet based on the tracks associated to the seed clusters. It is distinguished between double-track candidates, for which the tracks of both the electron and positron are found, and single-track candidates, for which only one of those tracks is reconstructed. In addition, differences are made depending in which component of the InDet hits are found. If a conversion-vertex candidate is found, a fit decides if it matches the seed cluster. It is ensured that maximally one conversion vertex is assigned to a seed cluster.

As last step, the final clusters are formed. The particle type defining the cluster size is determined based on the finding of tracks and a conversion vertex matched to the seed cluster. Ambiguities may arise between a reconstructed electron with an associated track and a reconstructed photon with a conversion vertex matched to it. Such an ambiguity is tried to be resolved by a dedicated procedure, while a physics object with an unresolved ambiguity is removed in this analysis. After determining the particle type, the energy of the cluster is computed. First, cells in the middle layer of the ECAL are added around the seed position. Then iteratively, cells of the first layer, those of the presampler if $|\eta| < 1.8$, and those of the last layer are added, while in each step a layer-dependent seed position is used. After the energy computation, the energy is calibrated by the procedure described in Ref. [160] which is tuned as described in Ref. [161].

5.2.2 Reconstruction using the supercluster algorithm

The supercluster algorithm is based on a dynamically sized window to build clusters [155]. The improvements of calibration techniques [161] by using a multivariate analysis (MVA) enabled to use this algorithm. By it, photons from bremsstrahlung effects and electrons from photon conversions are better incorporated into the cluster than done in the SW algorithm. This improves the energy reconstruction.

First, topological calorimeter clusters are built. Seed cells are searched for in the calorimeter system, excluding the presampler and first layers of the ECAL to reduce noise. Such a seed cell is required to have an energy larger than four times its expected energetic noise. This energetic noise is specified for each cell. As soon as a seed cell is found, neighbouring cells of the seed are iteratively added if their energy is twice as high as their noise level. After this iterative procedure, all neighbouring cells with an energy above their noise level are added to form a topological calorimeter cluster. After visiting all seed cells, any overlap between two topological calorimeter clusters is removed. If two topological calorimeter clusters contain the same cell with an energy above twice its noise level, they are merged. If two topological calorimeter clusters contain the same cell with an energy below twice its noise level, fractional weights are computed for this cell how to be added to each cluster. If a topological calorimeter cluster contains two or more cells with an energetic maximum, the topological calorimeter cluster is split. A cell with an energetic maximum is defined to have an energy above 500 MeV and to have at least four neighbouring cells with a lower energy.

After building the topological calorimeter clusters, electromagnetic topological clusters are selected. Therefore, the energy of the topological calorimeter cluster must exceed 400 MeV and the fraction of energy deposited in the ECAL is required to be larger than 50 %. Furthermore, such clusters must pass certain requirements on variables describing the shower development in the ECAL.

Subsequently, reconstructed tracks and conversion-vertex candidates reconstructed using information from the InDet are matched to the electromagnetic topological clusters. The matching procedure is similar to that used for the SW algorithm, while certain adaptions are implemented.

As next step, seed clusters are searched for and satellite clusters are added to form so-called superclusters. This procedure goes on in parallel for assuming a photon and an electron. For a photon, the minimal energy of a seed cluster is 1.5 GeV. For electrons, a seed cluster must have a minimal energy of 1 GeV and a matched track with at least four hits in the SCT. If a seed cluster is found, satellite clusters are added from all unused clusters. Such a satellite cluster is assumed to represent secondary electromagnetic showers from the same physics object. The energy of a satellite cluster is required to be below the energy of the seed cluster. In general, a cluster is added as satellite cluster if it lies within $\Delta\eta \times \Delta\phi = 0.075 \times 0.125$ around the barycentre of the seed cluster. Additionally for converted photons, clusters are added that share the same conversion vertex or any track from the conversion vertex of the seed cluster. For electrons, additional satellite clusters are searched for that lie within a window of $\Delta\eta \times \Delta\phi = 0.125 \times 0.3$ and whose best matched track is the same as that for the seed cluster. After a supercluster is built, the next seed cluster is searched for, until all electromagnetic topological clusters are visited.

Then, the supercluster energy is computed by only taking into account cells in the ECAL associated to this cluster. The supercluster size is restricted to three or five cells in η direction in the barrel or in the end-cap region, respectively, centred around the barycentre. This restriction excludes cells that do not contain a significant amount of the particles' energy, but potentially energy from other physics objects. Subsequently, the energy of the supercluster is calibrated using an MVA technique and the position of the barycentre is corrected [161].

Next, reconstructed tracks and conversion vertices are matched to the superclusters and the particle type is determined. As superclusters for photons and electrons are formed in parallel, ambiguities may occur which are tried to be resolved by a dedicated procedure. If an ambiguity cannot be resolved, the physics object is rejected in this analysis.

As last step, the energy is recalibrated in dependence of the particle type following the procedure described in Ref. [161].

5.2.3 Other requirements on photons

After the photon reconstruction, ID and isolation requirements are placed on the photon candidates. These requirements are meant to distinguish between prompt and fake photons. The ID and its criteria are described in Section 6 in detail. As isolation, two working points (WPs) are defined which are called *loose* and *tight*. They are based on the track isolation variable, $p_{\mathrm{T}}^{\mathrm{cone20}}$, and the topological energy, $E_{\mathrm{T}}^{\mathrm{coneX}}$, with a cone size of $\Delta R = X/100$. The track isolation variable describes the sum of the p_{T} of all tracks with an energy above 1 GeV in a cone of $\Delta R < 0.2$ around the photon candidate, while excluding tracks associated to it. The topological energy is the energy deposited in a cone of $\Delta R < 0.2$ or $\Delta R < 0.4$ around the photon candidate, excluding the inner core of 5×7 cells in the η-ϕ plane. The two WPs are defined as

$$\text{loose:} \quad p_{\mathrm{T}}^{\mathrm{cone20}} < 0.05\,p_{\mathrm{T}} \quad \text{and} \quad E_{\mathrm{T}}^{\mathrm{cone20}} < 0.065\,p_{\mathrm{T}}\,, \tag{21}$$

$$\text{tight:} \quad p_{\mathrm{T}}^{\mathrm{cone20}} < 0.05\,p_{\mathrm{T}} \quad \text{and} \quad E_{\mathrm{T}}^{\mathrm{cone40}} < 0.022\,p_{\mathrm{T}} + 2.45\,\mathrm{GeV}\,. \tag{22}$$

Scale factors (SFs) are derived for the ID and isolation separately for both reconstruction algorithms. These SFs are based on comparisons between data and MC simulation and used to correct the simulation for any inefficiencies. Only photons with $E_{\mathrm{T}} > 20\,\mathrm{GeV}$ and $|\eta| < 2.37$, excluding the transition region of $1.37 \leq |\eta| \leq 1.52$, are selected. The ID, isolation and extraction methods for the SFs are described in Ref. [152, 153, 162].

5.3 Electrons

The reconstruction of electrons proceeds in parallel to the reconstruction of photons as described above [163]. Reconstructed electrons are required to satisfy dedicated ID criteria [163] set on variables describing the shower shape in the ECAL. These criteria are optimised by using a likelihood discriminant. In addition, isolation requirements must be met. They take into account the track isolation in a cone with variable size around the electron candidate and $E_{\mathrm{T}}^{\mathrm{cone20}}$. The defined WP aims at a steadily raising efficiency in dependence of the transverse momentum. SFs based on comparisons between data and simulation are used to correct the simulation for any inefficiencies [153], and are determined separately for both reconstruction algorithms.

Reconstructed electrons are required to have a minimal transverse momentum of 27 GeV and a pseudorapidity of $|\eta| < 2.47$, excluding the transition region. In addition, the absolute value of the transverse impact parameter in relation to its uncertainty, $|d_0|/\sigma\,(d_0)$, is required to be below five. The absolute value of the distance between the track origin of the electron candidate and the main primary vertex in z-direction, $|\Delta z_0 \sin(\theta)|$, must be smaller than 0.5 mm. In Ref. [153], the ID, isolation and extraction methods for the SFs are detailed.

5.4 Muons

The reconstruction of muons is based on the detector response in the MS and in the InDet. In both components, the track of the reconstructed muon is independently fitted and subsequently, their output is combined in a global fit. The track is required to be associated to the main primary vertex. Reconstructed muons must fulfil dedicated ID criteria based on variables describing the detector response and fit performance. Moreover, an isolation WP is defined using track- and calorimeter-based isolation variables. Both the ID and isolation are designed to suppress physics objects mainly stemming from pion or kaon decays. SFs determined in comparisons between data and simulation correct the simulation for any inefficiencies. Reconstructed muons with a transverse momentum of $p_{\mathrm{T}} > 27\,\mathrm{GeV}$ and $|\eta| < 2.5$ are selected. The ratio of the absolute value of the transverse impact parameter to its uncertainty, $|d_0|/\sigma\,(d_0)$, is required to be lower than three, and the absolute value of the difference between the track origin and the main primary vertex, $|\Delta z_0 \sin(\theta)|$, is required to be smaller than 0.5 mm. Details about the reconstruction, ID, calibrations and SF extraction methods are found in Ref. [164], about the isolation in Ref. [162].

5.5 Jets

The reconstruction of jets proceeds in two steps. First, topological calorimeter clusters [156, 165] are built as described in Section 5.2.2. These clusters are weighted to the hadronic scale. Then, they are merged to form jets with the anti-k_{T} algorithm [166] using the FastJet package [167, 168]. This algorithm features infrared and collinear safety and forms cone-shaped objects. In an iterative procedure, it computes the value d_{ix} for each cluster, i, to every other object, x, being either another cluster, j, or the beam pipe, B, by

$$d_{ij} = \min\left(p_{\mathrm{T},i}^{-2}, p_{\mathrm{T},j}^{-2}\right)\frac{\Delta R_{ij}^2}{R^2} \quad \text{with} \quad \Delta R_{ij} = \sqrt{(\phi_i - \phi_j)^2 + (y_i - y_j)^2}\,, \tag{23}$$

$$d_{iB} = p_{\mathrm{T},i}^{-2}\,, \tag{24}$$

with the rapidities y_i and y_j, and the azimuthal angles ϕ_i and ϕ_j. The radius parameter, R, is set to 0.4. The algorithm searches for the minimal value of d_{ij} and d_{iB}. If the minimal value is d_{iB}, it declares the cluster i as a jet and removes it from the iterative procedure. Otherwise, it combines the clusters i and j into a joint cluster which is added to the list of clusters, while removing the individual entities. The iteration stops when all clusters are removed from the list.

After building the jets, the jet energy scale (JES) and jet energy resolution (JER) are calibrated as described in Ref. [169]. The transverse momentum of jets must be greater than 25 GeV and they are required to lie within $|\eta| < 2.5$. In order to reject jets from pile-up, jets fulfilling both $p_{\mathrm{T}} < 120\,\mathrm{GeV}$ and $|\eta| < 2.4$ are required to have a jet vertex tagger (JVT) discriminant [170] larger than 0.59. This discriminant is based on the origin of the tracks associated to the jet. The efficiency of the JVT cut in simulation is corrected by a SF which is extracted from comparisons between data and simulation. Moreover, a quality criterion must be met that is designed to reject jets stemming from non-collision background and detector readout issues.

5.5.1 *b*-tagging algorithms

Flavour tagging algorithms are used to identify the quark flavour which initiated a jet. In this analysis, jets originating from a b quark are of interest, which are also called b-jets. Analogously, c-jets are defined. Light jets are initiated by a u, d and s quark or a gluon. Shortly after the creation of a b quark, it forms a hadron which has a lifetime of $\mathcal{O}(1\,\mathrm{ps})$. Consequently, this hadron flies a macroscopic distance in the detector before it decays. This behaviour is reflected in characteristic properties of the jet like the presence of a secondary vertex or a large impact parameter of the associated tracks. These properties are exploited in algorithms used to determine the initial quark flavour of a jet.

In this search, the b-tagging algorithm MV2c10 [171] is used to identify b-jets. In an MVA, it combines kinematic variables of a jet and variables established in the b-tagging algorithms IP2D, IP3D [172], SV1 [173] and JetFitter [174]. The first two methods are impact-parameter based. For each jet, the number of tracks is determined and its probabilities being a b-, c- or light jet are estimated from templates. These pieces of information are combined in log-likelihood ratios which are used to test the b-jet, c-jet and light-jet hypotheses against each other. These ratios are used as input in the MV2c10 algorithm. The SV1 tagger reconstructs a displaced secondary vertex in a jet by fitting tracks from all two-track secondary vertices, while it iteratively removes tracks from other sources and from outliers. A single secondary vertex is finally obtained whose properties are used as input for the MV2c10 algorithm. The JetFitter algorithm aims to reconstruct the whole decay chain of the hadron including a b quark by fitting a common line on which the main primary, all secondary and tertiary vertices lie. Different features describing the main primary and displaced vertices enter the MVA of the MV2c10 algorithm.

After training the MVA of the MV2c10 algorithm, different WPs are defined for various purposes. In this thesis, the WP is chosen whose b-tagging efficiency equals 60 % as found in simulated $t\bar{t}$ events. At the same time, the rejection of c-quark initiated jets amounts to 22, which is defined as the inverse efficiency. The rejection of light jets amounts to 1 200. A SF is applied which is computed from comparisons between data and simulation and is meant to correct for flavour-tagging inefficiencies in simulation [175–177]. Other WPs were tested and are found to give similar results.

5.6 Missing transverse momentum

The reconstructed missing transverse momentum [178, 179], $\vec{E}_{\mathrm{T}}^{\mathrm{miss}}$, accounts for physics objects which escape the detector without being measured, and for imperfections in the energy measurement of the reconstructed physics objects. It is computed as the negative vectorial sum over the transverse momenta of all reconstructed, fully calibrated physics objects and those of all reconstructed tracks associated to the main primary vertex which are not assigned to any physics objects. The latter contribution is called soft term. The definition is given by

$$\vec{E}_{\mathrm{T}}^{\mathrm{miss}} = -\sum_{i}^{N_{\mathrm{PO}}} \vec{p}_{\mathrm{T},i} - \sum_{j}^{N_{\mathrm{soft}}} \vec{p}_{\mathrm{T},j} \,, \tag{25}$$

with N_{PO} being the number of reconstructed physics objects and N_{soft} the number of reconstructed tracks not associated to any physics objects. The magnitude of this measure is denoted as $E_{\mathrm{T}}^{\mathrm{miss}} = \left|\vec{E}_{\mathrm{T}}^{\mathrm{miss}}\right|$, for simplicity called missing transverse momentum in the following.

5.7 Object overlap removal

In order to ensure that each energy deposition in the calorimeter system and reconstructed track is only used once, an overlap-removal procedure is applied. This procedure is based on reconstructed tracks and the angular distance ΔR between two physics objects. The following sequence is executed:

1. Electrons are removed that share a track with a muon;
2. Jets close to an electron within $\Delta R < 0.2$ are removed;
3. Electrons nearby a jet within $\Delta R < 0.4$ are removed;
4. Muons close by a jet within $\Delta R < 0.4$ are removed if the jet has more than two associated tracks;
5. Jets within $\Delta R < 0.4$ of a muon are removed;
6. Photons are removed with an angular distance of $\Delta R < 0.4$ to an electron or a muon;
7. Jets nearby a photon with $\Delta R < 0.4$ are removed.

Note that for technical reasons, photons used in the overlap removal have a transverse energy above 15 GeV and pass neither any ID nor isolation criteria. However, the impact of the different definitions was tested in Ref. [115] and found to be negligible.

6 Measurement of the photon identification efficiency

Photons play an important role in the physics programme of the ATLAS collaboration. For instance, as the Higgs boson may decay into two photons, which leaves a clear signature in the detector, this decay channel is often used in measurements of the properties of the Higgs boson. Moreover, measurements of the inclusive prompt-photon and diphoton cross sections are well suited to probe perturbative QCD computations of the SM.

In order to distinguish photons from other physics objects, their ID is a crucial part in their selection. ID criteria are defined on variables describing the shower development in the ECAL. The efficiency of these criteria must be precisely determined in data and MC simulation to correct the simulation for any inefficiencies. In general, photons are classified as prompt or fake. Prompt photons are produced in the hard scattering process, e.g. through quark-gluon scattering, $qg \rightarrow q\gamma$, or quark-anti-quark annihilation, $q\bar{q} \rightarrow \gamma g$, or in the fragmentation of a high-p_{T} parton. Fake photons may originate from hadron decays within a jet, like a pion decay, or from mis-reconstructed physics objects. Such photons are meant to be rejected by both ID and isolation criteria. In the following, the photon ID criteria, measurement methods for the efficiency and the determination of the SF are described.

6.1 Photon identification

After reconstructing photon candidates as described in Section 5.2, they must fulfil ID criteria which distinguish well between prompt and fake photons. Those criteria are based on shower-shape variables measured in the calorimeter system and describe the longitudinal and lateral shower development. Those variables are nicely illustrated in Figure 4.3 in Ref. [180] and briefly described in the following.

f_1: Ratio of the energy in the first layer of the ECAL deposited by the photon candidate to its total energy. Prompt photons deposit at least a small amount of their energy in this layer.

f_{side}: Ratio of the energy deposited around the inner core of the photon candidate to the energy deposited in the inner core. The inner core is defined as the three strips around the maximum in η direction, and the outer part includes seven strips around the maximum. Prompt photons tend to deposit their energy centrally in contrast to fake photons.

R_η: Ratio of the energy measured in the second layer of the ECAL in a window of 3×7 cells around the cluster position in the η-ϕ plane to that in a window of 7×7 cells. The energy deposition of prompt photons is typically narrower than that of fake photons.

R_ϕ: Ratio of the energy measured in the second layer of the ECAL in a window of 3×3 cells around the cluster position in the η-ϕ plane to that in a window of 3×7 cells. As for the variable R_η, the energy deposition of prompt photons is characteristically narrow in contrast to that of fake photons. This variable also separates unconverted from converted photons as the solenoid magnet disperses electron-positron pairs in ϕ direction.

R_{had} and R_{had_1}: Ratio of the transverse energy of the photon candidate measured in the HCAL in $0.8 < |\eta| < 1.37$, or in $|\eta| < 0.8$ and $|\eta| > 1.52$ in the first layer of the HCAL, respectively, to the transverse energy measured in the ECAL. As this variable indicates the energy leakage in the HCAL, prompt photons tend to have a low value, while fake photons arising from jets characteristically have a large leakage.

w_{η_2}: Lateral shower width computed as pseudorapidity-weighted energy in a window of 3×5 cells around the cluster position in the η-ϕ plane in the second layer of the ECAL. Prompt photons typically shower in a small window in contrast to fake photons.

$w_{\text{s,tot}}$: Total lateral shower width in a window of 20×2 strips around the cluster position in the first layer of the ECAL in η-ϕ direction computed by the cell energies. Prompt photons tend to produce a narrow shower in the calorimeter system.

w_{s3}: Total lateral shower width in a window of 3×2 cells around the cluster position in the first layer of the ECAL in η-ϕ direction computed using the cell energies. Prompt photons typically produce a small shower in the calorimeter system.

ΔE: Difference between the second energy maximum in the first layer of the ECAL and the minimum between the two maxima found in the cluster. Fake photons characteristically have a second maximum, while prompt photons typically have only one maximum.

E_{ratio}: Ratio of the difference between the first and second energy maximum found in the cluster in the first layer of the ECAL to its sum. As prompt photons typically have only one maximum, this value tends to unity. Fake photons, however, tend to show a second maximum and have a value different from unity.

For all these variables, the observed and simulated distributions are compared to each other. It is found that the simulated showers are systematically narrower than those measured. To correct for this effect, the mean value of affected predicted distributions is shifted to match the measured distributions. Therefore, a correction factor is computed by moving the predicted distribution in steps along the observed distribution. In each step, the χ^2 value is calculated. The shift corresponding to the minimal χ^2 value is finally taken to shift the simulated distribution.

The ID criteria are optimised using all shower-shape variables mentioned above. In the optimisation, an ensemble of rectangular cuts on those variables is established in dependence of intervals in $|\eta|$ and separately for unconverted and converted photons. When the supercluster algorithm is used to reconstruct photon candidates, the optimisation is additionally split in sections of the transverse energy. Two WPs are provided which are called *loose* and *tight*. The loose WP is mainly used for trigger purposes and only takes into account the variables R_{had} or R_{had_1}, R_η and w_{η_2}. It aims at a prompt photon efficiency above 97 % with a background rejection of 1 000 [181]. In contrast, the tight WP is used in physics analyses. It is designed for an efficiency of 85 % with a background rejection about 5 000.

6.2 Measurement methods

The photon ID efficiency for the tight WP is determined in data and simulation, and used to derive SFs to correct for any inefficiencies in simulation related to the photon ID. The photon ID efficiency is defined as

$$\varepsilon^{\text{tight-ID}} = \frac{N^{\text{s}}_{\text{ID}}}{N^{\text{s}}} \tag{26}$$

with the total number of prompt photons, N^{s}, and the number of prompt photons passing the ID criteria, N^{s}_{ID}. The ratio of the observed to the expected efficiency is used as SF. For the efficiency determination, three independent methods are used. They measure the efficiency in four $|\eta|$ intervals in dependence of the transverse energy, E_{T} separately for converted and unconverted photons. Each method exploits characteristic features of photons and covers a different, but overlapping energy range. The techniques are briefly explained in the following.

Radiative Z-Boson Method For this method, events are selected which include a Z boson decaying into two charged leptons in association with a photon, $Z \to \ell\ell\gamma$. Only reconstructed electrons and muons are considered. The selection results in a pure sample of prompt photons. Next, the distribution of the invariant mass $m(\ell, \ell, \gamma)$ is fitted with a signal and background template. The ratio of the photons passing the ID criteria to the normalisation of the signal template is taken as efficiency. The method covers an energy range of 10 GeV to 100 GeV. Of all three methods, it provides an efficiency for the lowest energies, but is statistically limited due to the mass of the Z boson.

Electron Extrapolation Method For this technique, a clean sample of events with a Z boson decaying into two electrons is selected. For the selection, the tag-and-probe approach is used: the *tag electron* passes the electron ID criteria, while the *probe electron* fulfils loosened requirements. This method exploits that the showers in the calorimeter system induced by a photon or an electron look similar. The shower shapes of the probe electrons are transformed by a Smirnov transformation [182] to match those of photons. Since small background contributions are present, which arise from events including a physics object mis-reconstructed as electron, a template fit is performed to the invariant mass distribution $m(e, e)$ taking into account signal and background contributions. Subsequently, the photon ID criteria are applied to the probe electrons. While subtracting the background contributions, the ratio of the number of probe electrons passing the photon ID criteria to the total number of probe electrons is taken as the photon ID efficiency. This method covers an energy range of $25\,\text{GeV} < E_\text{T} < 150\,\text{GeV}$ and typically comes along small uncertainties.

Matrix Method The matrix method uses events selected by single-photon triggers. It exploits that the track isolation is only weakly correlated to the ID variables that are measured in the first layer of the ECAL. Both the number of prompt photons and that of prompt photons passing the ID requirements are expressed by track isolation efficiencies. The energy covered by this procedure ranges from 25 GeV up to 1500 GeV, which is the largest of all methods. In the next section, the matrix method is explained in more detail.

By each method, the photon ID efficiency is determined and SFs are computed. These SFs are finally combined to obtain a single set of SFs separately for converted and unconverted photons in dependence of the transverse energy and the pseudorapidity.

6.2.1 Matrix method

The matrix method presented in this thesis uses data recorded by the ATLAS detector in the years 2015 and 2016 at $\sqrt{s} = 13\,\text{TeV}$. They correspond to an integrated luminosity of $36.7\,\text{fb}^{-1}$. The events are required to pass at least one single-photon trigger which applies loose ID criteria to photon candidates. The triggers differ in their lower energy threshold ranging from 10 GeV up to 140 GeV. For the reconstruction of photons, the SW algorithm is used which is presented in Section 5.2.1. Events are selected that contain at least one reconstructed photon in the pseudorapidity range of $|\eta| < 2.37$, excluding the transition region of $1.37 \leq |\eta| \leq 1.52$. The transverse energy of the reconstructed photon is required to exceed 25 GeV. In addition, the photon candidate must fulfil the loose ID criteria and the loose isolation requirements as defined in Equation (21).

The signal present in the selected dataset arises from events whose final state contains a prompt photon and either a quark or gluon. The background consists dijets events of which one jet is mis-reconstructed as photon. Both the signal and background processes are simulated using the event and shower generator Pythia 8 with the A14 tune and NNPDF2.3LO PDF set. The detector response is simulated by Geant 4 using the full simulation of the ATLAS detector.

For the matrix method, the photon ID efficiency as defined in Equation (26) is expressed using purities P by

$$\varepsilon^{\text{tight-ID}} = \frac{P^{\text{pass}} \cdot N_{\text{ID}}^{\text{total}}}{P^{\text{total}} \cdot N^{\text{total}}} \tag{27}$$

with the number of all photon candidates being tightly identified $N_{\text{ID}}^{\text{total}}$, and the total number of photon candidates, N^{total}. Those purities are defined as

$$P^{\text{pass}} = \frac{N_{\text{ID}}^{\text{s}}}{N_{\text{ID}}^{\text{total}}} \quad \text{and} \quad P^{\text{total}} = \frac{N^{\text{s}}}{N^{\text{total}}} \ . \tag{28}$$

They are extracted by using a track isolation requirement. This requirement forbids any track being present in a cone of $\Delta R = 0.4$ around the photon candidate, while excluding tracks associated to the photon cluster. Using this isolation requirement, the equations for the purities are simplified by using only terms of track isolation efficiencies, $\hat{\varepsilon}$, to

$$P^{\text{pass}} = \frac{\hat{\varepsilon}_{\text{ID}}^{\text{total}} - \hat{\varepsilon}_{\text{ID}}^{\text{bkg}}}{\hat{\varepsilon}_{\text{ID}}^{\text{s}} - \hat{\varepsilon}_{\text{ID}}^{\text{bkg}}} \quad \text{and} \quad P^{\text{total}} = \frac{\hat{\varepsilon}^{\text{total}} - \hat{\varepsilon}^{\text{bkg}}}{\hat{\varepsilon}^{\text{s}} - \hat{\varepsilon}^{\text{bkg}}} \ . \tag{29}$$

Hereby, the superscripts *s* and *bkg* refer to prompt and fake photons, respectively, the superscript *total* to all prompt+fake photons, and the index ID to photon candidates passing the tight ID criteria.

The track isolation efficiencies $\hat{\varepsilon}^{\text{total}}$ and $\hat{\varepsilon}_{\text{ID}}^{\text{total}}$ are determined in data and those for prompt photons, $\hat{\varepsilon}^{\text{s}}$ and $\hat{\varepsilon}_{\text{ID}}^{\text{s}}$, are computed from MC simulation. The efficiencies for fake photons, $\hat{\varepsilon}^{\text{bkg}}$ and $\hat{\varepsilon}_{\text{ID}}^{\text{bkg}}$, are estimated using both data and MC simulation. Dedicated regions are constructed by splitting the photon ID variables into two groups. The first group contains the shower-shape variables f_{side}, w_{s3}, ΔE and E_{ratio}, which are called *narrow-strip* variables. They are measured in the first layer of the ECAL and describe the inner core of the photon candidate. For this reason, they are only weakly correlated, by a few percent, to the track isolation variable, which describes the environment around the inner core of the photon candidate. The second category is built up from the remaining shower-shape variables and is called *relaxed-tight*. Those variables reflect the shower development in the whole calorimeter system. In Figure 14, the four regions constructed by those two groups are illustrated. Photon candidates in region 1 pass the tight photon ID criteria and are typically prompt, while the other regions are enriched with fake photons.

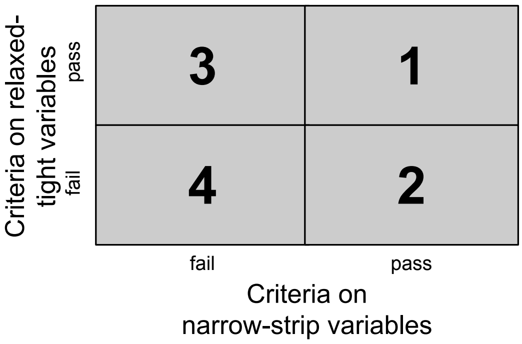

Figure 14: Illustration of the regions used for the categorisation of the photon candidates in the matrix method. The regions are defined by splitting the photon ID variables into the narrow-strip and relaxed-tight group.

For the computation of the track isolation efficiencies for the fake photons, $\hat{\varepsilon}^{\text{bkg}}$ and $\hat{\varepsilon}^{\text{bkg}}_{\text{ID}}$, two assumptions are made. The first assumption is that the track isolation efficiency of fake photons passing the tight ID criteria is almost equal to that of fake photons failing the cuts on the narrow-strip variables, while passing the relaxed-tight criteria. It is summarised by

$$\hat{\varepsilon}^{\text{bkg}}_{\text{ID}} = \frac{\hat{N}^{\text{bkg}}_1}{N^{\text{bkg}}_1} \approx \frac{\hat{N}^{\text{bkg}}_3}{N^{\text{bkg}}_3}\,, \tag{30}$$

whereby N^{bkg}_i denotes the number of fake photons in region $i = 1, 3$ and $\hat{N}^{\text{bkg}}_i$ refers to the number of fake photons passing the track isolation requirement in region $i = 1, 3$. This assumption exploits the weak correlation of the narrow-strip variables to the isolation variable. As second assumption, the amount of fake photons in region 1 is ignored in the computation of the overall track isolation efficiency, $\hat{\varepsilon}^{\text{bkg}}$, since their amount is negligible compared to the number of fake photons in the other regions. This assumption is written as

$$\hat{\varepsilon}^{\mathrm{bkg}} = \frac{\hat{N}_1^{\mathrm{bkg}} + \hat{N}_2^{\mathrm{bkg}} + \hat{N}_3^{\mathrm{bkg}} + \hat{N}_4^{\mathrm{bkg}}}{N_1^{\mathrm{bkg}} + N_2^{\mathrm{bkg}} + N_3^{\mathrm{bkg}} + N_4^{\mathrm{bkg}}} \approx \frac{\hat{N}_2^{\mathrm{bkg}} + \hat{N}_3^{\mathrm{bkg}} + \hat{N}_4^{\mathrm{bkg}}}{N_2^{\mathrm{bkg}} + N_3^{\mathrm{bkg}} + N_4^{\mathrm{bkg}}} \,. \tag{31}$$

Hereby N_i^{bkg} denotes the number of fake photons in region $i = 1, 2, 3, 4$ and $\hat{N}_i^{\mathrm{bkg}}$ refers to the number of fake photons passing the track isolation requirement in region $i = 1, 2, 3, 4$. In both assumptions, the number of fake photons is estimated by the observed number of photon candidates in regions 2 to 4, while subtracting the predicted prompt photon leakage.

The prompt photon, fake photon and total track isolation efficiencies without applying the tight ID criteria are shown for unconverted photons with $|\eta| < 0.6$ in dependence of E_{T} in Figure 15a. For prompt photons, the track isolation efficiency is independent of the energy as they are typically isolated objects. In contrast, for fake photons, the efficiency decreases with rising energy since jets faking photons become more collimated, i.e. single objects from a hadron decay fly in the same direction as the hadron did before, and are not isolated anymore. The total track isolation efficiency lies between the prompt and fake photon efficiencies. At low E_{T}, it slightly decreases caused by the non-negligible background contribution. In contrast, it becomes constant at high energies since the prompt photon contribution strongly dominates. The same behaviour is observed for unconverted photons in the other η regions and for converted photons in all η intervals.

In the next step, the purities P^{pass} and P^{total} are computed based on Equation (28). They are shown as a function of E_{T} for unconverted photons with $|\eta| < 0.6$ in Figure 15b. Both purities similarly climb with increasing energy because the contribution of fake photons steadily decreases. As expected, the purity P^{pass} surpasses the purity P^{total} as relatively more fake photons are rejected by the tight ID criteria than prompt photons. For unconverted photons in the other η regions and for converted photons in all η intervals, the same behaviour is observed.

Next, the photon ID efficiency is computed following Equation (27). As the selected photons in this method must fulfil trigger and loose ID requirements, a correction factor derived from MC simulation is applied to the photon ID efficiency in order to correct for any impact of the selection. As this correction factor is close to unity, no dedicated uncertainty is assigned due to it. Several other sources of

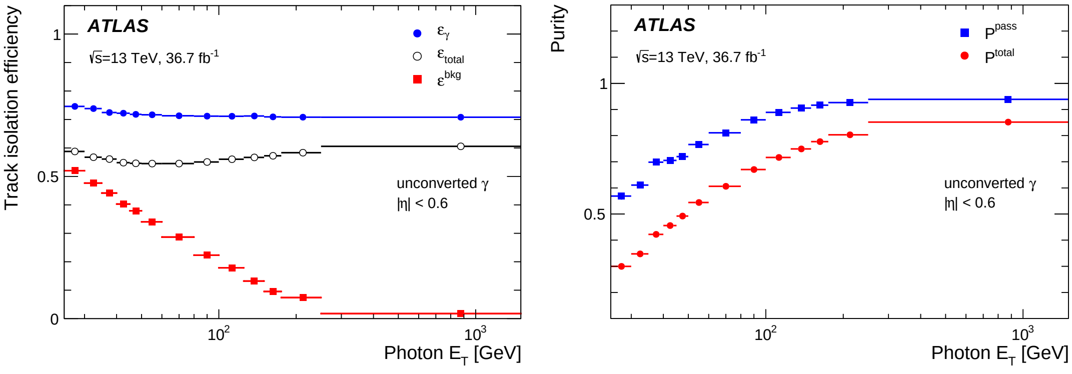

(a) Track-isolation efficiencies $\hat{\varepsilon}$

(b) Purities P^{pass} and P^{total}

Figure 15: Track-isolation efficiency for all, prompt and fake photons (a) and the purities P^{pass} and P^{total} (b) in dependence of E_{T} for unconverted photons with $|\eta| < 0.6$. In Figure (a), the variables translate as $\varepsilon_{\gamma} = \hat{\varepsilon}^{\mathrm{s}}$, $\varepsilon_{\text{total}} = \hat{\varepsilon}^{\text{total}}$ and $\varepsilon^{\text{bkg}} = \hat{\varepsilon}^{\text{bkg}}$. The plots are published in Ref. [152].

uncertainties are considered which are either related to the methodology or the dataset used. They are briefly described below.

Closure test A systematic uncertainty is assigned for the assumptions done in the estimation of the track isolation efficiencies for fake photons, presented in Equations (30) and (31). The track isolation efficiencies $\hat{\varepsilon}^{\text{bkg}}_{\text{ID}}$ and $\hat{\varepsilon}^{\text{bkg}}$ are separately varied up and down by the relative difference between the observed and predicted efficiencies. In total, four variations are obtained. Two of them lead to an increase of the photon ID efficiency, while the other two variations lead to a decrease. The variations resulting in a higher ID efficiency are added in quadrature and the square root is computed. Analogously, the same is done for the variations leading to a lower value. The largest square root is assigned as symmetric uncertainty.

MC stat. The impact of the limited number of simulated events is estimated by performing pseudo-experiments. For each pseudo-experiment, the simulated events are randomly drawn from the nominal MC samples, while the number of drawn events follows a Poisson distribution with the mean value being the total number of simulated events. Then, the matrix method is redone. In total, 200 pseudo-experiments are conducted. A histogram is filled with all photon ID efficiencies obtained resulting in a Gaussian distribution. Its width is assigned as symmetric uncertainty.

Distorted geometry The effect of the modelling of the detector material is estimated by exchanging the nominal MC samples for prompt photons by samples produced with a varied geometry of the ATLAS detector. This geometry assumes more material upstream of the ECAL. The matrix method is repeated with this setup. The absolute value of the difference between the newly derived and the nominal photon ID efficiency is assigned as symmetric uncertainty.

Track isolation An uncertainty is assigned due to the choice of the track isolation requirement. As both the cone size, ΔR, and the cut value on the track isolation variable are highly correlated, only the cone size is varied from 0.4 to 0.2. As a consequence, less fake photons are rejected compared to the nominal setup. The measurement is redone and the absolute value of the difference between the varied and the nominal ID efficiency is taken as symmetric uncertainty.

Statistical uncertainty The statistical uncertainty is estimated by performing 200 pseudo-experiments, analogously to the estimation of the impact of the limited number of simulated events. Now the observed events are drawn instead of the simulated events. Again, a histogram is filled with the obtained photon ID efficiencies which follow a Gaussian distribution. Its width is used as symmetric uncertainty.

The total uncertainty on the photon ID efficiency, $\Delta\varepsilon^{\text{tight-ID}}$, is obtained by summing up the individual uncertainties, σ_i, in quadrature and extracting the root as

$$\Delta\varepsilon^{\text{tight-ID}} = \sqrt{\sum_i \sigma_i^2}\,. \tag{32}$$

In Figure 16, the total uncertainty and the individual components are shown for unconverted and converted photons with $|\eta| < 0.6$ as a function of E_{T}. In general for unconverted photons at low energies, the total uncertainty is around 10 %. The dominant contributions arise from the closure test and the varied track isolation criterion. At high energies, the uncertainty of the detector geometry becomes most important. The total uncertainty at high energies falls below 1 %, except for the $|\eta|$ region of $1.52 < |\eta| < 1.81$ where it amounts to 5 %. For converted photons at low energies, the total uncertainty raises up to 18 % driven by the uncertainty for the closure test and that for the track isolation requirement. At high energies, the total uncertainty is below 1 % and no specific uncertainty dominates.

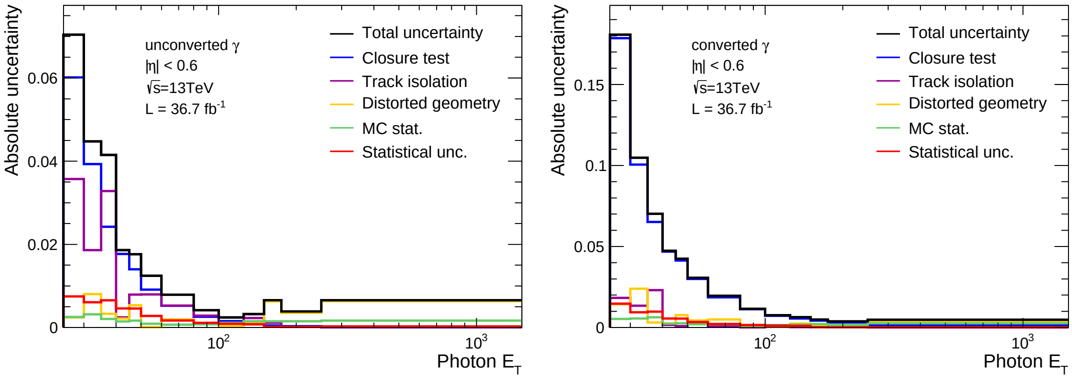

(a) Unconverted photons

(b) Converted photons

Figure 16: Total and individual uncertainties on the photon ID efficiency in dependence of E_{T} in the pseudorapidity interval of $|\eta| < 0.6$ for unconverted (a) and converted photons (b).

The photon ID efficiency obtained by the matrix method is shown in dependence of E_{T} for both unconverted and converted photons in the pseudorapidity interval of $|\eta| < 0.6$ in Figure 17, where this method is called *Inclusive photons* method. For both unconverted and converted photons, the efficiency at 25 GeV is around 85 % and converges to unity at high energies. The uncertainties decrease with increasing energy since the contamination of fake photons diminishes. The behaviour of the efficiency in the other pseudorapidity intervals is similar.

The dependence of the photon ID efficiency on the isolation WP used in the event selection and on the pile-up condition is investigated. Different isolation WPs are tested which all give similar results. The dependence on the pile-up conditions is probed by performing the matrix method in intervals of the average number of reconstructed primary vertices. The efficiency shows a decreasing trend with a raising number. This behaviour is expected since the photon ID criteria were optimised with data recorded in 2015 where the average number of primary vertices was lower than that in data collected in 2016.

The results of all three techniques are shown in Figure 17 for both unconverted and converted photons in the pseudorapidity interval of $|\eta| < 0.6$. The efficiencies of all three methods are in good agreement which is also seen in the other pseudorapidity intervals. For the radiative Z-boson method and the electron extrapolation method, only data with the ATLAS detector being fully operational were used, while for the matrix method additional data with relaxed requirements on the performance of the MS are used. The overlapping energy ranges as well as the strengths of the different methods are apparent. The radiative Z-boson decay method covers the lowest energies. However, it is statistically limited to 100 GeV due to the Z-boson mass. The electron extrapolation method covers intermediate energies and gives precise results. The matrix method covers the highest energies and the uncertainty on the efficiency decreases with increasing energy.

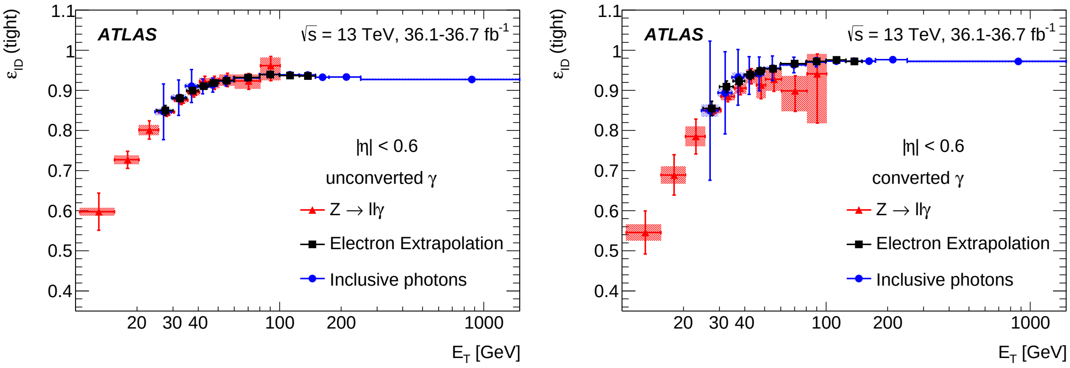

(a) Unconverted photons

(b) Converted photons

Figure 17: Photon ID efficiency in the pseudorapidity interval of $|\eta| < 0.6$ for unconverted (a) and converted photons (b) measured by the three different techniques [152]. The matrix method is here called *Inclusive photons* method.

6.3 Combination of results

Each individual method yields a set of photon ID SFs which are computed as the ratio of the measured to the predicted photon ID efficiency. All these SFs are compatible with unity for each pseudorapidity and energy interval. The three sets of SFs are combined by using the BLUE method [183, 184]. It linearly combines the SFs of each method which are weighted by the inverse of their uncertainty. As shown in Figure 18, the SFs measured by the different methods and their combination are in good agreement. At energies above 30 GeV, the uncertainty on the combined SF is equal to or below 1 %, except for $E_{\mathrm{T}} = 1.5\,\mathrm{TeV}$ in the interval $1.52 \leq |\eta| < 1.81$ where it is 4 %. Below energies of 30 GeV, the uncertainty reaches values up to 25 % due to the limited size of the photon samples.

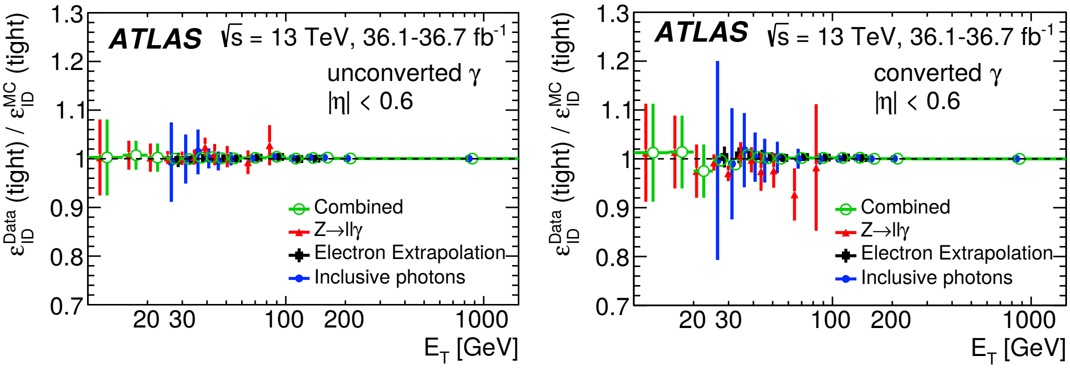

(a) Unconverted photons

(b) Converted photons

Figure 18: SFs for the photon ID in dependence of E_{T} in the pseudorapidity interval of $|\eta| < 0.6$ for unconverted (a) and converted photons (b) measured by the three different techniques and their combination [152].

The measurements of the photon ID efficiency and their combination were redone including data recorded in 2017. In those measurements, the supercluster algorithm was exclusively used for the photon reconstruction, instead of the SW algorithm. In addition, the photon ID criteria were reoptimised in order to account for the new reconstruction algorithm and for the increased pile-up. More details are found in Ref. [153].

7 Event selection

For the search of FCNCs in processes including a top quark and a photon, only a subset of data is selected out of the huge amount of events recorded by the ATLAS detector. This selection is realised by assigning selected events to statistically independent regions. These regions are constructed for different purposes. An important region is the signal region (SR) which is aimed to achieve a high signal-over-background ratio. Moreover, control regions (CRs) are used to estimate background contributions. In validation regions (VRs), the agreement between observation and MC simulation is demonstrated.

In this thesis, events are studied that contain at least one lepton to suppress multi-jet events, which arise from QCD processes. As the tau is neither explicitly reconstructed nor selected, only events with either an electron or a muon in the final state are analysed. As both types of events have similar kinematic properties, the combined electron+muon channel is analysed and presented in the following.

7.1 Preselection of events

Every event is required to pass definite preselection criteria, which are the same for all regions. Each event must have at least one reconstructed primary vertex and is required to have fired at least one trigger. The used triggers select events which include an electron-like or a muon-like physics objects. After the physics objects reconstruction, only events are selected in which either the reconstructed electron matches the electron-like particle of the trigger, or the reconstructed muon matches the muon-like particle of the trigger. The matching is based on the angular distances between the objects.

7.2 Signal region

The selection criteria for the SR are motivated by the final state of an event of the production-mode process, as shown in the Feynman diagram in Figure 2a. There, a single top quark is produced in association with a photon via an FCNC. The top quark is assumed to decay into a b quark and a W boson which is supposed to decays into a neutrino and a charged lepton. Consequently, the final state of an event is required to contain exactly one reconstructed photon, either one reconstructed electron or one reconstructed muon, one b-tagged jet, and $E_{\mathrm{T}}^{\mathrm{miss}}$ larger than 30 GeV. The reconstruction of the physics objects, their ID and isolation are described in Sections 5 and 6. Photons are reconstructed using the supercluster algorithm. For both the photon ID and isolation, the tight WPs are used.

Four different signal couplings are assumed, while only one is supposed to be present at a time. The coupling is assumed to be either LH or RH, and to include either an up quark or a charm quark. In the following, the differences of the assumed signal couplings and modes, the scaling of the signal, and the background contributions in the SR are discussed.

7.2.1 Differences between the signal processes and couplings

The $tu\gamma$ and $tc\gamma$ couplings allowing for the FCNC under study may appear in the production mode and decay mode, as shown for the LO processes in Figure 2. This search is optimised for the production mode. This mode features unique properties which facilitate to separate potential signal from background events. Generally, the kinematic properties of signal events strongly depend on the signal mode and coupling. In Figure 19, the normalised distributions of the photon p_{T}, the charged lepton p_{T} and the angular distance between the photon and b-jet are shown for the different signal couplings in the production and decay mode. All these distributions differ depending on the signal mode and coupling, which is explained in the following.

Events of the production mode are typically more energetic than those in the decay mode. This behaviour is caused by the limited energy available in the decay mode, which is approximately twice the top-quark mass. Such a limitation, however, is absent in the production mode. Consequently, the energy of the reconstructed physics objects as well as angular distances among them differ depending on the signal mode, as seen in all distributions in Figure 2.

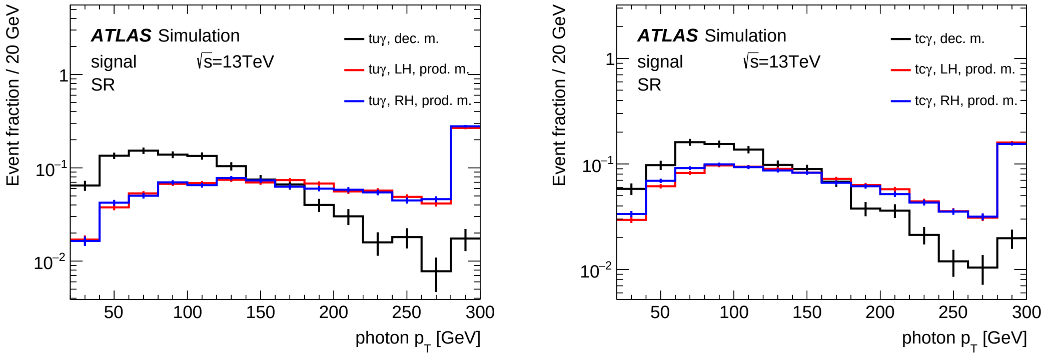

(a) Photon p_{T} for the $tu\gamma$ couplings **(b)** Photon p_{T} for the $tc\gamma$ couplings

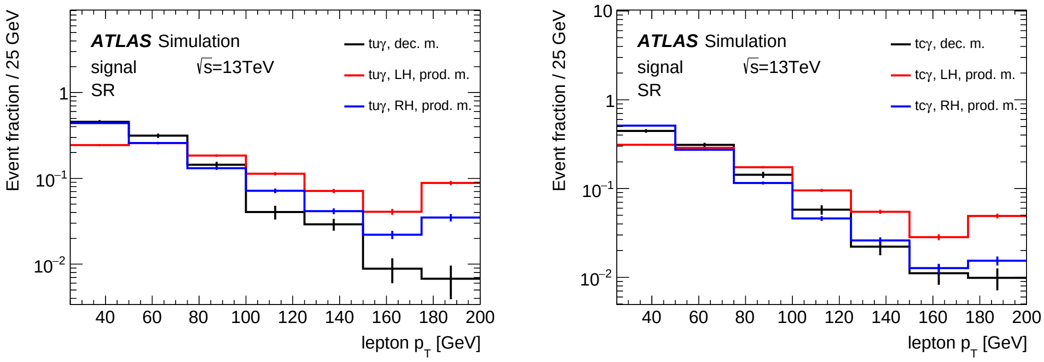

(c) Lepton p_{T} for the $tu\gamma$ couplings **(d)** Lepton p_{T} for the $tc\gamma$ couplings

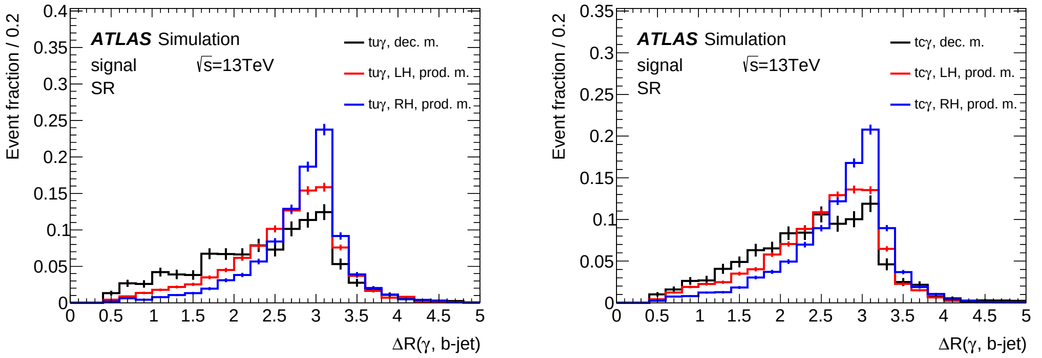

(e) $\Delta R(\gamma, b\text{-jet})$ for the $tu\gamma$ couplings **(f)** $\Delta R(\gamma, b\text{-jet})$ for the $tc\gamma$ couplings

Figure 19: Distributions of different kinematic variables of the signal for the $tu\gamma$ (left) and $tc\gamma$ couplings (right) in the production and decay mode in the SR: photon p_{T} (a,b), lepton p_{T} (c,d) and $\Delta R(\gamma, b\text{-jet})$ (e,f). In the production mode, the LH and RH couplings are separately shown. All distributions are normalised to unity and the over- and underflow are included, if present. The plots are published in the auxiliary material of Ref. [11].

Moreover, the handedness of the coupling impacts the kinematic properties of the signal events. It is distinguished between LH and RH couplings. When a top quark is produced via a RH coupling, its RH component is typically larger than the LH component. Thus, the phase space available in its subsequent electroweak decay is small, which happens in a purely LH interaction. Consequently, the W boson tends to receive only a small fraction of the total energy of the top quark, while the b quark is provided with a large amount of energy and typically flies in the same direction as the top quark did before. In the case of a LH signal coupling, the left-handed projection of the top quark as well as the phase space available in its electroweak decay is larger. Thus, the energy fraction transferred by the W boson tends to larger values. As a consequence of these different fractions of transferred energy, the kinematic properties of the final-state particles differ, as seen in the lepton p_{T} spectra in Figures 19c and 19d, and in the distributions of $\Delta R(\gamma, b\text{-jet})$ in Figures 19e and 19e. For the decay mode, however, the impact of the handedness is negligible at energies reached at the LHC since there is no such strong preference connected to the top-quark decay via an FCNC, as present in the production mode.

Furthermore, the flavour of the up-type quark plays an important role. In the production mode, events arising from the $tu\gamma$ couplings tend to be more energetic than event from the $tc\gamma$ coupling. This effect is caused by the proton's PDFs as the up quark is a valence quark of the proton. On average, the u quark in the initial state takes more of the energy of the proton than the c quark does. Consequently, the physics objects in the final state are typically more energetic for the $tu\gamma$ couplings. This behaviour is seen when comparing the peak positions of the photon p_{T} spectra in Figures 19a and 19b. While the peaks of the photon p_{T} spectra of the $tu\gamma$ couplings are above 100 GeV in the production mode, the analogue peaks of the $tc\gamma$ couplings are below 100 GeV. The same effect is visible in the lepton p_{T} spectra in Figures 19c and 19d. In the decay mode, differences appear due to the different masses of the up-type quarks, against which the photon recoils. As the charm quark is more massive than the up quark, the energy of the photon typically amounts to higher values for the $tc\gamma$ couplings. This phenomenon is also seen in the photon p_{T} spectra of the decay-mode signals in Figures 19a and 19b, although it is much smaller than the effect for the production mode.

Besides the kinematic properties, the selection efficiency including the detector acceptance and branching ratio for the leptonic decay of the W boson depends on the signal coupling. The efficiencies are about 3 % in the production mode and 0.5 % in the decay mode as listed in Table 2. The efficiencies of the decay mode are lower than to those in the production mode since only one jet is allowed in the final state. Typically, events of the decay mode exhibit a higher jet multiplicity. Furthermore, the efficiencies for the $tc\gamma$ couplings are higher than those for the $tu\gamma$ couplings in both modes. In the production mode, this effect is caused by the proton's PDFs. In the decay mode, it is caused by the b-tagging algorithm which potentially mis-tags the c-jet as b-jet. Lastly, in the production mode, the efficiencies for the LH couplings are higher compared to their RH counterparts due to the differences of the kinematic properties of the W boson's decay products.

Table 2: Selection efficiencies of the production- and decay-mode processes. These efficiencies include the detector acceptance and branching ratio for the leptonic decay of the W boson. Only statistical uncertainties are shown.

Coupling	Production mode	Decay mode
$tu\gamma$, LH	$3.03\,\% \pm 0.03\,\%$	$0.45\,\% \pm 0.01\,\%$
$tu\gamma$, RH	$2.45\,\% \pm 0.03\,\%$	
$tc\gamma$, LH	$3.79\,\% \pm 0.03\,\%$	$0.51\,\% \pm 0.01\,\%$
$tc\gamma$, RH	$3.14\,\% \pm 0.03\,\%$	

7.2.2 Scaling of signal

Since contributions of both the production and decay mode are present in the SR when assuming one of the signal couplings, the contributions of both processes are consistently scaled in the context of the EFT, which is described in Section 2.3. Interference effects between of both processes are negligible, as described in Section 2.4. For the scaling, the same values for the Wilson coefficients are assumed which accompany the two operators $\mathcal{O}_{\mathrm{uB}}^{(ij)}$ and $\mathcal{O}_{\mathrm{uW}}^{(ij)}$ as shown in Equations (16) and (17). The scale of new physics Λ is set to 1 TeV. With those coefficients, effective cross sections $\sigma_{\text{eff.,in}}^{\text{coup.}}$ are computed. As first guess, the order of magnitude of the previously best experimental limits on the branching ratio $\mathcal{B}(t \to q\gamma)$ with $q = u, c$ is used as baseline, which amounts to $\mathcal{O}\left(10^{-3}\right)$.

To connect both the Wilson coefficients and the branching ratio, their definitions are examined. As the top quark almost exclusively decays into a W boson and a b quark in the SM, the branching ratio $\mathcal{B}(t \to q\gamma)$ is approximated by

$$\mathcal{B}(t \to q\gamma) \approx \frac{\Gamma(t \to q\gamma)}{\Gamma(t \to Wb) + \Gamma(t \to q\gamma)} \approx \frac{\Gamma(t \to q\gamma)}{\Gamma(t \to Wb)} \tag{33}$$

with the partial decay widths $\Gamma(t \to q\gamma)$ and $\Gamma(t \to Wb)$, and assuming that $\Gamma(t \to q\gamma) \ll \Gamma(t \to Wb)$. The width $\Gamma(t \to Wb)$ in LO [2] is defined as

$$\Gamma(t \to Wb) = \frac{\alpha_{\text{QED}}(Q)}{16 \sin^2 \theta_W} |V_{\text{tb}}|^2 \frac{m_{\text{top}}^3}{m_{\text{W}}^2} \left(1 - 3\frac{m_{\text{W}}^4}{m_{\text{top}}^4} + 2\frac{m_{\text{W}}^6}{m_{\text{top}}^6}\right) \tag{34}$$

and the partial decay width $\Gamma(t \to q\gamma)$ in LO [106] is

$$\Gamma(t \to q\gamma) = \frac{\alpha_{\text{QED}}(Q) m_{\text{top}}^5}{\Lambda^4} \sum_{a \in \{1,2\}} \left(\left| C_{\text{uB}}^{(a3)*} + C_{\text{uW}}^{(a3)*} \right|^2 + \left| C_{\text{uB}}^{(3a)} + C_{\text{uW}}^{(3a)} \right|^2 \right) . \tag{35}$$

The index a indicates the first or second generation for the up-type quark. The complex conjugated Wilson coefficients refer to the LH couplings, while the RH coupling is represented by the non-conjugated coefficients. Both the branching ratio $\mathcal{B}(t \to q\gamma)$ and the width $\Gamma(t \to q\gamma)$ are proportional to the absolute value of the sum of the Wilson coefficients, which is hereafter also referred to as $|C^{\text{sum}}|$ commonly for all couplings. The difference between the branching ratio $\mathcal{B}(t \to q\gamma)$ at LO and that at NLO is of $\mathcal{O}(0.1\,\%)$ [185] and thus, negligible. Assuming the branching ratio $\mathcal{B}_{\text{in}}(t \to q\gamma)$ of 10^{-3} and that only one coupling is present at a time, the initial absolute value of the sum of Wilson coefficients yields

$$\mathcal{B}_{\text{in}}(t \to q\gamma) = 10^{-3} \Longrightarrow |C_{\text{in}}^{\text{sum}}| = 1.11\,. \tag{36}$$

Next, the effective cross sections are determined for this absolute value of the sum of Wilson coefficients. In the production mode, the effective cross section $\sigma_{\text{eff.,in}}^{\text{prod. m.}}$ equals

$$\sigma_{\text{eff.,in}}^{\text{prod. m.}} = \sigma_{\text{in}}(pp \to t\gamma) \times \mathcal{B}(t \to Wb) \times \mathcal{B}(W \to \ell\nu_\ell) \tag{37}$$

with $\mathcal{B}(t \to Wb) \approx 1$ and $\mathcal{B}(W \to \ell\nu_\ell) = 32.58\,\%$ for $\ell = e, \mu, \tau$ [22]. The cross section $\sigma_{\text{in}}(pp \to t\gamma)$ is taken from MC simulation and scaled to the absolute value of the sum of Wilson coefficients $|C_{\text{in}}^{\text{sum}}|$. As the matrix element is linearly proportional to the strength of the operators, the cross section shows a quadratic dependence on the sum of Wilson coefficients. This dependence was verified in cross-section scans when varying the Wilson coefficients. Any SM contribution to this cross section is neglected since it is suppressed by the GIM mechanism. In the decay mode, the effective cross section, $\sigma_{\text{eff.,in}}^{\text{dec. m.}}$, is given by

$$\sigma_{\text{eff.,in}}^{\text{dec. m.}} = 2 \times \sigma(pp \to t\bar{t}) \times \mathcal{B}(t \to Wb) \times \mathcal{B}(W \to \ell\nu_\ell) \times \mathcal{B}_{\text{in}}(t \to q\gamma)\,, \tag{38}$$

with $\sigma(pp \to t\bar{t}) = 831.76\,\text{pb}$ [112, 127–130]. The factor two accounts for the interchangeability of the top-quark and anti-top-quark decay. In the decay mode, the effective cross sections are the same for both the $tu\gamma$ and $tc\gamma$ couplings. In Table 3, the obtained effective cross sections and the corresponding numbers of events are shown for both modes and all couplings. For the $tu\gamma$ couplings, the ratio of the expected number of events in the production mode to that in the decay mode yields about 5:1 or 4:1 for the LH or RH coupling, respectively. In contrast, the contributions of both modes are comparably large for the $tc\gamma$ couplings. This effect is mainly driven by the different effective cross sections for the $tu\gamma$ and $tc\gamma$ couplings in the production mode. In all other regions defined later, the signal contributions are scaled to the same effective cross sections.

Table 3: Effective cross sections, $\sigma_{\text{eff.,in}}^{\text{coup.}}$, and the corresponding numbers of signal events in the SR for both the production and decay mode and for all couplings. The absolute value of the sum of Wilson coefficients is assumed to be $|C_{\text{in}}^{\text{sum}}| = 1.11$ at a scale of new physics of $\Lambda = 1\,\text{TeV}$. Only the statistical uncertainties are shown.

Mode	Coupling	$\sigma_{\text{eff.,in}}^{\text{coup.}}$ [fb]	Expected number of events
Production	$tu\gamma$, LH	416.70	$1\,012 \pm 15$
	$tu\gamma$, RH	416.40	810 ± 13
	$tc\gamma$, LH	59.47	179.5 ± 2.2
	$tc\gamma$, RH	59.49	148.3 ± 1.9
Decay	$tu\gamma$	541.97	192.3 ± 6.1
	$tc\gamma$	541.97	216.7 ± 6.5

7.2.3 Background processes

Events of several background processes contribute to the SR which are predicted by the SM. They either exhibit the same final-state topology or pass the selection due to mis-reconstructed or misidentified physics objects. The background events stem from single top-quark, $t\bar{t}$, W+jets, Z+jets or diboson processes which pass the photon requirements by the presence of either a prompt or a fake photon.

The dominant background contribution arises from the $t\bar{t}$ process. Such events pass the selection criteria when either both W bosons of the top-quark decays decay into a pair of leptons of which one is an electron faking a photon, or one of the W bosons decays into quarks and the other into leptons and one of any jet in this event mimics a photon. The second main background contribution arises from events of the W+γ+jets process. They exhibit the same final-state topology as the signal does. Events containing a Z boson are another important part of the background. Such events are selected when the Z boson decays into an electron and a positron of which one fakes a photon. Another background contribution originates from the $t\bar{t}$+γ process when final-state objects are not reconstructed. Events with a single top quark are almost exclusively selected from the t- or tW-channel when a photon is emitted in the hard scattering or, in the case of the tW-channel, a photon is faked by an electron. Other background contributions arise from events with a radiative Z-boson decay, diboson or W+jets processes when either final-state objects are failed to be reconstructed or a photon is faked by a jet or an electron. In total, 9 557 events are observed and 8 300 ± 120 events are expected, indicating only the statistical uncertainty. The expected number already includes the background estimations described in Section 8. In Figure 20, the fractions of the background processes are illustrated. The ratio of the expected number of signal events to that of background events, S/B, amounts to 9.3 % and the significance defined as $S/\sqrt{B}$ is equal to 8.31. Consequently, the SR provides a good potential to observe a signal contribution, if present.

In MC simulation, each background event with a photon in the final state is categorised into one of three classes in dependence of the photon origin, as described in Section 4.2.2. If a truth electron or hadron is close to the reconstructed photon, the event is classified as $e \to \gamma$ or $j \to \gamma$ fake, respectively. Otherwise, the photon is supposed to originate from the hard scattering and to be prompt. 48 % of all

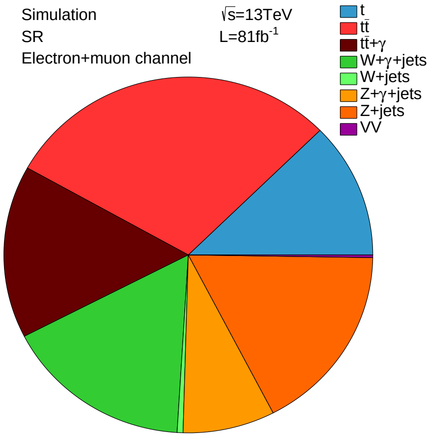

Figure 20: Illustration of the fractions of the different background processes which are present in the SR.

events contain a prompt photon. 46 % of all events are classified as $e \to \gamma$ fake, while only 6 % stem from events with a $j \to \gamma$ fake. In Figure 47, the observed and expected distributions of the photon and lepton p_T, the angular distance $\Delta R(\gamma, b\text{-jet})$ and the invariant mass $m(\ell, \gamma)$ are shown after the statistical analysis presented in Section 11. They include the estimations of all uncertainties which are described in Section 10. The signal distribution for the LH $tu\gamma$ coupling is overlaid. A good agreement between the observation and background prediction is found.

7.3 Control and validation regions

In this search, several CRs and VRs are used for different purposes, while their selections are as close to the SR as possible. This ensures that the estimations done in and the conclusions drawn from those regions are transferable to the SR.

The CR W+γ+jet is used to determine the normalisation of the W+γ+jets process. Therefore, it is enriched in events of this process by reversing the b-tagging requirement, while all other requirements of the SR are kept. Additionally, the invariant mass of the photon-lepton system, $m(\ell, \gamma)$, must lie outside a window around the Z-boson mass of 60 GeV to 100 GeV. This minimises the $e \to \gamma$ fake contribution, which dominantly stems from events with a Z boson. The purity of W+γ+jets events, defined as the ratio of the expected number of W+γ+jets events to that of all events, amounts to 74 %. The other events in this region mainly arise from processes including a Z boson. The relative composition of the SM processes is illustrated in Figure 21a. In total, 127 864 events are observed and 110 950 ± 790 events are expected, only including the statistical uncertainty. The expected number already includes the background estimations described in Section 8. The signal significance $S/\sqrt{B}$ amounts to 4.04 and the ratio S/B is 1.2, i.e the signal contribution is non-negligible and must be properly treated.

Another CR is devoted to estimate the normalisation of the $Z{+}\gamma$+jets contribution and called CR $Z{+}\gamma$. Events in this region are required to have a pair of charged leptons of the same flavour with opposite sign and a photon in the final state. The purity of the $Z{+}\gamma$+jets events is equal to 93 %, while minor contributions of the $t\bar{t}$ $+\gamma$ and Z+jets processes are present. The relative contributions of the SM processes are depicted in Figure 21b. 85 347 events are observed, while 78 430 ± 550 are expected including the statistical uncertainty. The expected number already includes the background estimations described in Section 8. The signal significance is below 0.01 and the ratio S/B is smaller than 0.01 %. Consequently, the signal contamination is neglected.

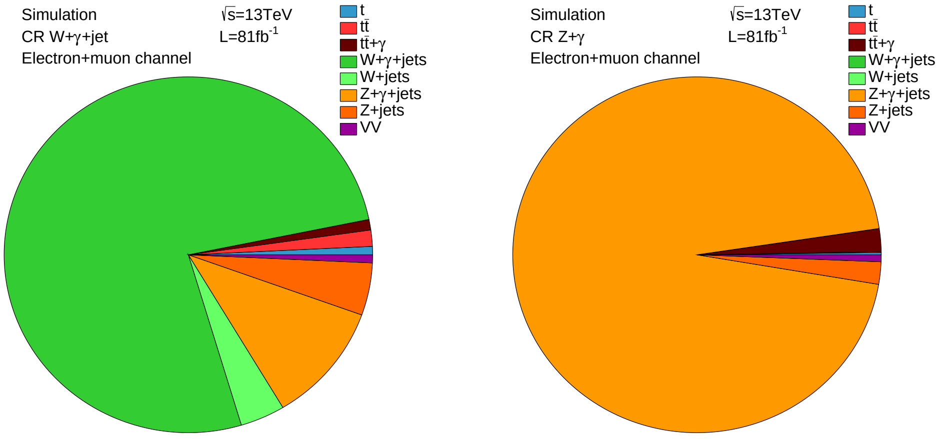

(a) CR $W{+}\gamma$+jet **(b)** CR $Z{+}\gamma$

Figure 21: Illustration showing the composition of the SM processes in the CR $W{+}\gamma$+jet (a) and CR $Z{+}\gamma$ (b).

Other regions used in this analysis are the electron fake estimation regions (EFRs), hadronic fake estimation regions (HFRs) and their respective VRs. These regions are used in methods to determine SFs for the $e \to \gamma$ and $j \to \gamma$ contributions and are described in Section 8.

7.4 Photon p_{T} reweighting

In both the CR W+γ+jet and CR Z+γ, a slope is observed in the ratio of the observed to the expected photon p_{T} spectrum when comparing data to the background prediction, as shown in Figure 22. This slope amounts to roughly 10 % in the CR Z+γ and about 25 % in the CR W+γ+jet. It is caused by the imperfect p_{T} modelling of the Z and W bosons in MC simulation. In both CRs, the slope is too large to be caused by a signal contribution. To revise this systematic bias, a shape correction is computed for the Z+γ+jets and W+γ+jets processes by reweighting their photon p_{T}. At first, the simulated Z+γ+jets events are reweighted in the CR Z+γ, as in this region the contribution of the W+γ+jets process is negligible. Then, the correction for the simulated W+γ+jets events is determined in the CR W+γ+jet taking into account the reweighting of the Z+γ+jets process.

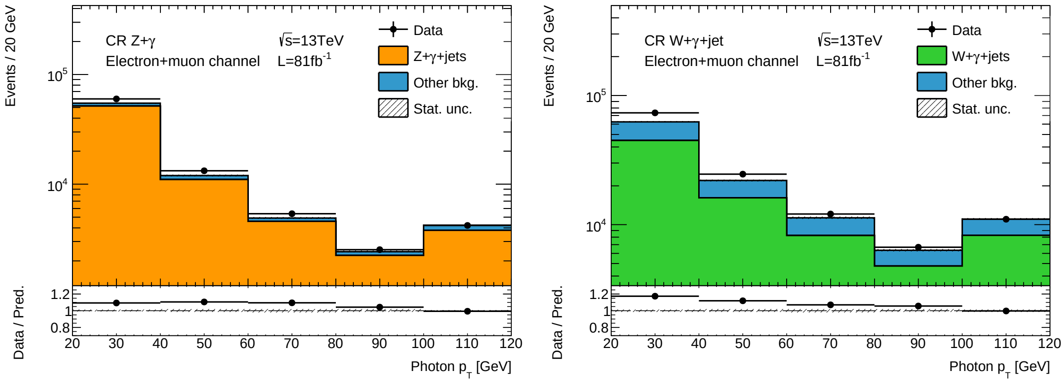

(a) CR Z+γ (b) CR W+γ+jet

Figure 22: Observed and expected distributions of the photon p_{T} in the CR Z+γ (a) and in the CR W+γ+jet (b). In the bottom plot, the ratio between data and background prediction is depicted. Only the statistical uncertainties are shown and the overflow is included.

In both regions, the same reweighting procedure is applied. In the first step, the data are corrected by subtracting the contributions from other SM processes than the process under study. Any signal contribution is neglected in this procedure. Then, the ratio between the corrected data and the prompt photon contribution under study is fitted by a linear function in five equidistant bins ranging from 20 GeV to 120 GeV, as shown in Figure 23. As last step, the prompt photon contribution is reweighted using the per-bin weight extracted from the fit function. The overall normalisation is preserved, i.e. only the shape is corrected. An uncertainty of 100 % is assigned to the reweighting. A down variation of 100 % equals the simulated distributions without the p_{T} reweighting.

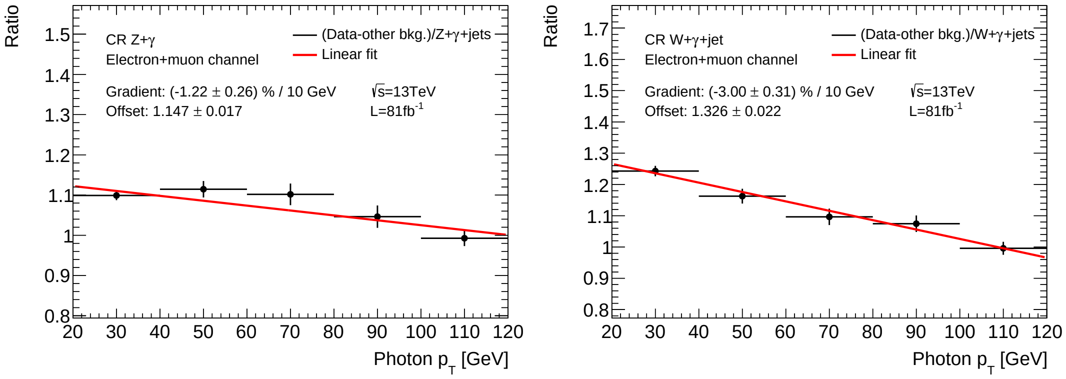

(a) CR Z+γ **(b)** CR W+γ+jet

Figure 23: Fitted ratio of corrected data to the prompt photon contribution under study of the photon p_{T} spectrum in the CR Z+γ (a) and in the CR W+γ+jet (b). Only the statistical uncertainties are shown and the overflow is included.

The slope determined in the CR Z+γ is about 10 % over the full p_{T} range and amounts to 20 % in the CR W+γ+jet. In Figure 24, the observed and expected photon p_{T} distributions in both CRs after the reweighting are shown. In the bottom panel, the ratio between observation and background prediction is drawn, which is flatter in comparison to the ratio seen before the reweighting in Figure 22. The normalisation between observation and expectation still disagrees since the contributions of the W+γ+jets and Z+γ+jets processes are estimated later on in the statistical analysis presented in Section 11. Other kinematic variables in both CRs and in other regions showed an improved agreement between observation and MC simulation by using the reweighting. Conclusively, a significant improvement of the agreement between data and background prediction is achieved by the photon p_{T} reweighting.

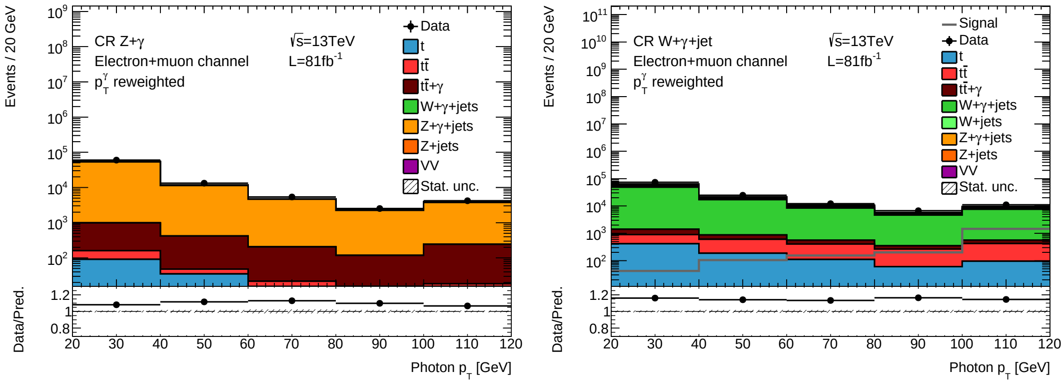

(a) CR Z+γ

(b) CR W+γ+jet

Figure 24: Observed and expected distributions of the photon p_{T} spectrum after the p_{T} reweighting in the CR Z+γ (a) and in the CR W+γ+jet (b). In the CR Z+γ, the signal contribution is negligible and not drawn, while it is overlaid in the CR W+γ+jet. In the bottom panel, the ratio between data and background prediction is depicted. Only the statistical uncertainties are shown and the overflow is included.

8 Background estimations

Photons may be faked by an electron or a jet. As events with both fake types are present in this search, separate SFs are determined using dedicated methods to correct the simulation for any imperfections.

8.1 Electron-to-photon fakes

Both electrons and photons leave similar signatures in the detector which reasons their parallel reconstruction using the same algorithm as described in Section 5. In order to estimate the amount of electrons mis-reconstructed as photons, a technique commonly used in analyses of the ATLAS collaboration [152] is employed. It is based on estimating the probability of an electron faking a photon, $f_{e\rightarrow\gamma}$. Therefore, the numbers of events are estimated that contain a Z boson decaying into an electron-positron pair. In such events, either both leptons are correctly reconstructed or one of them is mis-reconstructed as photon. The fake rate is measured and compared to the expected value. The ratio of these fake rates is defined as the electron-to-photon scale factor, $SF(e \rightarrow \gamma)$.

8.1.1 Regions for the electron-to-photon-fake estimation

Two regions, named EFR $Z \rightarrow ee$ and EFR $Z \rightarrow e\gamma$, are constructed by selecting events which contain a Z boson decaying into an electron-positron pair. In the EFR $Z \rightarrow ee$, both leptons are reconstructed as electrons. In contrast in the EFR $Z \rightarrow e\gamma$, one of them is correctly reconstructed and the other is mis-reconstructed as a photon. Furthermore, the VR SF($e \rightarrow \gamma$) is defined to validate the $SF(e \rightarrow \gamma)$. The definitions of the regions are given in Table 4. In all regions, a window on the invariant mass of the Z boson's decay products is introduced which lies around the mass of the Z boson. In the VR SF($e \rightarrow \gamma$), this window is smaller to increase the purity of events with an $e \rightarrow \gamma$ fake. Moreover, a maximal amount of missing transverse momentum is required to ensure statistical independence to the SR. The number of jets is exploited to build the EFRs and the VR. In both EFRs, no jet is allowed, while in the VR, only events with at least one jet are selected. In this way, the VR is similarly defined as the SR, but enriched in events of the Z+jets and $t\bar{t}$ processes which contain a photon faked by an electron. In all those regions, the signal contamination is negligible.

Table 4: Overview of the selection criteria for the EFR $Z \to ee$, EFR $Z \to e\gamma$ and VR SF($e \to \gamma$) used for the electron-to-photon fake estimation. A hyphen means that no requirement is made.

Object	EFR $Z \to ee$	EFR $Z \to e\gamma$	VR SF($e \to \gamma$)
Photons	$= 0$	$= 1$	$= 1$
Electrons	$= 2$ w/ opposite sign	$= 1$	$= 1$
Jets	$= 0$	$= 0$	≥ 1
$E_{\mathrm{T}}^{\mathrm{miss}}$	$< 30\,\mathrm{GeV}$	$< 30\,\mathrm{GeV}$	$< 30\,\mathrm{GeV}$
$m(e,\gamma)$	-	$[60\,\mathrm{GeV},\ 120\,\mathrm{GeV}]$	$[70\,\mathrm{GeV},\ 110\,\mathrm{GeV}]$
$m(e,e)$	$[60\,\mathrm{GeV},\ 120\,\mathrm{GeV}]$	-	-

For the EFR $Z \to ee$, almost exclusively events from the Z+jets process are selected. The EFR $Z \to e\gamma$ is also dominated by Z+jets events which contain an $e \to \gamma$ fake. Moreover, a notable number of events with a prompt photon is present, which mainly stems from the Z+γ+jets and W+γ+jets processes. Their fraction amounts to $(8.83 \pm 0.06)\,\%$ with only the statistical uncertainty. In the VR SF($e \to \gamma$), a similar composition as in the EFR $Z \to e\gamma$ is observed.

In Figure 25, the observed and expected distributions of the invariant mass $m(e,e)$ in the EFR $Z \to ee$ and $m(e,\gamma)$ in the EFR $Z \to e\gamma$ are shown. All these distributions peak around the Z-boson mass. In the EFR $Z \to ee$, the agreement between data and MC simulation is good, while there are differences in the tails in the EFR $Z \to e\gamma$. As in both regions only the normalisation is of interest, the discrepancies in the tails are not important as their impact on the normalisation is below $1\,\%$.

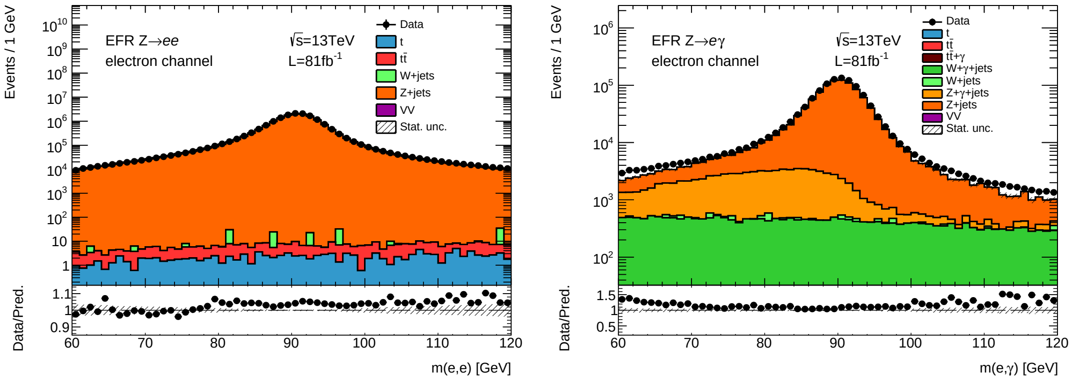

(a) Invariant mass $m(e,e)$ in EFR $Z \to ee$

(b) Invariant mass $m(e,\gamma)$ in EFR $Z \to e\gamma$

Figure 25: Observed and expected distributions of the invariant mass $m(e,e)$ in the EFR $Z \to ee$ (a) and $m(e,\gamma)$ in the EFR $Z \to e\gamma$ (b). In the bottom plot, the ratio between data and MC simulation is shown. Only statistical uncertainties are shown.

8.1.2 Measurement of electron-to-photon fake rate

In order to extract the number of events containing a Z boson in both regions, the invariant mass distributions are fitted by a signal function and a background function. In both regions, a double-sided Crystal Ball function scaled by a normalisation parameter is used as signal function. It is supposed to model all events with a Z-boson decay. In the EFR $Z \to e\gamma$, it also includes events with a radiative Z-boson decay, $Z \to ee\gamma$, whose contribution is subtracted later. As background function, a forth-order Bernstein polynomial scaled by another normalisation parameter is used in both regions. It is meant to model events not including a Z boson, e.g. events with only one lepton and a jet faking an electron.

The fit outcome for both regions is shown in Figure 26. The individual signal and background functions are depicted, too. In both regions, the fit is able to reproduce the observed distribution. To estimate a systematic uncertainty for the choice of the fit functions, the fit is redone with a Gaussian function scaled by a normalisation parameter as background function, and the parameters of the signal function set to the values obtained from a fit to the MC expectation, except for the normalisation parameter. The difference of the nominal and varied SFs, determined as described below, is used as uncertainty on the SF. Another systematic uncertainty is assigned due to the choice of the fit range. Therefore, the nominal range from 60 GeV to 120 GeV is varied to 65 GeV - 115 GeV. Again, the difference between the nominal and varied SFs is taken as uncertainty.

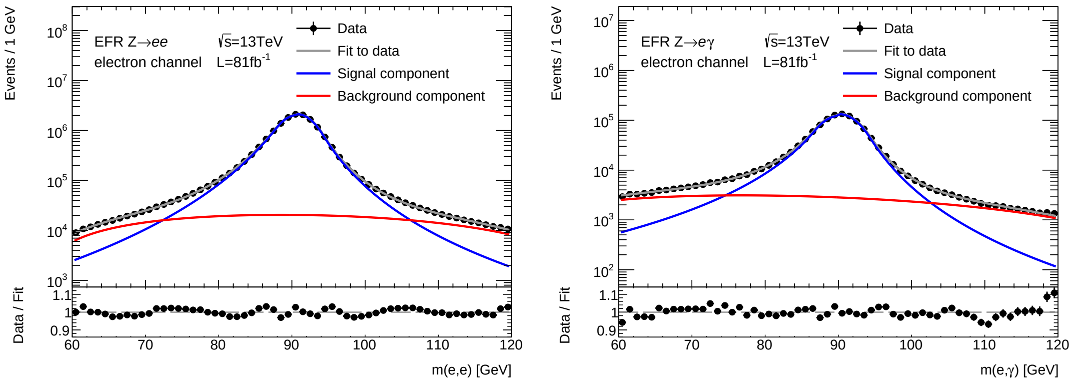

(a) EFR $Z \to ee$ (b) EFR $Z \to e\gamma$

Figure 26: Observed and fitted distributions of the invariant mass $m(e, e)$ in the EFR $Z \to ee$ (a) and $m(e, \gamma)$ in the EFR $Z \to e\gamma$ (b). The signal and background functions are separately shown. In the bottom panel, the ratio between observation and the fit outcome is shown. Only statistical uncertainties are shown.

The probability for an electron to fake a photon, $f_{e\to\gamma}$, is defined as the number of signal events, $N(e\gamma)$, in the EFR $Z \to e\gamma$ over twice the number of signal events, $N(ee)$, in the EFR $Z \to ee$ by

$$f_{e\to\gamma} = \frac{N(e\gamma)}{2 \cdot N(ee)} \,. \tag{39}$$

The factor two in the denominator accounts for the fact that either the electron or the positron in the EFR $Z \to e\gamma$ mimics a photon, while such a permutation is not possible in the EFR $Z \to ee$.

The number of signal events in the EFR $Z \to ee$ is given by the integral of the fitted signal function. In the EFR $Z \to e\gamma$, the number of signal events is obtained by the integral of the signal function, while subtracting the relative fraction of 8.83 % of the number of events with a prompt photon. As systematic uncertainty, the expected number of events with a prompt photon is subtracted instead of its relative fraction and the difference between the nominal and varied SF is assigned as uncertainty. This variation covers the cross-section uncertainties of the prompt photon contributions. The measured and expected fake rates are

$$f_{e\to\gamma}^{\text{data}} = 3.11\,\% \pm 0.01\,\%\,(\text{stat.}) \pm 0.13\,\%\,(\text{syst.}) \tag{40}$$

$$\text{and} \quad f_{e\to\gamma}^{\text{MC}} = 3.18\,\% \pm 0.01\,\%\,(\text{stat.})\,, \tag{41}$$

respectively, with the statistical and systematic uncertainties. The systematic uncertainty is driven by the variation of the fit functions whose impact amounts to 0.11 %. The uncertainty due to the variation of the fit range is equal to 0.06 % and the impact of the variation of the background subtraction is 0.01 %.

8.1.3 Scale factor for electron-to-photon fakes

The $SF(e \to \gamma)$ is defined as the ratio of the observed to the expected fake rate and yields

$$SF(e \to \gamma) = \frac{f_{e\to\gamma}^{\text{data}}}{f_{e\to\gamma}^{\text{MC}}} = 0.978 \pm 0.004\,(\text{stat.}) \pm 0.040\,(\text{syst.})\,. \tag{42}$$

Since it is in good agreement with unity, it does not hint at any systematic bias in the modelling of $e \to \gamma$ fakes.

The $SF(e \to \gamma)$ is validated in the VR SF($e \to \gamma$) after performing the statistical analysis as described in Section 11. In Figure 48b, the observed and expected distributions of the jet p_{T} is shown including all uncertainties. A good agreement between data and MC expectation is achieved. As data and expectation also agree in other distributions in this and other regions, the $SF(e \to \gamma)$ and its uncertainty are considered validated. Since in other analyses, e.g. the cross-section measurement of the $t\bar{t}$+γ process presented in Ref. [115], the total uncertainty on the $SF(e \to \gamma)$ is of $\mathcal{O}(10\,\%)$, the uncertainty is increased from 4 % to 10 % in the statistical analysis described in Section 11. This increase accounts for a possible underestimation of the uncertainty on the $SF(e \to \gamma)$.

8.2 Hadronic fakes

A jet may fake a photon when any hadron inside the jet decays into two photons which are reconstructed as one photon. The hadronic fake contribution in the SR is estimated by the ABCD method which is based on the matrix method used for the photon ID efficiency measurement as presented in Section 6. With the ABCD method, the number of events with a hadronic fake in the SR is directly estimated. It exploits that hadronic fakes are strongly suppressed by isolation requirements, while prompt photons are isolated physics objects.

8.2.1 Regions for the hadronic fake estimation

Four HFRs are constructed by inverting some requirements on the photon candidate, while all other criteria of the SR selection are kept. In this way, regions close to the SR are obtained that are enriched in events with a hadronic fake. For the photon candidates in the different regions, the isolation criteria of the tight WP and the cuts on the narrow-strip variables of the photon ID are changed. The narrow-strip variables are f_{side}, w_{s3}, ΔE and E_{ratio} and explained in Section 6.1. As these variables describe the shower development in the inner core of the photon cluster in the finely granular first layer of the ECAL, they are only weakly correlated, by a few percent, to the isolation variables. These variables measure energy depositions or tracks outside the core. The criteria on the other photon ID variables are kept.

In Figure 27, the regions and their definitions are illustrated. In HFR A, the photon candidate fulfils the isolation criteria, but fails at least one cut on the narrow-strip variables. An event is classified into HFR B when the photon candidate fails criteria on both the isolation and the narrow-strip variables. If the photon candidate meets the isolation requirements, but fails at least one criterion on the narrow-strip variables, the event is categorised into HFR C. HFR D is equal to the SR where the photon candidate fulfils both the isolation requirements and criteria on the narrow-strip variables. In the HFRs A, B and C, the signal contamination is negligible.

The observed and expected number of events of the HFRs are shown in Figure 28a, which only includes statistical uncertainties. The agreement between data and background prediction is off by 20 % to 30 % in all regions since the normalisation of events with a hadronic fake and that of events with a prompt photon are imperfectly modelled in simulation. The HFRs A, B and C are enriched with events including a hadronic fake due to the loosening of the photon requirements. In contrast in HFR D, the $j \to \gamma$ contribution is only a minor background. In Figure 28b, the contribution of events with a hadronic fake split by SM processes is shown for all HFRs. In all

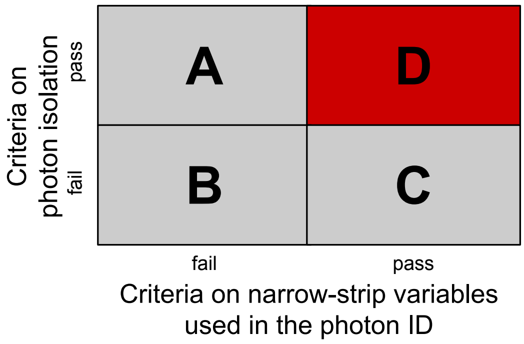

Figure 27: Illustration of the regions used in the ABCD method to estimate the number of events with a hadronic fake in the SR.

regions, the dominant contribution stems from the $t\bar{t}$ process. Another important contribution arises from single top-quark events. In HFRs A, B and C, the fraction of W+jets events is larger than that in HFR D. As in the SR, both the b-tagging and photon requirements strongly suppress the contribution of W+jets events, only the b-tagging requirement is left in the other HFRs leading to this increase.

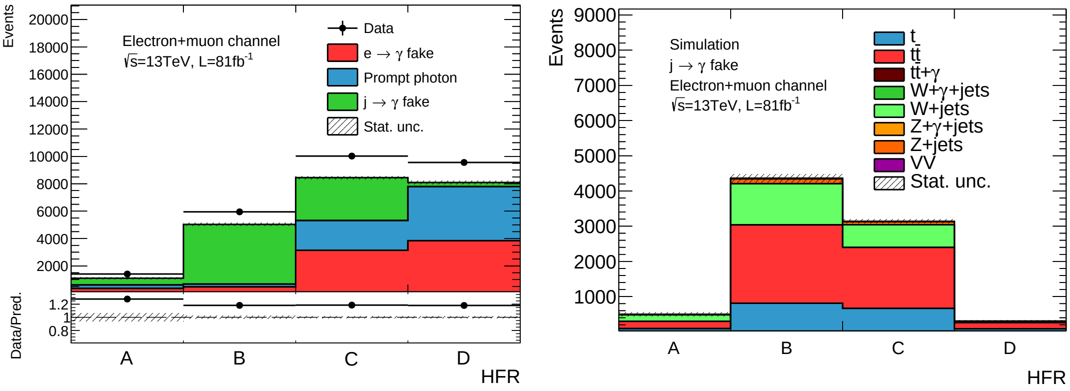

(a) Observed and expected number of events

(b) Events with a hadronic fake

Figure 28: Observed and expected number of events in the different HFRs (a) and the composition of events with a hadronic fake in the HFRs split by SM processes (b).

The $SF(j \to \gamma)$ is validated in the *VR for combined background*. Its event selection is close to that of the SR. Contrary to the selection in the SR, an event in this VR must have at least two jets with none of them being b-tagged and the photon p_T is restricted to 100 GeV in order to increase the fraction of events with a hadronic fake. The ratio S/B equals 1.5 and the significance $S/\sqrt{B}$ is 6.63. These numbers are driven by the signal of the decay-mode process which typically has a higher jet multiplicity.

8.2.2 ABCD method

For the ABCD method, the isolation criteria are assumed to be uncorrelated to the narrow-strip variables. Under this assumption, the following equation holds:

$$N_{j\to\gamma}(D) = \frac{N_{j\to\gamma}(A)\cdot N_{j\to\gamma}(C)}{N_{j\to\gamma}(B)} \tag{43}$$

with the number of events with a hadronic fake, $N_{j\to\gamma}(i)$, in HFR $i = A, B, C$ or D. A closure test is done with the expected number of events with a hadronic fake. It results in a correction factor, θ_MC, which accounts for the non-zero correlations between the narrow-strip and isolation variables of the hadronic fakes. This factor is defined as

$$\theta_\mathrm{MC} = \frac{N^\mathrm{pred.}_{j\to\gamma}(D)\cdot N^\mathrm{pred.}_{j\to\gamma}(B)}{N^\mathrm{pred.}_{j\to\gamma}(A)\cdot N^\mathrm{pred.}_{j\to\gamma}(C)} = 0.85 \pm 0.14\,(\mathrm{stat.}) \tag{44}$$

with the expected number of events with a hadronic fake, $N^\mathrm{pred.}_{j\to\gamma}(i)$, in HFR $i = A, B, C$ or D. A total uncertainty of 50 % is assigned to this correction factor to account for any imperfect modelling in simulation.

To obtain the observed number of events with a hadronic fake, $N^\mathrm{data}_{j\to\gamma}(i)$, in the HFR $i = A, B$ or C, the contributions from events with an $e\to\gamma$ fake and from events with a prompt photon are subtracted from the observed number of events, summarised as

$$N^\mathrm{data}_{j\to\gamma}(i) = N^\mathrm{data}_\mathrm{total}(i)\left(1 - \frac{N^\mathrm{pred.}_{\text{prompt-}\gamma}(i)}{N^\mathrm{pred.}_\mathrm{total}(i)}\right) - SF(e\to\gamma)\cdot N^\mathrm{pred.}_{e\to\gamma}(i)\,, \tag{45}$$

whereby $N^\mathrm{data}_\mathrm{total}(i)$ and $N^\mathrm{pred.}_\mathrm{total}(i)$ denote the observed and expected number of events in HFR i, respectively, $N^\mathrm{pred.}_{\text{prompt-}\gamma}(i)$ is the expected number of events with a prompt photon and $N^\mathrm{pred.}_{e\to\gamma}(i)$ is the expected number of events with an $e\to\gamma$ fake. Note that the data in HFR D, which is the SR, are not used in the estimation of the events with a hadronic fake. For estimating a systematic uncertainty for the subtraction of prompt photons, the relative subtraction is replaced by the subtraction of the expected number of events with a prompt photon. The difference of the nominal to the varied SF, determined as described below, is taken as uncertainty. Another uncertainty accounts for the subtraction of the $e \to \gamma$ fake contribution by varying the $SF(e \to \gamma)$ up and down by one standard deviation[1], while the largest absolute value of the difference between the nominal to varied SFs is assigned as uncertainty.

Finally, the observed number of events with a hadronic fake in HFR D, being the SR, is computed using Equation (43) and the correction factor defined in Equation (44) as

$$N^{\text{data}}_{j\to\gamma}(D) = \theta_{\text{MC}} \cdot \frac{N^{\text{data}}_{j\to\gamma}(A) \cdot N^{\text{data}}_{j\to\gamma}(C)}{N^{\text{data}}_{j\to\gamma}(B)} = 511 \pm 87\,(\text{stat.}) \pm 275\,(\text{syst.})\ . \tag{46}$$

The total uncertainty is dominated by the systematic component. The largest impact comes from the variation of the correction factor, θ_{MC}, which amounts to ±256. The variation of the prompt-photon subtraction has an impact of ±98 on the number of observed events, while the variation of the $SF(e \to \gamma)$ varies the number by ±24.

8.2.3 Scale factor for hadronic fakes

The $SF(j \to \gamma)$ is defined as the ratio of the observed to the expected number of events with a hadronic fake in HFR D as

$$SF(j \to \gamma) = \frac{N^{\text{data}}_{j\to\gamma}(D)}{N^{\text{pred.}}_{j\to\gamma}(D)} = 1.69 \pm 0.34\,(\text{stat.}) \pm 0.91\,(\text{syst.})\,. \tag{47}$$

It is in agreement with unity, not hinting at any systematic bias in simulation. Its total uncertainty is dominated by the systematic variation of the correction factor. As the $j \to \gamma$ contribution in the SR only amounts to 6 %, it is the smallest background and plays a small role in this search. Hence, a large uncertainty on it is tolerated.

The $SF(j \to \gamma)$ is validated in the VR for combined background after performing the statistical analysis as presented in Section 11. In Figure 48d, the observed and expected distributions of the jet p_{T} spectrum are shown including all uncertainties. A good agreement between data and background expectation is found. Since further distributions in this and other regions also show a good agreement between observation and background prediction, the $SF(j \to \gamma)$ is considered validated.

---

[1] Here, the total uncertainty on the $SF(e \to \gamma)$ is assumed to be 4 %.

9 Separation of signal from background with a deep neural network

In many measurements and searches, a discriminating variable is constructed which separates signal-like events from background candidates. Such a variable is typically built by a machine-learning (ML) algorithm which uses different pieces of information as input and exploits the correlations among them. In this search, a deep NN is used. Its architecture is defined by characteristic parameters which are optimised in the training of signal against background events in the SR. After the optimisation, an NN output value is computed for each event which lies between zero and unity. While a value close to unity means that the event is a signal candidate, a small value indicates that it is background-like.

For each signal coupling, a separate NN is trained to achieve the best discriminating power. As this analysis focuses on the production of a single top quark via an FCNC, only the signal of the production mode is trained against the SM contributions. In the following, the architecture of the deep NN, its input variables, optimisation and output are discussed.

9.1 Neural network architecture

The general architecture of an NN follows the structure of the human brain with its synapses which are connected to each other to process information. An NN consists of an input layer which comprises numerous input nodes, also called neurons. In this layer, the input features are fed in. Subsequently, hidden layers are connected in series which are composed of an adjustable number of nodes. If several hidden layers are used, the NN is denoted as deep and belongs to the class of deep learning architectures. The last layer of an NN is the output layer. It consists of at least one node which provides the discriminating variable.

In this thesis, different architectures of an NN are tested to achieve the best performance. All of the tested NN are feedforward, i.e. information is only passed monodirectionally from the first to the last layer, and optimised by using a backpropagation algorithm. As implementation, the `TensorFlow` system [186] in the `Keras` framework [187] for deep learning architectures is utilised. The final structure of the deep NN, as found to perform best as explained below, is visualised in Figure 29.

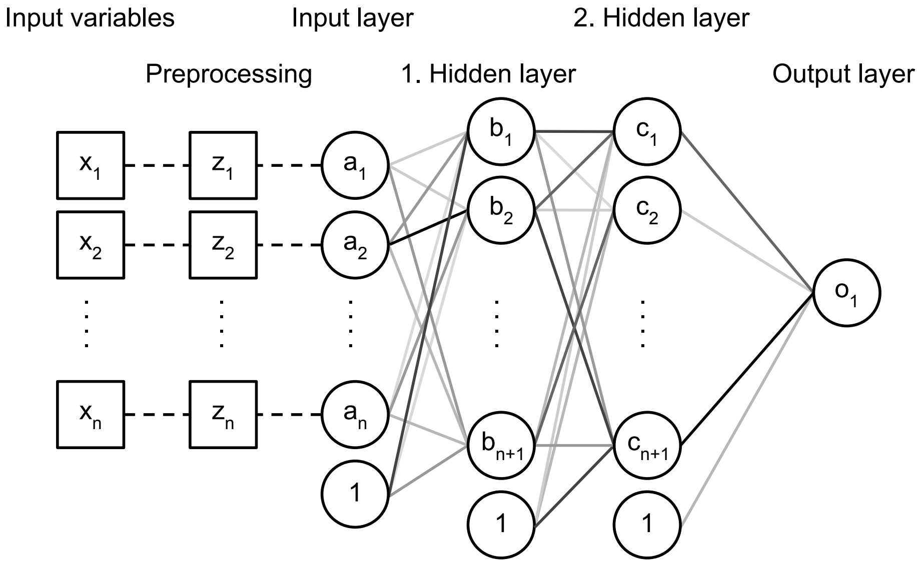

Figure 29: Illustration of the architecture of the deep NN with its input features, x_i, the transformed features, z_i, and the different layers. The output value of each node is referred to as a_i, b_i, c_i and o_i. The bias neurons are shown as nodes with the value of unity. The connections between the nodes are drawn as grey line, while the colour strength indicates the magnitude of the weight.

At first, the input variables, x_i with $i = 1, ..., n$, are transformed in the preprocessing step in order to simplify their handling for the optimisation algorithm. For this purpose, the `RobustScaler` algorithm implemented in the `scikit-learn` package [188] is used. It scales all variables to a similar order of magnitude and is robust against statistical outliers. The transformation formalism of x_i to z_i follows

$$z_i = \frac{x_i - m_i}{q_{3,i} - q_{1,i}} , \tag{48}$$

where m_i is the median of x_i and the properties $q_{1,i}$ and $q_{3,i}$ are the first and third quartile of the variable x_i, respectively. After this transformation, the distribution of z_i is approximately centred around zero.

Next, the n transformed variables are passed into the input layer. Each feature is represented by a separate node. An additional bias node is added to the input layer, whose role is explained below. Each neuron of the input layer is linked to the nodes of the first hidden layer. It consists of $n+1$ nodes and a subjoined bias node. The number $n+1$ is grounded on the number of input features, while the additional neuron increases the flexibility of the NN. A second hidden layer is implemented which also contains $n+1$ neurons and a bias node. While the numbers of neurons for the different layers are found to be sufficient, the inclusion of the second layer is tested in the optimisation. As a single discriminating variable is wanted, the output layer comprises only one node.

Each connection between two nodes is assigned a weight. It indicates the contribution of a node to the neuron in the successive layer. All weights between a bias node and another neuron are initialised with a value of zero. The remaining weights of the links between the input and hidden layers are initialised by a random number which follows a centred normal distribution with truncated tails and a width of $\sqrt{2/(N_\text{in}+N_\text{out})}$ [189]. N_in and N_out are equal to the numbers of incoming and outgoing neurons, respectively. The initial values for the weights of the links to the output layer are randomly drawn from a uniform function. The final values of the weights are optimised in the training.

Each node provides an output value, a_i, b_i, c_i or o_i with $i = 1, ..., n$. It is computed by an activation function, $f(x)$. The input of this function is computed by the sum of the output values of the nodes in the previous layer multiplied by the weights of the respective connection. The bias node allows to shift the activation function of a node along the x-axis by adding constant terms, while the weights of the links to the other neurons only impact the gradient of the function. Thus, the bias nodes add more freedom to the NN. As activation function in the input and both hidden layers, the computationally efficient Rectified Linear Unit function, $R(x)$, is used which is defined as

$$R(x) = \begin{cases} x, & \text{if}\, x \geq 0\,, \\ 0, & \text{if}\, x < 0\,. \end{cases} \tag{49}$$

Its function values covers all positive values, while it is zero for a negative input. This allows the NN to disable a node. For the node in the output layer, the sigmoid function, $\sigma(x)$, is in use which is defined as

$$\sigma(x) = \frac{1}{1 + e^{-x}} \,. \tag{50}$$

Its function values range from zero for small input values to unity for large input values with a smooth transition region. The output value, o_i, determined by this function yields the final discriminating variable, named NN output. While a small NN output means that the event is background-like, an event with an NN output close to unity is a signal candidate.

In the training, the `Adam` algorithm [190] is used which is a gradient descent optimisation algorithm using backpropagation. Such an algorithm tries to find a minimum of a given function by knowing all its derivatives with respect to the weights and by following the steepest descending gradient. Here, the binary cross-entropy loss, $l(\vec{p}, \vec{q})$, is minimised which quantifies the separation of signal from background events achieved by the NN. The vector $\vec{p} = (p_1, ..., p_{N_\mathrm{events}})$ contains the true label of each simulated event with the total number of simulated events, N_events. The true label is unity for signal and zero for background. The vector $\vec{q} = (q_1, ..., q_{N_\mathrm{events}})$ represents the current estimate of the NN. The loss function is defined as

$$l(\vec{p}, \vec{q}) = -\sum_{i}^{N_\mathrm{events}} \left[p_i \log q_i + (1 - p_i) \log(1 - q_i) \right] \,, \tag{51}$$

whereby the index i runs over the number of simulated events. The contributions of correctly assigned events are small, whereas wrongly assigned events cause large penalty terms.

Next to the numbers of layers and nodes, the NN involves hyper-parameters which impact the training. These parameters are the number of epochs, the batch size and the learning rate. The number of epochs indicates how often the algorithm goes through the full training dataset. The batch size states how many simulated events are simultaneously used in a training step. The learning rate limits how much a weight may be varied in each batch. For each hyper-parameter, several possible values are tested. The number of epochs ranges from 10 to 60 with a step size of 5 and the batch size lies between 200 and 1400 in intervals of 100. A certain minimal batch size is set to ensure to train with a sufficient number of events at a time. For the learning rate, the two values of 0.0005 and 0.001 are tested. Since the hyper-parameters depend on each other, all possible permutations are tested in a grid search. The best permutation is defined by the highest accuracy, A, of the NN output. The accuracy is computed by

$$A = \frac{N^{\mathrm{s}}_{\mathrm{pass}} + N^{\mathrm{bkg}}_{\mathrm{pass}}}{N^{\mathrm{s}}_{\mathrm{total}} + N^{\mathrm{bkg}}_{\mathrm{total}}} \tag{52}$$

as the ratio of the number of correctly assigned signal and background events, $N^{\mathrm{s}}_{\mathrm{pass}}$ and $N^{\mathrm{bkg}}_{\mathrm{pass}}$, respectively, to the total number of signal and background events, $N^{\mathrm{s}}_{\mathrm{total}}$ and $N^{\mathrm{bkg}}_{\mathrm{total}}$, respectively. For the classification, a cut value of 0.5 on the NN output is chosen.

9.2 Input variables

The input features for the NN used in this search describe kinematic properties of the individual reconstructed physics objects and the whole event in the SR. In the preselection of potential input features, the separation power S is computed for each variable. For a binned distribution, it is defined as

$$S = \sum_{i}^{N_{\mathrm{bins}}} \frac{(s_i - b_i)^2}{2\,(s_i + b_i)}\,, \tag{53}$$

whereby i runs over the bins, N_{bins} is the total number of bins, $s_i = N^{\mathrm{s}}_i / N^{\mathrm{s}}_{\mathrm{total}}$ is the fraction of the number of signal events, N^{s}_i, in bin i to the total number of signal events, N^{s}_{total}, and analogously for background events, $b_i = N^{\mathrm{bkg}}_i / N^{\mathrm{bkg}}_{\mathrm{total}}$. Additionally, the correlations among the variables are considered to ensure a large variety of information.

After preselection, twelve input variables remain for the NN optimisation. For all couplings, the variables are the same. In Table 5, these features[1] are listed ranked by their separation power, S, for the LH $tu\gamma$ coupling. For all couplings, the photon p_{T} is ranked the highest with a separation power of about 60 % for both $tu\gamma$ couplings

---

[1] The variable H_{T} is defined as the sum of the transverse momenta of all selected reconstructed particles, $H_{\mathrm{T}} = \sum_i p_{\mathrm{T,i}}$. The transverse mass of the W boson, $m_{\mathrm{T}}(W)$, is defined by the kinematic properties of the reconstructed lepton and the missing transverse momentum as $m_{\mathrm{T}}(W) = \sqrt{2\left(p_{\mathrm{T}}(\ell) E^{\mathrm{miss}}_{\mathrm{T}} - \vec{p}_{\mathrm{T}}(\ell)\cdot \vec{E}^{\mathrm{miss}}_{\mathrm{T}}\right)}$.

and 50 % for both $tc\gamma$ couplings. Since in the production mode the photon recoils against the top quark, it receives a large amount of energy which distinguishes it from photons in background events. For all couplings, other highly ranked variables are the invariant mass $m(\ell,\gamma)$, H_{T} and $\Delta R(b\text{-jet},\ell)$. While the latter two variables represent the unique kinematic properties of signal events, the former quantity characterises events with an $e \to \gamma$ fake. The separation power and rank of the other variables depend on the signal coupling, while no systematic pattern is found.

The correlation coefficient, $\rho_{x,y}$, between the variables x and y is defined as

$$\rho_{x,y} = \frac{\sum\limits_{j}^{N_{\text{events}}} (x_j - \langle x \rangle)(y_j - \langle y \rangle)}{\sqrt{\sum\limits_{j}^{N_{\text{events}}} (x_j - \langle x \rangle)^2 \sum\limits_{j}^{N_{\text{events}}} (y_j - \langle y \rangle)^2}} \tag{54}$$

with the mean values of variable x and y, $\langle x \rangle$ and $\langle y \rangle$, and the values of those variables for event j, x_j and y_j. The coefficients of the signal for the LH $tu\gamma$ coupling in the SR are shown in Figure 30. They range between -0.6 and 0.7, while most of them lie in a window of $[0.00, 0.30]$. The variable H_{T} is highly correlated to the transverse momenta of the individual physics objects, as expected. Moreover, the invariant mass $m(\ell,\gamma)$ shows a high correlation to the lepton and photon p_{T} since these physics objects are combined to obtain the mass. The angular distance $\Delta R(b\text{-jet},\ell)$ is negatively correlated to the momenta of all reconstructed physics objects since the higher the energy of the event is, the more collimated the decay products of the top quark are emitted. The other variables show typical correlation coefficients. As all these variables describe unique properties common for events with a top quark and a photon in the final state, the correlations look different for the background, which is dominated by events that either do not include a prompt photon or do not contain a top quark.

The signal and background shapes of the four top ranked variables for the LH $tu\gamma$ coupling are shown in Figure 31. The distributions of both the production and decay mode are drawn separately. In all these distributions, the differences among the signal modes and the background contributions are apparent, as discussed in Section 7.2.1.

Table 5: List of potential input variables with their separation power, S, including the statistical uncertainties and ranking for the signal of the LH $tu\gamma$ coupling in the production mode in the SR.

Variable	S [%]	Rank
Photon p_{T}	62 ± 16	(1)
$m(\ell, \gamma)$	49 ± 17	(2)
H_{T}	40 ± 20	(3)
$\Delta R(b\text{-jet}, \ell)$	32 ± 17	(4)
$\Delta R(\gamma, \ell)$	22 ± 15	(5)
$m(\ell, b\text{-jet})$	15 ± 13	(6)
$m_{\mathrm{T}}(W)$	10 ± 13	(7)
Lepton p_{T}	10 ± 11	(8)
Lepton charge	9.8 ± 5.4	(9)
$E_{\mathrm{T}}^{\mathrm{miss}}$	7.5 ± 8.8	(10)
$\Delta R(\gamma, b\text{-jet})$	5.2 ± 9.3	(11)
b-jet p_{T}	3.8 ± 7.3	(12)

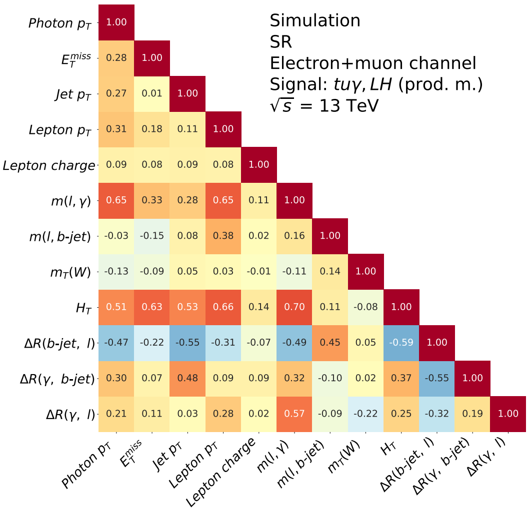

	Photon p_T	E_T^{miss}	Jet p_T	Lepton p_T	Lepton charge	$m(l,\gamma)$	$m(l, b\text{-}jet)$	$m_T(W)$	H_T	$\Delta R(b\text{-}jet,\ l)$	$\Delta R(\gamma,\ b\text{-}jet)$	$\Delta R(\gamma,\ l)$
Photon p_T	1.00											
E_T^{miss}	0.28	1.00										
Jet p_T	0.27	0.01	1.00									
Lepton p_T	0.31	0.18	0.11	1.00								
Lepton charge	0.09	0.08	0.09	0.08	1.00							
$m(l,\gamma)$	0.65	0.33	0.28	0.65	0.11	1.00						
$m(l, b\text{-}jet)$	-0.03	-0.15	0.08	0.38	0.02	0.16	1.00					
$m_T(W)$	-0.13	-0.09	0.05	0.03	-0.01	-0.11	0.14	1.00				
H_T	0.51	0.63	0.53	0.66	0.14	0.70	0.11	-0.08	1.00			
$\Delta R(b\text{-}jet,\ l)$	-0.47	-0.22	-0.55	-0.31	-0.07	-0.49	0.45	0.05	-0.59	1.00		
$\Delta R(\gamma,\ b\text{-}jet)$	0.30	0.07	0.48	0.09	0.09	0.32	-0.10	0.02	0.37	-0.55	1.00	
$\Delta R(\gamma,\ l)$	0.21	0.11	0.03	0.28	0.02	0.57	-0.09	-0.22	0.25	-0.32	0.19	1.00

Figure 30: Illustration for the correlation coefficients of the potential input variables for signal of the LH $tu\gamma$ coupling in the production mode in the SR.

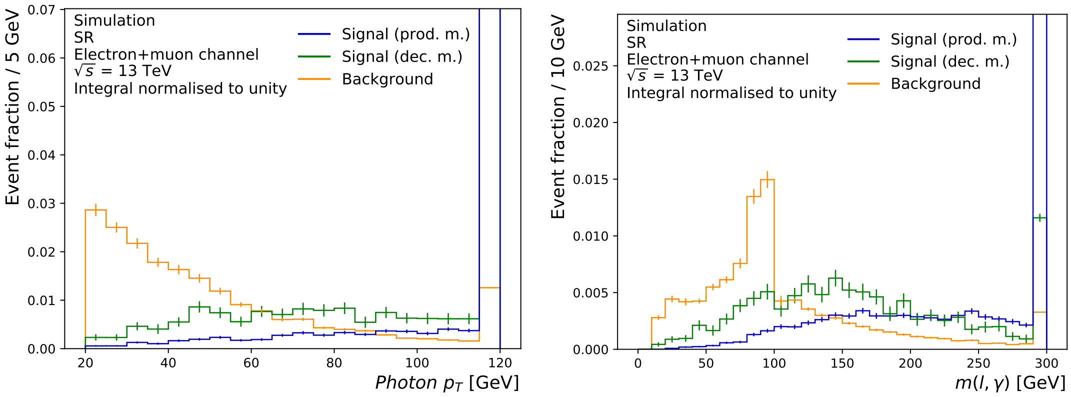

(a) Photon p_T **(b)** Invariant mass $m(\ell, \gamma)$

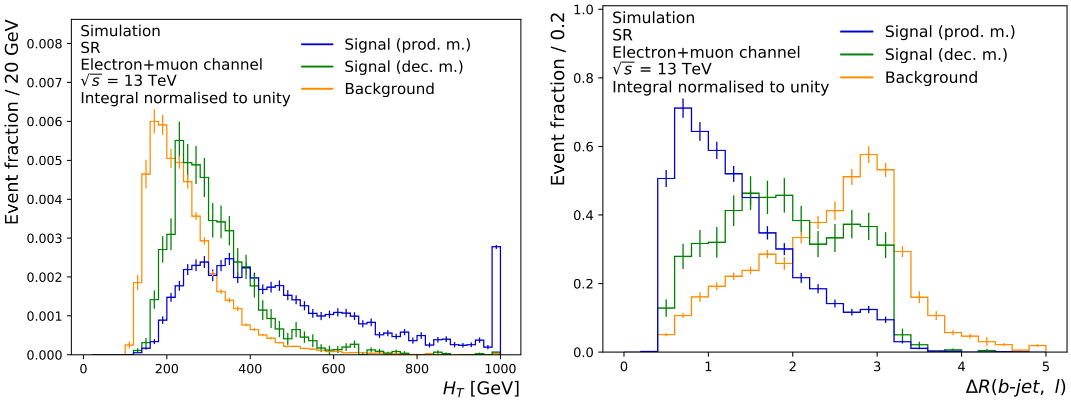

(c) H_T **(d)** $\Delta R(b\text{-jet}, \ell)$

Figure 31: Shape distributions of kinematic properties for the signal for the LH $tu\gamma$ coupling of both the production and decay mode, and those for the background in the SR: photon p_T (a), invariant mass $m(\ell, \gamma)$ (b), total sum of all transverse momenta, H_T, (c) and the angular distance $\Delta R(b\text{-jet}, \ell)$ (d). The integral of each distribution is scaled to unity. The over- and underflow are included, if present. Only statistical uncertainties are shown.

The modelling of all potential input variables is checked in the CR W+γ+jet. The observed and expected mean values of each variable are computed in dependence of every other variable. In MC simulation, only events of SM processes are considered since any signal contribution would have a negligible impact. In Figure 32, the observed and expected two-dimensional distributions of the average of the jet p_{T} plotted against the photon p_{T}, and those of the average of the distance $\Delta R(\gamma, \mathrm{jet})$ plotted against the invariant mass $m(\ell, \gamma)$ in the CR W+γ+jet are shown as examples. Both the observed and expected correlation coefficients are displayed. The observed and expected two-dimensional distributions are in good agreement and the correlation coefficients are compatible with each other. As a good agreement is also observed in all other distributions, no indication for a systematic bias of the modelling of the input variables is found.

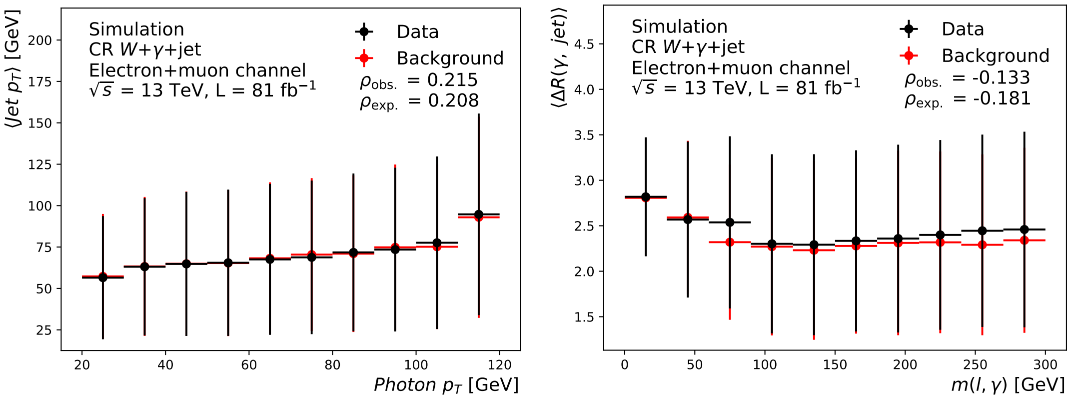

(a) $\langle$Jet $p_{\mathrm{T}}\rangle$ plotted against the photon p_{T} **(b)** $\langle\Delta R(\gamma, \mathrm{jet})\rangle$ plotted against $m(\ell, \gamma)$

Figure 32: Observed and expected two-dimensional distributions of the average of the jet p_{T} plotted against the photon p_{T} (a) and those of the average of the distance $\Delta R(\gamma, \mathrm{jet})$ plotted against the invariant mass $m(\ell, \gamma)$ (b) in the CR W+γ+jet. Both the observed and expected correlation coefficient are shown. The overflow is included.

9.3 Optimisation

The optimisation of the NN consists of the training of the NN, the optimisation of the hyper-parameters and the comparison of the different architectures to each other, and is done separately for each signal coupling. In the training, 80 % of the simulated signal and background events are used, while the residual 20 % are used for testing. In addition, the training dataset is randomly split into three statistically independent sets for a threefold cross validation. Two sets are used for the training, while the performance is quantified by the accuracy, A, computed for the third set. This technique protects against over-training, i.e. any artificial effects arising from the selection of events in the training, or any other artificial bias. The number of simulated signal events for the different signal couplings ranges from 9 947 to 16 427 in the SR. The number of simulated background events amounts to 79 331. The scale factors $SF(e \to \gamma)$ and $SF(j \to \gamma)$ for the fake contributions are taken into account, while the photon p_{T} reweighting is ignored. In the training, the ratio between the number of signal events and that of background events is set to 1:1.

Optimal numbers of input variables and hidden layers

The optimal numbers of input variables and hidden layers are determined by testing four different scenarios which are:

Scenario 1: one hidden layer and all twelve input variables are used;

Scenario 2: two hidden layers and all twelve input variables are used;

Scenario 3: one hidden layer and only ten input variables are used;

Scenario 4: two hidden layers and only ten input variables are used.

The subset of ten input variables dismisses the variables H_{T} and $m_{\mathrm{T}}(W)$. As H_{T} is highly correlated to the transverse momenta of the individual reconstructed physics objects and since all main background contributions contain a W boson like the signal, both features do not add unique and essential information to the NN.

For all four scenarios, the NN is trained and the hyper-parameters are optimised in the grid search. Each scenario yields a specific receiver operating characteristic (ROC) curve which visualises the signal and background efficiencies by scanning the NN output distribution. In Figure 33, the curves for all four scenarios are shown for the LH $tu\gamma$ coupling. In addition, the area under a curve (AUC) is calculated. It indicates how well a model separates signal and background candidates. The larger the AUC is, the better the NN separates signal from background. All four ROC curves are similar to each other and show a strong separation between signal and background. For the AUCs of the different configurations, similar values are obtained. For the other signal couplings, the ROC curves and AUCs show the same behaviour.

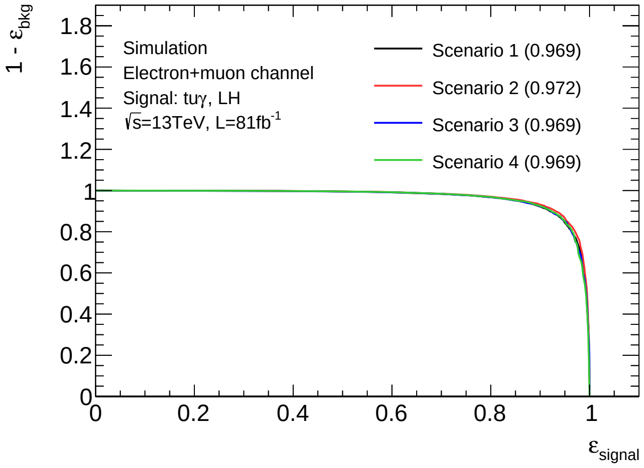

Figure 33: ROC curves for all four tested NN configurations for the LH $tu\gamma$ coupling. The AUC is written in parentheses in the legend.

The decision for one scenario is based on the separation power of the NN output distribution and the AUC. Both quantities are listed in Table 6. In general, their values are alike and the NN output distributions for the scenarios behave similarly. As the separation power is high for all setups for the $tu\gamma$ couplings, but lower for the $tc\gamma$ couplings, more weight is given to the performance of the NN for the $tc\gamma$ couplings. As for these couplings, scenario 4 is the best for the LH case and the second best for the RH coupling, scenario 4 is selected for all couplings as NN configuration. This configuration uses the minimal set of input variables and two hidden layers. Thus, a deep NN is chosen to build the discriminant. The minimal set of ten variables provides almost as much information as the set of twelve variables, while the second hidden layer enables the NN algorithm to learn and exploit more complex correlations among the input features.

In comparison to the separation power, S, of the top ranked variable being the transverse momentum of the photon, the separation power of the NN output distribution exceeds it by more than ten percentage points for all couplings. For scenario 4, the optimal combination of the learning rate, number of epochs and batch

Table 6: The AUC and separation power, S, of the NN output for all four scenarios tested for each coupling. Only the statistical uncertainties are included.

Scenario	AUC	S [%]	AUC	S [%]
Coupling	$tu\gamma$, LH		$tu\gamma$ RH	
1	0.969	74.4 ± 1.9	0.962	65.2 ± 2.0
2	0.972	75.6 ± 1.9	0.969	67.8 ± 2.0
3	0.969	74.5 ± 1.9	0.966	66.5 ± 2.0
4	0.969	73.7 ± 1.9	0.968	67.4 ± 2.0
Coupling	$tc\gamma$, LH		$tc\gamma$ RH	
1	0.948	65.8 ± 1.6	0.940	61.3 ± 1.6
2	0.948	66.7 ± 1.6	0.949	64.0 ± 1.6
3	0.949	66.7 ± 1.6	0.934	59.3 ± 1.6
4	0.953	68.7 ± 1.6	0.946	63.0 ± 1.6

size for all couplings are given in Table 7. The loss function, $l(\vec{p}, \vec{q})$, and accuracy, A, plotted against the number of epochs for the LH $tu\gamma$ coupling are shown in Figures 34. Both quantities show that the performance improves after each epoch, and reach excellent values. For the other couplings, the same behaviour is observed. For none of the couplings, any hint for an over-training or for any other artificial bias is found.

Table 7: Best combination of hyper-parameters determined in the NN optimisation for each signal coupling when using for scenario 4.

	Coupling			
Hyper-parameter	$tu\gamma$, LH	$tu\gamma$, RH	$tc\gamma$, LH	$tc\gamma$, RH
Learning rate	0.001	0.001	0.001	0.001
Number of epochs	30	50	45	25
Batch size	200	300	200	200

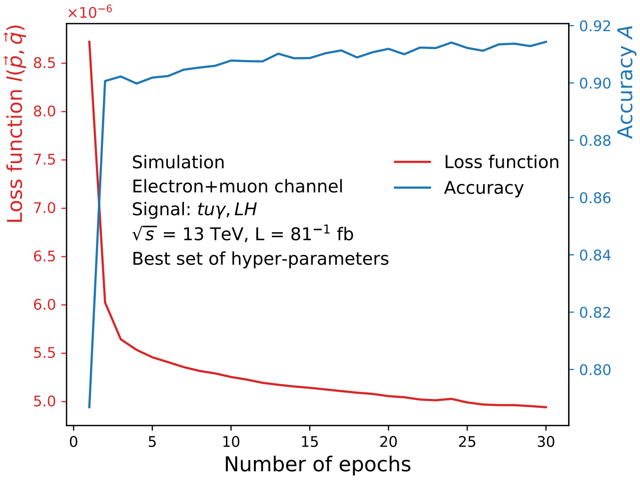

Figure 34: Loss function, $l(\vec{p}, \vec{q})$, in red and accuracy, A, in blue for the LH $tu\gamma$ coupling using scenario 4 with the best combination of hyper-parameters plotted against the number of epochs.

9.4 Deep neural network output

The normalised NN output distribution after the optimisation of the deep NN with two hidden layers and ten input features for the LH $tu\gamma$ coupling in the SR is shown in Figure 35. The production-mode signal and background shapes of both the training and test datasets are compared to each other. They are in good agreement and no hint for any bias is found. In both the training and test datasets, the signal is strongly separated from the background contributions. For higher NN output values, the fraction of signal events increases. For the background, the opposite behaviour is observed. For the other couplings, the outcomes look similar and the same conclusions are drawn.

9.4.1 Cross check with data

For a cross check of the deep NN output, the agreement between observation and background expectation is assessed in the SR and in the CR W+γ+jet as depicted in Figure 43a and 44a including all uncertainties. The signal shape is overlaid which includes both the production and decay mode. In both regions, the fractions of the prompt photon contributions decrease with increasing NN output value. Only the

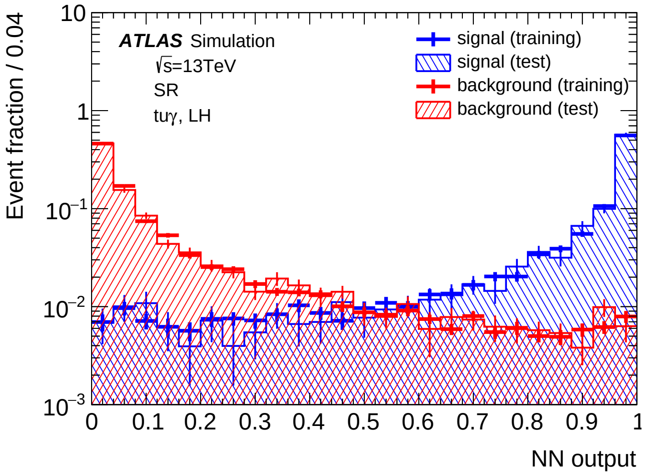

Figure 35: Shapes of the training and test datasets for both the production-mode signal and the background for the deep NN output for the LH $tu\gamma$ coupling. Only the statistical uncertainties are included. The plot is published in the auxiliary material of Ref. [11].

Z+γ+jets contribution in the CR W+γ+jet shows the opposite behaviour. The fraction of events with an $e \rightarrow \gamma$ fake increases in both regions as well as the $j \rightarrow \gamma$ contribution. Both rises are driven by the $t\bar{t}$ process of which a number of events resembles the signal. The overall expected normalisation systematically underestimates the observed number of events since the normalisation of both the W+γ+jets and Z+γ+jets contributions is only estimated in the statistical analysis. In the ratio of data to background expectation, a slight slope is observed in both regions that is corrected for in the statistical analysis by estimating the impact of each source of uncertainty. For the other couplings, the same behaviour is found. Conclusively, the output of the deep NN shows a reasonable agreement between observation and background prediction.

9.4.2 Comparison between the signal processes

Since only the signal of the production-mode process is considered in the training of the deep NN, the NN output distribution for the decay-mode signal shows a different behaviour compared to that of the production-mode signal. In Figure 36, the shapes of both modes are drawn for the LH $tu\gamma$ coupling. While the signal events of the production mode accumulate around unity, the decay-mode signal is flatly distributed with small peaks at both sides of the distribution. They are caused by the different kinematic properties of the decay-mode signal, as discussed in Section 7.2.1 and seen in Figures 31. This deludes the NN to classify some of its events as background. Thus, the shape of the decay-mode signal looks like a mixture of the production-mode signal and the background. For the other couplings, the same behaviour is observed.

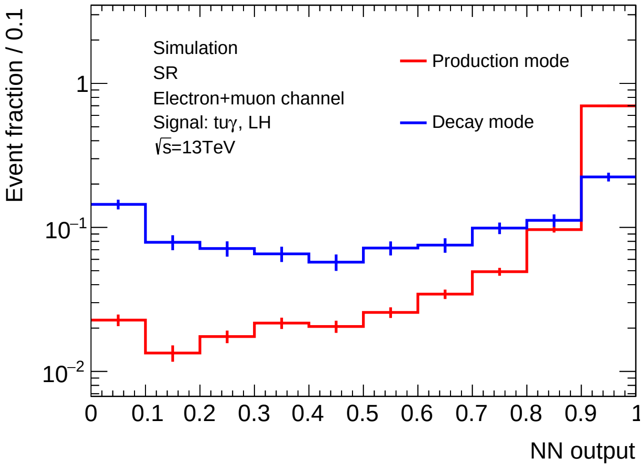

Figure 36: Shapes of the production- and decay-mode signal for the NN output for the LH $tu\gamma$ coupling. Only the statistical uncertainties are included.

9.4.3 Impact of the selection of a signal coupling

As for each signal coupling a separate NN is trained, their outputs differ. In Figure 37, the shapes of the signal including both the production and decay mode and the shapes of background are shown for the NNs optimised for the different couplings. The signal of the $tu\gamma$ couplings peaks at higher values than that of the $tc\gamma$ couplings. The differences between the LH $tu\gamma$ and RH $tu\gamma$ couplings are marginal, which is also true for the $tc\gamma$ couplings. For the $tu\gamma$ couplings, background events are more often categorised as background candidates in comparison to the $tc\gamma$ couplings. When comparing the LH $tu\gamma$ to RH $tu\gamma$ coupling, background events are more often categorised as signal-like for the RH $tu\gamma$ coupling. As the NN output distribution is most sensitive to the signal contribution at high values, this difference is reflected in the results presented in Section 11.4. In contrast, for the $tc\gamma$ coupling, such a difference only exists in a range not sensitive to any signal and the results are not concerned. All these effects are caused by the different kinematic properties of the signal couplings as discussed in Section 7.2.1.

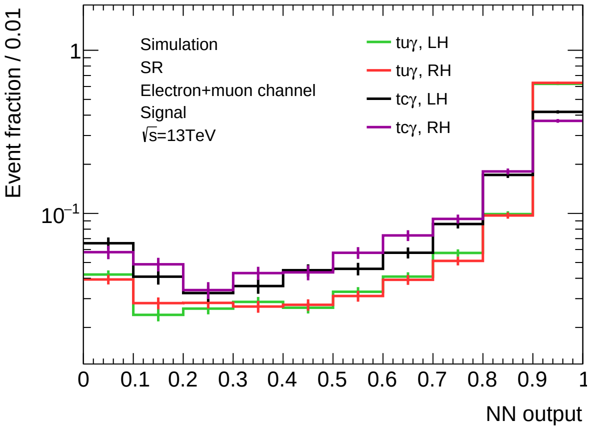

(a) Signal

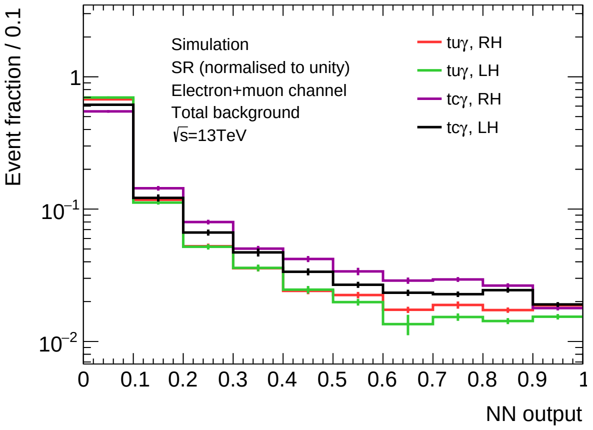

(b) Background

Figure 37: Shapes of the signal (a) and background distributions (b) of the deep NN optimised for the different couplings. The signal of both the production and decay mode is included. Only the statistical uncertainties are shown.

10 Estimation of uncertainties

In each analysis, numerous sources of uncertainties must be taken into account and quantified. For most sources considered in this search, the estimation follows a technique recommended by the ATLAS collaboration. Other sources are specific to this analysis for which an own estimation is developed. Each uncertainty enters the successive statistical analysis as individual nuisance parameter (NP). In the following, techniques to evaluate an uncertainty and the estimation of all sources of systematic uncertainties are explained.

10.1 Techniques for smoothing, symmetrising and pruning

When estimating an uncertainty, varied distributions are computed which represent its impact. Each uncertainty is described by either two varied distributions, which indicate the up and down variations, or only one varied distribution. To avoid any artificial bias, every uncertainty is preprocessed. The preprocessing consists of the methods of smoothing, symmetrising and pruning. In the case of a single-sided variation, the varied distribution is first smoothed and then the uncertainty is symmetrised. If two variations are available, the uncertainty is first symmetrised and subsequently, the symmetrised distributions are smoothed. As last step, each uncertainty is probed to be pruned.

The technique of smoothing removes statistical fluctuations in a distribution to avoid a double-counting of statistical uncertainties. In an iterative procedure, the distribution is rebinned, until the statistical uncertainty in each bin is below the tolerance set to 8 % and the number of sign changes of the slope is less than five. If both criteria cannot be fulfilled at the same time, the tolerance is halved, until both requirements are met. Subsequently, the 353QH algorithm [191] is run which takes the rebinned distribution as input. This algorithm avoids an artificially flat distribution potentially introduced by the previous rebinning procedure. The output of this algorithm is used as smoothed distribution.

As all uncertainties are assumed to approximately follow a Gaussian distribution, they are symmetrised. This stabilises the complex statistical analysis. When an uncertainty is symmetrised, it is centred around the nominal value in each bin in order to receive equidistant up and down variations. A *two-sided* symmetrisation is performed when both the up, σ^{up}, and down variation, σ^{down}, are available. In this case, half the sum of the absolute values of the difference to the nominal value, x_i^{nominal}, in bin i is taken as symmetric variation, $\sigma_i^{\text{sym.}}$, as

$$\sigma_i^{\text{sym.}} = \frac{\left|\sigma_i^{\text{up}} - x_i^{\text{nominal}}\right| + \left|\sigma_i^{\text{down}} - x_i^{\text{nominal}}\right|}{2} \,. \tag{55}$$

In the further analysis, the nominal value is varied up and down by this symmetrised value. A *one-sided* symmetrisation is performed when only either the up or down variation is available. The missing variation is obtained by mirroring the already smoothed distribution on the nominal distribution.

An illustration of the smoothing technique and two-sided symmetrisation is given in Figure 38. There, the impact of the scale uncertainties of the Z+jets process on the $e \to \gamma$ fake contribution in the SR is shown. The nominal distribution is depicted in combination with the initially varied and the modified distributions. While the initially varied distributions are affected by statistical fluctuations, the modified distributions are smooth and lie symmetric around the nominal distribution as visible in the ratio.

After smoothing and symmetrising, the pruning technique is applied which separately assesses the normalisation and shape impacts. If an impact is below a certain threshold, it is pruned away since it would have a negligible effect on the outcome. This method reduces the number of NP and stabilises the complex statistical analysis. The normalisation component is ignored if the integral of the modified distribution deviates less than 1 % from that of the nominal distribution. The shape component is pruned away if in each bin the modified content differs less than 1 % from the nominal value. A reduced pruning parameter for both the normalisation and shape component of 0.5 % was tested and is found to have a negligible impact on the results.

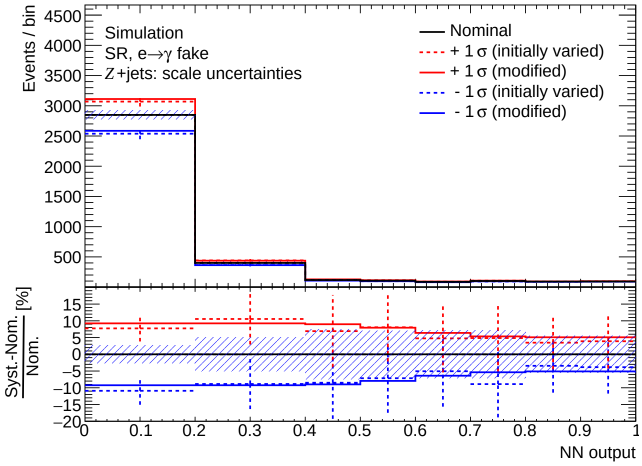

Figure 38: Illustration of the smoothing and symmetrising technique by the example of the scale uncertainties of the Z+jets process on the events with an $e \to \gamma$ fake in the SR. The nominal distribution is shown in black. The initially up and down varied distributions including statistical uncertainties are shown as dashed lines in red and blue, respectively. The modified distributions after smoothing and symmetrising are shown as solid lines. The statistical uncertainty on the nominal distribution is represented by the shaded area. In the bottom panel, the relative difference between the nominal and varied distributions are drawn.

10.2 Theory uncertainties

Cross section Each MC sample is weighted according to the cross section, σ_{process}, computed for the simulated process. In its calculation, approximations and parameters are used which are assigned individual uncertainties propagated to the cross section. Separately for each process, its cross section is varied up and down by one standard deviation. The relative uncertainties are given in Table 8. Since the normalisation of the prompt photon contributions of the W+γ+jets and Z+γ+jets processes are each assigned a free floating NP, their cross-section uncertainties are not considered. For the $t\bar{t}$+γ process, an increased uncertainty on the cross section multiplied by a factor of five was tested and is found to have a negligible impact on the results.

Table 8: Relative uncertainties on the cross section, σ_{process}, for the different processes relevant in the statistical analysis.

Processes	$\frac{\Delta\sigma_{\text{process}}}{\sigma_{\text{process}}}$ [%]		Reference
$t\bar{t}$	+5.6	-5.6	[112, 127–130]
$t\bar{t}+\gamma$	+8.0	-8.0	[114, 115]
single top quark, t-channel	+4.0	-3.4	[131]
single anti-top quark, t-channel	+5.0	-4.5	[131]
single top quark, s-channel	+3.6	-3.1	[132]
single anti-top quark, s-channel	+4.8	-4.3	[132]
single top quark, tW-channel	+5.3	-5.3	[133]
diboson	+6	-6	[192]
W+jets and Z+jets	+5	-5	[193]

Signal modelling

Renormalisation and factorisation scale An uncertainty is assigned due to the choice of the renormalisation, μ_{r}, and factorisation scale, μ_{f}, in the computation of the matrix element. The scales are independently or simultaneously doubled or halved with respect to the nominal value, while a simultaneous doubling and halving is excluded. In each bin of the discriminating variable, the minimal and maximal value is taken as down and up variation, respectively.

Proton's PDFs The uncertainty on the choice of the PDF set in the computation of the matrix element is estimated by using the PDF4LHC15 error set [194]. It contains 30 eigenvectors giving one-sided variations. Each variation enters the statistical analysis separately and is correlated among all signal and background processes.

Background modelling

Renormalisation and factorisation scale For all SM processes except for the single top-quark and $t\bar{t}$ processes, a separate uncertainty is assigned to the choice of the scales μ_{r} and μ_{f}, analogously to the signal. For the single top-quark and

$t\bar{t}$ processes, the variation of the scales is part of the uncertainty on the ISR. An approach by correlating each scale variation among all processes was tested and is found to give a similar result.

Proton's PDFs The same procedure as for the signal is used to estimate the uncertainty on the choice of the proton's PDFs for the SM processes, while the eigenvariations are correlated among all signal and background processes.

Initial state radiation The uncertainty on the modelling of the ISR is estimated by decreasing and increasing the QCD radiation activity in the hadronisation and parton shower modelling and is only available for the single top-quark and $t\bar{t}$ processes. For both, another parameter set of the A14 tune is used which describes the QCD radiation activity. At the same time, the scales μ_r and μ_f are doubled or halved, giving an up and down variation. For the up variation of the $t\bar{t}$ process, a sample with an increased parameter of $h_\mathrm{damp} = 3\,m_\mathrm{top}$ is used in combination with the varied A14 tune and scales. For both the single top-quark and $t\bar{t}$ processes, a separate NP is assigned.

Final state radiation The impact of the modelling of the final state radiation (FSR) is assessed by varying the parameter set of the A14 tune in the hadronisation and parton-shower description, giving an up and down variation. This uncertainty is only available for the single top-quark and $t\bar{t}$ processes.

Normalisation of the W+γ+jets and Z+γ+jets contributions The normalisation of the W+γ+jets and Z+γ+jets processes enters the statistical analysis as separate free floating NPs to obtain a data-driven estimate for their normalisation.

Photon p_T reweighting For the photon p_T reweighting, a symmetric uncertainty of 100 % is assumed separately for the W+γ+jets and Z+γ+jets contributions. A variation of 100 % is equal to the simulated distributions without the reweighting.

$t\bar{t}$ matrix element and parton shower generator For the choice of the matrix element and parton shower generator for simulating the $t\bar{t}$ process, a one-sided uncertainty is obtained by replacing the nominal sample with the sample produced with another generator. For the variation of the matrix element computation, a sample is produced with the generators MadGraph5_aMC@NLO + Pythia, while for the variation of the parton shower generator, the combination of Powheg-Box + Herwig is used.

Single top-quark matrix element and parton shower generator The same procedure as for the $t\bar{t}$ process is applied using the same generators for replacement.

Single top-quark overlap removal An uncertainty is assigned due to the overlap removal between the production of a single top quark in the tW-channel and the production of a $t\bar{t}$ system. The nominal single top-quark tW-channel samples using the DR scheme are replaced with samples using the DS scheme, giving a one-sided variation.

10.3 Experimental uncertainties

Electron and muon efficiencies The SFs for the trigger, reconstruction, ID and isolation efficiencies for charged leptons are varied up and down by one standard deviation. The efficiencies for both leptons are measured using a tag-and-probe method which is based on events with a $Z \to \ell\ell$ decay, and in the case of electrons also with a $J/\Psi \to ee$ decay [153, 164].

Electron and muon energy (momentum) scale and resolution The energy and momentum of the charged leptons are calibrated using MC-based techniques. Correction factors are obtained by measuring events with a $Z \to \ell\ell$ decay. Those factors are varied up and down by one standard deviation [153, 164]. In case of electrons, the calibration proceeds in parallel with that for photons. The calibration uncertainties are indicated by the term *EGamma* in the following.

Photon efficiencies The SFs for the photon ID and isolation are varied up and down by one standard deviation. The former are determined as described in Section 6.

Photon energy (momentum) scale and resolution The calibration of the photon energy and momentum goes along with that for electrons as described above.

Jet energy scale For the JES, a parameter set containing 30 NPs is used to estimate its uncertainty. Each NP results in an up and down variation and enters the statistical analysis separately. The different components are categorised into the η inter-calibration, b-jet energy scale, pile-up, single-hadron high-p_{T}, flavour composition and response, and in-situ jet energy corrections [195]. The NPs for the jet flavour composition and response are treated as uncorrelated among the regions because the jet flavour composition in the regions differ.

Jet flavour fraction An uncertainty for the ratio of light to gluon initiated jets is introduced. Here, the u, d, s and c quark are counted as light quarks. A ratio of 1:1 is assumed in simulation with an uncertainty of 100 % [196]. Additionally in the SR, the shape of the distribution of b-jets and that of non-b-jets are exchanged, while preserving their normalisation. In the other regions, the contribution of b-jets is negligible.

Heavy flavour normalisation The normalisation of events containing a b-jet of the W+γ+jets process is assigned an uncertainty of 50 % to account for an imperfect modelling in simulation. This approach is based on observations for the W+jets process reported in Ref. [197–200].

Jet energy resolution For the JER, a parameter set of 8 NPs is used to estimate its uncertainty. Those NPs are measured by in-situ techniques [196] in data and simulation and give one-sided variations.

Jet vertex tagging An uncertainty is assigned for the SF of the JVT estimated by varying the cut on the JVT discriminant [170] up and down. This uncertainty has an up and down variation.

***b*-tagging** The uncertainty on the b-tagging efficiency is measured in data in dependence of the jet flavour. This uncertainty is split into several components which are evaluated by propagating the calibration uncertainties of the flavour tagging for b-, c- and light jets and result in up and down variations [175–177]. Here, a u, d or s quark or a gluon initiated the jet. As in the CR Z+γ, no b-tagging requirements are used, this uncertainty is only present in the SR and CR W+γ+jet.

$E_{\mathrm{T}}^{\mathrm{miss}}$ The uncertainties of the lepton, photon and jet energy scales and resolutions are propagated to the $E_{\mathrm{T}}^{\mathrm{miss}}$ computation by construction. An uncertainty for the soft-term contributions is estimated by varying the respective scales and resolutions up and down by one standard deviation [179]. This uncertainty is only applied in the SR and CR W+γ+jet, as no requirement on $E_{\mathrm{T}}^{\mathrm{miss}}$ is made in the CR Z+γ.

Pile-up To account for an imperfect modelling of the pile-up, the average number of pile-up is varied up and down by 9 % as done for data recorded in 2015 and 2016.

Luminosity The uncertainty on the integrated luminosity is 2.0 % [98], as determined by measurements of the LUCID-2 detector. This uncertainty is not considered for the W+γ+jets and Z+γ+jets contributions as it is superseded by their normalisation factors.

Background estimation The data-driven scale factor $SF(e \rightarrow \gamma)$ is varied by 10 %, superseding the uncertainty of 4 % derived by the method itself in order to protect against an underestimation of the uncertainty as seen by other analyses. This increase improves the agreement of data and background prediction in the VR SF($e \rightarrow \gamma$), while the impact on the results is negligible. The $SF(j \rightarrow \gamma)$ is varied up and down by one standard deviation.

11 Statistical analysis and results

The last step of this search is the statistical analysis. Separately for each signal coupling, a fit is performed simultaneously in the SR, CR $W+\gamma+$jet and CR $Z+\gamma$ taking into account all NPs. As signal, both the production- and decay-mode processes are considered and their signal strength is determined in the fit. As the data are consistent with the background prediction, an exclusion limit is computed on the signal strength testing the background+signal against the background-only hypothesis. This limit is further interpreted as upper limits on the production cross section $\sigma(pp \to t\gamma)$, on the absolute value of the sum of Wilson coefficients $|C^{\text{sum}}|$ and on the branching ratios $\mathcal{B}(t \to u\gamma)$ and $\mathcal{B}(t \to c\gamma)$. In the following, mainly the results for the LH $tu\gamma$ coupling are presented. The outcomes for the other couplings are similar and documented in Appendix B.

11.1 Fit strategy

For the simultaneous fit, the NN output distribution is taken as input in the SR and CR $W+\gamma+$jet. In the CR $Z+\gamma$, the photon p_{T} spectrum is used since no requirement on the number of jets is made. Thus, some events in this region miss input variables of the NN and the NN output is not well-defined. The inclusion of both CRs aims at a precise determination of the normalisation of the $W+\gamma+$jets and $Z+\gamma+$jets processes. As signal, both the production and decay mode are considered. The background events are categorised depending on the photon origin as either $e \to \gamma$ fake, $j \to \gamma$ fake or prompt photon, while the latter contribution is split into the $W+\gamma+$jets, $Z+\gamma+$jets and *other prompt* γ categories.

The parameter of interest in the fit is the signal strength, μ. It is defined as the fraction of the fitted number of signal events, $N^{\text{s}}_{\text{fit}}$, and the input number of signal events, N^{s}_{in}, as

$$\mu = \frac{N^{\text{s}}_{\text{fit}}}{N^{\text{s}}_{\text{in}}} \,. \tag{56}$$

The input number of signal events corresponds to the initial absolute value of the sum of Wilson coefficients $|C_{\text{in}}^{\text{sum}}|$ for which the branching ratio $\mathcal{B}_{\text{in}}(t \to q\gamma) = 10^{-3}$ is assumed, as described in Section 7.2.2.

In the fit, the binned profile likelihood function, $\mathcal{L}$, is maximised by minimising its double, negative logarithm, $-2\ln\mathcal{L}$. It includes the set of NPs, $\vec{\theta} = (\theta_1, ..., \theta_{\text{N}_{\text{NP}}})$, with the number of NPs, N_{NP}, and the signal strength. The likelihood function is defined as

$$\mathcal{L} = \mathcal{L}(\mu, \vec{\theta}|\text{NN output}, p_{\text{T}}^{\gamma}) = \prod_{r}^{N_{\text{regions}}} \prod_{i}^{N_{\text{r,bins}}} P\left(N_{r,i}^{\text{data}} \middle| N_{r,i}^{s} + \sum_{b}^{N_{\text{bkg}}} N_{r,i}^{b}\right) \cdot \prod_{j}^{N_{\text{NP}}} G\left(\theta_j\right) \tag{57}$$

with the following parameters:

- r runs over the number of regions, N_{regions};
- i runs over the number of bins, $N_{\text{r,bins}}$, of the respective distribution in region r;
- $P(x|\lambda)$ is the Poisson function with mean λ;
- $N_{r,i}^{\text{data}}$ is the observed number of events in region r in bin i;
- $N_{r,i}^{\text{s}}$ is the expected number of signal events in region r in bin i;
- b runs over the number of background categories, N_{bkg};
- $N_{r,i}^{b}$ is the expected number of events of background b in region r in bin i;
- j runs over the number of NPs;
- $G(x)$ is the Gaussian function with a mean of zero and a width of unity. In the case of the uncertainty due to the MC statistics, a Poisson function with the mean being the expected number of events replaces the Gaussian function.
- θ_j is the strength of the NP for the systematic effect j, where its up and down variations serve as templates for $\theta_j = +1$ and $\theta_j = -1$, respectively. This treatment requires a continuous interpolation between the distributions.

The Gaussian term, $G(x)$, equals a penalty to the likelihood value, as soon as a NP is pulled and used to change the expected distribution. Such a constraint protects against a large pull of a NP. The signal strength enters the fit via

$$N^{\mathrm{s}}_{r,i} = \mu \cdot \rho_{r,i} \cdot N^{\mathrm{s}}_{\mathrm{in},r} \tag{58}$$

with the input number of signal events, $N^{\mathrm{s}}_{\mathrm{in},r}$, in region r and the fraction of signal events, $\rho_{r,i}$, in region r of bin i.

In the fit, the background-only hypothesis, H_b, is tested assuming that only SM processes are present and that signal is absent, i.e. the signal strength is fixed to zero. To probe the fit setup and the systematic model, different tests were performed which all succeeded. First, a setup was probed which only used the MC simulation, while the data were replaced by an Asimov dataset. Such a dataset is a single representative of the ensemble of simulated datasets and its parameters perfectly match those of the background expectation. The fit result of this setup reflected the background prediction: none of the NPs were pulled and the fitted signal strength was zero. In another test setup with Asimov data, signal was additionally injected in order to test the signal+background hypothesis, H_{s+b}. For this setup, the fit determined the signal strength as injected and none of the NPs were pulled. Another test was the inclusion of the data in the CRs, while Asimov data were still used in the SR. The post-fit background expectation was in good agreement with the observation. Some NPs were pulled to correct for deviations between the observed and pre-fit expected distributions. As expected, the fitted signal strength was still zero because the CRs are not sensitive to a signal contribution. Since all these tests succeeded and the behaviour of the fit and its outcome were understood, the data of the SR are included in the fit which is presented in the following.

11.2 Fit result

Before performing the fit, the normalisation and shape impact of each NP having a systematic nature is computed and probed for pruning. In Figure 40, they are listed and their treatment in the fit is illustrated in the different regions and for the signal and background processes. Most of the NPs are neglected, while only for a minority both the shape and normalisation components are kept. For several NPs, either the normalisation or shape impact is pruned away. In general, no atypical behaviour is found. The NPs are kept that are expected to have a non-negligible impact, like the uncertainty for the JES flavour composition in the SR or the scale uncertainties for the different processes. In contrast, those NPs are pruned that are expected to be negligible, e.g. several components of the JES uncertainty and most of the components of the b-tagging uncertainty. The reduction of NPs helps to stabilise the fit. For the other couplings, the pruning outcome looks similar.

The correlation of the NPs between each other is visualised in Figure 39 where only systematic uncertainties with the absolute value of at least one correlation coefficient, ρ, above 0.2 are drawn. The scale uncertainties of the $W+\gamma+$jets and $Z+\gamma+$jets contributions are highly negatively correlated to the normalisation of the respective process as both scale variations have a large impact on the normalisation. The same is seen for the pile-up uncertainty for which the same argument holds. The photon p_{T} reweighting for the $W+\gamma+$jets process shows moderate correlations to some other NPs that describe a slope in the discriminating distribution in the SR and CR $W+\gamma+$jet, e.g. some scale uncertainties and components for the JES flavour composition. All other correlations do not show any systematic pattern.

The observed and expected number of events before the fit are given in Table 9. In the SR, the $e \to \gamma$ contribution dominates followed by events of the $W+\gamma+$jets process. The SM expectation deviates by more than one standard deviation from observation due to the missing estimation of and a priori uncertainty on the normalisation for the $W+\gamma+$jets and $Z+\gamma+$jets contributions. Both CRs are enriched in the respective process, while other processes only play a subdominant role. While the SM expectation agrees with the data in the CR $Z+\gamma$ within one standard deviation, it deviates by $1.5\,\sigma$ in the CR $W+\gamma+$jet for the same reason as in the SR.

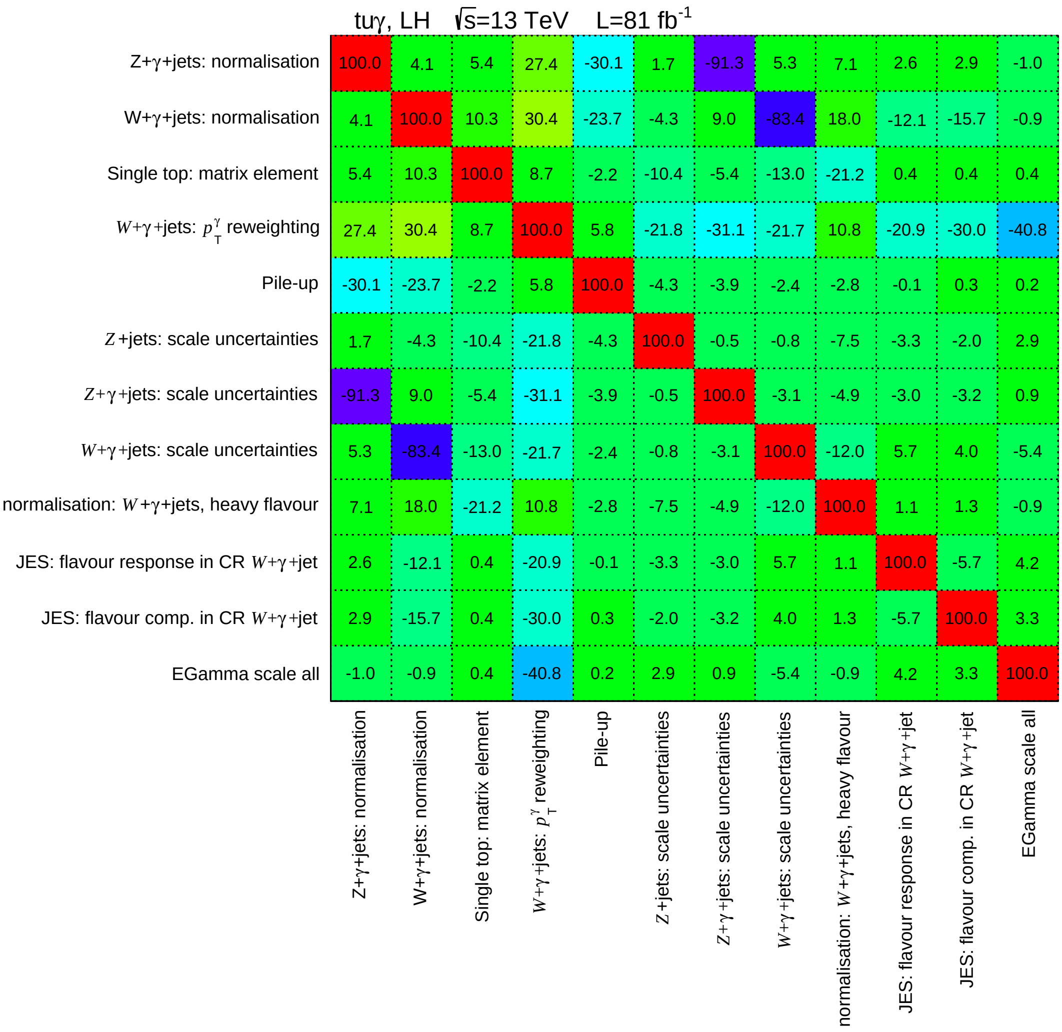

	Z+γ+jets: normalisation	W+γ+jets: normalisation	Single top: matrix element	W+γ+jets: p_T^γ reweighting	Pile-up	Z+jets: scale uncertainties	Z+γ+jets: scale uncertainties	W+γ+jets: scale uncertainties	normalisation: W+γ+jets, heavy flavour	JES: flavour response in CR W+γ+jet	JES: flavour comp. in CR W+γ+jet	EGamma scale all
Z+γ+jets: normalisation	100.0	4.1	5.4	27.4	-30.1	1.7	-91.3	5.3	7.1	2.6	2.9	-1.0
W+γ+jets: normalisation	4.1	100.0	10.3	30.4	-23.7	-4.3	9.0	-83.4	18.0	-12.1	-15.7	-0.9
Single top: matrix element	5.4	10.3	100.0	8.7	-2.2	-10.4	-5.4	-13.0	-21.2	0.4	0.4	0.4
W+γ+jets: p_T^γ reweighting	27.4	30.4	8.7	100.0	5.8	-21.8	-31.1	-21.7	10.8	-20.9	-30.0	-40.8
Pile-up	-30.1	-23.7	-2.2	5.8	100.0	-4.3	-3.9	-2.4	-2.8	-0.1	0.3	0.2
Z+jets: scale uncertainties	1.7	-4.3	-10.4	-21.8	-4.3	100.0	-0.5	-0.8	-7.5	-3.3	-2.0	2.9
Z+γ+jets: scale uncertainties	-91.3	9.0	-5.4	-31.1	-3.9	-0.5	100.0	-3.1	-4.9	-3.0	-3.2	0.9
W+γ+jets: scale uncertainties	5.3	-83.4	-13.0	-21.7	-2.4	-0.8	-3.1	100.0	-12.0	5.7	4.0	-5.4
normalisation: W+γ+jets, heavy flavour	7.1	18.0	-21.2	10.8	-2.8	-7.5	-4.9	-12.0	100.0	1.1	1.3	-0.9
JES: flavour response in CR W+γ+jet	2.6	-12.1	0.4	-20.9	-0.1	-3.3	-3.0	5.7	1.1	100.0	-5.7	4.2
JES: flavour comp. in CR W+γ+jet	2.9	-15.7	0.4	-30.0	0.3	-2.0	-3.2	4.0	1.3	-5.7	100.0	3.3
EGamma scale all	-1.0	-0.9	0.4	-40.8	0.2	2.9	0.9	-5.4	-0.9	4.2	3.3	100.0

Figure 39: Visualisation of the correlation coefficients between the NPs of systematic nature for the LH $tu\gamma$ coupling. Only uncertainties with the absolute value of at least one coefficient above 0.2 are drawn.

Table 9: Observed and expected number of events for the different background contributions in the SR, CR W+γ+jet and CR Z+γ before the fit. The statistical uncertainties and all systematic uncertainties are included.

Photon origin	SR	CR W+γ+jet	CR Z+γ
$e \to \gamma$	$3\,840 \pm 660$	$6\,800 \pm 1\,500$	227 ± 34
$j \to \gamma$	510 ± 340	$8\,200 \pm 6\,300$	$2\,800 \pm 1\,700$
Z+γ+jets	670 ± 160	$11\,700 \pm 1\,600$	$73\,300 \pm 8\,700$
W+γ+jets	$1\,650 \pm 480$	$82\,400 \pm 6\,700$	5.1 ± 3.1
Other prompt γ	$1\,630 \pm 430$	$1\,790 \pm 470$	$2\,110 \pm 220$
Expectation	$8\,300 \pm 1\,100$	$111\,000 \pm 11\,000$	$78\,400 \pm 9\,000$
Data	9 557	127 864	85 347

Next, the fit is run varying the background expectation by considering the non-pruned NPs. The variation and constraint of each systematic NP is indicated by its pull value, δ, and its uncertainty, σ_δ, being defined as

$$\delta = \frac{\hat{\theta} - \theta_0}{\sigma_0} \quad \text{and} \quad \sigma_\delta = \frac{\hat{\sigma}}{\sigma_0} \tag{59}$$

with the input and fitted value for the NP, θ_0 and $\hat{\theta}$, respectively, and the uncertainty on the input and fitted value, σ_0 and $\hat{\sigma}$, respectively. In Figure 41, the pull values are shown as determined in the fit. The values on both photon p_{T} reweightings are constrained as they are assigned a conservative uncertainty of 100 %. In addition, the reweighting for the W+γ+jets process is slightly pulled to a smaller value since other NPs also introduce a slope in the NN output distributions in both the SR and CR W+γ+jet. Those NPs are the scale uncertainties and several JES components which are also slightly pulled. All these NPs are correlated to each other and depend on each other in a complex interplay. The scale factor $SF(j \to \gamma)$ is pulled unsurprisingly as it was determined exclusively for the SR, but is used in other regions, too. As it only describes a minor background almost exclusively present in the SR, this behaviour is tolerated. The scale factor $SF(e \to \gamma)$ is moved to higher values still being compatible with the pre-fit value. All other pull values do not show a peculiar behaviour. The pull values obtained in the fit of the other couplings look similar.

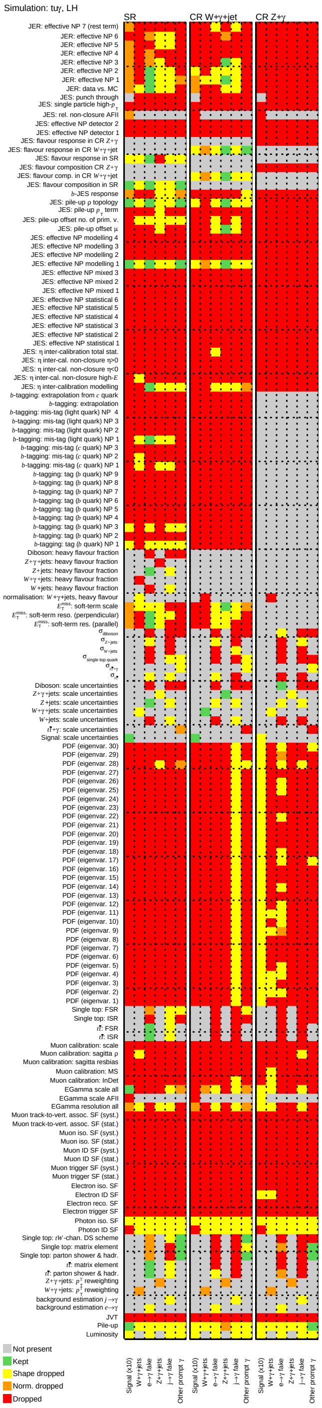

Figure 40: Illustration of the treatment of every systematic NP considered in the fit for the LH $tu\gamma$ coupling in each region for each signal and background category.

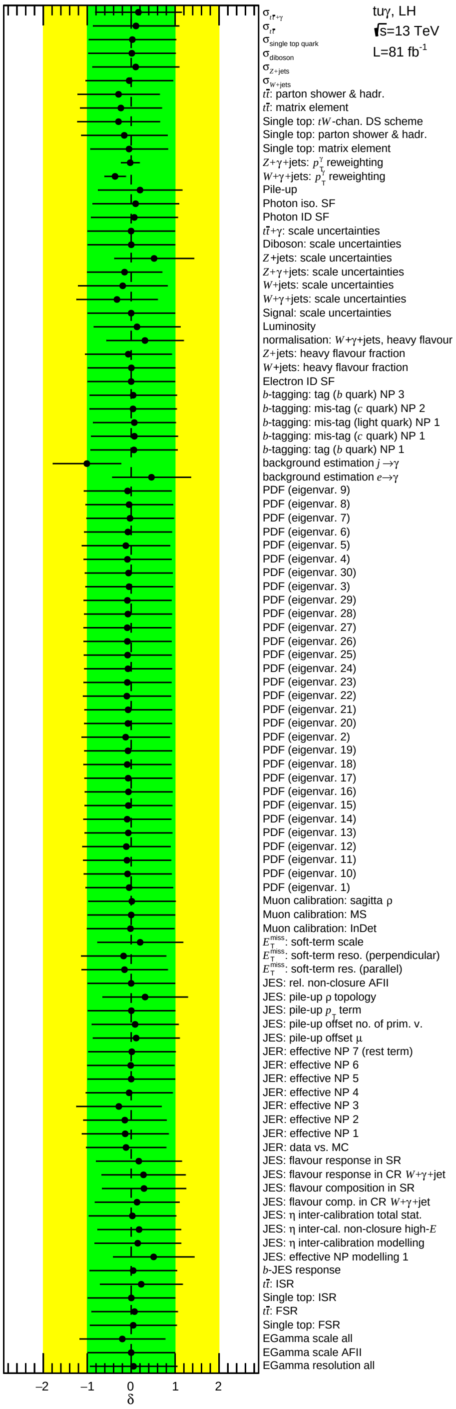

Figure 41: Pull values, δ, for the systematic NPs considered and determined in the fit for the LH $tu\gamma$ coupling.

Analogously to the pull values for the systematic NPs, the normalisation factors, γ, for the MC statistical uncertainty for each bin and region are varied in the fit. Those values are defined as multiplicative factor to the bin content and shown in Figure 42. The majority of these values is compatible with unity. The large deviations for the fifth bin in the SR and bin five in the CR W+γ+jet are caused by a down fluctuation of the $e \to \gamma$ fake simulation. However, both are acceptable at the $3\,\sigma$ level.

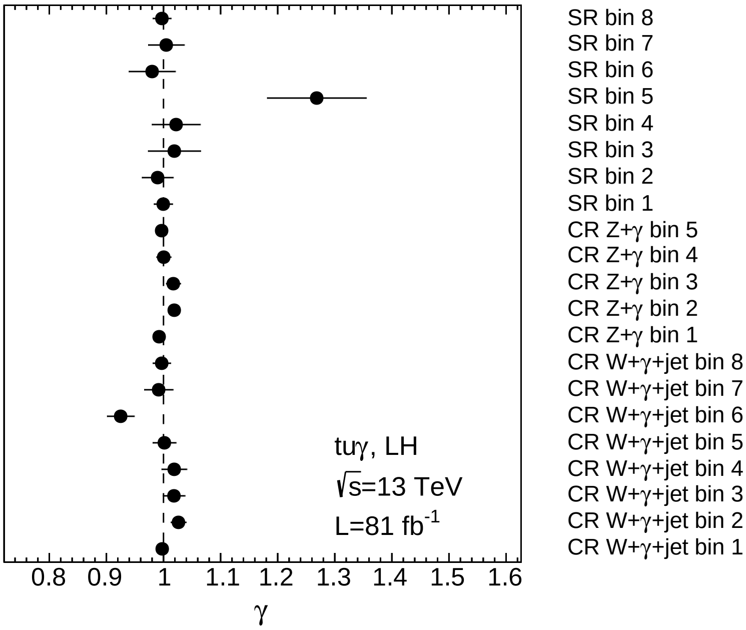

Figure 42: Normalisation factors, γ, for the different regions and bins determined in the fit for the LH $tu\gamma$ coupling.

The normalisation factors for the prompt photon contributions of the W+γ+jets and Z+γ+jets processes are measured to be $SF(W+\gamma+jets) = 1.25 \pm 0.09$ and $SF(Z+\gamma+jets) = 1.12 \pm 0.12$, respectively, and are comparable for all couplings.

In Figures 43 and 44, the pre- and post-fit distributions for all three regions are shown. In the SR and CR W+γ+jet, the signal is overlaid scaled to the observed limit multiplied by ten, as derived in Section 11.4. In the CR Z+γ, the signal is negligible. In the pre-fit distributions, the background expectation systematically underestimates the data since the normalisation of the W+γ+jets and Z+γ+jets contributions is not known a priori and only determined in the fit. Moreover, in most bins the expectation deviates about one standard deviation from observation since pre-fit uncertainties are missing for the normalisation of the W+γ+jets and Z+γ+jets processes. At post-fit level, however, the background expectation agrees well with the observation within one standard deviation in most bins, while only a few differ up to two standard deviations. The total uncertainty is significantly reduced.

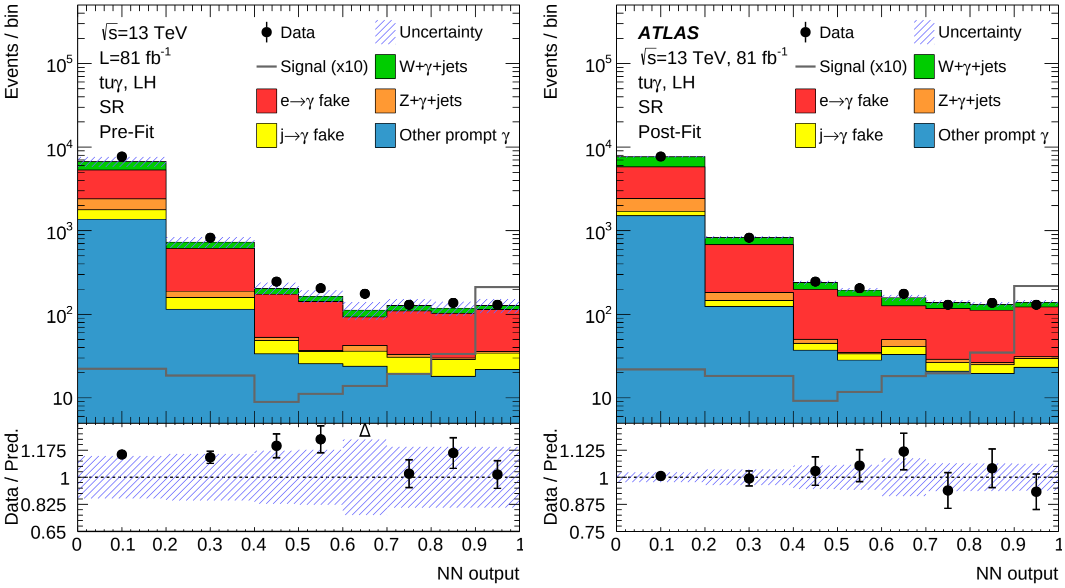

(a) Pre-fit distribution in the SR

(b) Post-fit distribution in the SR

Figure 43: Pre- (a) and post-fit distributions (b) of the NN output in the SR for the LH $tu\gamma$ coupling. All NPs are included. The signal shape is overlaid scaled to the observed limit multiplied by ten. The post-fit plot is published in Ref. [11].

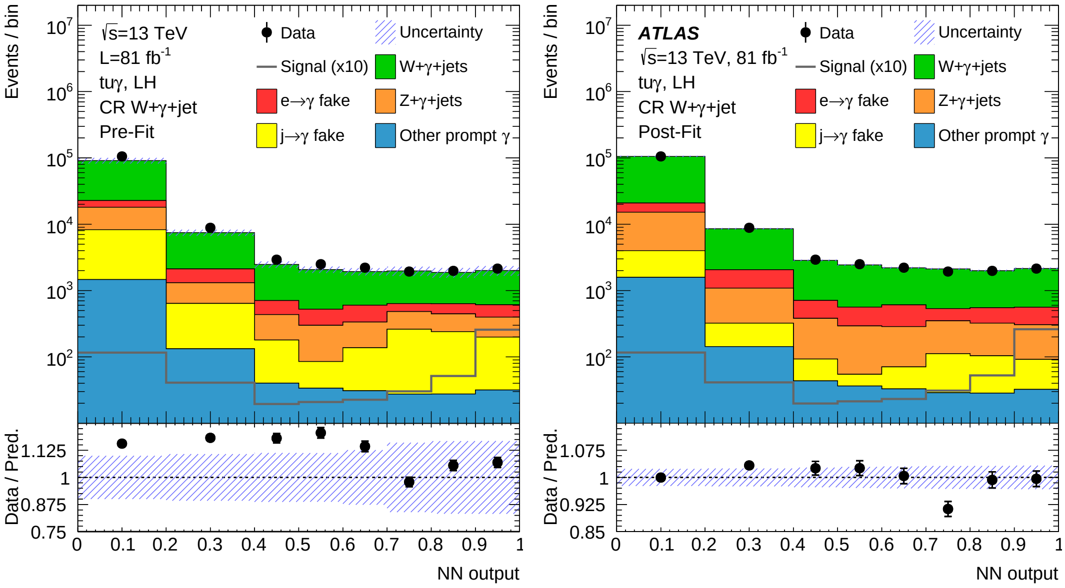

(a) Pre-fit distribution in the CR $W{+}\gamma{+}$jet **(b)** Post-fit distribution in the CR $W{+}\gamma{+}$jet

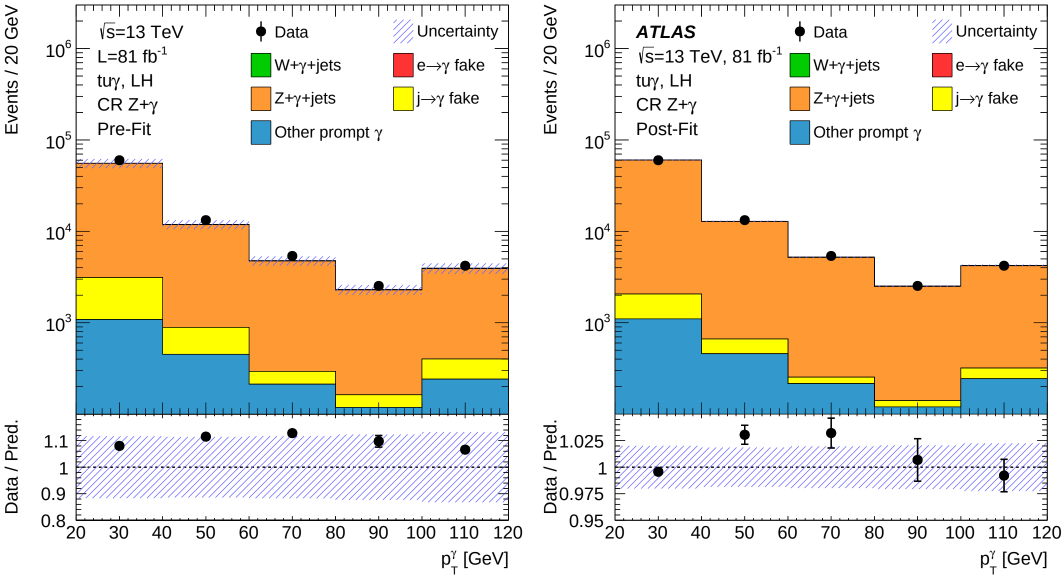

(c) Pre-fit distribution in the CR $Z{+}\gamma$ **(d)** Post-fit distribution in the CR $Z{+}\gamma$

Figure 44: Pre- and post-fit distributions of the NN output in the CR $W{+}\gamma{+}$jet (a,b) and those of the photon p_{T} in the CR $Z{+}\gamma$ (c,d) for the LH $tu\gamma$ coupling. All uncertainties are included. In the CR $W{+}\gamma{+}$jet, the signal shape is overlaid scaled to the observed limit multiplied by ten. Since the signal contribution is negligible in the CR $Z{+}\gamma$, its shape is not overlaid. The post-fit plots are published in Ref. [11].

In Table 10, the observed and expected number of events at post-fit level are shown for each region and each background category. Compared to the values at pre-fit level, the agreement between observation and the background expectation in each region is improved, lying within one standard deviation. For the other couplings, the same behaviour is observed.

Table 10: Observed and expected number of events for the different background contributions in the SR, CR $W+\gamma$+jet and CR $Z+\gamma$ after the fit for the LH $tu\gamma$ coupling. The statistical uncertainty and all systematic uncertainties are included.

Photon origin	SR	CR $W+\gamma$+jet	CR $Z+\gamma$
$e \to \gamma$	$4\,470 \pm 410$	$8\,200 \pm 1\,300$	236 ± 32
$j \to \gamma$	260 ± 200	$2\,900 \pm 2\,000$	$1\,300 \pm 970$
$Z+\gamma$+jets	780 ± 100	$13\,400 \pm 1\,300$	$81\,400 \pm 1\,900$
$W+\gamma$+jets	$2\,200 \pm 440$	$101\,200 \pm 2\,800$	5.8 ± 1.8
Other prompt γ	$1\,790 \pm 380$	$1\,930 \pm 470$	$2\,140 \pm 200$
Expectation	$9\,500 \pm 220$	$127\,700 \pm 3\,000$	$85\,100 \pm 1\,600$
Data	9 557	127 864	85 347

The NN output distributions in the SR at post-fit stage for the other signal couplings are shown in Figure 45, while the signal is overlaid scaled to the respective observed limit multiplied by ten. Again, a good agreement between observation and background prediction is achieved for all couplings. The distributions in both CRs are similar to those for the LH $tu\gamma$ coupling as shown in Figures 44b and 44d.

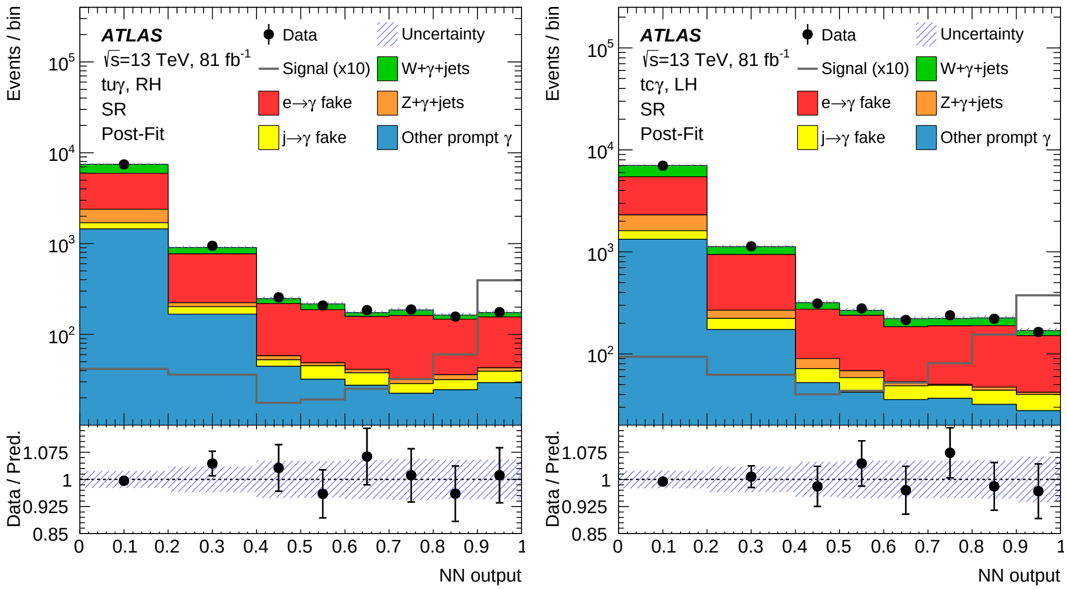

(a) RH $tu\gamma$ coupling (b) LH $tc\gamma$ coupling

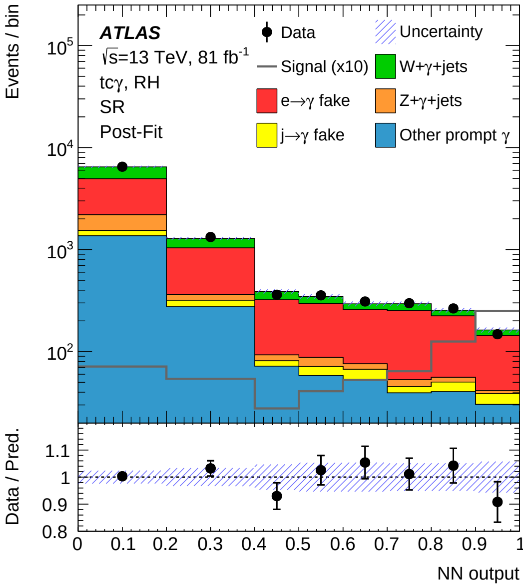

(c) RH $tc\gamma$ coupling

Figure 45: Post-fit distributions of the NN output in the SR for the RH $tu\gamma$ (a), LH $tc\gamma$ (b) and RH $tc\gamma$ coupling (c). All uncertainties are included. The signal shape is overlaid scaled to the respective observed limit multiplied by ten. The plots are published in the auxiliary material of Ref. [11].

The impact of each NP is determined by the following ranking procedure. For each NP, four fits are performed with the NP fixed to the pre-fit value adding or subtracting the pre-fit uncertainty, $\theta_0 \pm \sigma_0$, or to the post-fit value adding or subtracting the post-fit uncertainty, $\hat{\theta} \pm \hat{\sigma}$. For each variation, the difference of the signal strength, $\Delta\mu$, to the nominal signal strength is computed, indicating its impact. The maximal absolute value of the difference of the post-fit configurations is used to rank the NPs. The ranking of the 20 leading NPs is shown in Figure 46. The top ranked NP is the JER component data vs. MC followed by two other JER components within the top four. The thirdly ranked NP is the photon p_T reweighting for the W+γ+jets process. All these NPs describe a slope in the NN distribution in the SR and in the CR W+γ+jet. As any signal contribution would also introduce a slope in the NN output distribution, the impact of those NPs on the signal strength is the largest. Other highly ranked NPs impact the normalisation of single processes or vary their shape. In general, the impact halves from the first to the fifth NP, while the next bisection happens at the 15th NP, i.e. the step size between the NPs becomes smaller. However, as the statistical uncertainty on the signal strength amounts to 0.019, this search is statistically limited. For the other couplings, similar NPs appear within the top ranked uncertainties showing the same behaviour.

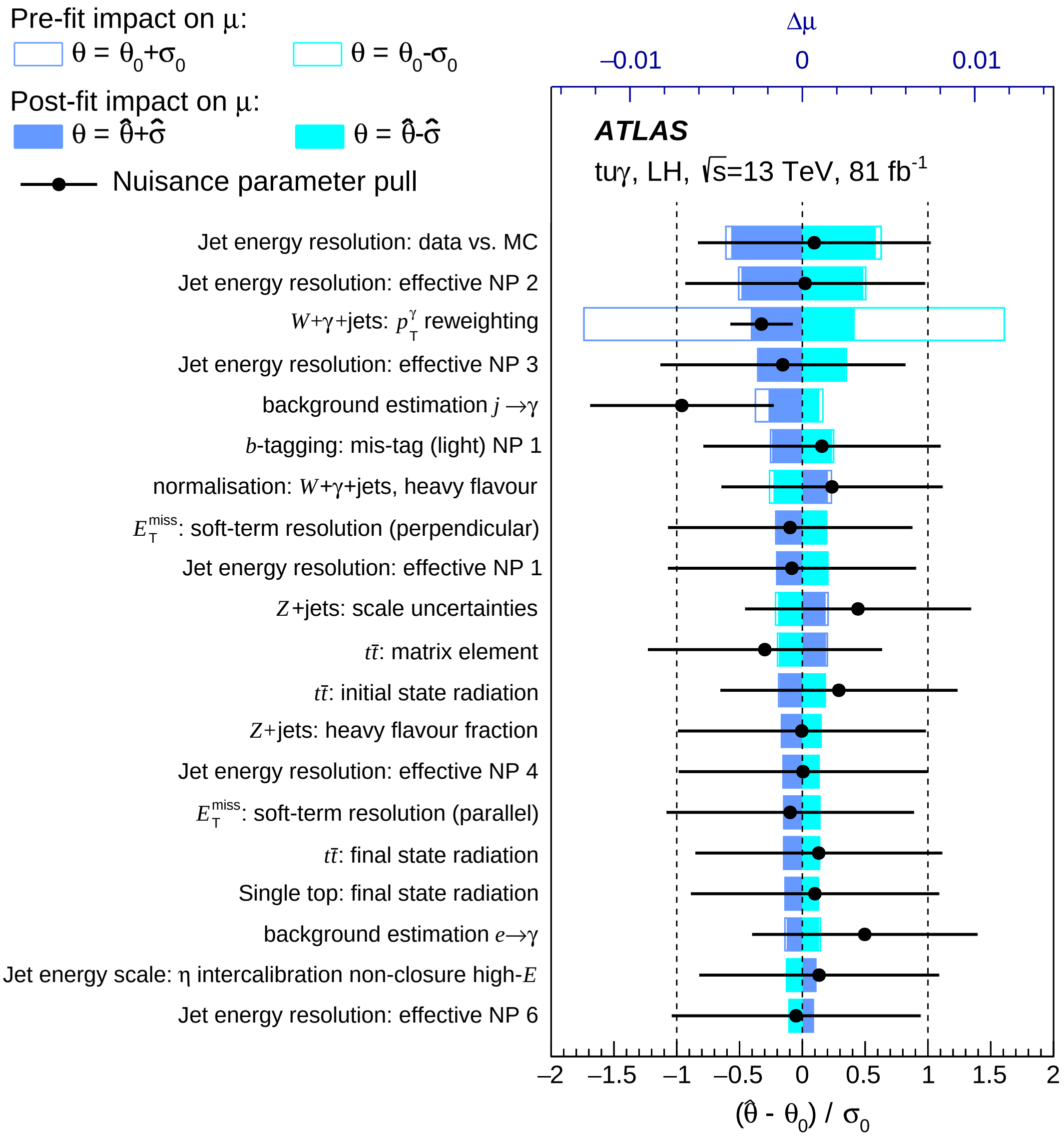

Figure 46: Ranking of the NPs with the largest impact on the signal strength, μ, for the LH $tu\gamma$ coupling. The signal strength of unity corresponds to the branching ratio $\mathcal{B}_{\text{in}}(t \to u\gamma) = 10^{-3}$. The ranking is determined in fits fixing the NP under study to its pre-fit value θ_0 and adding or subtracting its pre-fit uncertainty, σ_0, and analogously for the post-fit value, $\hat{\theta}$, and its uncertainty, $\hat{\sigma}$. The rectangles refer to the upper axis, while the black dots refer to the bottom scale. The plot is published in the auxiliary material of Ref. [11].

11.3 Validation

The fit outcome is validated using the input variables of the NN in the SR and other variables in the VR SF($e \to \gamma$) and the VR for the combined background. In Figure 47, the post-fit distributions of the photon and lepton p_{T}, the angular distance between the b-tagged jet and photon, and the invariant mass $m(\ell, \gamma)$ are shown. The distributions of the other NN input variables are shown in Appendix C. In all of them, the signal is overlaid scaled to the observed limit multiplied by ten. All the distributions show a good agreement between data and background prediction, and no indication of any misbehaviour or bias is found.

In Figure 48, pre- and post-fit distributions of the jet p_{T} in the VR SF ($e \to \gamma$) and in the VR for the combined background are compared to each other. The signal is not drawn as it is negligible in both VRs. While the background prediction underestimates the data in the pre-fit distributions, the agreement improves significantly after the fit. The total uncertainty in the VR SF($e \to \gamma$) is only slightly reduced as the composition of processes in this region differs strongly from that of the regions used in the fit. The total uncertainty in the VR for the combined background is reduced after the fit as the main contribution stems from the W+γ+jets process which is constrained in the CR W+γ+jet. In addition, other variables in these regions also show an excellent agreement. Consequently, these regions do not hint to any misbehaviour or bias of the fit.

For the other couplings, the same distributions are checked and a good agreement between observation and background prediction at post-fit level is found.

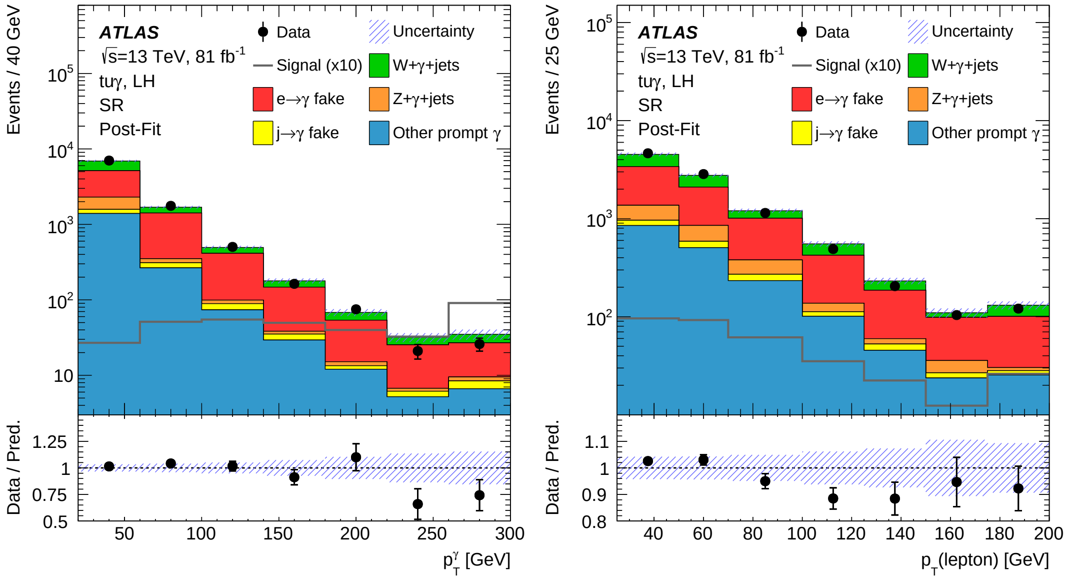

(a) Photon p_{T} **(b)** Lepton p_{T}

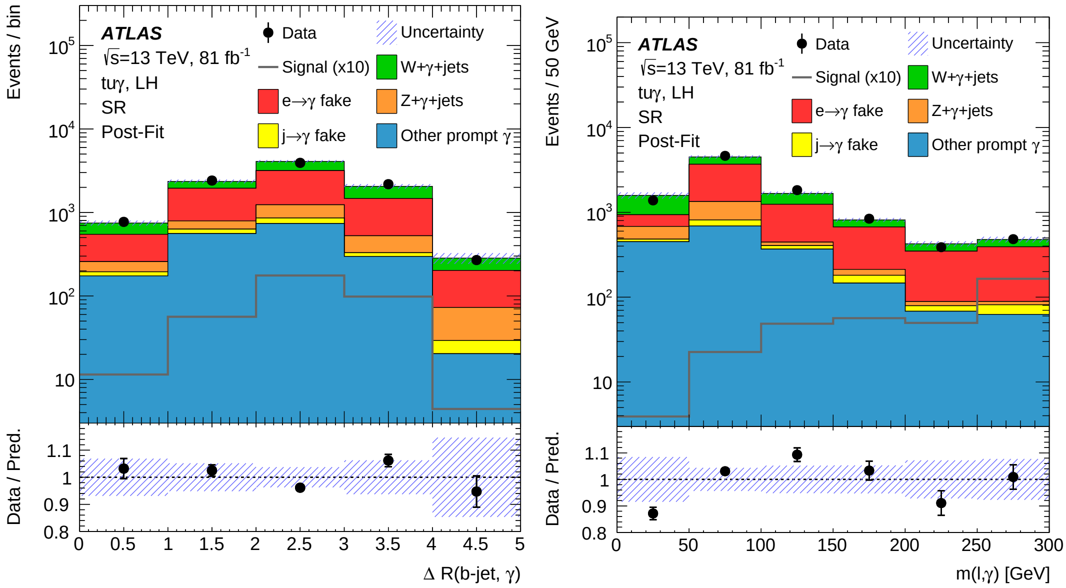

(c) $\Delta R(b\text{-jet}, \gamma)$ **(d)** $m(\ell, \gamma)$

Figure 47: Post-fit distributions of the photon p_{T} (a), lepton p_{T} (b), distance ΔR between the b-tagged jet and photon (c) and the invariant mass $m(\ell, \gamma)$ (d) in the SR for the LH $tu\gamma$ coupling. All uncertainties are included. The signal is overlaid scaled to the observed limit multiplied by ten. The plots are published in the auxiliary material of Ref. [11].

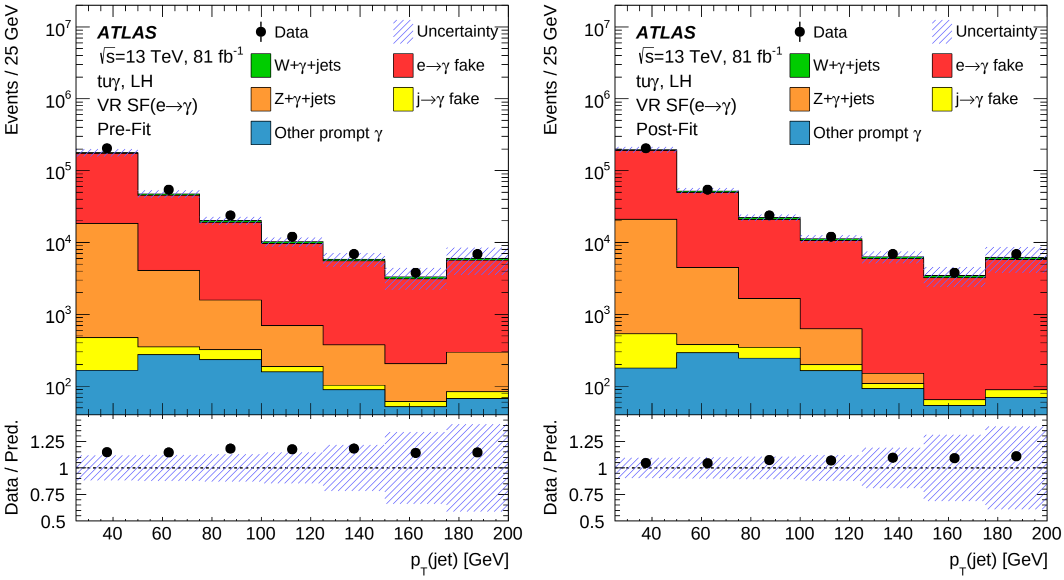

(a) Pre-fit distribution in the VR SF$(e \to \gamma)$ (b) Post-fit distribution in the VR SF$(e \to \gamma)$

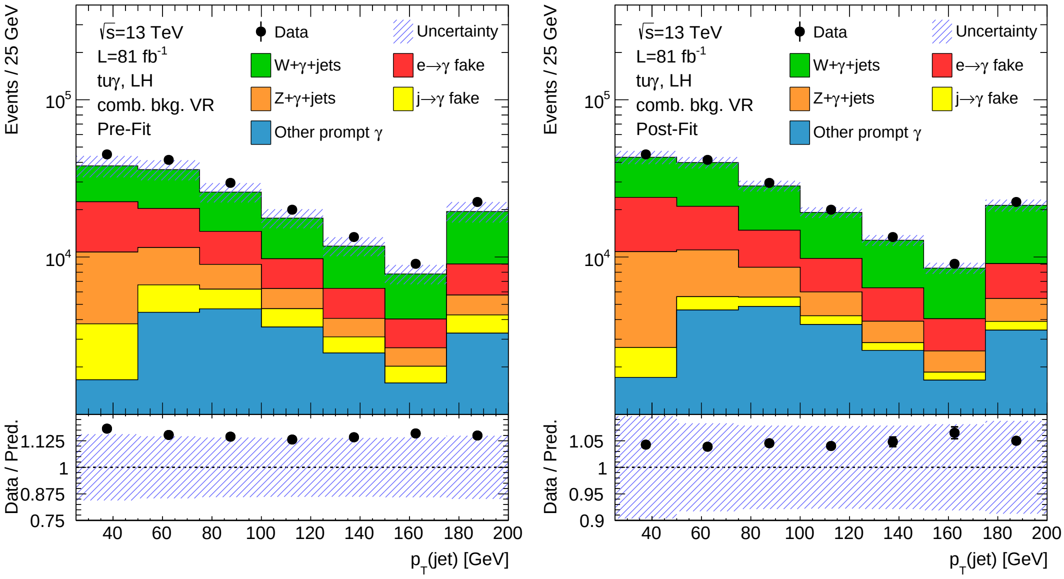

(c) Pre-fit distribution in the VR for combined background (d) Post-fit distribution in the VR for combined background

Figure 48: Pre- and post-fit distributions of the jet p_{T} in the VR SF$(e \to \gamma)$ (a,b) and in the VR for combined background (c,d) for validating the fit outcome of the LH $tu\gamma$ coupling. All uncertainties are included. The plots for the VR SF$(e \to \gamma)$ are published in the auxiliary material of Ref. [11].

11.4 Exclusion limits

As the SM expectation agrees with the data within the uncertainties and no significant signal contribution of FCNCs in processes with a top quark and a photon is observed, an exclusion limit is set on the signal strength using the CL_s method [201, 202]. This limit is computed separately for all four signal couplings in the EFT presented in Section 2.3. For this EFT, a scale of new physics of $\Lambda = 1\,\mathrm{TeV}$ is assumed. The limit on the signal strength is then interpreted as limits on the production cross section $\sigma(pp \to t\gamma)$, the absolute value of the sum of Wilson coefficients $|C^{\mathrm{sum}}|$ and the branching ratio $\mathcal{B}(t \to q\gamma)$ with $q = u, c$.

The CL_s method is a modified frequentist technique and computes an upper exclusion limit on the parameter of interest at a certain CL, here set to 95 %. It tests the hypothesis H_1 against the hypothesis H_0. For both hypotheses, the profile likelihood function, $\mathcal{L}(\mu, \vec{\theta})$, is optimised. The hypothesis H_1 contains the signal strength, $\hat{\mu}$, and set of NPs, $\vec{\theta}_{\hat{\mu}}$, that maximise the likelihood function. In the hypothesis H_0, for a given signal strength, μ, the set of NPs, $\vec{\theta}_{\mu}$, maximises this conditional likelihood function. For $\hat{\mu}$ and μ, only non-negative values are allowed as any signal contribution is expected to increase the total number of events. The compatibility of both hypotheses is quantified by the profile likelihood ratio, $\tilde{\lambda}(\mu)$, or equivalently by the test statistic, $\tilde{q}_{\mu}$, which is constructed as

$$\tilde{q}_{\mu} = \begin{cases} -2\ln\tilde{\lambda}(\mu)\,, & \text{for} \quad \hat{\mu} \leq \mu\,, \\ 0\,, & \text{for} \quad \hat{\mu} > \mu\,, \end{cases} \quad = \quad \begin{cases} -2\ln\frac{\mathcal{L}(\mu,\vec{\theta}_{\mu})}{\mathcal{L}(0,\vec{\theta}_{0})}\,, & \text{for} \quad \hat{\mu} < 0\,, \\ -2\ln\frac{\mathcal{L}(\mu,\vec{\theta}_{\mu})}{\mathcal{L}(\hat{\mu},\vec{\theta}_{\hat{\mu}})}\,, & \text{for} \quad 0 \leq \hat{\mu} \leq \mu\,, \\ 0\,, & \text{for} \quad \hat{\mu} > \mu\,. \end{cases} \tag{60}$$

The test statistic, $\tilde{q}_{\mu}$, is set to zero for $\hat{\mu} > \mu$ since such a behaviour indicates an upward fluctuation in data not covered by this technique. If the likelihood ratio is close to unity, the hypothesis H_0 is confirmed, while a value close to zero rejects it.

For $\tilde{q}_{\mu}$, the probability density function, $f(\tilde{q}_{\mu}|\mu)$, following a χ^2 distribution is estimated using Asimov datasets, with an arbitrary amount of signal being injected [203]. Eventually, the interval from $\tilde{q}_{\mu_{\mathrm{obs.}}}$ to infinity of the probability density function for the p-value of $p_{\mu} = 0.05$ is calculated by

$$p_{\mu} = 1 - 95\,\% = \int\limits_{\tilde{q}_{\mu_{\mathrm{obs.}}}}^{\infty} f(\tilde{q}_{\mu}|\mu)\, d\tilde{q}_{\mu} \tag{61}$$

with $\mu_{\text{obs.}}$ being the 95 % CL upper limit on the signal strength.

After the limit on the signal strength is computed, upper exclusion limits on other quantities are set, while any SM contributions for the process $pp \to t\gamma$ are neglected due to the suppression by the GIM mechanism. Although both the production- and decay-mode signal are considered in the fit, the signal strength as introduced in Equation (56) can be expressed separating both modes as

$$\mu = \frac{N_{\text{fit}}^{\text{prod. m.}} + N_{\text{fit}}^{\text{dec. m.}}}{N_{\text{in}}^{\text{prod. m.}} + N_{\text{in}}^{\text{dec. m.}}} = \frac{N_{\text{fit}}^{\text{prod. m.}}}{N_{\text{in}}^{\text{prod. m.}}} = \frac{\sigma_{\text{eff,fit}}^{\text{prod. m.}}}{\sigma_{\text{eff,in}}^{\text{prod. m.}}} \tag{62}$$

with the input and fitted numbers of signal events per coupling, $N_{\text{in}}^{\text{coup.}}$ and $N_{\text{fit}}^{\text{coup.}}$, respectively, and the fitted effective cross section, $\sigma_{\text{eff,fit}}^{\text{prod. m.}}$, for the production mode as defined in Equation (37). This simplification exploits that the cross sections of both modes equally depend on the sum of Wilson coefficients, and that the detector acceptance and signal efficiency is independent of the signal strength. The same relation holds in case of limits.

As the branching ratios $\mathcal{B}(t \to Wb) \times \mathcal{B}(W \to \ell\nu_\ell)$ cancel out when factorising the effective cross section, a linear dependence is found between the limit on the signal strength and that on the production cross section. As the branching ratio $\mathcal{B}(t \to q\gamma)$ with $q = u, c$ scales proportionally to the production cross section, the limit on the branching ratio depends linearly on that of the signal strength. Since the branching ratio is proportional to the quadratic sum of Wilson coefficients, $|C^{\text{sum}}|^2$ (cf. Equations (33) and (35)), the signal strength is also proportional to the square of Wilson coefficients. In total, the limit on the signal strength is translated to the other quantities using the following relations:

$$\mu_{\text{obs.}} = \frac{\sigma_{\text{obs.}}(pp \to t\gamma)}{\sigma_{\text{in}}(pp \to t\gamma)} = \frac{|C_{\text{obs.}}^{\text{sum}}|^2}{|C_{\text{in}}^{\text{sum}}|^2} = \frac{\mathcal{B}_{\text{obs.}}(t \to q\gamma)}{\mathcal{B}_{\text{in}}(t \to q\gamma)}\,. \tag{63}$$

Hereby, the index *in* corresponds to the input values referring to a branching ratio of $\mathcal{B}_{\text{in}}(t \to q\gamma) = 10^{-3}$ for both $q = u, c$ as introduced in Section 7.2.2, while the index *obs.* means the observed limit.

The observed and expected limit on the signal strength, μ_{obs}, is of $\mathcal{O}\left(10^{-2}\right)$ and $\mathcal{O}\left(10^{-1}\right)$ for both $tu\gamma$ and both $tc\gamma$ couplings, respectively. The expected limits are obtained by using an Asimov dataset. In Table 11, the observed and expected 95 % CL upper exclusion limits on all physics quantities for all couplings are shown in the context of the EFT, assuming a scale of new physics of $\Lambda = 1\,\text{TeV}$.

Table 11: Observed and expected 95 % CL upper limits on the production cross section $\sigma(pp \to t\gamma)$, on the absolute value of the sum of Wilson coefficients $|C^{\mathrm{sum}}|$ and on the branching ratios $\mathcal{B}(t \to q\gamma)$ with $q = u, c$ for the four different assumed signal couplings. The scale of new physics is assumed to be $\Lambda = 1\,\mathrm{TeV}$.

	$\sigma(pp \to t\gamma)$ [fb]		$\lvert C^{\mathrm{sum}}\rvert$		$\mathcal{B}(t \to q\gamma)$ $[10^{-5}]$	
Coupling	Obs.	Exp.	Obs.	Exp.	Obs.	Exp.
$tu\gamma$, LH	36	52^{+21}_{-14}	0.19	$0.22^{+0.04}_{-0.03}$	2.8	$4.0^{+1.6}_{-1.1}$
$tu\gamma$, RH	78	75^{+31}_{-21}	0.27	$0.27^{+0.05}_{-0.04}$	6.1	$5.9^{+2.4}_{-1.6}$
$tc\gamma$, LH	40	49^{+20}_{-14}	0.52	$0.57^{+0.11}_{-0.09}$	22	27^{+11}_{-7}
$tc\gamma$, RH	33	52^{+22}_{-14}	0.48	$0.59^{+0.12}_{-0.09}$	18	28^{+12}_{-8}

All observed and expected limits are in good agreement with respect to the uncertainty on the expected limits. For the LH $tu\gamma$ and both $tc\gamma$ couplings, the observed limits lie below the expected values by one standard deviation due to a downward fluctuation of data in the last bin in the SR as seen in Figure 43b. This bin has the largest sensitivity to the signal. The limits on both $tu\gamma$ couplings agree well and the same holds for both $tc\gamma$ couplings. While the limits on the production cross section are of the same order of magnitude for both the $tu\gamma$ and $tc\gamma$ couplings, the limits on the absolute value of the sum of Wilson coefficients and the branching ratio are stronger in the case of the $tu\gamma$ and $tc\gamma$ couplings. This is due to the fact that the input values $|C^{\mathrm{sum}}_{\mathrm{in}}|$ and $\mathcal{B}_{\mathrm{in}}(t \to q\gamma)$ are the same for both $tq\gamma$ couplings, while the input value for the production cross section, $\sigma_{\mathrm{in}}(pp \to t\gamma)$, depend on the coupling type, as presented in Section 7.2.2.

These observed limits are the best limits to date on FCNCs including either a $tu\gamma$ or $tc\gamma$ coupling which improve the previously best experimental limits obtained by the CMS collaboration [13] by an order of magnitude. In addition, in this search, LH and RH couplings were distinguished, while commonly in previous analyses, they were assumed to have the same strength.

12 Conclusion

In this thesis, the search for flavour-changing neutral currents in processes with a singly produced top quark and a photon using a deep neural network is presented. As in many BSM theories, the cross sections of such processes are increased compared to the SM prediction, this analysis both tested the SM and searched for hints of BSM physics. In this analysis, proton-proton collision data were used which were collected by the ATLAS detector at the LHC at a centre-of-mass energy of $\sqrt{s} = 13\,\mathrm{TeV}$ during 2015, 2016 and 2017. The data correspond to an integrated luminosity of $81\,\mathrm{fb}^{-1}$.

The signal was simulated in the context of an effective field theory assuming a scale of new physics of $\Lambda = 1\,\mathrm{TeV}$. The signal coupling was assumed to be either left- or right-handed and to involve either an up quark or a charm quark. Such a coupling may appear in the production of a single top quark in association with a photon, or in the decay of a top quark of a $t\bar{t}$ pair. The contributions of both the production and decay mode were taken into account. Events were selected with exactly one photon, one charged lepton, one b-tagged jet and a certain amount of missing transverse momentum in the final state. Each event was categorised depending on the origin of the photon as an event with an $e \to \gamma$ fake, a $j \to \gamma$ fake or a prompt photon. The background contributions arising from fake photons were estimated by data-driven techniques.

Assuming the presence of only one signal coupling at a time, a deep neural network was used to construct a discriminating variable which separates signal-like events from background candidates. In the statistical analysis, this discriminant was simultaneously fitted with two other distributions. These distributions were the neural network output distribution in a region enriched with events of the W+γ+jets process and the photon p_{T} spectrum in a region which was enhanced with events of the Z+γ+jets process. In the fit, the prompt photon contributions of the W+γ+jets and Z+γ+jets processes and the signal strength were determined by maximising a profile likelihood function. The sources of systematic and statistical uncertainties were taken into account.

Since no signal contribution was observed and the data were found to be consistent with the background expectation, a 95 % confidence level upper limit was computed on the signal strength using the CL_s method. This exclusion limit was further interpreted in the context of the effective field theory. Limits on the production cross section $\sigma(pp \to t\gamma)$, the absolute value of the sum of Wilson coefficients $\left|C_{uB}^{(ij)*} + C_{uW}^{(ij)*}\right|$ for the left-handed and $\left|C_{uB}^{(ij)} + C_{uW}^{(ij)}\right|$ for the right-handed couplings, respectively, and the branching ratio $\mathcal{B}(t \to q\gamma)$ with $q = u, c$ were set. For the left-handed $tu\gamma$ coupling, the observed limit on the branching ratio is 2.8×10^{-5}, while for the right-handed $tu\gamma$ it amounts to 6.1×10^{-5}. The observed limit on the branching ratio for the left-handed and right-handed $tc\gamma$ coupling is 22×10^{-5} and 18×10^{-5}, respectively.

The obtained limits improved the previously best experimental limits set by the CMS collaboration [13] by an order of magnitude and yield the best limits to date. As a consequence, the parameters in BSM models allowing for FCNCs are further constrained. In addition, as this analysis was the first search for the $tu\gamma$ and $tc\gamma$ couplings in the ATLAS collaboration, it has prepared the ground for subsequent searches with a larger amount of data or for successive analyses investigating another phase space optimised for both the production and decay mode.

Acknowledgements

This work and thesis would have never been accomplished without the assistance and help of many people over the last years. I am very thankful for the broad and patient support which I experienced!

First of all, I would like to thank my doctoral supervisor Prof. Dr. Kevin Kröninger for his steady support in both physics and non-physics related matter. Thanks for hiring me as doctoral candidate and in particular, for enabling me to stay at CERN for one and a half years. In addition, I would like to thank Prof. Dr. Wolfgang Wagner, my second reviewer. Thanks for critically reviewing and speaking up for this search in the ATLAS collaboration and to agree on reviewing this thesis. I would like to give special thanks to Priv.-Doz. Dr. Johannes Erdmann for his great support from the very beginning of this work to its successful ending.

Next, I would like to thank the members of the group EIV of the physics department at the TU Dortmund. Thanks for creating a familiar working atmosphere and for making work endurable at all! Many thanks go to Andrea Teichmann and Markus Alex for their administrative help and technical support. In particular, I would like to thank the people of the analysis group for all the discussions. Special thanks go to Tobias Kupfer for being my flatmate at CERN and in Dortmund, for all the trips and for making the last years much more joyful; to Dr. Olaf Nackenhorst for proof-reading my thesis and particularly for organising tickets and watching matches of our beloved BVB; to Dr. Diane Cinca for the support at CERN; to Dr. Isabel Nitsche and Lennart Rustige for sharing a flat at CERN making it a very pleasant time; to the PhD students Sonja Zeißner, Elena Freundlich, Cornelius Grunwald, Björn Wendland, Salvatore La Cagnina for many discussions about physics and non-physical topics; to my former colleagues Dr. Ingo Burmeister, Dr. Hendrik Esch and Dr. Christian Jung for recruiting me and motivating me to become a PhD student. Also many thanks go to Robert Temminghoff, his wife and dear daugther for spending holidays and much leisure time together, and to Marcel Gerhardt for encouraging me to run, run run.

I also would like to remember Priv.-Doz. Dr. Reiner Klingenberg who passed away far too early. He excellently supervised me as Bachelor and Master student, vividly discussed physics and motivated me to become a doctoral candidate.

Moreover, I would like to thank the ATLAS collaboration and its different groups: the photon ID group for a relaxed working atmosphere, the Top group for enabling this analysis, and the single top group and top+photon group (a.k.a ttgamma group) for discussing physics down to the smallest detail. Furthermore, I would like to give my thanks to Nuno Castro, Ana Peixoto and Maura Barros. Thanks for a productive collaboration and for fruitful discussions about physics.

As work is not everything in life, I would like to thank all my friends: Peter, Johannes, Philipp, Carolin, Jan, Theresa, Johannes, my football team, and many many more. Thanks for many joyful days and evenings, for nice trips and vacations, and primarily for distracting me from physics.

Last, but not least, my biggest thanks go to my family: my parents for their loving and never-ending support, for standing at my side in each situation and for so much more; my brother for being there whenever I need him and for sharing so many experiences!

Thanks!

Appendix

A List of abbreviations

2HDM	2-Higgs-Doublet model
AFII	AtlFastII
ALFA	Absolute Luminosity For ATLAS
ALICE	A Large Ion Collider Experiment
ATLAS	A Toroidal LHC ApparatuS
AUC	area under a curve
BCM	Beam Conditions Monitor
BSM	Beyond the Standard Model
CC	charged current
CDF	Collider Detector at Fermilab
CERN	European Organisation for Nuclear Research
CKM	Cabibbo-Kobayashi-Maskawa
CL	confidence level
CMS	Compact Muon Solenoid
CR	control region
CSC	Cathode Strip Chamber
DAQ	Data Acquisition

DR	diagram removal
DS	diagram subtraction
ECAL	Electromagnetic Calorimeter
EFR	electron fake estimation region
EFT	effective field theory
FCNC	flavour-changing neutral current
FSR	final state radiation
GIM	Glashow-Iliopolus-Maiani
HCAL	Hadronic Calorimeter
HERA	Hadron-Elektron-Ringanlage
HFR	hadronic fake estimation region
HLT	High Level Trigger
IBL	Insertable B-layer
ID	identification
InDet	Inner Detector
ISR	initial state radiation
JER	jet energy resolution
JES	jet energy scale
JVT	jet vertex tagger
L1	Level-1
LAr	liquid argon
LEP	Large Electron-Positron Collider

LH	left-handed
LHC	Large Hadron Collider
LHCb	Large Hadron Collider beauty
LINAC2	Linear Accelerator 2
LINAC3	Linear Accelerator 3
LO	leading order
LUCID-2	Luminosity Measurement Using Cerenkov Integrating Detector-2
MC	Monte-Carlo
MDT	Monitored Drift Tube
ML	machine-learning
MS	Muon Spectrometer
MSSM	minimal-supersymmetric Standard Model
MVA	multivariate analysis
NC	neutral current
NLO	next-to-leading order
NN	neural network
NP	nuisance parameter
PDF	parton distribution function
PS	Proton Synchrotron
PSB	Proton Synchrotron Booster
QCD	quantum chromodynamics
QED	quantum electrodynamics

QFT	quantum field theory
RFQ	Radio Frequency Quadrupole
RH	right-handed
ROC	receiver operating characteristic
RPC	Resistive Plate Chamber
SCT	Semiconductor Tracker
SF	scale factor
SM	Standard Model
SPS	Super Proton Synchrotron
SR	signal region
SW	sliding window
TDAQ	Trigger and Data Acquisition
TGC	Thin-Gap Chamber
TRT	Transition Radiation Tracker
UFO	Universal FeynRules Output
VR	validation region
WP	working point
ZDC	Zero-Degree Calorimeter

B Plots of the statistical analysis for the other signal couplings

In this appendix, different distributions and tables of the statistical analysis for the RH $tu\gamma$, LH $tc\gamma$ and RH $tc\gamma$ coupling are shown. As the behaviours of all signal couplings are similar to each other, mainly the distributions and tables for the LH $tu\gamma$ coupling are shown in Section 11. For none of the couplings, any hint for a bias or mis-modelling is found.

Plots and tables for the right-handed $tu\gamma$ coupling

Table 12: Observed and expected number of events for the different background contributions in the SR, CR W+γ+jet and CR Z+γ after the fit for the RH $tu\gamma$ coupling. The statistical uncertainties and all systematic uncertainties are included.

Photon origin	SR	CR W+γ+jet	CR Z+γ
$e \to \gamma$	4 880 ± 500	8 400 ± 1 400	250 ± 34
$j \to \gamma$	340 ± 230	3 900 ± 2 600	1 600 ± 1 100
Z+γ+jets	740 ± 100	13 200 ± 1 300	81 200 ± 2 000
W+γ+jets	1 780 ± 370	99 800 ± 3 400	6.0 ± 1.9
Other prompt γ	1 790 ± 390	1 900 ± 440	2 180 ± 220
Expectation	9 540 ± 220	127 300 ± 3 700	85 200 ± 1 600
Data	9 557	127 864	85 347

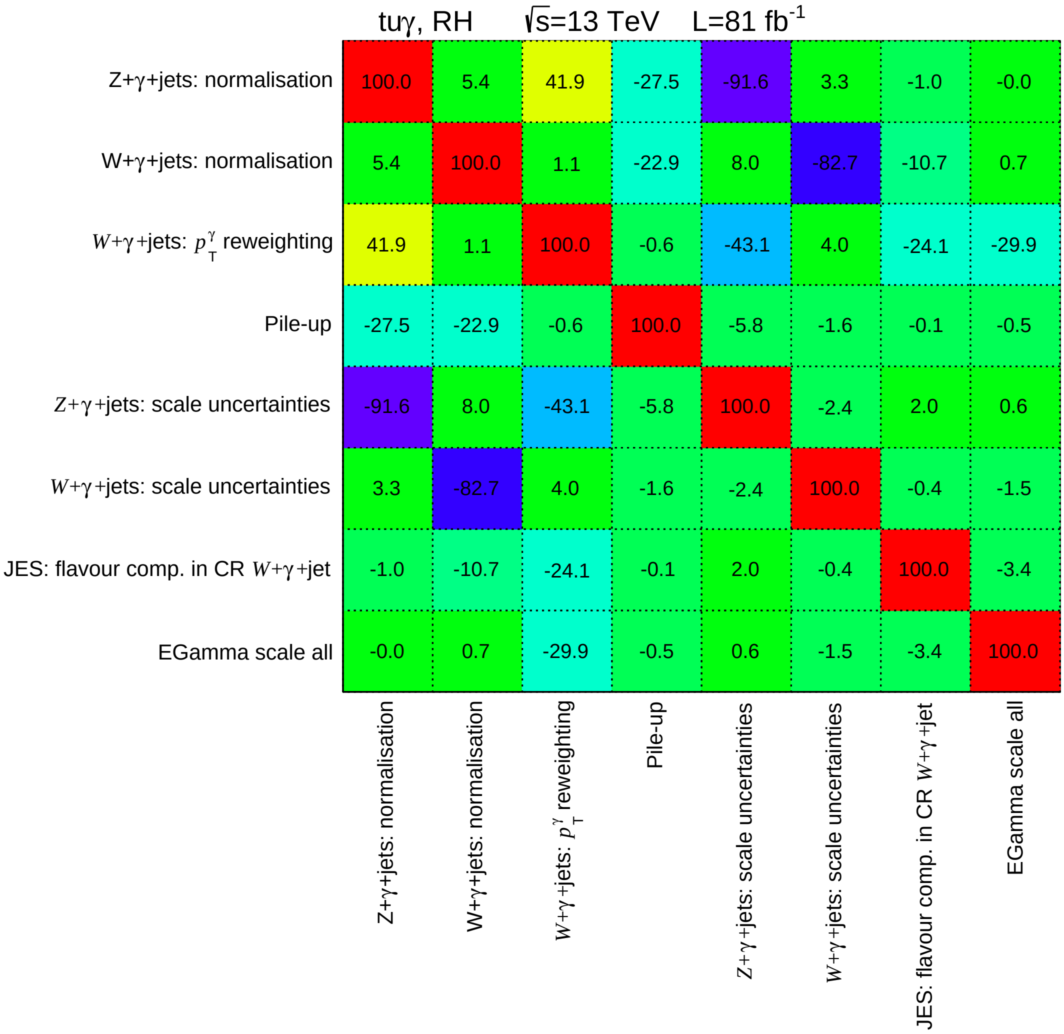

$tu\gamma$, RH $\sqrt{s}$=13 TeV L=81 fb^{-1}

	Z+γ+jets: normalisation	W+γ+jets: normalisation	W+γ+jets: p_T^γ reweighting	Pile-up	Z+γ+jets: scale uncertainties	W+γ+jets: scale uncertainties	JES: flavour comp. in CR W+γ+jet	EGamma scale all
Z+γ+jets: normalisation	100.0	5.4	41.9	-27.5	-91.6	3.3	-1.0	-0.0
W+γ+jets: normalisation	5.4	100.0	1.1	-22.9	8.0	-82.7	-10.7	0.7
W+γ+jets: p_T^γ reweighting	41.9	1.1	100.0	-0.6	-43.1	4.0	-24.1	-29.9
Pile-up	-27.5	-22.9	-0.6	100.0	-5.8	-1.6	-0.1	-0.5
Z+γ+jets: scale uncertainties	-91.6	8.0	-43.1	-5.8	100.0	-2.4	2.0	0.6
W+γ+jets: scale uncertainties	3.3	-82.7	4.0	-1.6	-2.4	100.0	-0.4	-1.5
JES: flavour comp. in CR W+γ+jet	-1.0	-10.7	-24.1	-0.1	2.0	-0.4	100.0	-3.4
EGamma scale all	-0.0	0.7	-29.9	-0.5	0.6	-1.5	-3.4	100.0

Figure 49: Visualisation of the correlation coefficients between the NPs of systematic nature for the RH $tu\gamma$ coupling. Only uncertainties with the absolute value of at least one coefficient above 0.2 are drawn.

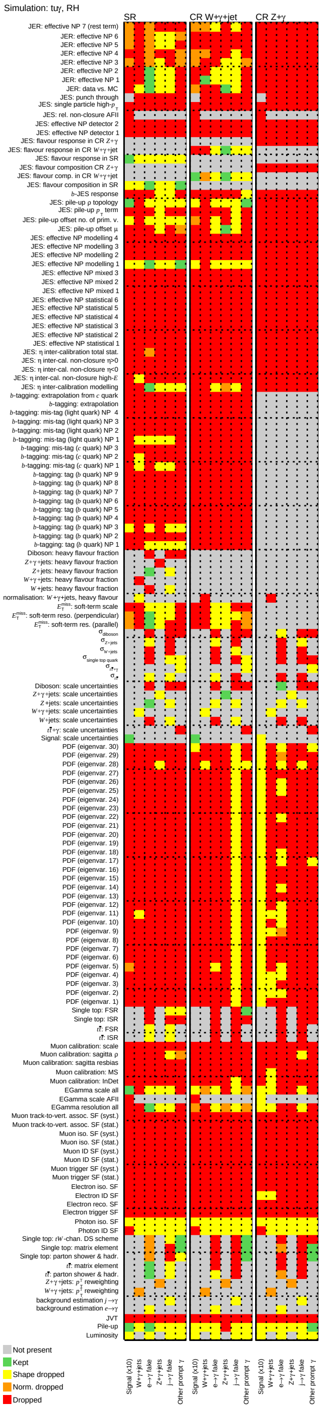

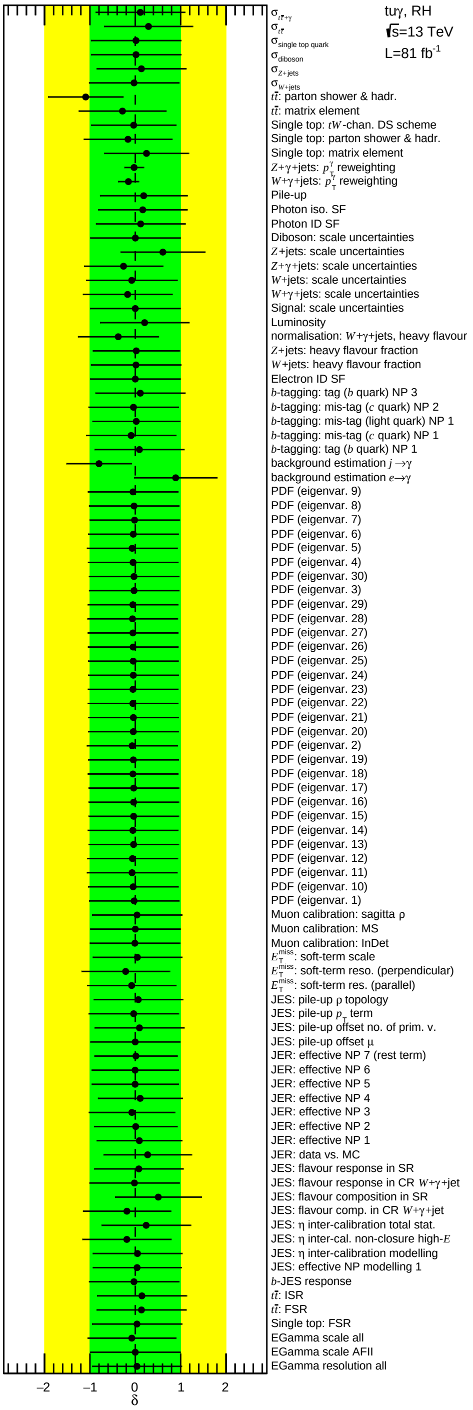

Figure 50: Illustration of the treatment of every systematic NP considered in the fit for the RH $tu\gamma$ coupling in each region for each signal and background categories.

Figure 51: Pull values, δ, for the systematic NPs considered and determined in the fit for the RH $tu\gamma$ coupling.

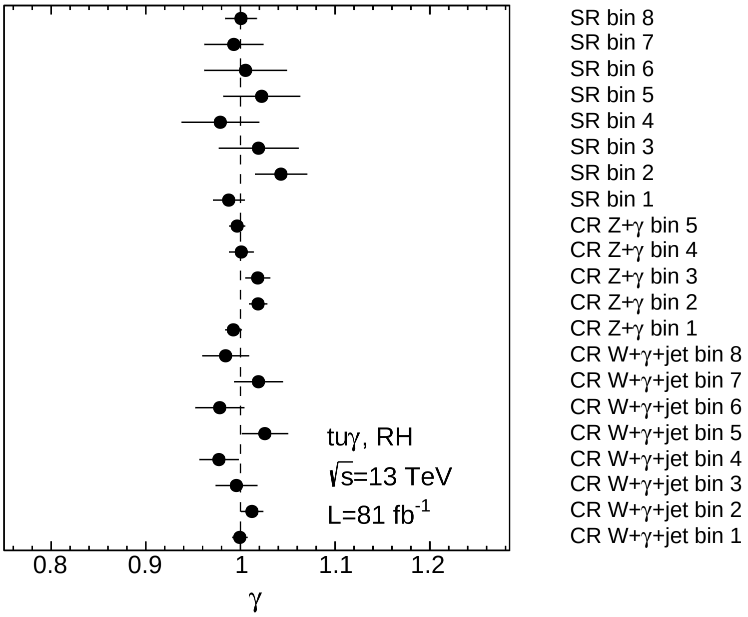

Figure 52: Normalisation factors, γ, for the different regions and bins determined in the fit for the RH $tu\gamma$ coupling.

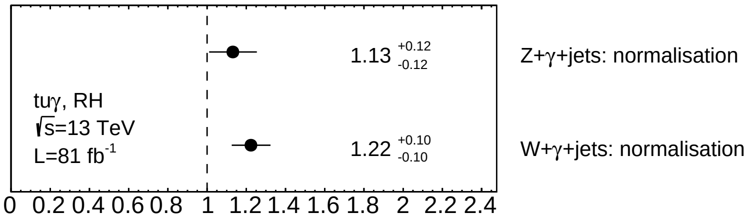

Figure 53: Normalisation factors for the prompt photon contributions of the W+γ+jets and Z+γ+jets processes determined in the fit for the RH $tu\gamma$ coupling.

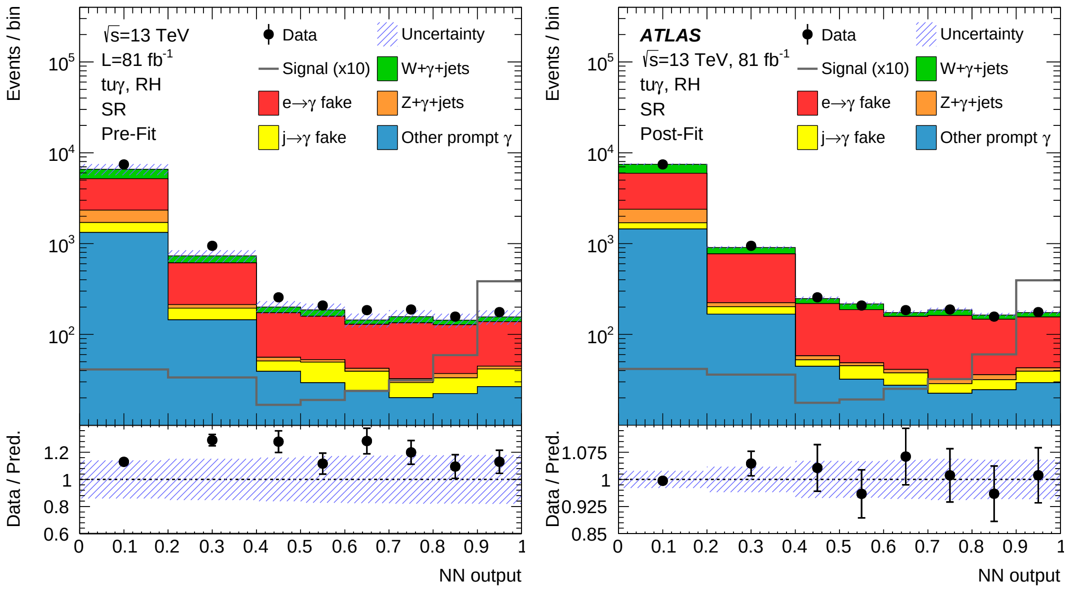

(a) Pre-fit distribution in the SR **(b)** Post-fit distribution in the SR

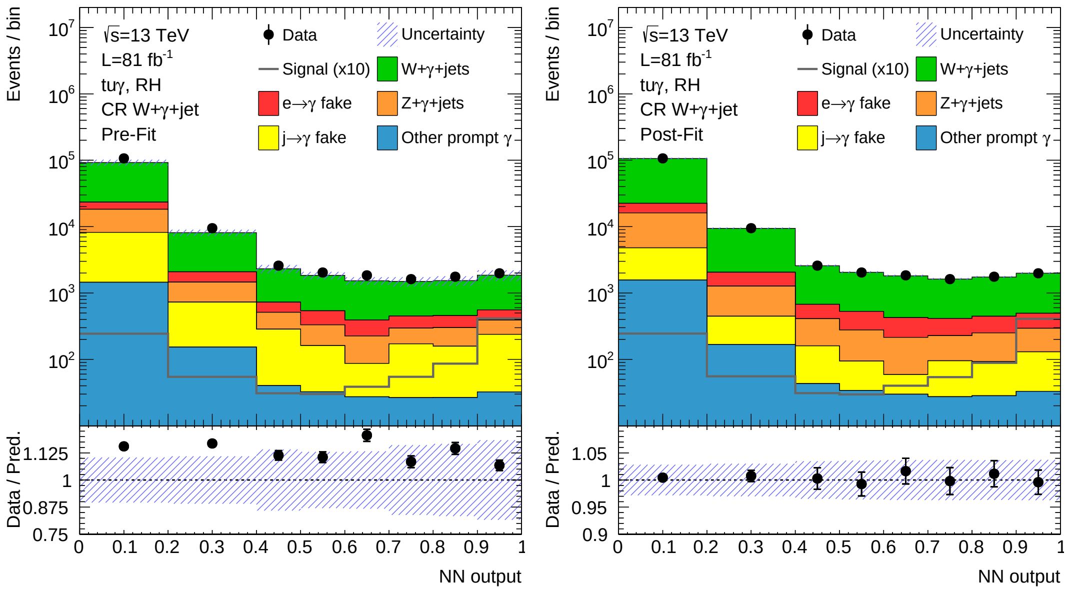

(c) Pre-fit distribution in the CR $W+\gamma$+jet **(d)** Post-fit distribution in the CR $W+\gamma$+jet

Figure 54: Pre- and post-fit distributions of the NN output in the SR (a,b) and CR $W+\gamma$+jet (c,d) for the RH $tu\gamma$ coupling. All NPs are included. The signal shape is overlaid scaled to the observed limit multiplied by ten. The post-fit plot for the SR is published in the auxiliary material of Ref. [11]. It is also shown in Figure 45a and here to enable for a direct comparison to the pre-fit plot.

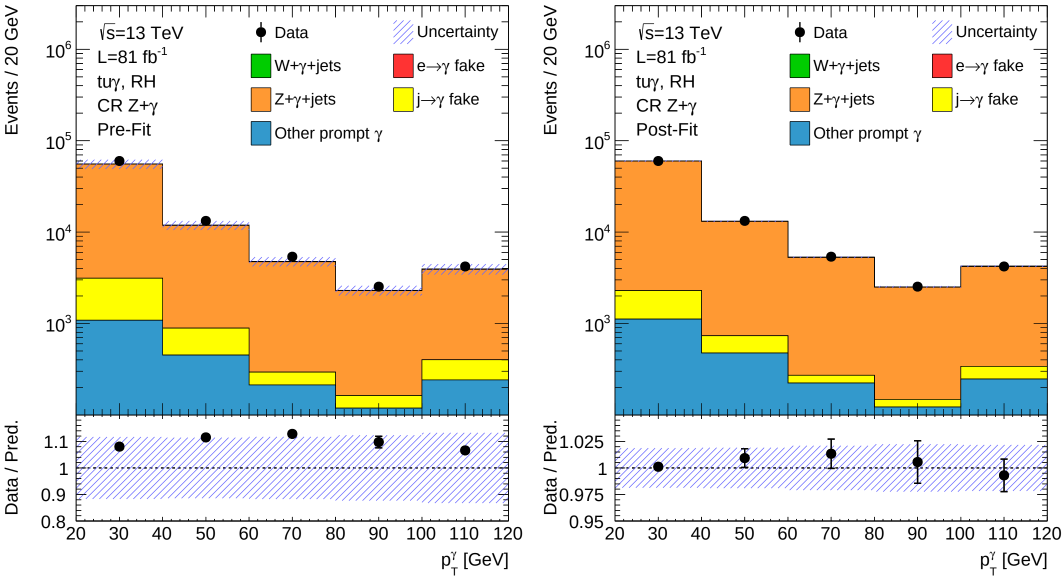

(a) Pre-fit distribution in the CR Z+γ **(b)** Post-fit distribution in the CR Z+γ

Figure 55: Pre- (a) and post-fit distribution (b) of the photon p_{T} spectrum in the CR Z+γ for the RH $tu\gamma$ coupling. All uncertainties are included. Since the signal contribution is negligible in this region, its shape is not overlaid.

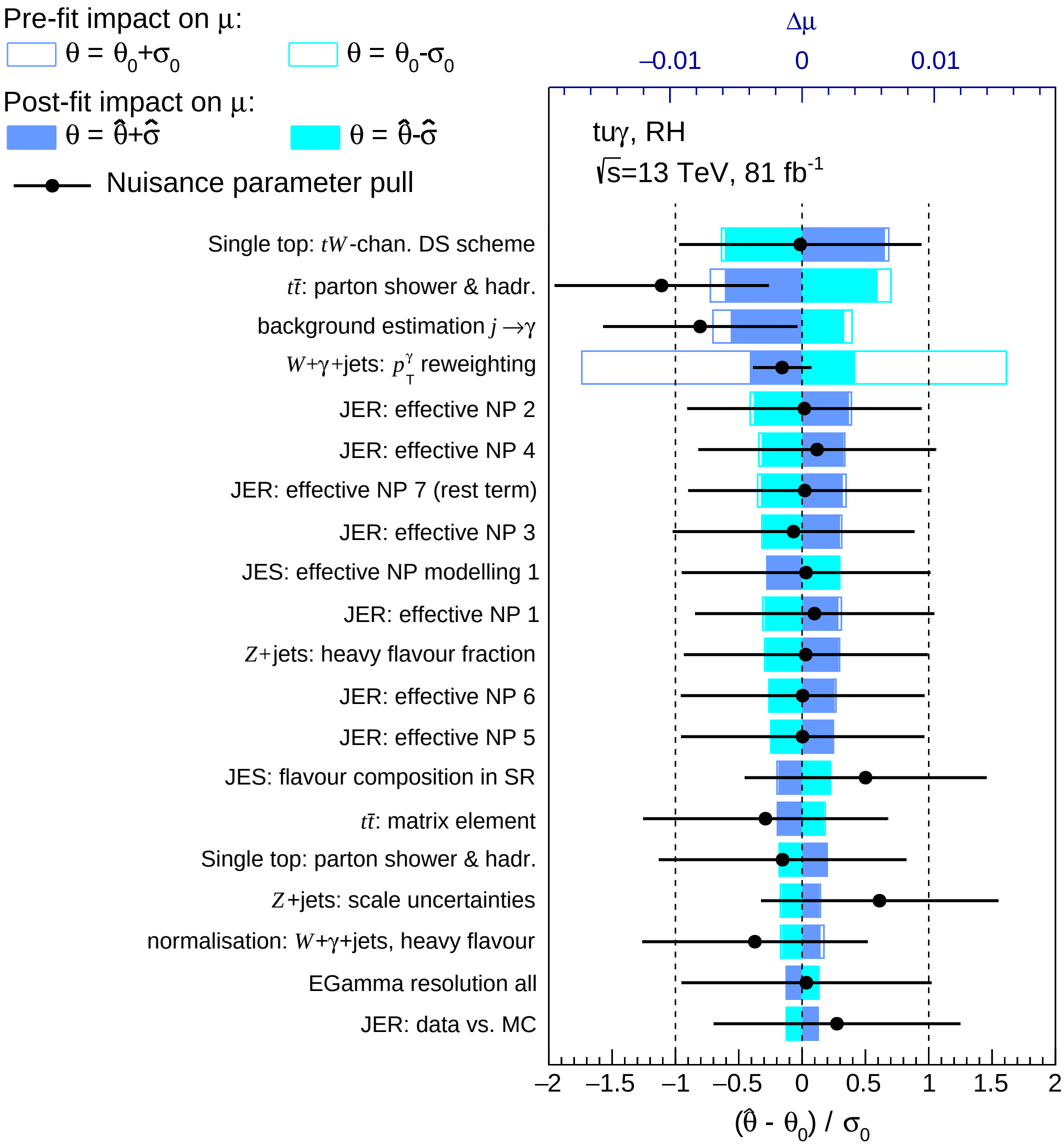

Figure 56: Ranking of the NPs with the largest impact on the signal strength, μ, for the RH $tu\gamma$ coupling. The signal strength of unity corresponds to the branching ratio $\mathcal{B}_{\text{in}}(t \to u\gamma) = 10^{-3}$. The ranking is determined in fits fixing the NP under study to its pre-fit value θ_0 and adding or subtracting its pre-fit uncertainty, σ_0, and analogously for the post-fit value, $\hat{\theta}$, and its uncertainty, $\hat{\sigma}$. The rectangles refer to the upper axis, while the black dots refer to the bottom scale.

Plots and tables for the left-handed $tc\gamma$ coupling

Table 13: Observed and expected number of events for the different background contributions in the SR, CR W+γ+jet and CR Z+γ after the fit for the RH $tu\gamma$ coupling. The statistical uncertainties and all systematic uncertainties are included.

Photon origin	SR	CR W+γ+jet	CR Z+γ
$e \to \gamma$	4 700 ± 500	8 600 ± 1 400	250 ± 33
$j \to \gamma$	420 ± 240	5 900 ± 3 500	2 100 ± 1 000
Z+γ+jets	770 ± 110	13 600 ± 1 400	81 200 ± 2 100
W+γ+jets	1 970 ± 400	98 500 ± 4 000	6.3 ± 2.0
Other prompt γ	1 730 ± 380	1 900 ± 440	2 160 ± 220
Expectation	9 590 ± 240	128 500 ± 4 100	85 700 ± 1 700
Data	9 557	127 864	85 347

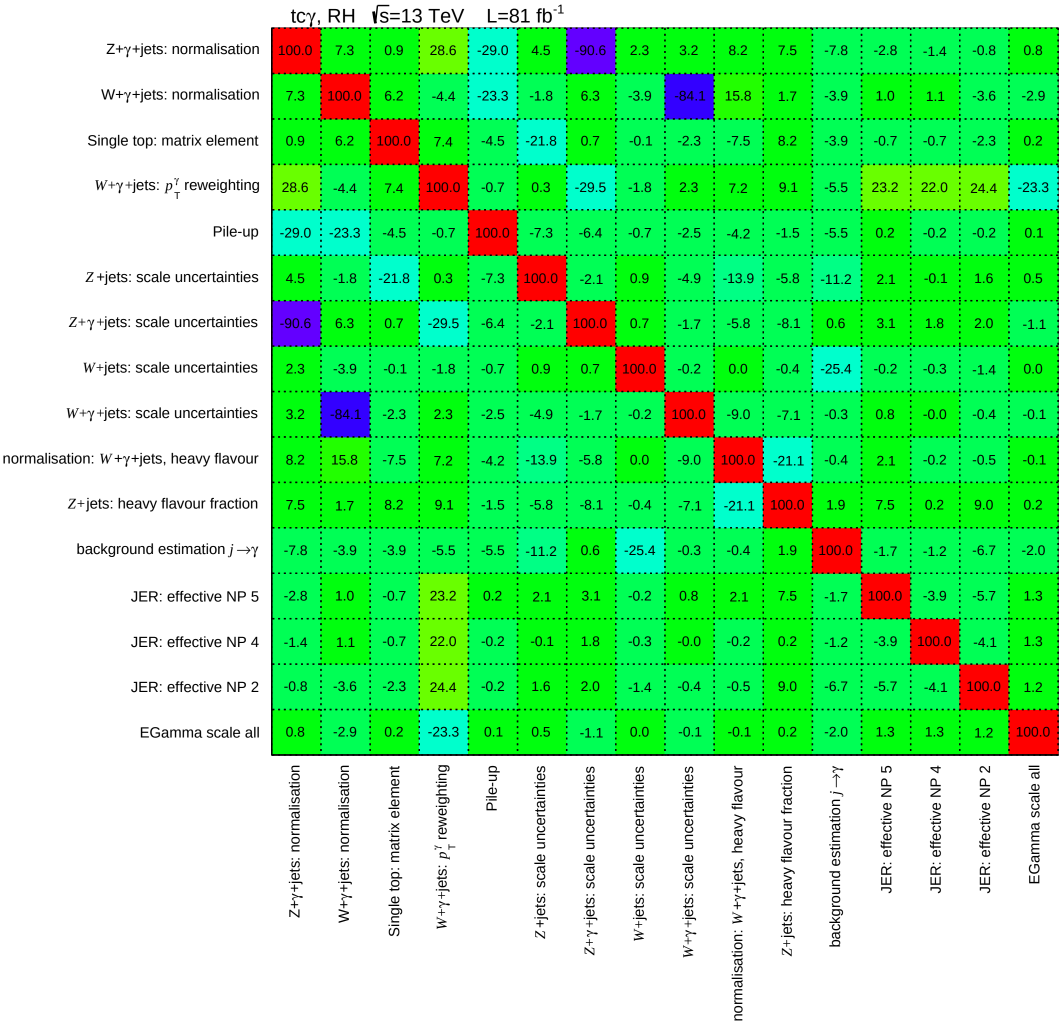

	Z+γ+jets: normalisation	W+γ+jets: normalisation	Single top: matrix element	W+γ+jets: p_T^{γ} reweighting	Pile-up	Z+jets: scale uncertainties	Z+γ+jets: scale uncertainties	W+jets: scale uncertainties	W+γ+jets: scale uncertainties	normalisation: W+γ+jets, heavy flavour	Z+jets: heavy flavour fraction	background estimation $j \rightarrow \gamma$	JER: effective NP 5	JER: effective NP 4	JER: effective NP 2	EGamma scale all
Z+γ+jets: normalisation	100.0	7.3	0.9	28.6	-29.0	4.5	-90.6	2.3	3.2	8.2	7.5	-7.8	-2.8	-1.4	-0.8	0.8
W+γ+jets: normalisation	7.3	100.0	6.2	-4.4	-23.3	-1.8	6.3	-3.9	-84.1	15.8	1.7	-3.9	1.0	1.1	-3.6	-2.9
Single top: matrix element	0.9	6.2	100.0	7.4	-4.5	-21.8	0.7	-0.1	-2.3	-7.5	8.2	-3.9	-0.7	-0.7	-2.3	0.2
W+γ+jets: p_T^{γ} reweighting	28.6	-4.4	7.4	100.0	-0.7	0.3	-29.5	-1.8	2.3	7.2	9.1	-5.5	23.2	22.0	24.4	-23.3
Pile-up	-29.0	-23.3	-4.5	-0.7	100.0	-7.3	-6.4	-0.7	-2.5	-4.2	-1.5	-5.5	0.2	-0.2	-0.2	0.1
Z+jets: scale uncertainties	4.5	-1.8	-21.8	0.3	-7.3	100.0	-2.1	0.9	-4.9	-13.9	-5.8	-11.2	2.1	-0.1	1.6	0.5
Z+γ+jets: scale uncertainties	-90.6	6.3	0.7	-29.5	-6.4	-2.1	100.0	0.7	-1.7	-5.8	-8.1	0.6	3.1	1.8	2.0	-1.1
W+jets: scale uncertainties	2.3	-3.9	-0.1	-1.8	-0.7	0.9	0.7	100.0	-0.2	0.0	-0.4	-25.4	-0.2	-0.3	-1.4	0.0
W+γ+jets: scale uncertainties	3.2	-84.1	-2.3	2.3	-2.5	-4.9	-1.7	-0.2	100.0	-9.0	-7.1	-0.3	0.8	-0.0	-0.4	-0.1
normalisation: W+γ+jets, heavy flavour	8.2	15.8	-7.5	7.2	-4.2	-13.9	-5.8	0.0	-9.0	100.0	-21.1	-0.4	2.1	-0.2	-0.5	-0.1
Z+jets: heavy flavour fraction	7.5	1.7	8.2	9.1	-1.5	-5.8	-8.1	-0.4	-7.1	-21.1	100.0	1.9	7.5	0.2	9.0	0.2
background estimation $j \rightarrow \gamma$	-7.8	-3.9	-3.9	-5.5	-5.5	-11.2	0.6	-25.4	-0.3	-0.4	1.9	100.0	-1.7	-1.2	-6.7	-2.0
JER: effective NP 5	-2.8	1.0	-0.7	23.2	0.2	2.1	3.1	-0.2	0.8	2.1	7.5	-1.7	100.0	-3.9	-5.7	1.3
JER: effective NP 4	-1.4	1.1	-0.7	22.0	-0.2	-0.1	1.8	-0.3	-0.0	-0.2	0.2	-1.2	-3.9	100.0	-4.1	1.3
JER: effective NP 2	-0.8	-3.6	-2.3	24.4	-0.2	1.6	2.0	-1.4	-0.4	-0.5	9.0	-6.7	-5.7	-4.1	100.0	1.2
EGamma scale all	0.8	-2.9	0.2	-23.3	0.1	0.5	-1.1	0.0	-0.1	-0.1	0.2	-2.0	1.3	1.3	1.2	100.0

Figure 57: Visualisation of the correlation coefficients between the NPs of systematic nature for the LH $tc\gamma$ coupling. Only uncertainties with the absolute value of at least one coefficient above 0.2 are drawn.

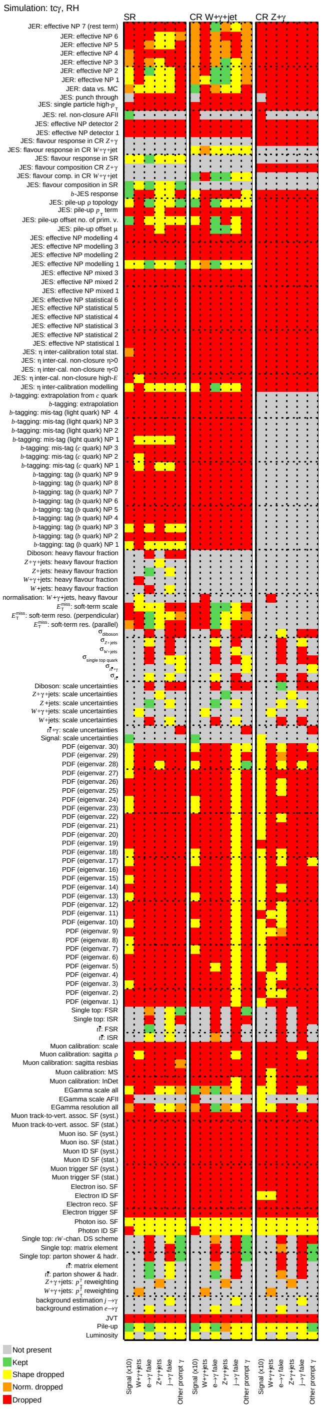

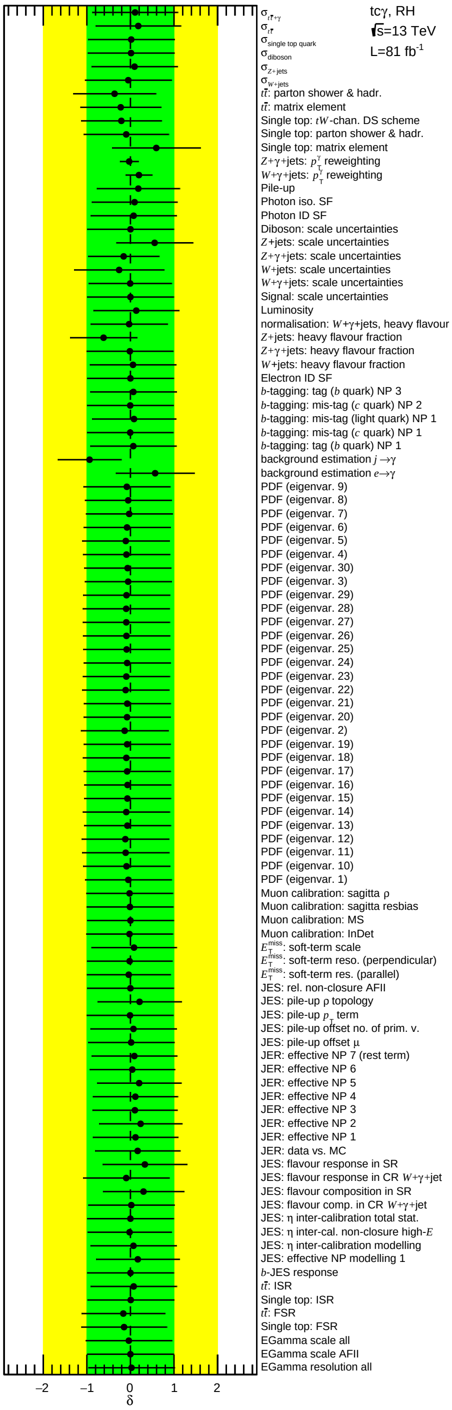

Figure 58: Illustration of the treatment of every systematic NP considered in the fit for the LH $tc\gamma$ coupling in each region for each signal and background categories.

Figure 59: Pull values, δ, for the systematic NPs considered and determined in the fit for the LH $tc\gamma$ coupling.

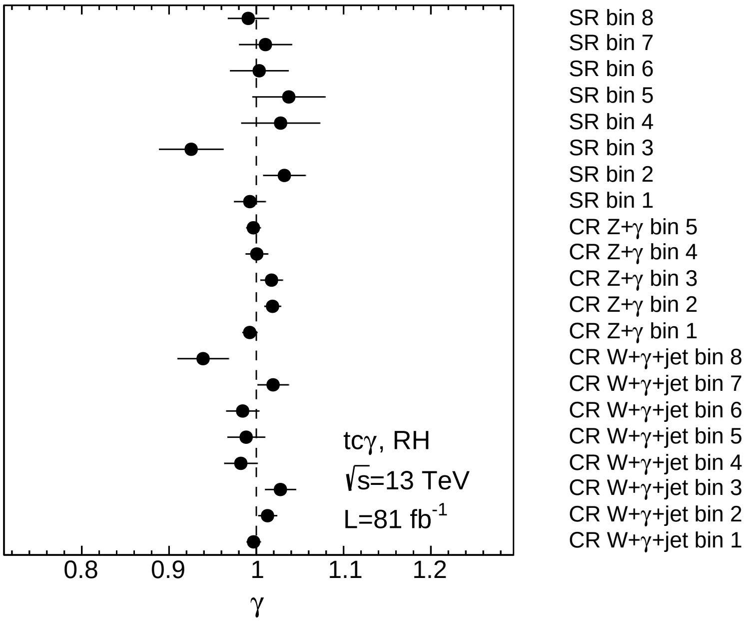

Figure 60: Normalisation factors γ for the different regions and bins determined in the fit for the LH $tc\gamma$ coupling.

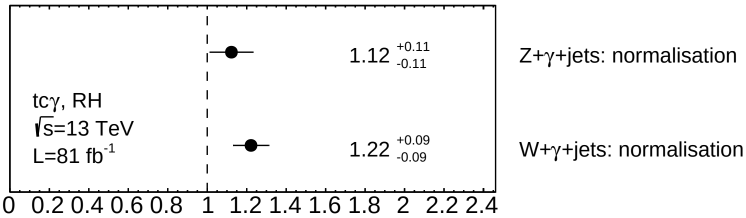

Figure 61: Normalisation factors for the prompt photon contributions of the W+γ+jets and Z+γ+jets processes determined in the fit for the LH $tc\gamma$ coupling.

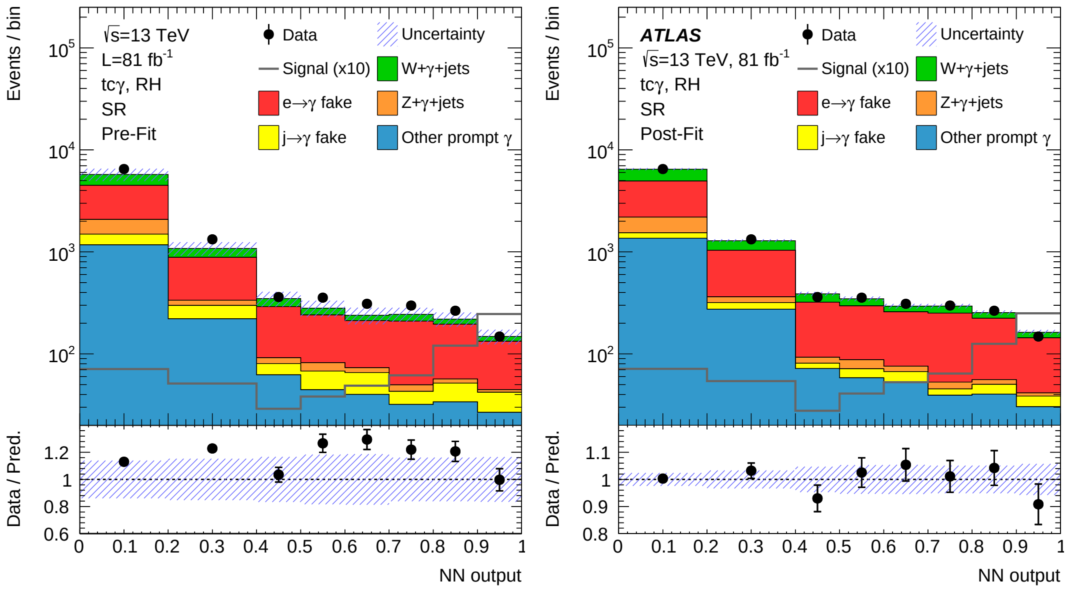

(a) Pre-fit distribution in the SR (b) Post-fit distribution in the SR

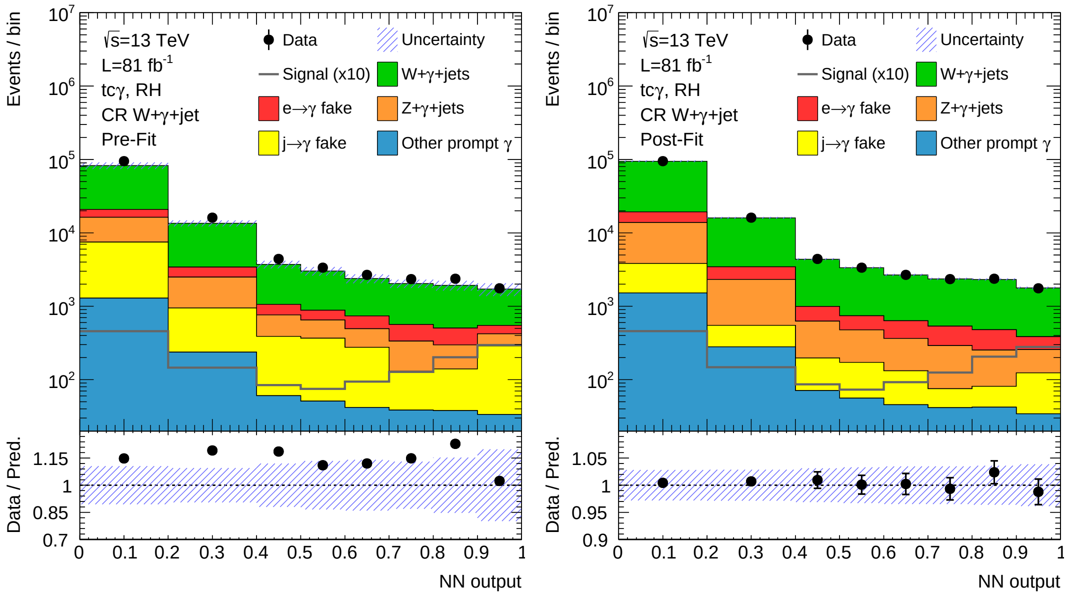

(c) Pre-fit distribution in the CR W+γ+jet (d) Post-fit distribution in the CR W+γ+jet

Figure 62: Pre- and post-fit distributions of the NN output in the SR (a,b) and CR W+γ+jet (c,d) for the LH $tc\gamma$ coupling. All NPs are included. The signal shape is overlaid scaled to the observed limit multiplied by ten. The post-fit plot for the SR is published in the auxiliary material of Ref. [11]. It is also shown in Figure 45b and here to enable for a direct comparison to the pre-fit plot.

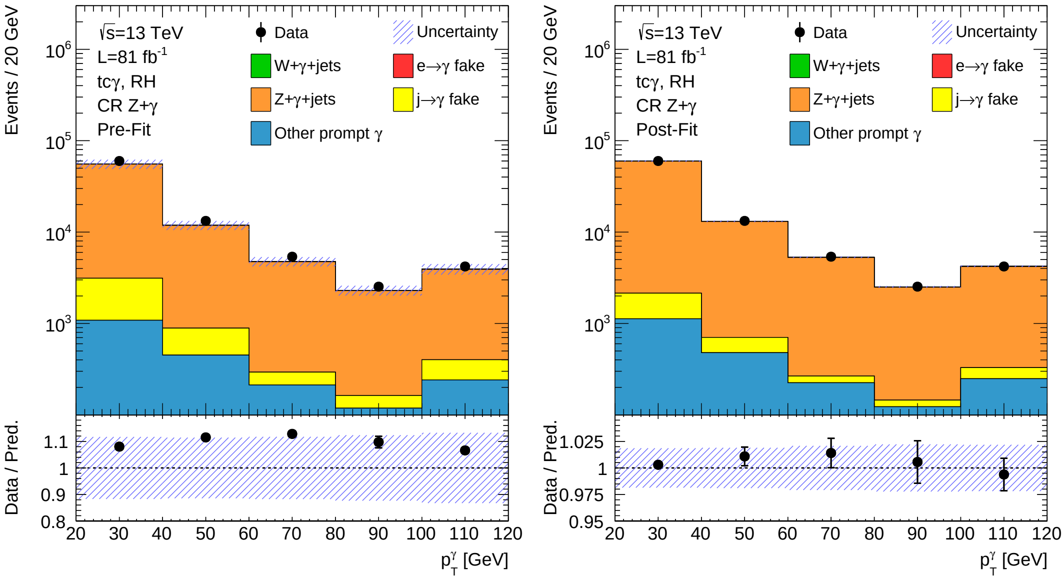

(a) Pre-fit distribution in the CR Z+γ

(b) Post-fit distribution in the CR Z+γ

Figure 63: Pre- (a) and post-fit distribution (b) of the photon p_T spectrum in the CR Z+γ for the LH $tc\gamma$ coupling. All uncertainties are included. Since the signal contribution is negligible in this region, its shape is not overlaid.

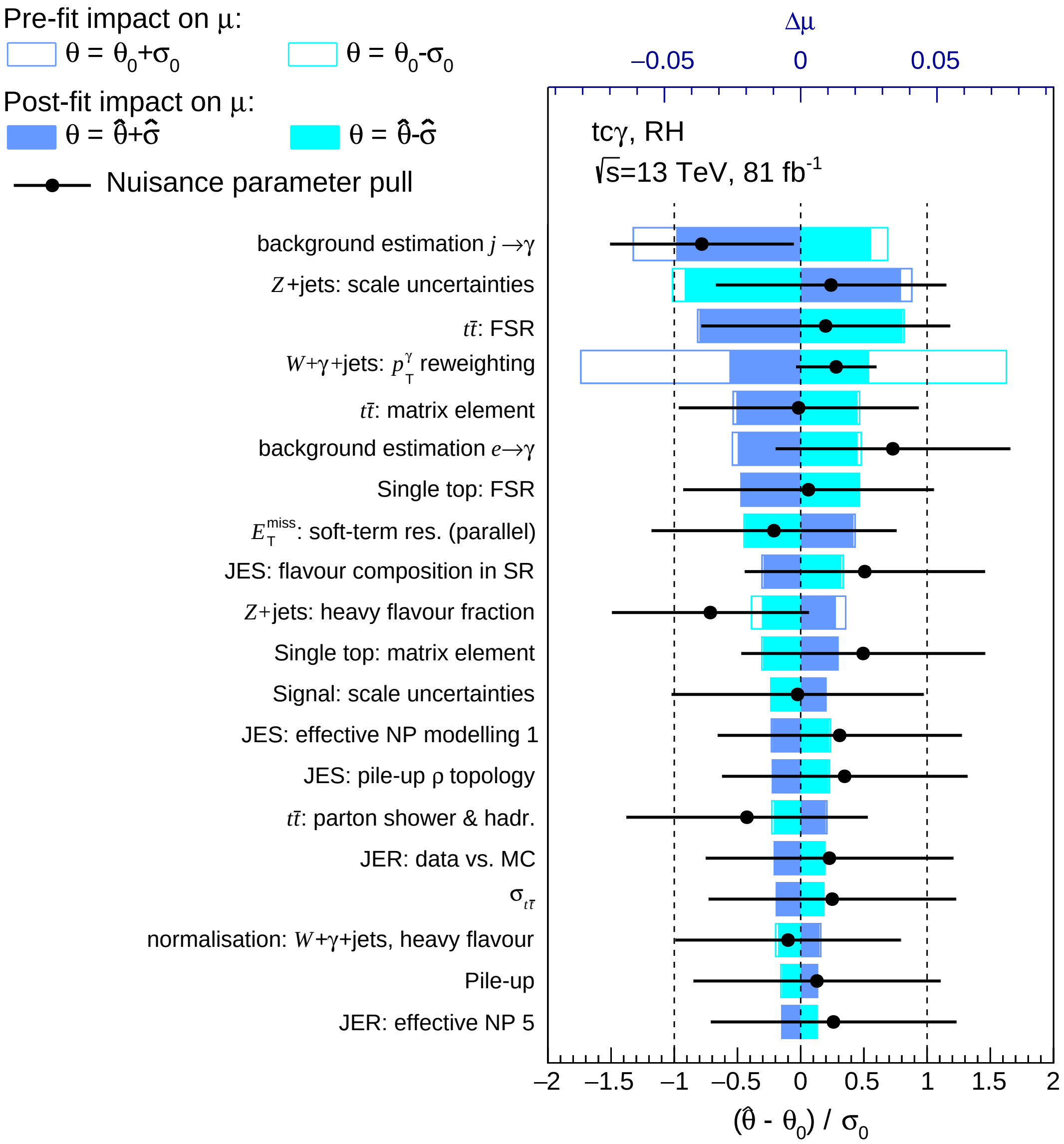

Figure 64: Ranking of the NPs with the largest impact on the signal strength, μ, for the LH $tc\gamma$ coupling. The signal strength of unity corresponds to the branching ratio $\mathcal{B}_{\text{in}}(t \to u\gamma) = 10^{-3}$. The ranking is determined in fits fixing the NP under study to its pre-fit value θ_0 and adding or subtracting its pre-fit uncertainty, σ_0, and analogously for the post-fit value, $\hat{\theta}$, and its uncertainty, $\hat{\sigma}$. The rectangles refer to the upper axis, while the black dots refer to the bottom scale.

Plots and tables for the right-handed $tc\gamma$ coupling

Table 14: Observed and expected number of events for the different background contributions in the SR, CR $W+\gamma$+jet and CR $Z+\gamma$ after the fit for the RH $tu\gamma$ coupling. The statistical uncertainties and all systematic uncertainties are included.

Photon origin	SR	CR $W+\gamma$+jet	CR $Z+\gamma$
$e \to \gamma$	4 520 ± 530	8 100 ± 1 400	237 ± 32
$j \to \gamma$	280 ± 190	3 100 ± 1 900	1 390 ± 950
$Z+\gamma$+jets	750 ± 110	13 300 ± 1 300	81 300 ± 1 900
$W+\gamma$+jets	2 020 ± 410	100 900 ± 3 200	6.3 ± 2.0
Other prompt γ	1 930 ± 450	2 090 ± 510	2 20 ± 220
Expectation	9 500 ± 240	127 500 ± 3 600	85 100 ± 1 600
Data	9 557	127 864	85 347

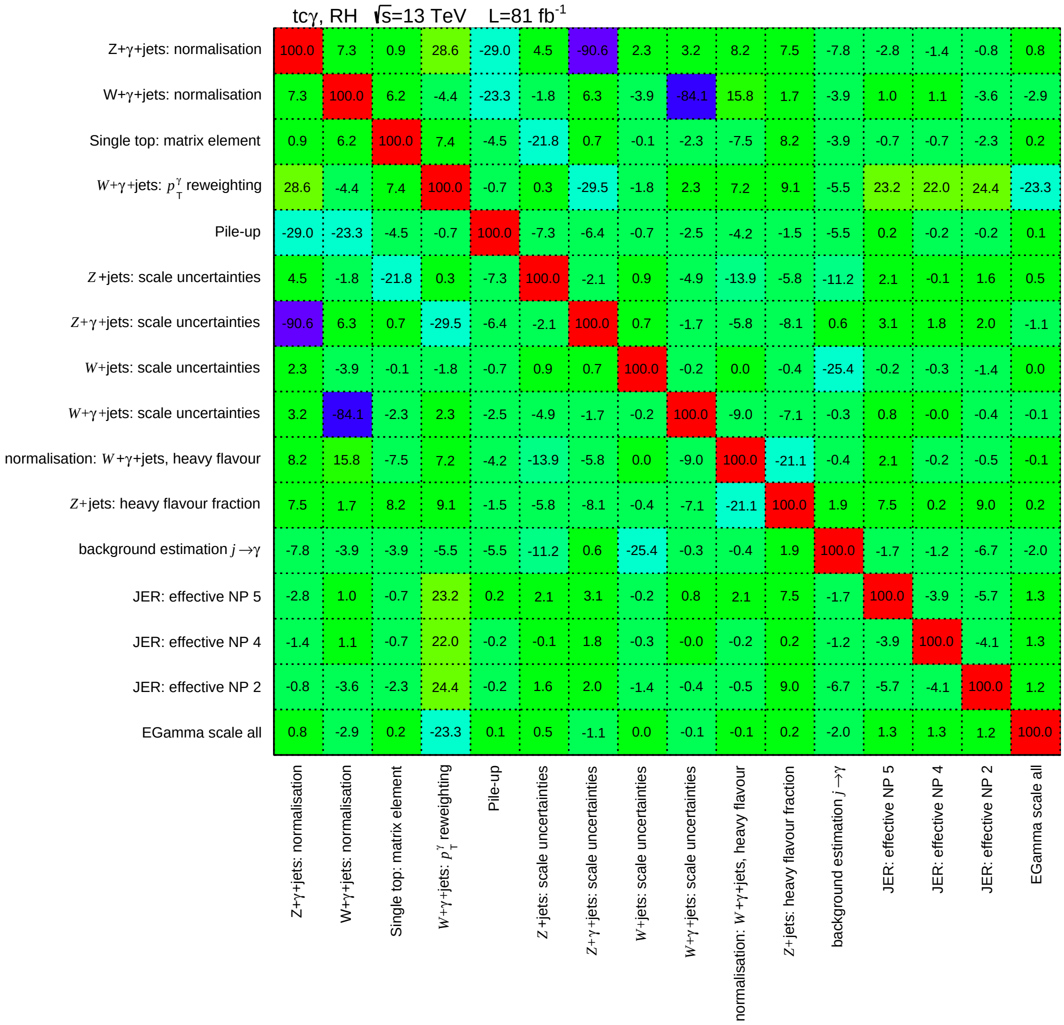

	Z+γ+jets: normalisation	W+γ+jets: normalisation	Single top: matrix element	W+γ+jets: p_{T}^{γ} reweighting	Pile-up	Z+jets: scale uncertainties	Z+γ+jets: scale uncertainties	W+jets: scale uncertainties	W+γ+jets: scale uncertainties	normalisation: W+γ+jets, heavy flavour	Z+jets: heavy flavour fraction	background estimation $j\to\gamma$	JER: effective NP 5	JER: effective NP 4	JER: effective NP 2	EGamma scale all
Z+γ+jets: normalisation	100.0	7.3	0.9	28.6	-29.0	4.5	-90.6	2.3	3.2	8.2	7.5	-7.8	-2.8	-1.4	-0.8	0.8
W+γ+jets: normalisation	7.3	100.0	6.2	-4.4	-23.3	-1.8	6.3	-3.9	-84.1	15.8	1.7	-3.9	1.0	1.1	-3.6	-2.9
Single top: matrix element	0.9	6.2	100.0	7.4	-4.5	-21.8	0.7	-0.1	-2.3	-7.5	8.2	-3.9	-0.7	-0.7	-2.3	0.2
W+γ+jets: p_{T}^{γ} reweighting	28.6	-4.4	7.4	100.0	-0.7	0.3	-29.5	-1.8	2.3	7.2	9.1	-5.5	23.2	22.0	24.4	-23.3
Pile-up	-29.0	-23.3	-4.5	-0.7	100.0	-7.3	-6.4	-0.7	-2.5	-4.2	-1.5	-5.5	0.2	-0.2	-0.2	0.1
Z+jets: scale uncertainties	4.5	-1.8	-21.8	0.3	-7.3	100.0	-2.1	0.9	-4.9	-13.9	-5.8	-11.2	2.1	-0.1	1.6	0.5
Z+γ+jets: scale uncertainties	-90.6	6.3	0.7	-29.5	-6.4	-2.1	100.0	0.7	-1.7	-5.8	-8.1	0.6	3.1	1.8	2.0	-1.1
W+jets: scale uncertainties	2.3	-3.9	-0.1	-1.8	-0.7	0.9	0.7	100.0	-0.2	0.0	-0.4	-25.4	-0.2	-0.3	-1.4	0.0
W+γ+jets: scale uncertainties	3.2	-84.1	-2.3	2.3	-2.5	-4.9	-1.7	-0.2	100.0	-9.0	-7.1	-0.3	0.8	-0.0	-0.4	-0.1
normalisation: W+γ+jets, heavy flavour	8.2	15.8	-7.5	7.2	-4.2	-13.9	-5.8	0.0	-9.0	100.0	-21.1	-0.4	2.1	-0.2	-0.5	-0.1
Z+jets: heavy flavour fraction	7.5	1.7	8.2	9.1	-1.5	-5.8	-8.1	-0.4	-7.1	-21.1	100.0	1.9	7.5	0.2	9.0	0.2
background estimation $j\to\gamma$	-7.8	-3.9	-3.9	-5.5	-5.5	-11.2	0.6	-25.4	-0.3	-0.4	1.9	100.0	-1.7	-1.2	-6.7	-2.0
JER: effective NP 5	-2.8	1.0	-0.7	23.2	0.2	2.1	3.1	-0.2	0.8	2.1	7.5	-1.7	100.0	-3.9	-5.7	1.3
JER: effective NP 4	-1.4	1.1	-0.7	22.0	-0.2	-0.1	1.8	-0.3	-0.0	-0.2	0.2	-1.2	-3.9	100.0	-4.1	1.3
JER: effective NP 2	-0.8	-3.6	-2.3	24.4	-0.2	1.6	2.0	-1.4	-0.4	-0.5	9.0	-6.7	-5.7	-4.1	100.0	1.2
EGamma scale all	0.8	-2.9	0.2	-23.3	0.1	0.5	-1.1	0.0	-0.1	-0.1	0.2	-2.0	1.3	1.3	1.2	100.0

Figure 65: Visualisation of the correlation coefficients between the NPs of systematic nature for the RH $tc\gamma$ coupling. Only uncertainties with the absolute value of at least one coefficient above 0.2 are drawn.

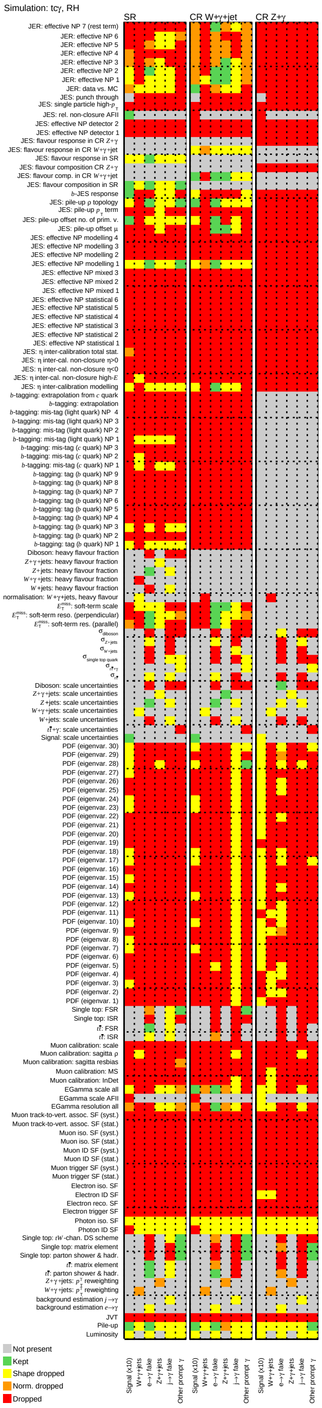

Figure 66: Illustration of the treatment of every systematic NP considered in the fit for the RH $tc\gamma$ coupling in each region for each signal and background categories.

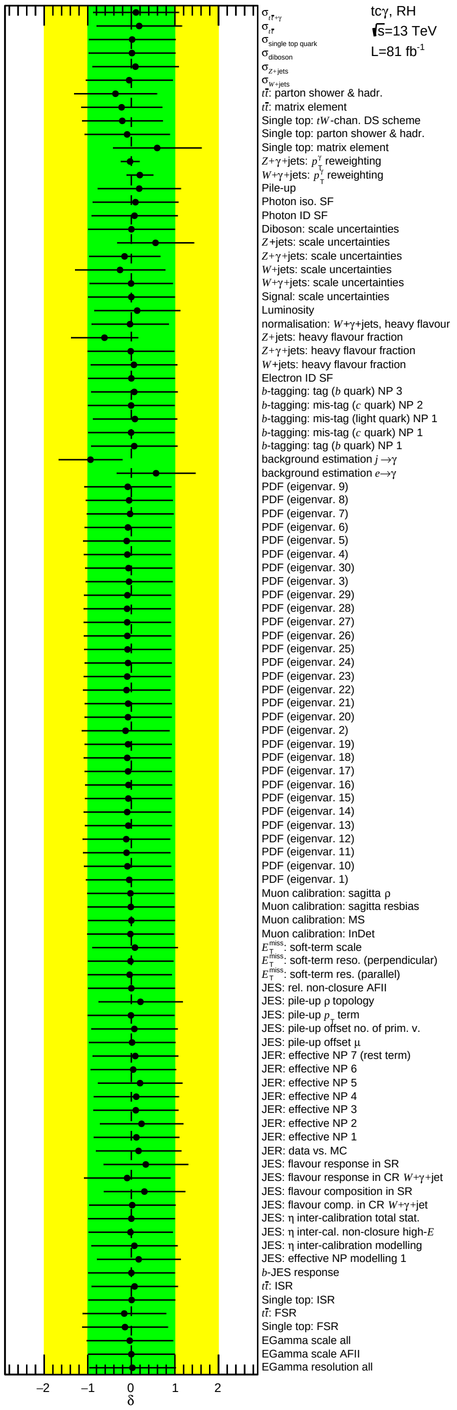

Figure 67: Pull values, δ, for the systematic NPs considered and determined in the fit for the RH $tc\gamma$ coupling.

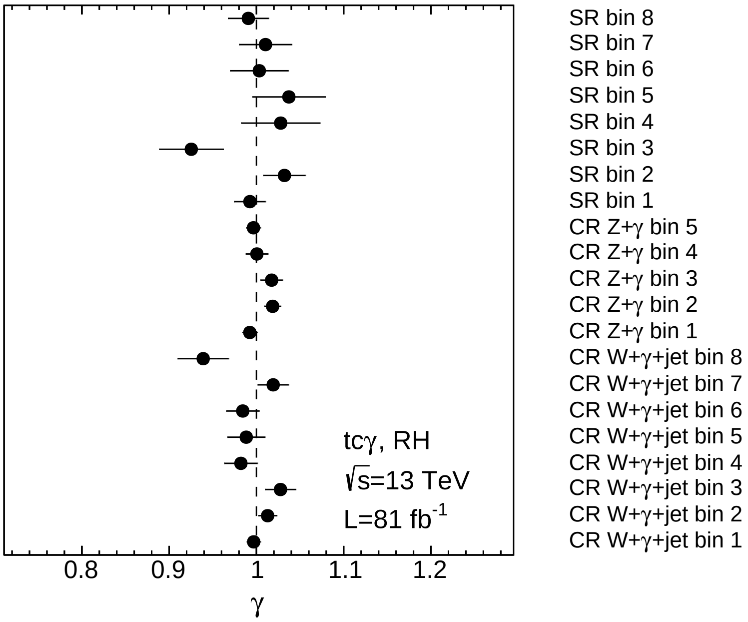

Figure 68: Normalisation factors γ for the different regions and bins determined in the fit for the RH $tc\gamma$ coupling.

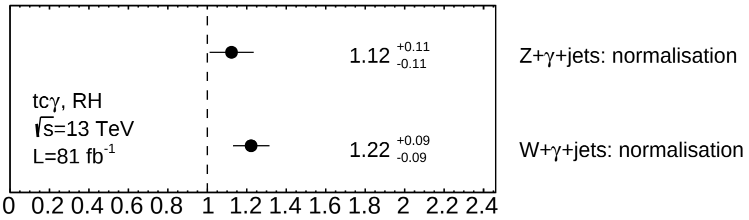

Figure 69: Normalisation factors for the prompt photon contributions of the W+γ+jets and Z+γ+jets processes determined in the fit for the RH $tc\gamma$ coupling.

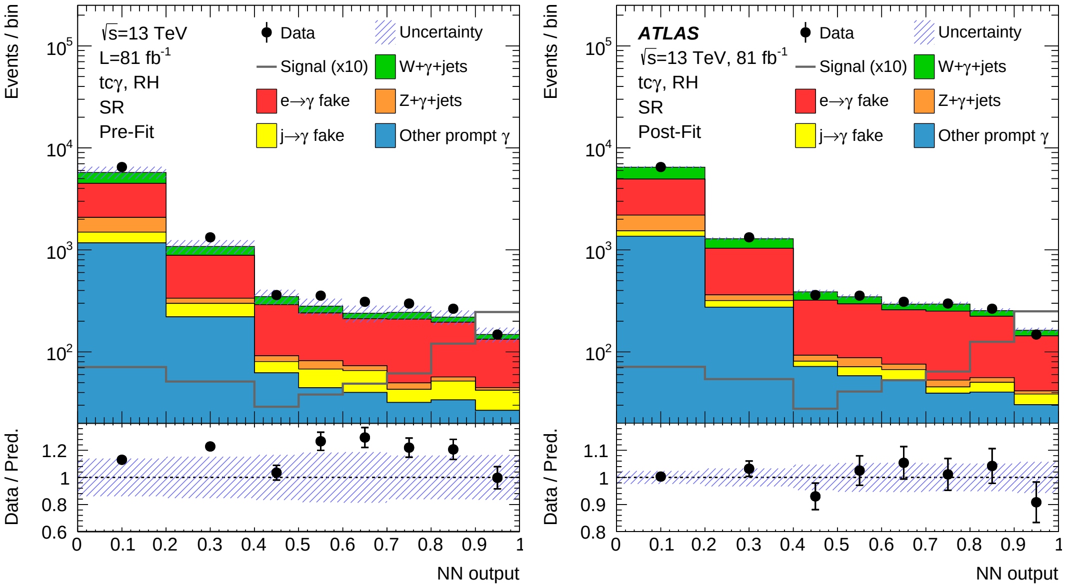

(a) Pre-fit distribution in the SR **(b)** Post-fit distribution in the SR

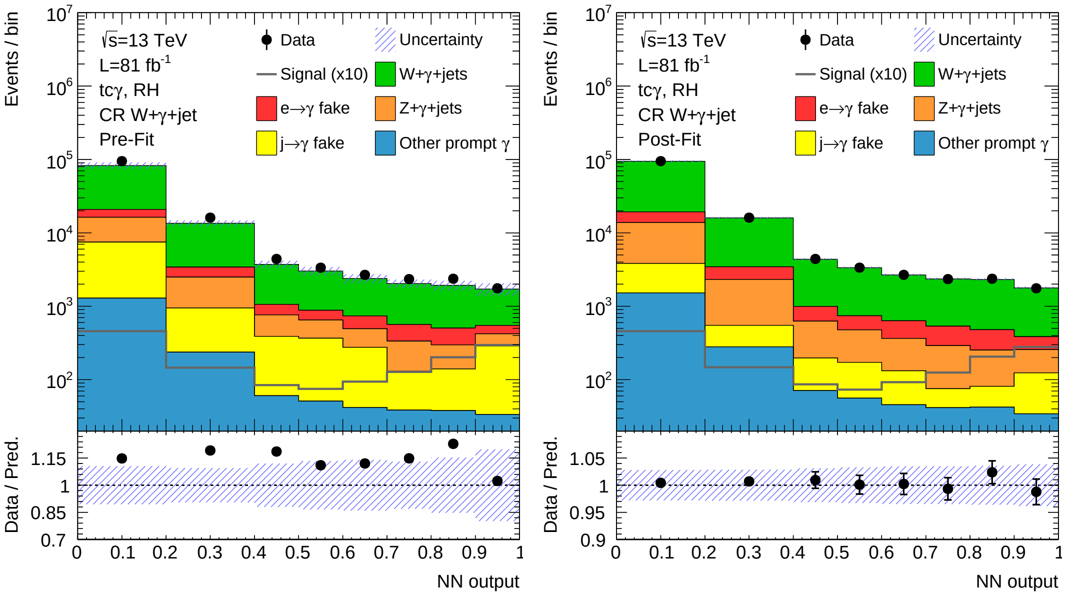

(c) Pre-fit distribution in the CR W+γ+jet **(d)** Post-fit distribution in the CR W+γ+jet

Figure 70: Pre- and post-fit distributions of the NN output in the SR (a,b) and CR W+γ+jet (c,d) for the RH $tc\gamma$ coupling. All NPs are included. The signal shape is overlaid scaled to the observed limit multiplied by ten. The post-fit plot for the SR is published in the auxiliary material of Ref. [11]. It is also shown in Figure 45c and here to enable for a direct comparison to the pre-fit plot.

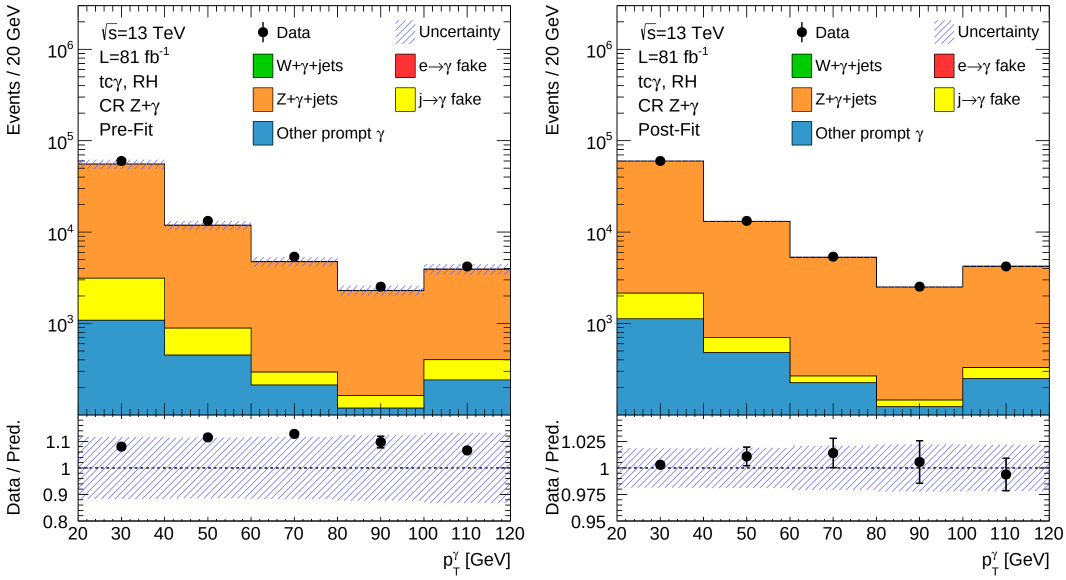

(a) Pre-fit distribution in the CR $Z+\gamma$

(b) Post-fit distribution in the CR $Z+\gamma$

Figure 71: Pre- (a) and post-fit distribution (b) of the photon p_{T} spectrum in the CR $Z+\gamma$ for the RH $tc\gamma$ coupling. All uncertainties are included. Since the signal contribution is negligible in this region, its shape is not overlaid.

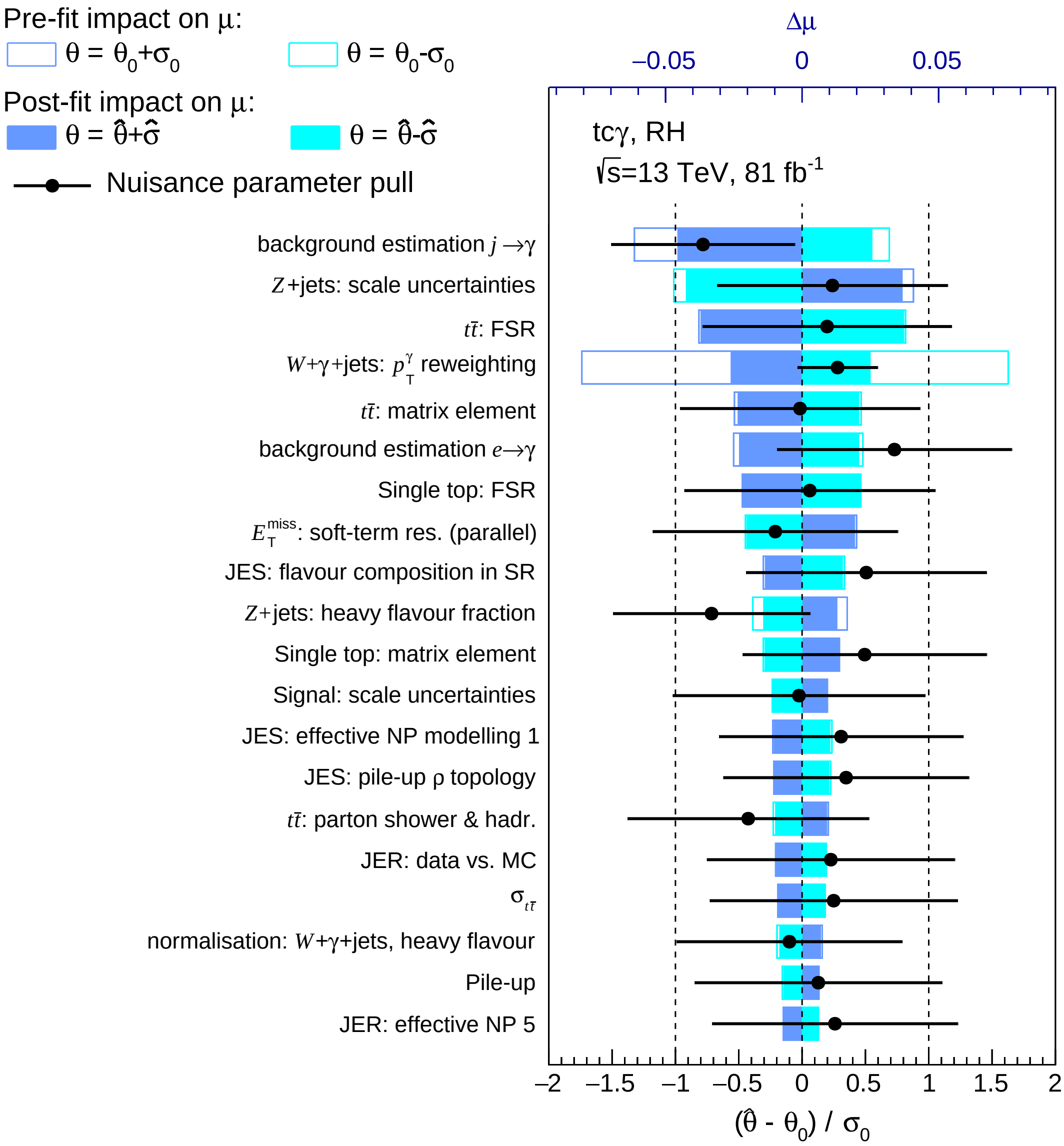

Figure 72: RRanking of the NPs with the largest impact on the signal strength, μ, for the RH $tc\gamma$ coupling. The signal strength of unity corresponds to the branching ratio $\mathcal{B}_{\text{in}}(t \to u\gamma) = 10^{-3}$. The ranking is determined in fits fixing the NP under study to its pre-fit value θ_0 and adding or subtracting its pre-fit uncertainty, σ_0, and analogously for the post-fit value, $\hat{\theta}$, and its uncertainty, $\hat{\sigma}$. The rectangles refer to the upper axis, while the black dots refer to the bottom scale.

C Additional plots for the validation of the statistical analysis

In this appendix, additional distributions for the validation of the fit in the statistical analysis for the LH $tu\gamma$ coupling are shown. These distributions depict the input variables of the deep NN in the SR at post-fit level; in Figure 47, other NN input variables are shown. A good agreement between data and expectation is observed in all of these distributions. No hint for any bias is found.

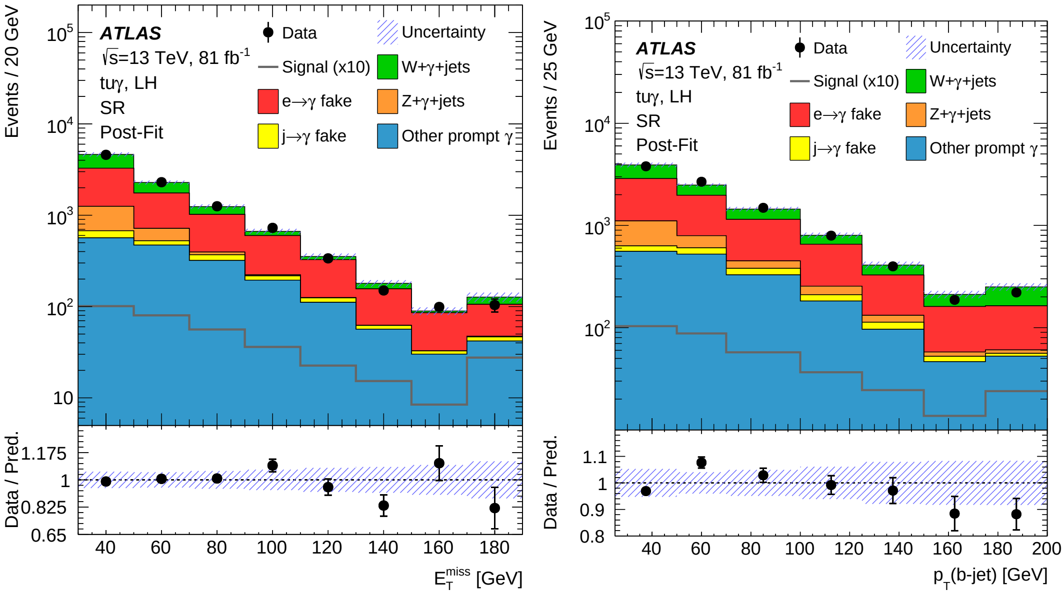

(a) $E_{\mathrm{T}}^{\mathrm{miss}}$

(b) b-jet p_{T}

Figure 73: Post-fit distributions of the $E_{\mathrm{T}}^{\mathrm{miss}}$ (a) and b-jet p_{T} (b) in the SR. All uncertainties are included. The signal shape is overlaid scaled to the observed limit. The plots are published in the auxiliary material of Ref. [11].

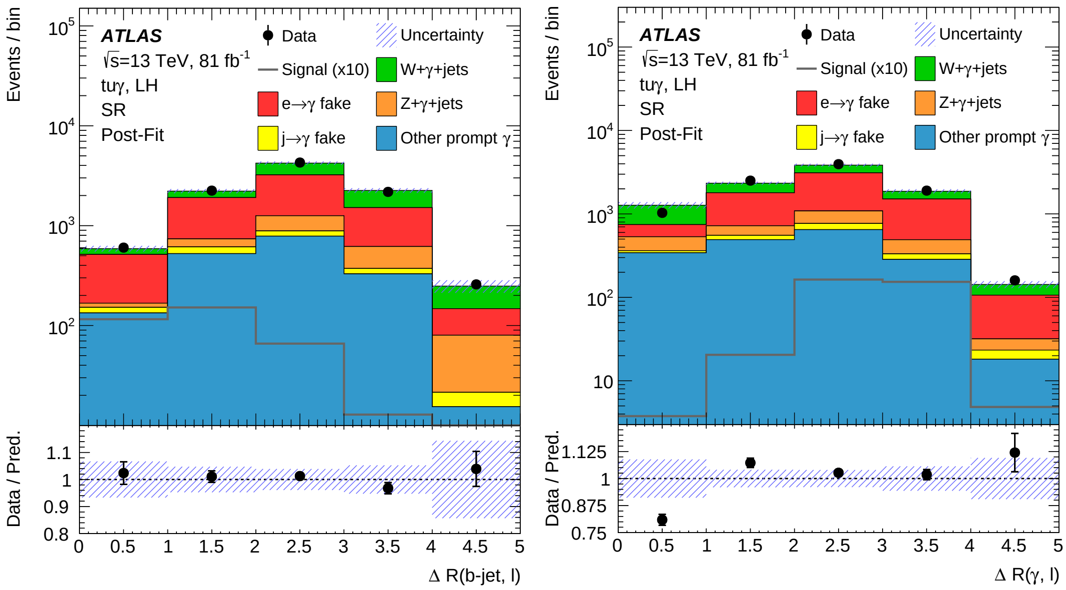

(a) $\Delta R(b\text{-jet}, \ell)$ **(b)** $\Delta R(\gamma, \ell)$

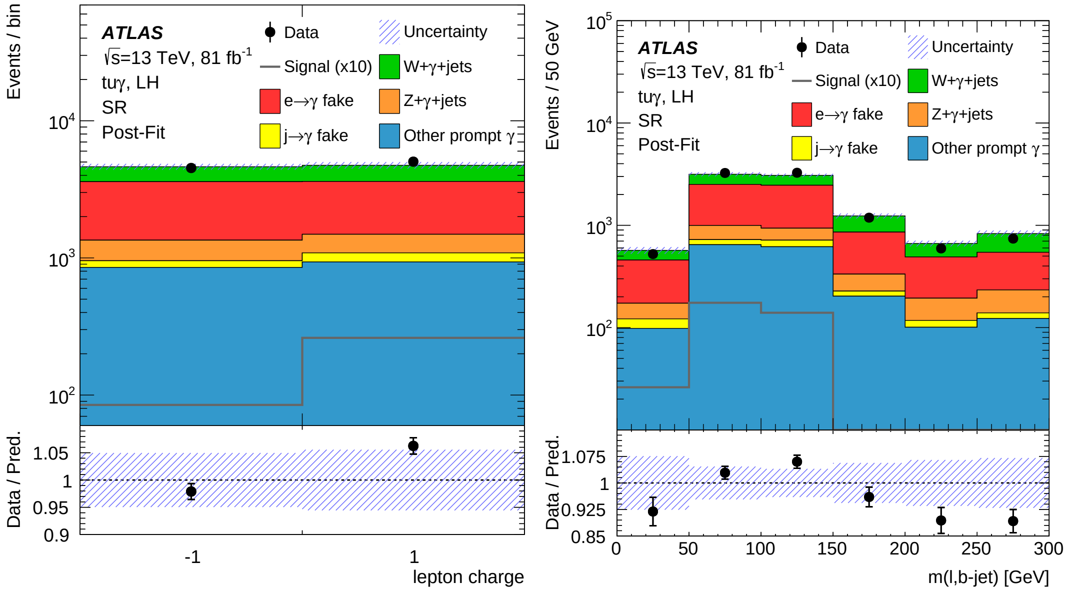

(c) Lepton charge **(d)** $m(\ell, b\text{-jet})$

Figure 74: Post-fit distributions of the distance ΔR between the b-tagged jet and charged lepton (a), the distance ΔR between the photon and charged lepton (b), the lepton charge (c) and the invariant mass of the lepton-b-jet system $m(\ell, b\text{-jet})$ (d) in the SR. All uncertainties are included. The signal shape is overlaid scaled to the observed limit. The plots are published in the auxiliary material of Ref. [11].

Bibliography

[1] ATLAS Collaboration, *Top Quark FCNC Summary Plots*, ATL-PHYS-PUB-2019-038, 2019, URL: `https://cds.cern.ch/record/2691201`.

[2] J. A. Aguilar-Saavedra, *Top flavor-changing neutral interactions: theoretical expectations and experimental detection*, Acta Phys. Polon. B **35** (2004) 2695, arXiv: `hep-ph/0409342 [hep-ph]`.

[3] D. Atwood, L. Reina, A. Soni, *Phenomenology of two Higgs doublet models with flavor-changing neutral currents*, Phys. Rev. D **55** (1997) 3156, arXiv: `hep-ph/9609279 [hep-ph]`.

[4] M. E. Luke, M. J. Savage, *Flavor changing neutral currents, weak-scale scalars and rare top decays*, Phys. Lett. B **307** (1993) 387, arXiv: `hep-ph/9303249 [hep-ph]`.

[5] S. B. Latonda, *Flavor changing neutral decay effects in models with two Higgs boson doublets: Applications to LHC Physics*, PhD thesis, Universitat Autònoma de Barcelona, 2006, arXiv: `hep-ph/0606138 [hep-ph]`.

[6] J. J. Cao *et al.*, *Supersymmetry-induced flavor-changing neutral current top-quark processes at the CERN Large Hadron Collider*, Phys. Rev. D **75** (2007) 075021, arXiv: `hep-ph/0702264 [hep-ph]`.

[7] J. M. Yang, B.-L. Young, X. Zhang, *Flavor-changing top quark decays in R-parity-violating supersymmetric models*, Phys. Rev. D **58** (1998) 055001, arXiv: `hep-ph/9705341 [hep-ph]`.

[8] G. Eilam *et al.*, *Top quark rare decay $t \to ch$ in R-parity-violating SUSY*, Phys. Lett. B **510** (2001) 227, arXiv: `hep-ph/0102037 [hep-ph]`.

[9] K. Agashe, G. Perez, A. Soni, *Collider signals of top quark flavor violation from a warped extra dimension*, Phys. Rev. D **75** (2007) 015002, arXiv: `hep-ph/0606293 [hep-ph]`.

[10] K. Agashe, R. Contino, *Composite Higgs-mediated flavor-changing neutral current*, Phys. Rev. D **80** (2009) 075016, arXiv: `0906.1542 [hep-ph]`.

[11] ATLAS Collaboration, *Search for flavour-changing neutral currents in processes with one top quark and a photon using 81 fb^{-1} of pp collisions at* $\sqrt{s} = 13$ *TeV with the ATLAS experiment*, Phys. Lett. B **800** (2020) 135082, arXiv: `1908.08461 [hep-ex]`.

[12] M. Barros *et al.*, *Study of interference effects in the search for flavour-changing neutral current interactions involving the top quark and a photon or a Z boson at the LHC*, 2019, arXiv: `1909.08443 [hep-ph]`.

[13] CMS Collaboration, *Search for anomalous single top quark production in association with a photon in pp collisions at* $\sqrt{s} = 8$ *TeV*, JHEP **04** (2016) 035, arXiv: `1511.03951 [hep-ex]`.

[14] S. L. Glashow, *Partial-symmetries of weak interactions*, Nucl. Phys. **22** (1961) 579.

[15] S. Weinberg, *A Model of Leptons*, Phys. Rev. Lett. **19** (1967) 1264.

[16] A. Salam, *Weak and electromagnetic interactions*, Conf. Proc. C **680519** (1968) 367.

[17] P. W. Higgs, *Broken symmetries and the masses of gauge bosons*, Phys. Rev. Lett. **13** (1964) 508.

[18] P. W. Higgs, *Broken symmetries, massless particles and gauge fields*, Phys. Lett. **12** (1964) 132.

[19] F. Englert, R. Brout, *Broken symmetry and the mass of gauge vector mesons*, Phys. Rev. Lett. **13** (1964) 321.

[20] Belle Collaboration, *Observation of a narrow charmonium-like state in exclusive* $B^{\pm} \to K^{\pm}\pi^{+}\pi^{-}J/\psi$ *decays*, Phys. Rev. Lett. **91** (2003) 262001, arXiv: `hep-ex/0309032 [hep-ex]`.

[21] LHCb Collaboration, *Observation of* $J/\psi p$ *resonances consistent with pentaquark states in* $\Lambda_b^0 \to J/\psi K^{-}p$ *decays*, Phys. Rev. Lett. **115** (2015), arXiv: `1507.03414 [hep-ex]`.

[22] M. Tanabashi *et al.* (Particle Data Group), *Review of Particle Physics*, Phys. Rev. D **98** (2018) 030001.

[23] N. Cabibbo, *Unitary Symmetry and Leptonic Decays*, Phys. Rev. Lett. **10** (1963) 531.

[24] M. Kobayashi, T. Maskawa, *CP-Violation in the Renormalizable Theory of Weak Interaction*, Prog. Theor. Phys. **49** (1973) 652.

[25] CDF Collaboration, *Observation of top quark production in $\bar{p}p$ collisions*, Phys. Rev. Lett. **74** (1995) 2626, arXiv: `hep-ex/9503002 [hep-ex]`.

[26] DØ Collaboration, *Observation of the Top Quark*, Phys. Rev. Lett. **74** (1995) 2632, arXiv: `hep-ex/9503003 [hep-ex]`.

[27] J. Goldstone, A. Salam, S. Weinberg, *Broken Symmetries*, Phys. Rev. **127** (1962) 965.

[28] ATLAS Collaboration, *Observation of a new particle in the search for the Standard Model Higgs boson with the ATLAS detector at the LHC*, Phys. Lett. B **716** (2012), arXiv: `1207.7214 [hep-ex]`.

[29] CMS Collaboration, *Observation of a new boson at a mass of 125 GeV with the CMS experiment at the LHC*, Phys. Lett. B **716** (2012), arXiv: `1207.7235 [hep-ex]`.

[30] Super-Kamiokande Collaboration, *Evidence for Oscillation of Atmospheric Neutrinos*, Phys. Rev. Lett. **81** (1998) 1562, arXiv: `hep-ex/9807003 [hep-ex]`.

[31] SNO Collaboration, *Measurement of the Rate of $\nu_e + d \rightarrow p + p + e^-$ Interactions Produced by ^8B Solar Neutrinos at the Sudbury Neutrino Observatory*, Phys. Rev. Lett. **87** (2001) 071301, arXiv: `nucl-ex/0106015 [nucl-ex]`.

[32] SNO Collaboration, *Direct Evidence for Neutrino Flavor Transformation from Neutral Current Interactions in the Sudbury Neutrino Observatory*, Phys. Rev. Lett. **89** (2002) 011301, arXiv: `nucl-ex/0204008 [nucl-ex]`.

[33] P. Schmüser, *The electron-proton colliding beam facility HERA*, Nucl. Inst. Meth. **A 235** (1985) 201.

[34] G. Jackson, *The Fermilab recycler ring technical design report. Revision 1.2*, FERMILAB-TM-1991, 1996, DOI: 10.2172/16029.

[35] LEP Collaboration, *LEP design report*, 1984, CERN-LEP-84-01, URL: `https://cds.cern.ch/record/102083`.

[36] ZEUS Collaboration, *Search for single-top production in ep collisions at HERA*, Phys. Lett. B **708** (2012) 27, arXiv: `1111.3901 [hep-ex]`.

[37] H1 Collaboration, *Search for single top quark production at HERA*, Phys. Lett. B **678** (2009) 450, arXiv: `0904.3876 [hep-ex]`.

[38] A. A. Ashimova, S. R. Slabospitsky, *The constraint on FCNC Coupling of the top quark with a gluon from ep-collisions*, Phys. Lett. B **668** (2008) 282, arXiv: `hep-ph/0604119 [hep-ph]`.

[39] CDF Collaboration, *Search for Flavor-Changing Neutral Current Decays of the Top Quark in $p\bar{p}$ Collisions at $\sqrt{s} = 1.8$ TeV*, Phys. Rev. Lett. **80** (1998) 2525.

[40] CDF Collaboration, *Search for the Flavor-Changing Neutral Current Decay $t \to Zq$ in $p\bar{p}$ Collisions at $\sqrt{s} = 1.96$ TeV*, Phys. Rev. Lett. **101** (2008) 192002, arXiv: `0805.2109 [hep-ex]`.

[41] CDF Collaboration, *Search for Top-Quark Production via Flavor-Changing Neutral Currents in W+1 Jet Events at CDF*, Phys. Rev. Lett. **102** (2009) 151801, arXiv: `0812.3400 [hep-ex]`.

[42] DØ Collaboration, *Search for flavor changing neutral currents in decays of top quarks*, Phys. Lett. B **701** (2011) 313, arXiv: `1103.4574 [hep-ex]`.

[43] DØ Collaboration, *Search for flavor changing neutral currents via quark-gluon couplings in single top quark production using 2.3 fb^{-1} of $p\bar{p}$ collisions*, Phys. Lett. B **693** (2010) 81, arXiv: `1006.3575 [hep-ex]`.

[44] ALEPH Collaboration, *Search for single top production in e^+e^- collisions at $\sqrt{s}$ up to 209 GeV*, Phys. Lett. B **543** (2002) 173, arXiv: `hep-ex/0206070 [hep-ex]`.

[45] DELPHI Collaboration, *Search for single top production via FCNC at LEP at $\sqrt{s} = 189$–208 GeV*, Phys. Lett. B **590** (2004) 21, arXiv: `hep-ex/0404014 [hep-ex]`.

[46] OPAL Collaboration, *Search for single top quark production at LEP2*, Phys. Lett. B **521** (2001) 181, arXiv: `hep-ex/0110009 [hep-ex]`.

[47] L3 Collaboration, *Search for single top production at LEP*, Phys. Lett. B **549** (2002) 290, arXiv: `hep-ex/0210041 [hep-ex]`.

[48] DELPHI Collaboration, ALEPH Collaboration, L3 Collaboration, OPAL Collaboration, and LEP EXOTICA Working Group, *Search for single top production via flavour changing neutral currents: preliminary combined results of the LEP experiments*, 2001, URL: `https://cds.cern.ch/record/1006392`.

[49] CMS Collaboration, *Search for top quark decays via Higgs-boson-mediated flavor-changing neutral currents in pp collisions at* $\sqrt{s} = 8$ *TeV*, JHEP **02** (2017) 079, arXiv: `1610.04857 [hep-ex]`.

[50] CMS Collaboration, *Search for the flavor-changing neutral current interactions of the top quark and the Higgs boson which decays into a pair of b quarks at* $\sqrt{s} = 13$ *TeV*, JHEP **06** (2018) 102, arXiv: `1712.02399 [hep-ex]`.

[51] CMS Collaboration, *Search for anomalous* Wtb *couplings and flavour-changing neutral currents in t-channel single top quark production in pp collisions at* $\sqrt{s} = 7$ *and 8 TeV*, JHEP **02** (2017) 028, arXiv: `1610.03545 [hep-ex]`.

[52] CMS Collaboration, *Search for associated production of a Z boson with a single top quark and for tZ flavour-changing interactions in pp collisions at* $\sqrt{s} = 8$ *TeV*, JHEP **07** (2017) 003, arXiv: `1702.01404 [hep-ex]`.

[53] CMS Collaboration, *Search for flavour changing neutral currents in top quark production and decays with three-lepton final state using the data collected at* $\sqrt{s} = 13$ *TeV*, CMS-PAS-TOP-17-017, 2017, URL: `https://cds.cern.ch/record/2292045`.

[54] ATLAS Collaboration, *Search for flavour-changing neutral current top-quark decays* $t \to qZ$ *in proton-proton collisions at* $\sqrt{s} = 13$ *TeV with the ATLAS detector*, JHEP **07** (2018) 176, arXiv: `1803.09923 [hep-ex]`.

[55] ATLAS Collaboration, *Search for top-quark decays* $t \to Hq$ *with 36* fb^{-1} *of pp collision data at* $\sqrt{s} = 13$ *TeV with the ATLAS detector*, JHEP **05** (2019) 123, arXiv: `1812.11568 [hep-ex]`.

[56] ATLAS Collaboration, *Search for single top-quark production via flavour changing neutral currents at 8 TeV with the ATLAS detector*, Eur. Phys. J. C **76** (2016) 55, arXiv: `1509.00294 [hep-ex]`.

[57] S. L. Glashow, J. Iliopoulos, L. Maiani, *Weak Interactions with Lepton-Hadron Symmetry*, Phys. Rev. D **2** (1970) 1285.

[58] T. D. Lee, *A Theory of Spontaneous* T *Violation*, Phys. Rev. D **8** (1973) 1226.

[59] T. D. Lee, *CP Nonconservation and Spontaneous Symmetry Breaking*, Phys. Rept. **9** (1974) 143.

[60] P. Fayet, *A gauge theory of weak and electromagnetic interactions with spontaneous parity breaking*, Nucl. Phys. B **78** (1974) 14.

[61] R. A. Flores, M. Sher, *Higgs Masses in the Standard, Multi-Higgs and Supersymmetric Models*, Annals Phys. **148** (1983) 95.

[62] M. Luke, M. J. Savage, *Flavour changing neutral currents, weak-scale scalars and rare top decays*, Phys. Lett. B **307** (1993) 387.

[63] S. Dimopoulos, H. Georgi, *Softly broken supersymmetry and SU(5)*, Nucl. Phys. B **193** (1981) 150.

[64] L. Randall, R. Sundrum, *Large Mass Hierarchy from a Small Extra Dimension*, Phys. Rev. Lett. **83** (1999) 3370, arXiv: `hep-ph/9905221 [hep-ph]`.

[65] L. Randall, R. Sundrum, *An Alternative to Compactification*, Phys. Rev. Lett. **83** (1999) 4690, arXiv: `hep-th/9906064 [hep-th]`.

[66] T. Kaluza, *Zum Unitätsproblem der Physik*, SBPAW Berlin (Math. Phys.) **37** (1921) 966, arXiv: `1803.08616`.

[67] O. Klein, *Quantentheorie und fünfdimensionale Relativitätstheorie*, Z. Phys. **37** (1926) 895.

[68] W. Buchmüller, D. Wyler, *Effective Lagrangian Analysis of New Interactions and Flavor Conservation*, Nucl. Phys. B **268** (1986) 621.

[69] B. Grzadkowski *et al.*, *Dimension-Six Terms in the Standard Model Lagrangian*, JHEP **10** (2010) 085, arXiv: `1008.4884 [hep-ph]`.

[70] E. Mobs, *The CERN accelerator complex - August 2018. Complexe des accélérateurs du CERN - Août 2018*, 2018, URL: `https://cds.cern.ch/record/2636343`.

[71] L. Evans, P. Bryant, *LHC Machine*, JINST **3** (2008) S08001.

[72] ALICE Collaboration, *The ALICE experiment at the CERN LHC*, JINST **3** (2008) S08002.

[73] ATLAS Collaboration, *The ATLAS Experiment at the CERN Large Hadron Collider*, JINST **3** (2008) S08003.

[74] CMS Collaboration, *The CMS Experiment at the CERN LHC*, JINST **3** (2008) S08004.

[75] LHCb Collaboration, *The LHCb Detector at the LHC*, JINST **3** (2008) S08005.

[76] J. Pequenao, *Computer generated image of the whole ATLAS detector*, CERN-GE-0803012, Web page, 2008, URL: `https://cds.cern.ch/record/1095924`.

[77] ATLAS Collaboration, *ATLAS Inner Detector: Technical Design Report. Volume 1*, CERN-LHCC-97-16, ATLAS-TDR-4, 1997, URL: `https://cds.cern.ch/record/331063`.

[78] ATLAS Collaboration, *ATLAS Inner Detector: Technical Design Report. Volume 2*, CERN-LHCC-97-17, ATLAS-TDR-5, 1997, URL: `https://cds.cern.ch/record/331064`.

[79] ATLAS Collaboration, *ATLAS Magnet System: Technical Design Report*, CERN-LHCC-97-18, ATLAS-TDR-6, 1997, URL: `https://cds.cern.ch/record/338080`.

[80] ATLAS Collaboration, *ATLAS Central Solenoid: Technical Design Report*, CERN-LHCC-97-021, ATLAS-TDR-9, 1997, URL: `https://cds.cern.ch/record/331067`.

[81] ATLAS Collaboration, *The ATLAS central solenoid*, Nucl. Instrum. Meth. A **584** (2008).

[82] ATLAS Collaboration, *ATLAS Insertable B-Layer: Technical Design Report*, CERN-LHCC-2010-013, ATLAS-TDR-19, 2010, URL: `https://cds.cern.ch/record/1291633`.

[83] ATLAS Collaboration, *ATLAS Insertable B-Layer: Technical Design Report Addendum*, CERN-LHCC-2012-009, ATLAS-TDR-19-ADD-1, Addendum to CERN-LHCC-2010-013, 2012, URL: `https://cds.cern.ch/record/1451888`.

[84] ATLAS Collaboration, *Technical Design Report for the ATLAS Inner Tracker Pixel Detector*, CERN-LHCC-2017-021, ATLAS-TDR-030, 2017, URL: `https://cds.cern.ch/record/2285585`.

[85] ATLAS Collaboration, *ATLAS pixel detector electronics and sensors*, JINST **3** (2008) P07007.

[86] ATLAS TRT Collaboration, *The ATLAS Transition Radiation Tracker (TRT) proportional drift tube: design and performance*, JINST **3** (2008) P02013.

[87] ATLAS Collaboration, *ATLAS Liquid Argon Calorimeter: Technical Design Report*, CERN-LHCC-96-041, ATLAS-TDR-2, 1996, URL: `https://cds.cern.ch/record/331061`.

[88] ATLAS Collaboration, *ATLAS Tile Calorimeter: Technical Design Report*, CERN-LHCC-96-042, ATLAS-TDR-3, 1996, URL: `https://cds.cern.ch/record/331062`.

[89] ATLAS Collaboration, *ATLAS Muon Spectrometer: Technical Design Report*, CERN-LHCC-97-022, ATLAS-TDR-10, 1997, URL: `https://cds.cern.ch/record/331068`.

[90] ATLAS Collaboration, *ATLAS Barrel Toroid: Technical design report*, CERN-LHCC-97-19, ATLAS-TDR-7, 1997, URL: `https://cds.cern.ch/record/331065`.

[91] ATLAS Collaboration, *ATLAS End-Cap Toroids: Technical design report*, CERN-LHCC-97-20, ATLAS-TDR-8, 1997, URL: `https://cds.cern.ch/record/331066`.

[92] V. Cindro *et al.*, *The ATLAS Beam Conditions Monitor*, JINST **3** (2008) P02004.

[93] ATLAS Collaboration, *ATLAS Forward Detectors for Measurement of Elastic Scattering and Luminosity*, CERN-LHCC-2008-004, ATLAS-TDR-18, 2008, URL: `http://cds.cern.ch/record/1095847`.

[94] G. Avoni *et al.*, *The new LUCID-2 detector for luminosity measurement and monitoring in ATLAS*, JINST **13** (2018) P07017.

[95] ATLAS Collaboration, *ATLAS High-Level Trigger, Data Acquisition and Controls: Technical Design Report*, CERN-LHCC-2003-022, ATLAS-TDR-16, 2003, URL: `https://cds.cern.ch/record/616089`.

[96] ATLAS Collaboration, *Technical Design Report for the Phase-I Upgrade of the ATLAS TDAQ System*, CERN-LHCC-2013-018, ATLAS-TDR-023, 2013, URL: `https://cds.cern.ch/record/1602235`.

[97] ATLAS Collaboration, *Performance of the ATLAS Trigger System in 2010*, Eur. Phys. J. C **72** (2012) 1849, arXiv: `1110.1530 [hep-ex]`.

[98] ATLAS Collaboration, *Luminosity determination in pp collisions at $\sqrt{s}$ = 13 TeV using the ATLAS detector at the LHC*, ATLAS-CONF-2019-021, 2019, URL: `https://cds.cern.ch/record/2677054`.

[99] S. Agostinelli *et al.*, *GEANT4—a simulation toolkit*, Nucl. Instrum. Meth. A **506** (2003) 250.

[100] ATLAS Collaboration, *The ATLAS Simulation Infrastructure*, Eur. Phys. J. C **70** (2010) 823, arXiv: `1005.4568 [physics.ins-det]`.

[101] ATLAS Collaboration, *The simulation principle and performance of the ATLAS fast calorimeter simulation FastCaloSim*, ATL-PHYS-PUB-2010-013, 2010, URL: `https://cds.cern.ch/record/1300517`.

[102] T. Sjöstrand *et al.*, *An introduction to PYTHIA 8.2*, Comput. Phys. Commun. **191** (2015) 159, arXiv: `1410.3012 [hep-ph]`.

[103] ATLAS Collaboration, *The Pythia 8 A3 tune description of ATLAS minimum bias and inelastic measurements incorporating the Donnachie-Landshoff diffractive model*, ATL-PHYS-PUB-2016-017, 2016, URL: `https://cds.cern.ch/record/2206965`.

[104] C. Degrande, *UFO - The Universal FeynRules Output*, Comput. Phys. Commun. **183** (2012) 1201, arXiv: `1108.2040 [hep-ph]`.

[105] C. Degrande, F. Maltoni, J. Wang, C. Zhang, *Automatic computations at next-to-leading order in QCD for top-quark flavor-changing neutral processes*, Phys. Rev. D **91** (2015) 034024, arXiv: `1412.5594 [hep-ph]`.

[106] G. Durieux, F. Maltoni, C. Zhang, *Global approach to top-quark flavor-changing interactions*, Phys. Rev. D **91** (2015) 074017, arXiv: `1412.7166 [hep-ph]`.

[107] J. Alwall *et al.*, *The automated computation of tree-level and next-to-leading order differential cross sections, and their matching to parton shower simulations*, JHEP **07** (2014) 79, arXiv: `1405.0301 [hep-ph]`.

[108] NNPDF Collaboration, *Parton distributions for the LHC run II*, JHEP **04** (2015) 040, arXiv: `1410.8849 [hep-ph]`.

[109] S. Frixione *et al.*, *Angular correlations of lepton pairs from vector boson and top quark decays in Monte Carlo simulations*, JHEP **04** (2007) 081, arXiv: `hep-ph/0702198 [HEP-PH]`.

[110] P. Artoisenet *et al.*, *Automatic spin-entangled decays of heavy resonances in Monte Carlo simulations*, JHEP **03** (2013) 015, arXiv: `1212.3460 [hep-ph]`.

[111] ATLAS Collaboration, *ATLAS Pythia 8 tunes to 7 TeV data*, ATL-PHYS-PUB-2014-021, 2014, URL: `https://cds.cern.ch/record/1966419`.

[112] NNPDF Collaboration, *Parton distributions with LHC data*, Nucl. Phys. B **867** (2013) 244, arXiv: `1207.1303 [hep-ph]`.

[113] D. J. Lange, *The EvtGen particle decay simulation package*, Nucl. Instrum. Meth. A **462** (2001) 152.

[114] K. Melnikov, M. Schulze, A. Scharf, *QCD corrections to top quark pair production in association with a photon at hadron colliders*, Phys. Rev. D **83** (2011) 074013, arXiv: `1102.1967 [hep-ph]`.

[115] ATLAS Collaboration, *Measurements of inclusive and differential fiducial cross-sections of $t\bar{t}\gamma$ production in leptonic final states at $\sqrt{s}$ =13 TeV in ATLAS*, Eur. Phys. J. C **79** (2019), arXiv: `1812.01697 [hep-ex]`.

[116] P. Nason, *A new method for combining NLO QCD with shower Monte Carlo algorithms*, JHEP **11** (2004) 040, arXiv: `hep-ph/0409146 [hep-ph]`.

[117] S. Frixione, P. Nason, C. Oleari, *Matching NLO QCD computations with parton shower simulations: the POWHEG method*, JHEP **11** (2007) 070, arXiv: `0709.2092 [hep-ph]`.

[118] J. M. Campbell *et al.*, *Top-pair production and decay at NLO matched with parton showers*, JHEP **04** (2015) 114, arXiv: `1412.1828 [hep-ph]`.

[119] S. Alioli *et al.*, *A general framework for implementing NLO calculations in shower Monte Carlo programs: the POWHEG BOX*, JHEP **06** (2010) 043, arXiv: `1002.2581 [hep-ph]`.

[120] S. Frixione, G. Ridolfi, P. Nason, *A positive-weight next-to-leading-order Monte Carlo for heavy flavour hadroproduction*, JHEP **0709** (2007) 126, arXiv: `0707.3088 [hep-ph]`.

[121] ATLAS Collaboration, *Improvements in $t\bar{t}$ modelling using NLO+PS Monte Carlo generators for Run 2*, ATL-PHYS-PUB-2018-009, 2018, URL: `https://cds.cern.ch/record/2630327`.

[122] R. Frederix, E. Re, P. Torrielli, *Single-top t-channel hadroproduction in the four-flavour scheme with POWHEG and aMC@NLO*, JHEP **09** (2012) 130, arXiv: `1207.5391 [hep-ph]`.

[123] S. Alioli *et al.*, *NLO single-top production matched with shower in POWHEG: s- and t-channel contributions*, JHEP **09** (2009) 111, Corrected in: *Erratum: NLO single-top production matched with shower in POWHEG: s- and t-channel contributions*, JHEP **02** (2010) 111, arXiv: `0907.4076 [hep-ph]`.

[124] E. Re, *Single-top Wt-channel production matched with parton showers using the POWHEG method*, Eur. Phys. J. C **71** (2011) 1547, arXiv: `1009.2450 [hep-ph]`.

[125] ATLAS Collaboration, *Studies on top-quark Monte Carlo modelling for Top2016*, ATL-PHYS-PUB-2016-020, 2016, URL: `https://cds.cern.ch/record/2216168`.

[126] S. Frixione *et al.*, *Single-top hadroproduction in association with a W boson*, JHEP **07** (2008) 029, arXiv: `0805.3067 [hep-ph]`.

[127] M. Czakon, A. Mitov, *Top++: A program for the calculation of the top-pair cross-section at hadron colliders*, Comput. Phys. Commun. **185** (2014) 2930, arXiv: `1112.5675 [hep-ph]`.

[128] M. Botje *et al.*, *The PDF4LHC Working Group Interim Recommendations*, 2011, arXiv: `1101.0538 [hep-ph]`.

[129] A. D. Martin *et al.*, *Uncertainties on α_s in global PDF analyses and implications for predicted hadronic cross sections*, Eur. Phys. J. C **64** (2009) 653, arXiv: `0905.3531 [hep-ph]`.

[130] J. Gao *et al.*, *CT10 next-to-next-to-leading order global analysis of QCD*, Phys. Rev. D **89** (2014) 033009, arXiv: `1302.6246 [hep-ph]`.

[131] N. Kidonakis, *Next-to-next-to-leading-order collinear and soft gluon corrections for t-channel single top quark production*, Phys. Rev. D **83** (2011) 091503, arXiv: `1103.2792 [hep-ph]`.

[132] N. Kidonakis, *Next-to-next-to-leading logarithm resummation for s-channel single top quark production*, Phys. Rev. D **81** (2010) 054028, arXiv: `1001.5034 [hep-ph]`.

[133] N. Kidonakis, *Two-loop soft anomalous dimensions for single top quark associated production with a* W^- *or* H^-, Phys. Rev. D **82** (2010) 054018, arXiv: `1005.4451 [hep-ph]`.

[134] M. Bähr *et al.*, *Herwig++ physics and manual*, Eur. Phys. J. C **58** (2008) 639, arXiv: `0803.0883 [hep-ph]`.

[135] J. Bellm *et al.*, *Herwig 7.0/Herwig++ 3.0 release note*, Eur. Phys. J. C **76** (2016) 196, arXiv: `1512.01178 [hep-ph]`.

[136] L. A. Harland-Lang*et al.*, *Parton distributions in the LHC era: MMHT 2014 PDFs*, Eur. Phys. J. C **75** (2015) 204, arXiv: `1412.3989 [hep-ph]`.

[137] T. Gleisberg *et al.*, *Event generation with SHERPA 1.1*, JHEP **02** (2009) 007, arXiv: `0811.4622 [hep-ph]`.

[138] T. Gleisberg, S. Höche, *Comix, a new matrix element generator*, JHEP **12** (2008) 039, arXiv: `0808.3674 [hep-ph]`.

[139] S. Schumann, F. Krauss, *A Parton shower algorithm based on Catani-Seymour dipole factorisation*, JHEP **03** (2008) 038, arXiv: `0709.1027 [hep-ph]`.

[140] S. Höche *et al.*, *A critical appraisal of NLO+PS matching methods*, JHEP **09** (2012) 049, arXiv: `1111.1220 [hep-ph]`.

[141] S. Höche *et al.*, *QCD matrix elements + parton showers. The NLO case*, JHEP **04** (2013) 027, arXiv: `1207.5030 [hep-ph]`.

[142] S. Catani et al., *QCD Matrix Elements + Parton Showers*, JHEP **11** (2001) 063, arXiv: `hep-ph/0109231`.

[143] S. Höche *et al.*, *QCD matrix elements and truncated showers*, JHEP **05** (2009) 053, arXiv: `0903.1219 [hep-ph]`.

[144] F. Cascioli, P. Maierhöfer, S. Pozzorini, *Scattering Amplitudes with Open Loops*, Phys. Rev. Lett. **108** (2012) 111601, arXiv: `1111.5206 [hep-ph]`.

[145] A. Denner, S. Dittmaier, L. Hofer, *Collier: A fortran-based complex one-loop library in extended regularizations*, Comput. Phys. Commun. **212** (2017) 220, arXiv: `1604.06792 [hep-ph]`.

[146] T. Cornelissen *et al.*, *Concepts, Design and Implementation of the ATLAS New Tracking (NEWT)*, ATL-SOFT-PUB-2007-007, 2007, URL: `https://cds.cern.ch/record/1020106`.

[147] T. Cornelissen *et al.*, *The new ATLAS track reconstruction (NEWT)*, J. Phys. Conf. Ser. **119** (2008) 032014.

[148] ATLAS Collaboration, *Track Reconstruction Performance of the ATLAS Inner Detector at* $\sqrt{s} = 13$ *TeV*, ATL-PHYS-PUB-2015-018, 2015, URL: `https://cds.cern.ch/record/2037683`.

[149] ATLAS Collaboration, *Performance of primary vertex reconstruction in proton–proton collisions at* $\sqrt{s} = 7$ *TeV in the ATLAS experiment*, ATLAS-CONF-2010-069, 2010, URL: `https://cds.cern.ch/record/1281344`.

[150] ATLAS Collaboration, *Vertex Reconstruction Performance of the ATLAS Detector at* $\sqrt{s} = 13$ *TeV*, ATL-PHYS-PUB-2015-026, 2015, URL: `http://cds.cern.ch/record/2037717`.

[151] S. Hageböck, E. v. Toerne, *Medical Imaging Inspired Vertex Reconstruction at LHC*, J. Phys. Conf. Ser. **396** (2012) 022021.

[152] ATLAS Collaboration, *Measurement of the photon identification efficiencies with the ATLAS detector using LHC Run 2 data collected in 2015 and 2016*, Eur. Phys. J. C **79** (2019), arXiv: `1810.05087 [hep-ex]`.

[153] ATLAS Collaboration, *Electron and photon performance measurements with the ATLAS detector using the 2015–2017 LHC proton-proton collision data*, JINST **14** (2019) P12006, arXiv: `1908.00005 [hep-ex]`.

[154] ATLAS Collaboration, *Measurement of the photon identification efficiencies with the ATLAS detector using LHC Run-1 data*, Eur. Phys. J. C **76** (2016), arXiv: `1606.01813 [hep-ex]`.

[155] W. Lampl *et al.*, *Calorimeter Clustering Algorithms: Description and Performance*, ATL-LARG-PUB-2008-002, 2008, URL: `https://cds.cern.ch/record/1099735`.

[156] ATLAS Collaboration, *Topological cell clustering in the ATLAS calorimeters and its performance in LHC Run 1*, Eur. Phys. J. C **77** (2017), arXiv: `1603.02934 [hep-ex]`.

[157] ATLAS Collaboration, *Electron and photon reconstruction and performance in ATLAS using a dynamical, topological cell clustering-based approach*, ATL-PHYS-PUB-2017-022, 2017, URL: `https://cds.cern.ch/record/2298955`.

[158] R. Frühwirth, *A Gaussian-mixture approximation of the Bethe-Heitler model of electron energy loss by bremsstrahlung*, Comp. Phys. Commun. **154** (2003) 131.

[159] ATLAS Collaboration, *Improved electron reconstruction in ATLAS using the Gaussian Sum Filter-based model for bremsstrahlung*, ATLAS-CONF-2012-047, 2012, URL: `http://cds.cern.ch/record/1449796`.

[160] ATLAS Collaboration, *Electron and photon energy calibration with the ATLAS detector using LHC Run 1 data*, Eur. Phys. J. C **74** (2014) 3071, arXiv: `1407.5063 [hep-ex]`.

[161] ATLAS Collaboration, *Electron and photon energy calibration with the ATLAS detector using 2015–2016 LHC proton-proton collision data*, JINST **14** (2019) P03017, arXiv: `1812.03848 [hep-ex]`.

[162] ATLAS Collaboration, *Electron, Photon and Muon Isolation in Run 2*, ATL-COM-PHYS-2017-290, 2017, URL: `https://cds.cern.ch/record/2256658`.

[163] ATLAS Collaboration, *Electron reconstruction and identification in the ATLAS experiment using the 2015 and 2016 LHC proton-proton collision data at $\sqrt{s}$ = 13 TeV*, Eur. Phys. J. C **79** (2019) 639, arXiv: `1902.04655 [physics.ins-det]`.

[164] ATLAS Collaboration, *Muon reconstruction performance of the ATLAS detector in proton-proton collision data at $\sqrt{s}$ =13 TeV*, Eur. Phys. J. C **76** (2016) 292, arXiv: `1603.05598 [hep-ex]`.

[165] ATLAS Collaboration, *Properties of jets and inputs to jet reconstruction and calibration with the ATLAS detector using proton–proton collisions at* $\sqrt{s}$ = 13 *TeV*, ATL-PHYS-PUB-2015-036, 2015, URL: `https://cds.cern.ch/record/2044564`.

[166] M. Cacciari, G. P. Salam, G. Soyez, *The anti-k_t jet clustering algorithm*, JHEP **04** (2008) 063, arXiv: `0802.1189 [hep-ph]`.

[167] M. Cacciari, G. P. Salam, G. Soyez, *FastJet User Manual*, Eur. Phys. J. C **72** (2012) 1896, arXiv: `1111.6097 [hep-ph]`.

[168] M. Cacciari, G. P. Salam, *Dispelling the N^3 myth for the k_t jet-finder*, Phys. Lett. B **641** (2006) 57, arXiv: `hep-ph/0512210 [hep-ph]`.

[169] ATLAS Collaboration, *Jet energy scale measurements and their systematic uncertainties in proton–proton collisions at $\sqrt{s} = 13$ TeV with the ATLAS detector*, Phys. Rev. D **96** (2017) 072002, arXiv: `1703.09665 [hep-ex]`.

[170] ATLAS Collaboration, *Performance of pile-up mitigation techniques for jets in pp collisions at $\sqrt{s} = 8$ TeV using the ATLAS detector*, Eur. Phys. J. C **76** (2016) 581, arXiv: `1510.03823 [hep-ex]`.

[171] ATLAS Collaboration, *ATLAS b-jet identification performance and efficiency measurement with $t\bar{t}$ events in pp collisions at $\sqrt{s} = 13$ TeV*, Eur. Phys. J. C **79** (2019) 970, arXiv: `1907.05120 [hep-ex]`.

[172] ATLAS Collaboration, *Optimisation and performance studies of the ATLAS b-tagging algorithms for the 2017-18 LHC run*, ATL-PHYS-PUB-2017-013, 2017, URL: `https://cds.cern.ch/record/2273281`.

[173] ATLAS Collaboration, *Secondary vertex finding for jet flavour identification with the ATLAS detector*, ATL-PHYS-PUB-2017-011, 2017, URL: `https://cds.cern.ch/record/2270366`.

[174] ATLAS Collaboration, *Topological B hadron decay reconstruction and identification of b-jets with JetFitter in the ATLAS experiment at the LHC*, ATL-PHYS-PUB-2018-025, 2018, URL: `https://cds.cern.ch/record/2645405`.

[175] ATLAS Collaboration, *Measurements of b-jet tagging efficiency with the ATLAS detector using $t\bar{t}$ events at $\sqrt{s}$=13 TeV*, JHEP **08** (2018) 089, arXiv: `1805.01845 [hep-ex]`.

[176] ATLAS Collaboration, *Measurement of b-tagging efficiency of c-jets in $t\bar{t}$ events using a likelihood approach with the ATLAS detector*, ATLAS-CONF-2018-001, 2018, URL: `https://cds.cern.ch/record/2306649`.

[177] ATLAS Collaboration, *Calibration of light-flavour b-jet mistagging rates using ATLAS proton-proton collision data at $\sqrt{s} = 13$ TeV*, ATLAS-CONF-2018-006, 2018, URL: `https://cds.cern.ch/record/2314418`.

[178] ATLAS Collaboration, *E_T^{miss} performance in the ATLAS detector using 2015-2016 LHC pp collisions*, ATLAS-CONF-2018-023, 2018, URL: `https://cds.cern.ch/record/2625233`.

[179] ATLAS Collaboration, *Performance of missing transverse momentum reconstruction with the ATLAS detector using proton-proton collisions at $\sqrt{s}$ = 13 TeV*, Eur. Phys. J. C **78** (2018) 903, arXiv: `1802.08168 [hep-ex]`.

[180] J. C. Saxon, *Discovery of the Higgs Boson, Measurements of its Production, and a Search for Higgs Boson Pair Production*, CERN-THESIS-2014-084, PhD thesis, University of Pennsylvania, 2014, URL: `https://cds.cern.ch/record/1746004`.

[181] ATLAS Collaboration, *Expected photon performance in the ATLAS experiment*, ATL-PHYS-PUB-2011-007, 2011, URL: `https://cds.cern.ch/record/1345329`.

[182] L. Devroye, *Non-Uniform Random Variate Generation*, Springer Verlag, 1986.

[183] L. Lyons, D. Gibaut, P. Clifford, *How to combine correlated estimates of a single physical quantity*, Nucl. Instrum. Meth. A **270** (1988) 110.

[184] A. Valassi, R. Chierici, *Information and treatment of unknown correlations in the combination of measurements using the BLUE method*, Eur. Phys. J. C **74** (2014) 2717, arXiv: `1307.4003 [physics.data-an]`.

[185] J. J. Zhang *et al.*, *Next-to-Leading-Order QCD Corrections to the Top-Quark Decay via Model-Independent Flavor-Changing Neutral-Current Couplings*, Phys. Rev. Lett. **102** (2009) 072001, arXiv: `0810.3889 [hep-ph]`.

[186] M. Abadi *et al.*, *TensorFlow: Large-Scale Machine Learning on Heterogeneous Systems*, Software available from tensorflow.org, 2015, URL: `https://www.tensorflow.org`.

[187] F. Chollet *et al.*, *Keras*, Software available from keras.io, 2015, URL: `https://keras.io`.

[188] F. Pedregosa *et al.*, *Scikit-learn: Machine Learning in Python*, JMLR **12** (2011) 2825, arXiv: `1201.0490 [cs.LG]`.

[189] X. Glorot, Y. Bengio, *Understanding the difficulty of training deep feedforward neural networks*, PMLR 9: 249-256 (2010).

[190] D. P. Kingma, J. L. Ba, *Adam: A Method for Stochastic Optimization*, CoRR **abs/1412.6980** (2014), arXiv: `1412.6980 [cs.LG]`.

[191] J. H. Friedman, *Data analysis techniques for high energy particle physics*, Proceedings of 3rd CERN School of Computing (1974) 271, URL: `https://cds.cern.ch/record/186223`.

[192] ATLAS Collaboration, *Multi-boson simulation for 13 TeV ATLAS analyses*, ATL-PHYS-PUB-2016-002, 2016, URL: `https://cds.cern.ch/record/2119986`.

[193] ATLAS Collaboration, *Monte Carlo Generators for the Production of a W or Z/γ^* Boson in Association with Jets at ATLAS in Run 2*, ATL-PHYS-PUB-2016-003, 2016, URL: `https://cds.cern.ch/record/2120133`.

[194] J. Butterworth *et al.*, *PDF4LHC recommendations for LHC Run II*, J. Phys. G **43** (2016) 023001, arXiv: `1510.03865 [hep-ph]`.

[195] ATLAS Collaboration, *Jet energy scale measurements and their systematic uncertainties in proton-proton collisions at $\sqrt{s} = 13$ TeV with the ATLAS detector*, Phys. Rev. D **96** (2017) 072002, arXiv: `1703.09665 [hep-ex]`.

[196] ATLAS Collaboration, *Jet Calibration and Systematic Uncertainties for Jets Reconstructed in the ATLAS Detector at $\sqrt{s} = 13$ TeV*, ATL-PHYS-PUB-2015-015, 2015, URL: `https://cds.cern.ch/record/2037613`.

[197] CMS Collaboration, *Measurement of the production cross section of a W boson in association with two b jets in pp collisions at $\sqrt{s} = 8$ TeV*, Eur. Phys. J. C **77** (2017) 92, arXiv: `1608.07561 [hep-ex]`.

[198] CMS Collaboration, *Measurements of the associated production of a Z boson and b jets in pp collisions at $\sqrt{s} = 8$ TeV*, Eur. Phys. J. C **77** (2017) 751, arXiv: `1611.06507 [hep-ex]`.

[199] ATLAS Collaboration, *Measurement of the cross-section for W boson production in association with b-jets in pp collisions at $\sqrt{s} = 7$ TeV with the ATLAS detector*, JHEP **06** (2013) 084, arXiv: `1302.2929 [hep-ex]`.

[200] ATLAS Collaboration, *Measurement of differential production cross-sections for a Z boson in association with b-jets in 7 TeV proton-proton collisions with the ATLAS detector*, JHEP **10** (2014) 141, arXiv: `1407.3643 [hep-ex]`.

[201] T. Junk, *Confidence level computation for combining searches with small statistics*, Nucl. Instrum. Meth. A **434** (1999) 435, arXiv: `hep-ex/9902006 [hep-ex]`.

[202] A. L. Read, *Presentation of search results: the CL_s technique*, J. Phys. G: Nucl. Part. Phys. **28** (2002) 2693.

[203] G. Cowan *et al.*, *Asymptotic formulae for likelihood-based tests of new physics*, Eur. Phys. J. C **71** (2011) 1554, Corrected in: *Erratum to: Asymptotic formulae for likelihood-based tests of new physics*, Eur. Phys. J. C **73** (2013) 2501, arXiv: `1007.1727 [physics.data-an]`.